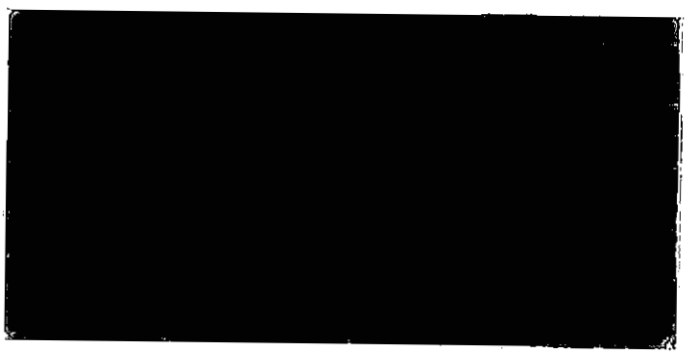

(NASA-CR-120431) FEASIBILITY AND TRADEOFF STUDY OF AN AEROMANEUVERING ORBIT-TO-ORBIT SHUTTLE (AMOOS) Final Report (Lockheed Missiles and Space Co.) 279 p HC $17.00
CSCL 22B G3/31

N74-32325

Unclas
47870

Lockheed

HUNTSVILLE RESEARCH & ENGINEERING CENTER

LOCKHEED MISSILES & SPACE COMPANY, INC.
A SUBSIDIARY OF LOCKHEED AIRCRAFT CORPORATION

HUNTSVILLE, ALABAMA

LOCKHEED MISSILES & SPACE COMPANY

HUNTSVILLE RESEARCH & ENGINEERING CENTER

HUNTSVILLE RESEARCH PARK

4800 BRADFORD DRIVE, HUNTSVILLE, ALABAMA

FEASIBILITY AND TRADEOFF STUDY OF AN AEROMANEUVERING ORBIT-TO-ORBIT SHUTTLE (AMOOS)

FINAL REPORT

July 1974

Contract NAS8-28586

Prepared for National Aeronautics and Space Administration
Marshall Space Flight Center, Alabama 35812

by

John White

APPROVED: C. Donald Andrews
C. Donald Andrews
Project Engineer

B. Hobson Shirley
B. Hobson Shirley, Supervisor
Aero-Mechanics Section

J. S. Farrior
J. S. Farrior
Resident Director

FOREWORD

The work reported herein was performed by the Lockheed-Huntsville Research & Engineering Center for the Aero-Astrodynamics Laboratory of the Marshall Space Flight Center under a supplemental agreement to Contract NAS8-28586. The MSFC technical monitor for this study is Mr. Jesco von Puttkamer, A&TS-CP-T.

ACKNOWLEDGMENTS

The author is grateful for the technical support and contributions during the analysis effort by the following Lockheed-Huntsville personnel: D. A. Love, W. G. Dean, Dr. A. Wernli, D. B. Merriman, F. C. Ketter and W. E. Jones.

Page intentionally left blank

SUMMARY

This study establishes that configurations satisfying the aeromaneuvering orbit-to-orbit shuttle (AMOOS) requirements can be designed with performance capabilities in excess of the purely propulsive Space Tug. In view of this improved potential of the AMOOS vehicle over the propulsive Space Tug concept it is recommended that the AMOOS studies be advanced to a stage comparable to those performed for the Space Tug. This advancement is needed in particular in areas that are either peculiar to AMOOS or not addressed in sufficient detail in these studies to date. These areas include the thermodynamics problems, navigation and guidance, operations and economics analyses, subsystems and interfaces.

The aeromaneuvering orbit-to-orbit shuttle (AMOOS) is evaluated herein as a candidate reusable third stage to the two-stage earth-to-orbit shuttle (EOS). AMOOS has the potential for increased payload capability over the purely propulsive Space Tug by trading a savings in consumables for an increase in structural and thermal protection system (TPS) mass. The savings in propellant is achieved by replacing the burn from return transfer orbit to phasing orbit with the EOS by one or more aerobraking passes through the atmosphere. To achieve the aerobraking maneuver, AMOOS is targeted to a perigee within the earth's atmosphere. The altitude of this target perigee increases with the desired number of passes to achieve the braking maneuver. After the first pass, AMOOS ascends to the perigee of its new orbit, which, of course, is EOS phasing orbit apogee for a one-pass maneuver. If the maneuver contains more than one pass, AMOOS is allowed to descend again toward its perigee, enter the atmosphere, lose energy, leave the atmosphere and ascend to a new, lower apogee. The revolutions and accompanying decay of the orbit continue until phasing orbit apogee is attained. At this apogee a small Δv is applied to raise the perigee to phasing orbit perigee altitude, thus terminating the aerobraking

maneuver. The arc length of these passes through the atmosphere are a small fraction of one revolution and is approximately centered at the perigee.

During these studies, AMOOS evolved as a lifting body. This was in order to provide a means of correcting deviations of the trajectory from nominal during atmospheric flight. These deviations may be due to any source, for example, navigation and guidance, unpredictable atmospheric density variations, etc. Furthermore, the lift force generated can be used to give AMOOS a modest lateral maneuvering capability of approximately 7 deg, if required. These uses of the lift force are truly a synergetic maneuver, for concurrently the drag force is increased thus to a small extent ameliorating the thermal environment by allowing a higher target perigee. To date, the AMOOS investigations have been essentially comprehensive feasibility studies in that all uses of aerodynamic forces typical of a wide range of vehicle geometries have been studied. Furthermore, the study of TPS for the vehicles has covered ablating, reradiating and insulating materials. Deployable high drag devices have also been evaluated. Finally, trades between possible mixed modes of operation, e.g., mixed propulsive and aerobraking orbit transfer and thrusting within the atmosphere to compensate for off-nominal conditions, have been established.

The results discussed in this summary encompass the efforts under the original contract, referred to as Phase I, and under the supplemental agreement, Phase II. This repetition is considered necessary to present a complete overview of the feasibility and potential of the AMOOS concept under one cover.

Phase I – Results Summary: The essence of the Phase 1 study was a literature survey, a general feasibility study and a systematic generation and evaluation of candidate configurations. The literature survey revealed results that led to the conclusions that: (1) compensation for off-nominal conditions was necessary during atmospheric flight, and (2) that synergetic plane change was not feasible for AMOOS during the maneuver to mission altitude transfer orbit. The latter conclusion resulted from the low maximum mission altitude below which a propellant savings was realized. The former conclusion was

drawn from the effects of overall atmospheric density variations. Exo-atmospheric trajectory correction eliminates the one-pass aerobraking transfer maneuver, in fact, integrated trajectory studies showed it also eliminated two and three pass maneuvers. For these reasons, the current AMOOS vehicles have developed as lifting bodies. A detailed navigation accuracy study for the Space Tug revealed that 1976 autonomous navigation systems will not be sufficiently accurate for an AMOOS vehicle nor probably will such systems be sufficiently accurate to place payloads in an acceptable geosynchronous orbit. A drift rate of not more than 1 deg/year is considered acceptable. The relevance of this conclusion has diminished since the selection of an interim tug for early EOS missions. The navigation accuracy study should be repeated in a 1984 time frame. This is discussed briefly in the recommendations, Section 4. The navigation hardware alternatives are discussed in Appendix A and include the state-of-the-art ground based update to development of a sufficiently accurate autonomous system.

A cursory study of the TPS requirements for the AMOOS concept revealed two potential modes of operation in which the AMOOS concept showed a favorable trade. The first, and more promising mode, consisted of a one-pass maneuver using an ablative TPS. The second mode was to use a deployable high drag device. A ballute was selected as representative since it would probably yield a stable configuration. However, detailed studies of the ballute were not performed until Phase II. Again, the choice of TPS was made, as directed by the contract, in the 1976 technology time frame. The findings should be reviewed using a 1984 time frame.

Realistic AMOOS configurations were obtained by a systematic variation of body and nose shape. These configurations were reduced to seven from internal volume and external geometry considerations set by propulsive maneuvering requirements and stowage capability in the EOS cargo bay. From these seven configurations, two were selected as worthy of further refinement and study. The other five were eliminated after a brief thermal, structural

and static stability analysis. The two survivors bore the designations configurations 1 and 5, respectively. An ablative TPS was specified for each configuration and hence a one pass braking maneuver since the recycling of ablative systems is not practical.

Phase II – Results Summary: The Phase II studies consisted of configuration refinements to improve stability, more precise feasibility, trajectory, thermal, structural and weights analyses together with a comprehensive evaluation of the ballute and preliminary operations and cost analysis.

The stability improvement studies eliminated configuration 1 since it could not be stabilized about all axes and retain its basic configuration identity. Refinements to configuration 5 produced a statically stable vehicle about all axes and was redesignated configuration 5B. An entirely new configuration, designated HB, was generated from drag and lift-to-drag considerations at hypersonic Mach numbers. The HB configuration proved to be statically stable about all axes. The HB configuration was eventually selected on the basis of flexibility of internal packaging. This was demonstrated, in particular, by its ease of adaption to the aft positioned large cargo bay configuration which has the potential for development to a modular vehicle. In the modular concept the payload bay is detachable from the propulsive unit so that the TPS and structure required to protect the payload is carried only when the mission includes a payload retrieval.

The choice of the one-pass maneuver using an ablative TPS was further substantiated by more detailed trajectory, thermal and weights analyses. The cost analysis further enhanced the position of the ablative TPS. The more detailed thermal analysis revealed that thermal protection was necessary on the leeward side, because the thermal environment proved too severe for the exposed structure, including titanium. Patching the vehicle with non-ablative TPS materials according to thermal environment did not surpass the purely ablative TPS on a mass basis.

Four materials, titanium (Ti-6Al-4V), and beryllium-aluminum (Be-38 Al), magnesium (HM21A-T8) and graphite/polyimide, were considered for the AMOOS structure. The 5B configuration was stressed for each material

whereas the HB vehicle was stressed for the beryllium-aluminum structure only. In each case the tentative structure was unpressurized and only standard gauges of materials were considered. Beryllium-aluminum yielded the lightest structure with the magnesium structure being a close second. However, the graphite/polyimide structural mass is considered conservative since low material property values were used to compensate for the lack of test data and fabrication technology. Further test data and development of reliable fabrication techniques allowing the use of the full potential of graphite/polyimide are expected to result in this material yielding the lightest structure. The analysis was restricted to these four materials in order to tolerate a 589°K (600°F) bondline temperature. In the analysis, the HB vehicle proved to be lighter than the 5B vehicle. However, the difference is small so that currently the two vehicles should be considered of equal mass.

The baseline and alternate mission payload capabilities of AMOOS are well in excess of those of the Space Tug. A typical comparison is 2642 kg (5812 lb) for AMOOS as compared to 1360 kg (3000 lb) for the Space Tug for the delivery and retrieval of a payload in one mission to equatorial geosynchronous orbit. This AMOOS payload is for the beryllium-aluminum HB vehicle, which proved to be the lightest. The magnesium structure, which is considerably cheaper, gave a 7% decrease in payload. The increased performance may be converted to dry mass contingencies for each mission. The resulting contingencies for the HB beryllium-aluminum vehicle for the baseline, alternate A and alternate B missions are 1272 (2804), 486 (1071) and 1724 kg (3800 lb), respectively.

The corresponding increased payloads are 2642 (5812), 4440 (9768) and 6475 kg (14,245 lb), respectively. The modular concept could result in a further increase in the alternate mission A payload since no protective structure is needed about the payload on a delivery only mission.

The AMOOS payload to orbits about Mars and Venus is 11,296 kg (24,900 lb) each as compared to the Space Tug payloads of 6345 kg (14,000 lb) and 5084 kg

(11,200 lb), respectively. AMOOS uses aerobraking at both Mars and Venus. The round trip payload to and from an orbit about the Moon is 8558 kg (18,828 lb) for AMOOS and 4407 kg (9695 lb) for the Space Tug.

The dimensions of the aft cargo bay will allow AMOOS to transport 100% of the NASA payloads by length and diameter. In this aft cargo bay configuration, the engine, consumables and avionics packages were mounted forward with a hinged nosecap for engine firing. The cargo bay of the HB configuration was, in general, longer than that of the 5B configuration for the same degree of complexity. A preliminary analysis of the HB configuration showed that the larger cargo bay results in no loss of payload capability. Furthermore, feasibility internal layouts yield acceptable c.g. locations and travel. This HB configuration also has the potential for development as a modular vehicle. These configurations require further study to reveal their full development potential.

Studies of the ballute showed this device to be impractical from a mass consideration. A ballute diameter of approximately 60 m (196 ft) was required to reduce the ballute surface temperatures to below the temperature limit of Goodyear Fiber B which is 1367°K (2000°F). The mass of a ballute of this diameter made from Fiber B exceeded the mass savings from reduced TPS and structure requirements. Furthermore, such temperatures are beyond the temperature range of conventional structural materials so that the basic AMOOS vehicle still requires a TPS.

The trade and optimization studies confirmed the selection of the HB configuration using a one-pass maneuver and an ablative TPS. An expansion flap with associated aft body shaping to give a straight hinge line at the extreme aft of the body was selected over an expansion flap with no body shaping and an aft body compression flap with a forward hinge line. The selection was made after aerodynamic, structural and thermal considerations. The mixed atmospheric and propulsive braking maneuver was reassessed resulting in the

confirmation of the desirability of the pure modes over the mixed modes. Propulsive compensation during atmospheric passage for off-nominal conditions proved expensive by requiring approximately 770 kg of propellant. The trade of propellant saved as a function of aeromaneuvering plane change has led to the nominal mode of operation of AMOOS being revised. The current mode of operation is to perform the plane change part propulsively at mission altitude and part aerodynamically at low altitude. This is practical since modulation of the bank angle to produce lift forces to compensate for off-nominal conditions produces only small losses of plane change. These small plane change variations can be corrected economically using the propulsion system. Nominally, the atmospheric passage is made at a bank angle of approximately 90 deg. The sensitivity analysis showed that the payload sensitivity was less for AMOOS than for the Space Tug to variations in I_{sp}, total mass delivered to orbit, and dry mass. This lower sensitivity yields a higher confidence that AMOOS will experience smaller percentage payload changes during development than the Space Tug. This relative position of AMOOS is further enhanced by the current AMOOS structural designs calling for state-of-the-art materials and fabrication techniques.

The operations analysis highlighted the differences between AMOOS and the Space Tug. The operation of AMOOS follows closely the operation of the Space Tug except during atmospheric flight. During this period, AMOOS requires a sophisticated navigation, guidance and control scheme, a requirement, although well recognized, that has not yet been addressed except for a brief literature survey which revealed no applicable technique. A brief company sponsored investigation has established a potential guidance technique which should be further addressed in future efforts. The guidance of AMOOS during atmospheric flight is among the areas recommended for further study. It should be noted, en passant, that temperature or heating rate dependent boundaries are, in general, not applicable to AMOOS since (1) AMOOS must leave the atmosphere with a predetermined energy, and (2) flight path angle and altitude are determined by inertial forces instead of aerodynamic forces during a successful atmospheric pass. This latter fact is due to the high excess energy of AMOOS over circular orbit energy at each

instantaneous altitude. The navigation subsystem alternatives are discussed briefly in Appendix A.4 and include fully autonomous ground based update and navigation or other satellite tracking.

A preliminary cost estimate in 1970 dollars has been prepared for AMOOS. The total first unit cost is $32M for beryllium-aluminum and $29M for the magnesium structure. Whenever possible, the Space Tug costs have been used as a basis for estimating AMOOS costs.

CONTENTS

CONTENTS (Concluded)

NOMENCLATURE

Nomenclature – Flight Mechanics

The following symbols were used in the discussion of flight mechanics and performance topics.

Symbol	Description
A	aerodynamic reference area of vehicle, constant, equal to 15.69 m^2 (168.9 ft^2)
C_D	aerodynamic drag coefficient
C_L	aerodynamic lift coefficient
$\hat{D}$	unit aerodynamic drag vector
g_o	reference gravitational acceleration (m/s^2, ft/sec^2)
I_{sp}	specific impulse of propulsive system (s)
$\hat{L}$	unit aerodynamic lift vector
m_o	vehicle mass before propulsive velocity change (kg, lb)
m_p	propellant mass required for velocity change (kg, lb)
m_f	vehicle mass after propulsive velocity change (kg, lb)
m	vehicle mass (kg, lb)
p	perigee altitude (km, n.mi.)
q	dynamic pressure = $1/2\ \rho\ v_r^2$ (N/m^2, lb/ft^2)
R	altitude (km, n.mi.)
$\ddot{\bar{r}}$	vehicle acceleration vector in inertial earth-centered coordinate system (m/s^2, ft/s^2)
$\bar{r}$	vehicle inertial radius vector in earth-centered coordinate system (m, ft)

NOMENCLATURE (Continued)

Symbol	Description
T	time taken for the vehicle to complete a rotation through a bank angle $\beta = 2\pi$ (s)
$\bar{v}$	inertial velocity vector in earth-centered coordinate system (m/s, ft/s)
$\bar{v}_r$	velocity vector of vehicle with respect to surrounding air mass (m/s, ft/s)
$\bar{v}_w$	wind velocity, combination of earth rotational effects and motion of atmosphere relative to the earth (m/s, ft/s)
β	bank angle, defined as the angle between the local vertical plane containing the relative velocity vector and the lift vector (deg)
$\dot{\beta}$	bank angle rate (deg/s)
$\ddot{\beta}$	bank angle acceleration (deg/s^2)
γ	flight path angle, the angle between the local horizontal plane and the inertial velocity vector (deg)
Δv	velocity change performed (m/s, ft/s)
μ	earth's gravitational constant (m^3/s^2, ft^3/s^2)
ρ	atmospheric density (kg/m^3, lb/ft^3)
ρ_{nom}	nominal atmospheric density at a given altitude (kg/m^3, lb/ft^3)
ρ_E	effective atmospheric density at a given altitude obtained by converting errors in target perigee to an equivalent atmospheric density variation (kg/m^3, lb/ft^3)

NOMENCLATURE (Continued)

Nomenclature – Aerodynamics

The following symbols were used in the discussion of aerodynamic topics.

Symbol	Description
C_D	drag force coefficient in the wind axis system, $F_D/q_\infty S_{ref}$ positive in the negative direction of X_w (dimensionless)
c.g.	abbreviation for center of gravity
C_L	lift force coefficient (stability or wind axis system) $F_L/q_\infty S_{ref}$, positive in the negative direction of Z_s or Z_w (dimensionless)
C_ℓ	rolling moment coefficient in the body axis system, $M_X/q_\infty S_{ref}\ell$ (dimensionless)
C_m	pitching moment coefficient in the body axis system, $M_Y/q_\infty S_{ref}\ell$ (dimensionless)
C_n	yawing moment coefficient in the body axis system, $M_Z/q_\infty S_{ref}\ell$ (dimensionless)
C_Y	side force coefficient (body or stability axis system), $F_Y/q_\infty S_{ref}$, positive in the positive direction of Y (dimensionless)
$\Delta C_m'$	incremental pitching moment coefficient defined as the pitching moment coefficient determined with flap deflection at a particular angle of attack minus the pitching moment coefficient with no flap deflection at the same angle of attack (dimensionless)
F_D	drag force in the wind axis system, positive in the negative direction of X_w (N, lb)
F_L	lift force (stability or wind axis system), positive in the negative direction of Z_s or Z_w (N, lb)
F_Y	side force, positive in the positive direction of Y (N, lb)
L/D	lift-to-drag ratio, C_L/C_D (dimensionless)

NOMENCLATURE (Continued)

Symbol	Description
ℓ_{ref}	reference length (body length) (m, ft), constant, equal to 17.88 m (58.66 ft)
M	Mach number (dimensionless)
M_X	rolling moment in the body axis system; i.e., moment about the X-axis (a positive rolling moment tends to rotate the positive Y-axis toward the positive Z-axis), (N-m, ft-lb)
M_Y	pitching moment in the body (or stability) axis system; i.e., moment about the Y-axis (a positive pitching moment tends to rotate the positive Z-axis toward the positive X-axis), (N-m, ft-lb)
M_Z	yawing moment in the body axis system; i.e., moment about the Z-axis (a positive yawing moment tends to rotate the positive X-axis toward the positive Y-axis), (N-m, ft-lb)
q_∞	dynamic pressure, $\rho_\infty V_\infty^2/2$ (N/m^2, psi)
Re_∞/L	freestream Reynolds number per unit length (1/m, 1/ft)
S_{ref}	reference area (m^2, ft^2), constant, equal to 15.69 m^2 (168.9 ft^2)
T_o	tunnel supply temperature (^oK, ^oR)
T_∞	freestream static temperature (^oK, ^oR)
V_∞	freestream airspeed or speed of the vehicle relative to the surrounding atmosphere (m/sec, ft/sec)
X, Y, Z	body axis system coordinates (the X, Z-plane is the plane of symmetry and the origin of the axis system is the center of gravity, center of mass, or any other convenient point) (m, ft)
Greek	
α	angle of attack, angle between the projection of the wind X_w-axis on the body X, Z-plane and the body X-axis (deg)
β	sideslip angle, angle between the wind X_w-axis and the projection of this axis on the body X, Z-plane (deg)
δ	flap deflection angle, positive when the trailing edge is deflected down (deg)
ρ_∞	freestream air density (kg/m^3, $slug/ft^3$)

NOMENCLATURE (Continued)

Nomenclature – Structures

The following symbols were used in the discussion of structures topics.

Symbol	Description
A_{skin}	skin area (m^2, in^2)
A_{str}	stringer area (m^2, in^2)
b_s	stringer flange width (m, in)
d	stringer spacing (m, in)
E	material elastic modulus (N/m^2, lb/in^2)
F_{cr}	critical stress (N/m^2, lb/in^2)
f	stress (N/m^2, lb/in^2)
g	acceleration factor
h_s	stringer web height (m, in)
ℓ	ring spacing (m, in)
ℓ_{cr}	stringer critical column length (m, in)
M	bending moment (N-m, in-lb)
N	axial line load (N/m, lb/in)
N_D	design line load (N/m, lb/in)
P	axial load (N, lb)
P_D	axial load per typical stringer spacing d (N, lb)
R	radius (m, in)
t	thickness (m, in)
t_s	stringer thickness (m, in)

NOMENCLATURE (Continued)

Greek	Description
μ	Poisson ratio
ρ	density (kg/m^3, lb/in^3)
σ	stress (kg/m^2, lb/in^2)

NOMENCLATURE (Continued)

Nomenclature – Thermodynamics

The following symbols were used in discussion of thermodynamics topics.

Symbol	Description
C_*	$\mu_r T/\mu T_r$ defined for specific geometries in Tables D-1 and D-3, dimensionless
C_H	Stanton Number, $q/(\rho_\infty U_\infty (H_\infty - H_W))$ dimensionless
H	Total enthalpy, (J/kg, Btu/lbm)
K	Thermal conductivity (W/m-^oK, Btu/ft-sec-^oR)
M	Mach number, dimensionless
q	Convective heat transfer rate, (W/m^2, Btu/ft^2-sec)
R	Local body radius, (ft, m)
Re_∞	Free stream Reynolds number, $\rho_\infty U_\infty R/\mu_\infty$, dimensionless
$\tilde{R}e$	Post shock Reynolds number, $\rho_\infty U_\infty R/\mu_\delta = \rho_\delta U_\delta R/\mu_\delta$, dimensionless
T	Temperature, (^oK, ^oR)
U_∞	Free stream velocity, (m/s, ft/s)
x	Surface distance, (m, ft)
Greek	
γ	Ratio of specific heats, dimensionless
θ	Local body angle with respect to free stream velocity vector, deg
θ_c	Cone semi vertex angle, deg
Λ	Sweep angle, deg

NOMENCLATURE (Concluded)

Symbol	Description
μ	Viscosity, (kg/m-sec, lbm/ft-sec)
ρ	Density, (kg/m^3, lbm/ft^3)
Subscripts	
c	Cone
o	Total
r	Reference
W	Wall
∞	Free stream
δ	Post shock conditions
si	Strong interaction

Section 1
INTRODUCTION

An orbit-to-orbit transfer vehicle will be an essential element of the future space transportation system required to accomplish the NASA mission spectrum. The orbit-to-orbit vehicle is a high performance propulsion stage designed to operate as a third stage for the two-stage space shuttle. Past studies have defined vehicle systems which are capable of performing a large number of NASA missions by using propulsive maneuvers in vacuum only. However, the accomplishment of high energy missions such as payload transfer to and from geosynchronous orbit exceeds the capabilities of most of the proposed vehicle systems which have the additional disadvantage of large sensitivity to small inert weight changes and specific impulse variations. To reduce the sensitivity and improve the payload capability of the transfer vehicle, the utilization of atmospheric entry and exit passes is an attractive alternate mode of mission operation due to the possible trade of propulsion requirements for aerodynamic forces for aerobraking and aeromaneuvering. The proposed direct-entry mode applicable to the aeromaneuvering orbit-to-orbit shuttle (AMOOS) vehicle at the associated high velocities, while offering a reduction in propulsion requirements, causes aerothermodynamic loads on the vehicle. Trade studies were developed to provide the data for subsequent concept design studies. During Phase I of the study effort (Ref. 1), the general feasibility of an AMOOS vehicle was investigated and substantiated. Trade studies were conducted which resulted in a number of promising systems. Early results indicate that the use of ablative thermal protection systems (TPS) and one-pass missions lead to improvements in the payload capability compared to a Space Tug-type system.

Because of the favorable results of Phase I, a second study (Phase II) was conducted to investigate in more detail the feasibility of the AMOOS concept, evaluate the specific vehicle systems derived in Phase I and conduct

trade studies for subsequent concept design in a later study phase. To accomplish the objectives of Phase II, the study was divided into the following five tasks:

1. Concepts analysis
2. Trade and optimization studies
3. Operations analysis
4. Technology identification, and
5. Economics analysis.

This document reports the results of the Phase II study.

1.1 DESCRIPTION OF THE AMOOS CONCEPT

The AMOOS concept requires that aerodynamic braking and lateral maneuvers achieved between entry and exit of the earth's atmosphere be substituted entirely or in part for propulsive orbital maneuvers. These atmospheric maneuvers may be on the ascent phase or the descent phase of the mission. However, the conclusion drawn early from the literature survey was that aeromaneuvering on the ascent phase was feasible for only modest mission altitudes and relatively large plane changes. Furthermore, ascent maneuvers were considered impractical for AMOOS since, from early studies, the temperature predictions were too high for 1976 technology reusable materials if the on-orbit time of the earth-to-orbit shuttle (EOS) was not extended. Updating this evaluation to the 1984 time frame is recommended for further study.

Using either present, 1976 or 1984 technology, the AMOOS mission will differ from that of the Space Tug only in the manner in which it achieves phasing orbit with the EOS during the return phase. AMOOS will be targeted to enter the earth's atmosphere a prescribed number of passes from which it will exit, after the last pass, with just sufficient velocity to carry it to phasing orbit apogee. When apogee is attained, a short burn is required to achieve

phasing orbit perigee. Once phasing orbit is achieved, then the AMOOS mission is again identical to the purely propulsive Space Tug. The AMOOS mission is depicted diagramatically in Fig. 1. For completion of the mission from launch to recovery and for comparison, the EOS-Space Tug mission profile has been extracted from Ref. 2 and incorporated as Fig. 2.

1.2 PRELIMINARY VEHICLE REQUIREMENTS FOR MISSION CRITERIA

The capabilities of the AMOOS vehicles are conveniently separated into (1) purely propulsive capability, and (2) aeromaneuvering capability. To perform a mission requiring a geosynchronous orbit, the AMOOS vehicle requires a propulsive incremental impulsive velocity, Δv, capability of approximately 6650 m/s and an aerobraking capability of approximately 2330 m/s. In order to achieve this propulsive Δv capability, it must carry approximately 22,465 kg (49,527 lb) of consumables.

The minimum enclosed volume of an AMOOS vehicle must be approximately 57% of the volume of the EOS cargo bay. Such a volume allows the consumables, payload, engine, avionics etc., to be enclosed for protection from the thermal environment.

The maximum gross mass allowable for the AMOOS vehicles was assumed the same as for the Space Tug. The relevant numbers were taken from Refs. 2 and 3. From these sources it was determined that the maximum mass of AMOOS as delivered to near earth orbit would be 28,848 kg (63,600 lb).

An interesting result of orbit transfer mechanics is that for a two burn transfer the total impulsive velocity increment required to achieve a given circular orbit increases to a maximum of 4200 m/s. The corresponding orbital altitude is approximately 100,000 km. This is due to an increasing fraction of the total Δv being required at the initial (perigee) burn and the steady reduction in orbital speed with increasing orbital altitude. The energy increment, of course, increases steadily. The one way Δv required is plotted

in Fig. 3. The Δv requirement for the Space Tug is just twice the values plotted. The AMOOS vehicle requires the same propulsive Δv outbound but only the apogee Δv on the return. The total propulsive Δv required for AMOOS is also plotted in Fig. 3. The peak Δv requirement is approximately 5520 m/s for an orbital altitude of about 55,000 km. The geosynchronous mission Δv is only 100 m/s less than this peak requirement. In the case of the Space Tug, the geosynchronous orbit Δv is some 500 m/s below the maximum requirement (recall that only one half the total Space Tug requirement is plotted in Fig. 3). The total Δv required by AMOOS is the sum of the propulsive Δv and the aerobraking Δv. This total Δv requirement is, of course, the same as the total Δv requirement for the Space Tug.

Now, the velocities discussed in conjunction with Fig. 3 are the major velocity changes. To these velocities there must be added the orbital correction Δv's, rendezvous and docking Δv's, etc. These Δv's are approximately identical for the two concepts. The only fundamental difference being that AMOOS requires a small Δv at the first passage of phasing orbit apogee to raise the aerobraking perigee to that of the phasing orbit.

Although the propulsive Δv's of AMOOS and the Space Tug reach maxima at some finite orbital altitude, the aerobraking Δv of AMOOS does not. Both the Δv and the energy to be dissipated by the aeromaneuver increase steadily (Fig. 3).

The above results and discussion apply strictly to the two body problem. The presence of the moon and sun influence these results when extrapolated to high orbital altitudes. However, high altitude in this sense is well beyond the geosynchronous in which we are primarily interested.

The baseline tug mission calls for an equatorial geosynchronous orbit and hence a 28 deg plane change. At geosynchronous altitude this plane change requires an increase of only 350 m/s in the Δv to circularize when the maneuvers

are combined. This incremental velocity decreases slowly with increasing altitude so that the results beyond geosynchronous altitude are practically unaffected. Although performing the entire plane change at geosynchronous altitude is not optimum, it is sufficiently close for this preliminary feasibility study. Optimum plane change technique for AMOOS is considered in the trade studies.

As the orbital altitude decreases then the plane change becomes more costly in incremental velocity. In fact, for even moderate plane changes at low orbital altitudes, the minimum Δv maneuver is to transfer to a highly elliptic orbit, perform the plane change at apogee and recircularize to the initial orbital altitude at perigee. This very high Δv (about 3800 m/s at atmospheric pass altitudes) requirement for plane change at low altitudes explains why the AMOOS vehicle requires an $L/D = 2$ to perform a 28 deg aeromaneuvering plane change (Ref. 1, Section 2.2).

1.2.1 General Guidelines

The AMOOS concept is an alternative to the purely propulsive concept as embodied in the Space Tug. It must, therefore, perform identical payload transportation and, in turn, be transported itself in a manner similar to the tug. To these ends, the following guidelines were incorporated into the contract by MSFC:

- Consider that the Space Shuttle will be used to deliver the AMOOS to low earth orbit and to retrieve it from there.
- The baseline payload capability of the Space Shuttle will be 65,000 lb to an orbit of 100 n.mi. circular altitude and 28 deg inclination. Dimensions of the Shuttle cargo bay, used for AMOOS delivery, will be 15 ft diameter x 60 ft length.
- Advanced materials and concepts are to be used with a materials and concepts technology of 1976 and an IOC of the end of 1979.

- AMOOS will be designed as an unmanned vehicle.
- The Space Tug (propulsive maneuvering only) will provide the baseline, to be used as comparison. Ground rules presently being applied to Space Tug studies will also apply to the AMOOS configurations wherever warranted and compatible with the AMOOS' operating environment and capabilities. These ground rules were provided by the government (Ref. 2).
- The atmospheric and exoatmospheric flight environment of the AMOOS were determined based on models provided by the government.

These guidelines, appropriately updated to Ref. 2, were followed. The appropriate updates were: (1) the EOS would deliver AMOOS to and retrieve it from a 296 km (160 n.mi) altitude circular orbit; (2) the EOS phasing orbit was changed to a 315 km (170 n.mi) by 720 km (388 n.mi) altitude elliptic orbit. The baseline (delivery and retrieval of 1360 kg) and alternate A and B (delivery of 3660 kg and retrieval of 1886 kg, respectively) missions were considered applicable to AMOOS.

1.2.2 Basic Mission Profile and Analysis

The basic mission profile consists of four major maneuvers. As stated previously, the maximum propulsive Δv requirement for the AMOOS concept is for the baseline mission. In this case, a propulsive Δv of approximately 6652 m/s is required. This Δv includes phasing orbit, rendezvous, docking and orbit trim maneuvers. The aerobraking Δv is approximately 2330 m/s. If the return phase plane change is performed aerodynamically then the propulsive Δv may be reduced by some 350 m/s and the aeromaneuvering Δv increased vectorially to approximately 5000 m/s. Because of this disproportionate Δv difference between purely propulsive and aerodynamic plane change requirements, the entirely propulsive plane change has been used for the basic AMOOS mission profile.

The propulsive Δv's for the AMOOS concept are given in Table 1. Where applicable the Space Tug Δv values were used. The Space Tug Δv values are given in Table 2 for comparison.

1.2.3 Payload, Propellant Requirements and Structural Weight Allowance

An analysis of the tug baseline and alternate A and B missions (Ref. 2) showed that each mission could be performed by AMOOS and concurrently result in a reasonable allowance for dry mass. The results were that: (1) the baseline mission required more propellant than the alternatives; (2) alternate mission A resulted in the minimum allowance for dry mass and (3) alternate mission B resulted in the maximum reentry mass. In turn then, these missions set the requirements for propellant tankage, structure allocation and TPS mass, respectively. These results show that the payloads of the baseline and alternate B missions could be increased by the AMOOS concept. A summary of the propellant and payload analysis is given in Table 3. This analysis was performed using a net mass (delivered to low earth orbit) of 28,848 kg, I_{sp} = 470s for the main engine at full thrust and 460s throttled, and I_{sp} = 380s for the RCS. The Δv values were taken from Table 1. Since alternate mission B has no outbound payload, its delivered mass was assumed to be 1360 kg less than the other missions. Contingencies, trapped propellant, venting losses, etc., were assumed identical to those for the Space Tug and were taken from Ref. 2.

1.2.4 Vehicle Design Requirements

Each discipline has an input into the vehicle design requirements. The flight mechanics requirement is to design a vehicle with a large lift. This is necessary to provide reserve capability to correct for variations in the vehicle's velocity and position from the nominal values.

The requirement to maximize drag is dictated by TPS mass requirements. Drag should be maximized in order to minimize the mass of the

TPS. A maximized drag minimizes TPS mass because of the higher allowable atmospheric pass to dissipate the same amount of energy as a lower pass, resulting in reduced heating effects.

The aerodynamic constraint, as spelled out in the statement of work (SOW), is that the AMOOS vehicle must be statically stable about all axes at $C_{L_{max}}$ without the use of auxiliary control surfaces. Also the vehicle should be capable of trimming at $C_{L_{max}}$. The requirement of stability about all axes is dictated more by control system design requirements than anything else. This requirement makes the problems associated with flight control system development much easier to solve. Also, control of the hypersonic phugoid mode during reentry is much more complicated if the vehicle is unstable.

The necessity of trimming at $C_{L_{max}}$ is dictated by the necessity of flying the vehicle near $C_{L_{max}}$. If the vehicle is stable and trims at $C_{L_{max}}$, the vehicle should automatically fly at $C_{L_{max}}$ without movement of the trim device.

1.2.5 Volume Requirements

The dimensions and volume of the AMOOS vehicle are governed by the consumables volume, payload dimensions and the restriction that it must be transported in the EOS cargo bay. Concurrently, from the guidelines, the AMOOS vehicle must be stable about each axis and trim at $C_{L_{max}}$. These requirements lead to two approaches: (1) the maximum payload dimension approach, and (2) the maximum body shaping approach. The first approach results in volumetric requirements that allow minimal body shaping to achieve the stability and trim criteria. The second approach results in the easier achievement of the required stability and trim characteristics but at the expense of allowable payload dimensions.

A study was performed to determine minimum volume requirements for the various AMOOS configurations consistent with the payload and propulsion system volumes. The resulting minimum volume for AMOOS was determined as 171.2 m^2 (6044 ft^2) which is approximately 57% of the EOS cargo bay volume. This volumetric analysis was performed in the Phase I study and is, therefore, presented in detail in Ref. 1. A representative, minimum volume, AMOOS packaging studied in Phase I is shown in Fig. 4.

The objective of the aft-mounted payload is primarily to accommodate the largest payload possible. Furthermore, since the payload is carried at the end of the vehicle rather than amidship, this configuration has the potential for development to a modular form. In the modular vehicle concept, the vehicle may be tailored to the mission, for example, for delivery only, the payload does not need a TPS, hence higher payload masses can be carried.

Also considered was a configuration towing a ballute in an attempt to reduce the temperatures on the basic vehicle and payload to the point where a TPS is not required. The design criterion chosen for the initial studies were that temperatures on the ballute would not exceed the capabilities of protected Goodyear Fiber B. This limit is approximately 1367°C (2000°F), which, unfortunately, is well beyond the capabilities of most unprotected structural materials.

Section 2
RESULTS AND DISCUSSION

The two AMOOS configurations selected from the first phase of the study were subjected to further modification and analysis. This further analysis eliminated configuration 1 since a fundamental configuration change was necessary to yield static stability about each axis. This left configuration 5B, a modification of the original configuration 5 to yield all axis static stability, as the only candidate configuration. A new configuration, designated HB, was obtained from drag considerations at hypersonic Mach numbers rather than from systematic geometric variations of vehicle shape as for configuration 5B. Configurations 5B and HB evolved, from performance and TPS considerations, as one-pass aerobraking maneuver vehicles with an ablative heat shield. Two internal layouts were considered. One with a relatively small integral cargo bay carried amidships and the other a large cargo bay carried on one end. This latter configuration yields the potential for a modular vehicle. Only the HB configuration was developed in the aft cargo bay configuration since it yielded a larger bay than the 5B. Since only cursory analysis of high drag deployable devices had been performed in prior studies, the ballute configuration was studied in detail comparable to the 5B and HB configurations.

The results of the study confirmed the feasibility of the one-pass ablative TPS vehicle which was expected from Phase I results. For round trip payload and retrieval missions (Tug baseline and alternate B) AMOOS vehicles showed a definite payload advantage, and a small advantage for payload delivery (alternate A). The ballute compared unfavorably with either configuration. This was due to the large diameter required for the ballute in order to obtain appreciable reductions in the temperature on the ballute surface.

The HB configuration was eventually chosen over the 5B on the basis of it yielding a longer aft payload bay and more readily adaptable to the modular concept.

Aerodynamically there is little difference between the 5B and HB vehicles. The HB vehicle is slightly more statically stable about each axis than the 5B vehicle. However, the degree of stabibility required for AMOOS was not studied nor has a quantitative requirement been established. The HB vehicle also has a dry mass advantage over the 5B vehicle, however, this advantage is so small that the dry masses should be considered equivalent at this point.

Operations analysis has been performed for the AMOOS vehicle with emphasis on those areas different from the Space Tug. No differences were apparent between the 5B and HB vehicles. An economics analysis was also performed. The emphasis here was on use of different types of materials, methods of construction etc., rather than on the differences between the 5B and HB vehicles. Costs would be expected to favor the 5B vehicle because of its simpler geometry, both internal and external.

2.1 CONCEPT ANALYSIS

The seven configurations derived in Phase I were briefly reviewed from a multi-discipline standpoint at the beginning of Phase II. The conclusions of this brief reevaluation were the same as those of the Phase I study (Ref. 1). The conclusions were:

1. AMOOS vehicles 1 and 5 best satisfied all requirements.
2. Both vehicles were longitudinally statically stable at α_{trim}, but additional body shaping was required to provide lateral-directional stability.
3. Trimmable center-of-gravity ranges can be increased through use of a body flap.

Therefore, the major objective of Phase II from an aerodynamics standpoint was to refine the design of AMOOS 1 and 5 such that lateral-directional stability could be obtained. Of course, design of an entirely new vehicle which could meet all design requirements was not ruled out in the beginning of this phase.

In pursuing the aforementioned objective, body shaping was performed on AMOOS 1 to provide roll stability but its directionality could not be improved. By rotating the nose of AMOOS 5, both lateral-directional stability and improved longitudinal static stability were obtained. In addition to attempting to modify AMOOS 1 and 5, a new configuration denoted HB was designed. Each of the configurations along with a summary of their basic aerodynamic characteristics are shown in Table 4.

Since configuration HB is entirely new, a brief description of its geometry is given. Basically, this configuration is a tapered elliptical cylinder, tapering from front to rear, but raked off at the forward end at approximately 45^{o}. This forward face is then shaped to yield maximum drag for a given lift-to-drag ratio. More specifically, the HB configuration is based on a class of forebodies, namely biconics which exhibit maximum drag at a given lift-to-drag ratio (Ref. 4). The HB has essentially three sections (Fig. 5): (1) a nose cap that follows a power-law longitudinal contour, an elliptic transverse contour, and is raked-off; (2) a forebody that has an elliptic transverse contour, a rectangular longitudinal section and is raked off to a triangular longitudinal section to match the nose cap; and (3) a body that has an elliptic transverse contour and a trapezoidal longitudinal section.

A decision was made early in Phase II to select the best two configurations from the four (Table 4) and study those in detail for the remainder of Phase II. The configurations selected were AMOOS 5B and HB (Fig. 6). These two were selected mainly because each met the static stability requirements about all three axes. Each had a higher drag coefficient at maximum C_L than either AMOOS 1 or 5. Initial mass estimates showed the HB vehicle to be heavier than any of the other vehicles. However, at that time, a slight mass increase was considered acceptable to obtain a larger C_D and improved static stability. Later mass estimates showed the HB configuration to be slightly lighter than the 5B configuration.

As mentioned previously, high drag is a desirable attribute for the AMOOS configuration. Both AMOOS 5B and HB exhibit fairly high C_D, but if this could

be increased through use of a deployable drag device, then their masses perhaps could be reduced. Higher drag produces a shallower penetration in the atmosphere, thus possibly enabling elimination of the TPS and some structure.

Several discussions were held with Goodyear Aerospace personnel during Phase I concerning potential materials that would withstand high temperatures. The best candidate was a material called Fiber B, which, when coated, can withstand 1367°K (2000°F). In Phase II a ballute configuration (Fig. 7) utilizing this material was suggested by Goodyear in conjunction with Lockheed, Ref. 5. The feasibility of the ballute was thoroughly investigated and is discussed in Sections 2.6 and 2.7.

2.2 ASSESSMENT OF RANGE OF SPECIFIC FEASIBILITY

2.2.1 Navigation Errors and Atmospheric Density Variations

Earlier studies of the aerobraking concept have indicated that navigation errors and atmospheric density variations have a significant effect on the flight environment and on the amount of aerobraking achieved during an atmospheric pass. Care was taken during the present study to fully account for these effects.

The maximum variations in atmospheric density which may be encountered during the atmospheric portion of the flight of the AMOOS vehicle were obtained from a study by the Aerospace Environment Division, Marshall Space Flight Center. The mean and range of the density in percent of the 1962 U.S. Standard Atmosphere are shown in Figs. 8 and 9. From these figures the appropriate unpredictable density variations were established as +40 and -35% of nominal.

In the Phase I studies these variations were tentatively established as +100 and -50% nominal. Superimposed on these variations were those due to an entry corridor width of $\pm$3.5 km. Since the corridor width may be expressed as an equivalent atmospheric density variation the reduced density variations were used to allow an increase in the entry corridor width to $\pm$6 km. The impact of this corridor width is discussed in Appendix A.4. The results of Ref. 6

are used to show that a landmark tracker is required to achieve the required precision and that the mid course maneuver must be delayed until 1400 s prior to perigee. Delaying the mid course maneuver to this time will require a propellant budget of approximately 140 kg in order to correct for navigational uncertainties of 50 km in position and 5 m/s in velocity as specified in Ref. 2 for high altitude orbits.

As inferred above, the effect of the variation in radial perigee position can be conveniently represented in terms of an associated density variation since the atmospheric density is approximately an exponential function of the altitude, (e.g., a decrease in altitude by 3.5 km results in an increase in density by a factor of 1.63). Thus, the effects of atmospheric density variation and navigation errors can be combined by first converting the navigation error into an associated density variation and then multiplying this associated density variation with the actual density variation. The result is then an effective density variation, which is usually expressed in terms of the ratio of effective density to nominal density, ρ_E/ρ_{nom}. The nominal atmospheric density was obtained from the 1962 U. S. Standard Atmosphere.

2.2.2 Trajectory Compensation Using Lift Force

The lift force resulting from the high angle of attack of the 5B and HB vehicles can be used to compensate for navigation errors and atmospheric density variations during the atmospheric portion of the flight. Some method of lift vector modulation is required. Since the angle of attack is fixed it cannot be used to vary the lift.

A technique of lift vector modulation extensively used was to rotate the vehicle about its velocity vector. A near-zero lift can be obtained if the rate of rotation is constant. A net lift in a direction β_o perpendicular to the velocity vector is obtained by decreasing the angular rate $\dot{\beta}$ if $\beta_o - \pi < \beta < \beta_o$ and increasing $\dot{\beta}$ if $\beta_o < \beta < \beta_o + \pi$ in a manner such that the average $\dot{\beta}$ over one

revolution remains unchanged. Bank angle β, angle of attack α, and flight path angle γ, are defined in Fig. 10. The change in angular rate was performed with an angular acceleration, $\ddot{\beta}$, of constant magnitude but alternating direction. Net lift is defined as

$$\frac{1}{T}\int_{t=0}^{T} \bar{L}\, dt = q S C_{L_{net}}$$

where T is the time for one revolution of β.

The effect that a constant $\dot{\beta}$ has on the trajectory was studied by changing the initial bank angle at atmospheric entry. The results of such a study are shown in Fig. 11 for $\dot{\beta}$ = 6, 8 and 10 deg/s. The variation in apogee altitude after one atmospheric pass is shown as a function of initial bank angle, β_I, at atmospheric entry. The apogee altitude variations with β_I for $\dot{\beta}$ = 6 and 8 deg/s are sufficiently large to cause noticeable changes in parameters used to converge the trajectory to phasing orbit apogee of 720 km. For this reason, $\dot{\beta}$ = 10 deg/s was chosen so that β_I could be ignored in these studies. However, in practice $\dot{\beta}$ = 8 deg/s may be more desirable because a smaller angular acceleration $\ddot{\beta}$ is required to achieve the same net lift. The effect of bank angle rate, $\dot{\beta}$, modulation on net C_L and net L/D has been investigated using a $\ddot{\beta}$ of constant magnitude but of alternating direction as outlined above. The value of $\ddot{\beta}$ which is just sufficient to reduce $\dot{\beta}$ to zero during one-half revolution marks a point of discontinuity in the net C_L versus $\ddot{\beta}$ curve (Fig. 12). For this investigation only values of $\ddot{\beta}$ less than this critical value were considered. The investigation was performed for $\dot{\beta}$ = 6, 8 and 10 deg/s with appropriate values of $\ddot{\beta}$. A constant atmospheric density was assumed over a revolution. This is not rigorous but is a close approximation over the revolution occurring in the most dense atmosphere.

In Fig. 12, the ratio $C_{L_{net}}/C_L$ is plotted against $\ddot{\beta}$ for the three values of $\dot{\beta}$. The ratio, $C_{L_{net}}/C_L$ is independent of C_L under the above definition of net lift. The maximum value of this ratio is independent of $\dot{\beta}$ but occurs at different values of $\ddot{\beta}$. This identical maximum value of $C_{L_{net}}/C_L$ occurs

because the ratio of dwell times in the appropriate half revolutions is independent of $\dot{\beta}$ for the corresponding critical value of $\ddot{\beta}$. The dependency of $C_{L_{net}}/C_L$ on $\dot{\beta}$ can be eliminated by plotting $\ddot{\beta}/\dot{\beta}^2$ on the abscissa. Figure 13 shows the net lift-to-drag ratio for the 5B and HB vehicles for $\dot{\beta}$ = 10 deg/s and for $\ddot{\beta}$ up to the critical value $\ddot{\beta}$ = 1.1 deg/s^2.

The range of navigation errors and atmospheric density variations which can be compensated for by this method of lift vector modulation were investigated. The effects of navigation errors and atmospheric density variations were combined in terms of the ratio of effective density to nominal density, ρ_E/ρ_{nom}, as outlined in Section 2.2.1. Figure 14 shows the magnitude of angular acceleration as a function of ρ_E/ρ_{nom}. The results are for the return from a geosynchronous mission in one atmospheric pass and an average rotation rate of 10 deg/s. A small upward net lift corresponding to $\ddot{\beta}$ = 0.2 deg/s^2 was applied to the nominal trajectory to give the AMOOS vehicle approximately the same capability for the high and low density side. The maximum value of $\ddot{\beta}$ shown in Fig. 14 is the value which reduces the angular rate, $\dot{\beta}$, to zero during one-half revolution. Only values of $\ddot{\beta}$ below this critical value were considered. From Fig. 14 it is seen that a range of ρ_E/ρ_{nom} from 0.32 to 3.5 can be achieved. With an atmospheric density variation from -35 to +40%, as obtained from Figs. 8 and 9, a variation in target perigee of +6 km and -8.5 km could be compensated for by this method of lift vector modulation. This assumes that the effects of navigation errors and density variation are combined by the RSS method. These results apply to missions with one atmospheric pass only.

The lift-to-drag (L/D) ratio required to compensate for navigation errors and density variations for single and multiple atmospheric passes was investigated in connection with the trade studies between lift requirements for orbit inclination change and compensation for off-nominal conditions. For this investigation the lift vector was held at a fixed bank angle such that the lift component in the local vertical direction was just sufficient to compensate for the off-nominal conditions. The L/D required to compensate

for off-nominal conditions is presented in Fig. 15 as a function of the ratio of effective density to nominal density for 1, 2 and 3 atmospheric passes. The results are for a return from geosynchronous mission orbit for vehicle HB. The L/D requirement is vehicle independent to first order and the data in Fig. 15 apply therefore as well to vehicle 5B. A small upward net lift was used for the nominal trajectories to obtain approximately equal vehicle capabilities for high and low density conditions. It was found that the L/D requirements to compensate for given off-nominal conditions increases approximately proportional to the number of atmospheric passes.

2.2.3 Orbital Inclination Change Using Lift Force

An orbital inclination change can be effected if there is a net lift component perpendicular to the orbital plane. To determine the inclination change capability for the candidate vehicles under nominal conditions (no navigation errors and nominal atmospheric density) the bank angle was held fixed such that the lift vector lies in the local horizontal plane. This vehicle attitude yields approximately the maximum orbital inclination change. If part of the lift force is to be used to correct for navigation errors and atmospheric density variations the inclination change capability is reduced. To investigate this reduction in inclination change capability, off-nominal conditions were simulated and the bank angle fixed at such an angle that the lift component in the vertical direction was just sufficient to correct for the chosen off-nominal conditions. The resulting inclination change via aeromaneuvering is the maximum possible under these conditions.

The maximum inclination change capability under nominal conditions is shown in Fig. 16 as a function of inertial velocity at atmospheric entry at 120 km altitude. Shown on the abscissa is the corresponding mission altitude for a return via a Hohman transfer ellipse. The results are presented with L/D as a parameter and are for 1 to 10 atmospheric passes. The results apply to both AMOOS vehicles, 5B and HB, since the L/D requirement to

effect a certain inclination change under given conditions is vehicle independent to first order. Entry velocities above 11,200 m/s correspond to returns from lunar and planetary missions.

Figure 17 shows the inclination change capability versus angle of attack for vehicles HB and 5B for nominal conditions. The results are for a return from geosynchronous mission orbit and are for 1 to 10 atmospheric passes. The inclination change capability proved to be independent of number of passes up to ten. Therefore, the curves of Figs. 16 and 17 apply to any number of passes from one to ten.

The results of the study of the conflicting requirements between the use of lift force for inclination change and for compensation for navigation errors and density variations are presented in Fig. 18. The orbital inclination change capability is shown as a function of the effective density to nominal density. The deviation of effective density from the nominal density represents the effect of navigation errors and atmospheric density variations which is compensated by using a portion of the lift force. Results are presented for atmospheric entry velocities, V_E, of 10,300, 13,000 and 16,000 m/s and for 1, 2 and 3 atmospheric passes. The inclination change capability for one atmospheric pass is not greatly reduced within the range of off-nominal conditions considered. The situation becomes less favorable as the number of passes, n, increases since the L/D requirements to compensate for given off-nominal conditions is approximately proportional to n (see Fig. 15).

2.2.4 Aerobraking Using High Drag Devices

From the outset of the study, the approach has been from the viewpoint that ability to compensate for off-nominal atmospheric conditions is of prime importance. Recall that these off-nominal conditions may arise from unpredictable variations in the atmosphere itself and from off-nominal trajectories arising from navigation, guidance and control errors. The evaluation of high drag devices must be from the same point of view.

The basic concept of the high drag device is, essentially, that it is an alternative to the TPS. By raising the drag area sufficiently the heating rate can be reduced to the point where an unprotected, lightweight structure of aluminum, say, can withstand the temperatures associated with atmospheric passage. Before proceeding with the specific discussion of the high drag device some of the general concepts learned or used in Phase I of the study will be reviewed.

During atmospheric passage a certain, predetermined quantity of energy must be dissipated. This energy excess is dependent upon mission altitude and, furthermore, for a given mission altitude the atmospheric entry velocity and the desired egress velocity are almost independent of parameters other than mission altitude and phasing orbit apogee. The Phase I studies showed that the energy dissipation is performed almost impulsively at perigee, which, of course, is within the atmosphere. Because of this impulsive effect combined with the velocity requirements the product, $n\ \rho_{max}\ C_D$, at design conditions, is a slowly varying function of n, the number of passes per mission and C_D, the drag coefficient based on an arbitrary fixed reference area. In practice, $n\ \rho_{max}\ C_D$ may be considered constant for wide ranges of n and C_D for a return from a given mission altitude. Next recall that in a multi-pass maneuver, very approximately, the velocity is reduced by $\Delta v/n$ each pass where Δv is the excess velocity of the return orbit over the transfer orbit to phasing orbit.

These approximate results may now be applied to discuss heating rates. Now, for a given mission altitude, elementary empirical results of heating rate studies show that, under the above conditions, the maximum heating rate will be proportional to $\rho_{max}^{1/2}$, and hence to $(1/n\ C_D)^{1/2}$. Therefore quite large increases in n, C_D or the product $n\ C_D$ must be expected in order to reduce the heating rate. The integrated trajectory studies have verified this conclusion. Furthermore, radiative type TPS materials are temperature sensitive rather than heating rate on heat load sensitive and the heating rate converts to a TPS temperature according to the fourth power radiative law. Hence the increase in the device parameters, namely n, C_D or the product $n\ C_D$, is

massive to achieve even moderate decreases in temperature, e.g., a 32-fold increase in diameter is required to halve the temperature on the unprotected spacecraft since C_D, as defined herein, is approximately proportional to the square of the scale of the device for a given shape. It is this massive drag area sensitivity that essentially defeats the high drag device.

The high drag device, as with other techniques, must have an associated technique for the compensation of the effects of off-nominal atmospheric and trajectory conditions. For the high drag device the principal techniques are: (1) drag modulation or termination; (2) modulation of the number of passes per maneuver; (3) thrusting to produce a normal force. Rigging the spacecraft in order to produce lift has also been suggested. Thrusting per se is considered in Section 2.7, and requires approximately 770 kg of propellant.

The modulation of the number of passes was used in Ref. 7 to compensate for unpredictable atmospheric density variations. The results validate the use of the product

$$\rho_{max}{}^{n} C_D.$$

When off-nominal trajectory effects are included, ρ_{max} varies by approximately an order of magnitude. Hence n must vary by an order of magnitude. Now a 10-pass maneuver is the maximum that can be accommodated in a six day on-orbit lifetime. Therefore, the design environment must be for a one pass mission to accommodate the high atmopsheric density low target perigee limits. The nominal maneuver would be approximately a three pass mission. Fractional passes would be interpreted as high drag termination in some way, e.g., deflating the device, stowing or discarding it. The design criteria for the pass modulation technique reduces, therefore, to the nominal one pass environment. Therefore device size, etc., is obtained on considerations of the one pass maneuver.

In order to use drag modulation to compensate for off-nominal conditions the drag coefficient must be modulated by an order of magnitude. This

interprets into a 10 to 1 variation in drag area which is probably difficult to achieve. Furthermore, the design criterion for the drag modulation case is obtained from the nominal conditions for the maneuver with the selected number of atmospheric passes. Hence, a one pass maneuver with a maximum drag coefficient of ten times that of the basic AMOOS configuration must be designed, in the worst case, to withstand the nominal thermal environment of AMOOS and hence require an ablative TPS. This simple result demonstrates the massive size to be expected of the high drag device.

To obtain a definite design point for a high drag device, integrated trajectories were obtained for the HB vehicle with a trailing ballute.

The drag coefficient of the ballute, based on EOS cargo bay diameter, was varied in order to achieve a range of thermal environment and hence establish the trade between partial thermal protection and amelioration of the thermal environment by the high drag device. The variation in target perigee, ρ_{max}, q_{max} with ballute diameter is given in Section 2.4.2.

2.3 MISSION DEFINITIONS

The incremental velocity requirements for a large spectrum of missions were computed for the AMOOS vehicle as well as for the Space Tug.

Incremental velocity requirements versus mission altitude are shown in Fig. 19. Curves are shown for missions involving a 28.5-deg inclination change as well as no inclination change. For the AMOOS vehicle the propulsive and the aeromaneuvering Δv requirements are shown separately. The sum of the two, of course, is identical to the Δv requirement of the propulsive Space Tug. Gravity losses, contingency and the Δv values for small orbital maneuvers are not included in the data shown on Fig. 19. The incremental velocities for orbital maneuvers, midcourse correction, docking, attitude control, gravity loss and contingency are given in Appendix A.

An interesting result of orbit transfer mechanics is that, under the assumption of two burn Hohman transfers, the total impulsive mission velocity increment decreases with increasing altitude after reaching a maximum at a certain altitude. This maximum occurs at about 70,000 km and 100,000 km for 28.5 and 0-deg orbit inclination change, respectively. This is due to an increasing fraction of the total Δv being required at the transfer ellipse perigees and the steady reduction in orbital speed with increasing orbital altitude. The energy increment, of course, increases steadily.

Schedules of the consumables expended in executing the baseline mission and alternate missions A and B are shown in Appendix A. A detailed description of these schedules is also given in Appendix A.

The payload mass capability for the AMOOS vehicle was determined on the basis of the Δv budget and the expendables schedule. The payloads were computed for the four structural materials of the 5B vehicle and for the beryllium-aluminum HB vehicle. Payloads for the baseline, alternate A and B missions are presented in Table 3. Each mission is to an equatorial geosynchronous orbit. Figures 20, 21 and 22 show the payload mass capability as a function of mission altitude for the baseline mission (deployment and retrieval of the same payload mass), alternate mission A (delivery of a payload only) and alternate mission B (retrieval of a payload only), respectively. A circular mission orbit was assumed. Curves are shown for missions involving 28.5-deg inclination change as well as no inclination change. Also shown for comparison is the payload mass capability of the purely propulsive tug as defined in the Baseline Tug Definition Document (Ref. 2). The payload mass capabilities shown in Figs. 20, 21 and 22 are for AMOOS dry masses of 3774 kg (8320 lb) and 4589 kg (10,117 lb) which represent the lightest and heaviest dry mass respectively.

The advantage of the AMOOS concept over the purely propulsive tug lies in missions to high orbits where the propellant savings as a result of

aerobraking are largest. This is clearly shown in Figs. 20, 21 and 22. The advantage of the AMOOS concept diminishes for lower mission orbits and the point is reached where the propellant saved by aerobraking cannot offset the additional mass due to TPS and heavier structural mass. For mission altitudes below this point the purely propulsive tug has a larger payload mass capability.

Total delivered mass capabilities to orbits about Mars and Venus were also computed. These masses were obtained using approximately minimum Δv transfer orbits and aerobraking at Mars and Venus. The round trip payload to the Moon was computed for a 72-hour transfer trajectory. The mission profile includes insertion into lunar orbit and return to near Earth orbit using aerobraking to transfer to EOS phasing orbit. The results are presented in Table 5. The payload to Mars and Venus is 11,318 kg (24,900 lb). These payloads are identical since the Δv values required for the transfer orbit from near earth orbit to either planet are negligibly different. These figures are well in excess of the payloads for the Space Tug which were estimated as 6836 kg (15,040 lb) and 5491 kg (12,080 lb) to Mars and Venus respectively. The round trip lunar payload for AMOOS is 8558 kg (18,828 lb) as compared to 4407 kg (9695 lb) for the Space Tug. The payload for the interplanetary and lunar missions is taken as the total mass delivered.

An investigation was made to determine the capability of the AMOOS vehicle to perform the projected Space Tug missions between 1983 and 1990. The basic source of data for this task was the Traffic Model for the Space Shuttle (Ref. 8). DoD missions were not considered for lack of information. The total number of missions studied were 149. The capability of performing a given mission was determined on the basis of payload mass, volume and dimensions (length and diameter). The results are given on the following page.

Percent of Missions AMOOS Can Perform on the Basis of Payload

Description	Mass	Volume	Length and Diameter
High Density Payload Configuration	98%	60%	45%
High Volume Payload Configuration (Aft Cargo Bay)	98%	100%	100%

It was found that all missions requiring a large orbital inclination (polar missions) could be performed in terms of payload mass. The 2% of the missions which could not be accommodated on the basis of payload mass require an expendable purely propulsive vehicle because of the high propulsive ΔV required. A kick stage and/or lunar slingshotting could possibly give AMOOS 100% capability. Lunar slingshotting with a kick stage would allow for the recovery of the AMOOS vehicle.

2.4 ANALYSIS OF FLIGHT ENVIRONMENT

The data required to perform the thermodynamic analysis of the flight environment and the structural analysis of the vehicle were obtained from trajectory simulations. These simulations were performed with a vehicle mass of 10,000 kg and an aerodynamic reference area of 15.69 m^2. The continuum drag and lift coefficients used to obtain the trajectory are presented on each figure. The vehicle mass of 10,000 kg corresponds to a payload retrieval mission with a payload mass of approximately 5500 kg. During the early phase of this contract, trajectory simulations for both vehicles, HB and 5B, were performed with preliminary aerodynamic data. It was found then that the flight environment for the two vehicles were similar. In particular it was found that the mass of the thermal protection system was mostly a function of the difference in vehicle geometry between vehicles HB and 5B rather than a function of the difference in flight environment. Based on this observation the trajectory data were recomputed only for vehicle HB with the more refined aerodynamic data, which became available after the wind tunnel test.

The aerodynamic drag coefficients for the ballute were estimated using the Hypersonic Arbitrary-Body Program. The shadowing effects of the HB configuration leading the ballute were not estimated.

The trajectories and hence trajectory parameters were obtained by numerical integration of the equations of motion. Drag and lift coefficients for continuum and free molecular flow are inputs to the trajectory simulation computer program. The Lockheed bridging scheme (Ref. 1, Appendix C.4) is an integral part of this program so that drag and lift coefficients are automatically varied along the trajectory as a function of Knudsen number. The 1962 U.S. Standard Atmosphere was used throughout these studies to give atmospheric density as a function of altitude.

A preliminary study was performed to determine the importance of transitional flow on the trajectories and hence the environment. To investigate the effects of this dependence upon apogee altitude after the aeromaneuver, the altitude at which transition from continuum to free molecular flow begins was varied from nominal. The results are presented in Fig. 23 for a one-pass mission.

For the favored one-pass mission, the current configurations are somewhat insensitive to such changes in transition altitude. However, the sensitivity increases with the number of passes. A preliminary study of a ten-pass maneuver showed that for C_L and C_D held constant at the continuum values the apogee altitude increased by 500 km. When the transition altitude was decreased by 10 km the vehicle reentered on the tenth pass. Both of these variations are unacceptably large and would require correction during atmospheric flight.

The thermal environment was computed using heating rate formulas dependent upon flow regime. These formulas are given in Section 2.5.2. It should be noted that the flow regimes designated continuum, transitional and free molecular for thermodynamic purposes do not necessarily correspond to the same designations for aerodynamic purposes.

2.4.1 Flight Environment for the 5B and HB Configurations

Figures 24, 25 and 26 present the target perigee altitude, maximum atmospheric density and maximum dynamic pressure, respectively, as a function of the inertial velocity at atmospheric entry at 120 km altitude. Also shown on the abscissa is the mission altitude corresponding to the entry velocity if a Hohman transfer ellipse is assumed. The data are for nominal atmospheric conditions and for a phasing orbit apogee altitude of 720 km. Entry velocities above 11,200 m/s correspond to returns from lunar and planetary missions. For missions involving multiple atmospheric passes and entry velocities above a certain value the constraint must be satisfied that during the first atmospheric pass enough energy is being dissipated to keep the vehicle from escaping the earth's gravitational field. In practice, the apogee altitude reached after the first atmospheric pass must not exceed a certain limit in order to satisfy the mission time line. This apogee altitude was chosen as 35,000 km for the data in Figs. 24, 25 and 26. The dashed portions of the curves represent trajectories where this constraint has been reached.

The advantage of the multipass aeromaneuvers is to reduce the severity of the flight environment. Below certain limits for the entry velocity, depending on the number of passes, the excess energy of the vehicle is dissipated in approximately equal increments during each pass of a multipass mission. The solid curves in Figs. 24, 25 and 26 represent this region. The advantage of multipass aeromaneuvers of more than two passes is lost at entry velocities above certain limits since the most severe flight environment is then encountered during the first atmospheric pass.

Typical nominal trajectories are presented in Figs. 27 and 28 for a one-pass and a five-pass aeromaneuver. These trajectories are computed using HB aerodynamic data. The plots of atmospheric density and dynamic pressure show the effect of the rotation about the velocity vector. In the

case of the five-pass mission the decay of the perigee is noticeable. The decay of the perigee is such that q_{max} for each pass varies slowly compared to ρ_{max}.

Nominal and off-nominal trajectories are shown in Figs. 29 and 30 for a one-pass aeromaneuver and for a return from a geosynchronous mission orbit. The two off-nominal trajectories shown are for a combination of navigation errors and atmospheric density variations. Navigation errors are represented by a $\pm$3.5 km variation in target perigee. The atmospheric density variation is +40 and -35.5% from its nominal value. The atmospheric entry and egress speeds are almost independent of target perigee. The low, dense atmospheric trajectories are shorter timewise than nominal and the high, sparse atmospheric trajectories are longer timewise than nominal.

As indicated in Section 2.2.1 the effect of the variation in atmospheric density and the variation in target perigee can be combined in terms of the ratio of effective density to nominal density, ρ_E/ρ_{nom}. This ratio is 0.395 for the low density and high target perigee condition and 2.28 for the high density and low target perigee condition. These ratios represent the density variations a ballistic vehicle would encounter.

The ratio of the maximum density the vehicle encounters during the low density and high target perigee condition to the maximum density during the nominal trajectory is 0.66 (see Fig. 29). The corresponding ratio for the high density and low target perigee condition is 1.41. If these ratios of actual encountered density are compared with the above mentioned ratios of effective density, the advantage of a maneuvering vehicle over a ballistic vehicle is evident.

Typical stagnation heat loads for configurations HB and 5B trajectories are presented in Table 6. For comparison purposes, the heat load to a 1-m radius sphere are presented. Various trajectories are presented to show the effect of atmospheric density variations and entry point altitude variations.

In Table 6, "RHOFAC" denotes the factor by which the nominal density is multiplied to get the variation effects. Flight times for atmospheric passage from 122 km (400,000 ft) altitude are shown for comparison purposes. Table 6 is for one-pass missions only.

Table 7 presents peak heating rates and total heat loads for multiple pass missions for configuration HB trajectories. Both nominal and off-nominal conditions are shown.

2.4.2 Flight Environment for Ballute Configuration

The flight environment was investigated for the ballute configuration under the assumption that drag modulation is employed to compensate for off-nominal conditions. A variation in target perigee of ± 3.5 km was used to represent navigation errors. These were coupled with +100 and -50% variations in atmospheric density at a given altitude. The fully inflated ballute yields the highest drag coefficient. The highest drag coefficient must be used to provide braking with the minimum design atmospheric density, namely 3.5 km high and $0.5\ \rho_{max}$. Increasing the atmospheric density to that corresponding to 3.5 km low and $2\ \rho_{max}$ yields approximately an order of magnitude increase in ρ_{max}. Atmospheric density, altitude and dynamic pressure are shown in Figs. 31 and 32 as a function of relative velocity for the two extreme trajectories.

A study was performed to determine the effect of the ballute diameter on the flight environment. The trajectory parameters were determined by assuming a ballute with a shape suggested by Goodyear Aerospace but with the diameter as the varying parameter. The number of atmospheric aerobraking passes was assumed as the control variable to compensate for density variations and navigation errors. The one-pass mission corresponds to the most dense atmosphere and thus to the most severe flight environment. Maximum density and target perigee altitude for such a one-pass mission are

shown in Fig. 33 as a function of ballute diameter. A return from geo-synchronous orbit was assumed.

The thermal environment and resulting temperatures for the ballute is given in Table 8.

2.5 DESIGN DATA PARAMETERS FOR THE 5B AND HB CONFIGURATIONS

The ground rules, sources and methods used for estimating the aerodynamic parameters, heating rates, TPS, structure, weights and costs of the TPS and structure are given in this section for the 5B and HB vehicles.

2.5.1 Aerodynamic Design Data Parameters

The aerodynamic design data parameters for both the AMOOS 5B and HB vehicles are presented in this section. Initially, a compression and an expansion flap (Fig. 34) were considered for use with AMOOS. The compression flap is body-curved with a hinge point located at the bottom of the aft fuselage, 2.532 m forward of the base. The expansion flap is a flat plate hinged at the bottom of the base. The compression flap was eliminated from further consideration following an experimental test program, which showed the flap to be ineffective at deflections greater than 10 deg.

The original data for the flaps and the basic configurations were generated by the Hypersonic Arbitrary-Body Program (Ref. 9) with Newtonian flow assumed. Although a Newtonian flow assumption is probably not completely valid, the accuracy was thought good enough to enable comparison of different configuration's aerodynamic characteristics. Therefore, data generated by this program were utilized to select both AMOOS HB and 5B for detailed study in Phase II.

In order to obtain more accurate aerodynamic characteristics a wind tunnel test program was conducted in the NASA-Ames 3.5 ft Hypersonic Tunnel. Both the AMOOS HB and 5B were tested with a compression and expansion flap (see Ref. 10). The basic conclusion of the test program was that Newtonian theory predicted the aerodynamics with reasonable accuracy except for compression flap deflections greater than 10 deg. Also, Newtonian theory apparently did not accurately predict the pressure distribution around the HB blunt nose resulting in a poorer comparison between theoretical and experimental data than for the 5B vehicle, but still acceptably accuracy for preliminary design data.

Since wind tunnel data was obtained and is more accurate than the Newtonian theory predicted data, all design data parameters shown in Figs. 35 through 46 were derived from the wind tunnel test data. From these plots the following conclusions may be made about the aerodynamics of both vehicles.

1. Both high C_L and C_D have been obtained (Fig. 35).
2. L/D is seen to be adequate for mission accomplishment when Figs. 36, 37 and 38 are compared to the L/D requirements in Fig. 15.
3. Both vehicles are stable about all three axes at a trimmed center-of-gravity corresponding to an angle of attack at $C_{L_{max}}$ with no flap (Figs. 39 through 42).
4. Both vehicles are capable of trimming througout the expected center-of-gravity range in a stable attitude utilizing the expansion flap (Figs. 43 through 46).

Some preliminary data have been generated for a modified expansion flap and vehicle afterbody (Fig. 47). This modification was made necessary by the observance during the wind tunnel test of flow over the top side of the flap. This would cause high heating rates on the top side of the flap, which is undesirable from a thermodynamic standpoint.

The new flap configuration is called the ramp flap. It consists of a ramp fore-surface with a flat plate hinged at the base. There is no slot for rocket nozzle clearance in the flap as existed in the expansion flap. The ramp flap must be deflected downward to avoid plume impingement while the main engine is fired. While stored in the orbiter cargo bay the flap will be deflected upward so it will be flush with the base for clearance. Aerodynamic characteristics for the ramp flap have been generated utilizing the Hypersonic Arbitrary-Body Program (Appendix B).

In general the ramp flap is better from a multi-discipline standpoint than the expansion flap. Therefore, any future work should involve this flap.

2.5.2 Thermodynamic Analysis Summary

During Phase I the convective aerodynamic heating rates were calculated using only continuum methods. However it was decided, due to the high altitude of the AMOOS trajectory, that a study should be made to determine if non-continuum flow was being encountered. If so, then different methods would be needed to more accurately calculate the heating. A short study was done and it was found that, for most of the heat load, the flow was in the transitional regime between continuum and free molecular. The criterion used in making this determination was as follows:

For

$$\frac{M_\infty}{\sqrt{Re_{\infty,R}}} > 3.0$$

the flow is free molecular, where M_∞ is the freestream Mach number and $Re_{\infty, R}$ is the freestream Reynolds number based on body radius.

For

$$\frac{M_\infty}{\sqrt{Re_{\infty, R}}} < 0.05$$

the flow is continuum.

These criterion were taken from a study by Engel (Ref. 11).

A computer program was then developed to calculate maximum non-continuum heating rates on spheres, flat plates, cones and cylinders. The equations used in this program were taken from Ref. 11 and are listed in Appendix D. This program was then used to calculate heating rates for numerous trajectories throughout Phase II.

Radiative heating rates were calculated by the method of Perrine (Ref. 12) and found to make an insignificant contribution to the total heat load.

Convective heating rate distributions around the bodies used for this study were taken from Ref. 13. These distributions were originally developed for continuum flow. However, according to Engel (Ref. 11), transitional flow regime distributions are generally similar to the continuum distributions.

Typical results of the heating environment are shown in Fig. 48.

Lee-side convective heating rates were determined using the experimental distributions of Ref. 14. See Appendix D for further details.

Various TPS materials were considered for AMOOS including the following: (1) coated columbium; (2) various superalloys; (3) an external rigid ceramic insulation known as LI-900 and presently being made by Lockheed for the Space Shuttle Orbiter; (4) carbon-carbon; and (5) two ablators, a Langley-developed low-density and SLA-561 developed by the Martin Company.

Pertinent thermal properties for these materials are given in Appendix D.

In the analyses of these materials various methods were used as required. For example, in the radiative type TPS materials such as coated Columbium and superalloys, the peak heating rates were used to determine the maximum radiative-equilibrium temperature for various trajectories, body locations and configurations, e.g., HB or 5B. These peak temperatures were then compared to the allowable temperature for each material according to Fig. 49 to see if that material was applicable and to determine the mass per unit area.

For the LI-900 material which is primarily an insulator and radiative material, the Lockheed Thermal Analyzer Program was used (Ref. 15). The program performs a detailed conduction and radiation analysis with a variable thermal properties capability. The LI-900 material has the advantage that it is lightweight but is still reusable. Its density is approximately 144 kg/m^3 (9 lbm/ft^3) as compared with an earlier version of the similar Lockheed material LI-1500 which had a density of 240 kg/m^3 (15 lbm/ft^3). The LI-1500 material was considered for AMOOS in the Phase I study.

To compute the required thicknesses for the ablative TPS materials, the NASA-Johnson Space Center STAB II ablative analysis program (Ref. 16) was used. A 589°K (600°F) bond-line temperature limit was used in sizing the ablative material thicknesses. The bondline is where the ablator is actually bonded to the substructure. *This criterion is from Apollo experience.*

The STAB II computer program was used to generate an ablator thickness versus total heat load curve for each material. This same curve was then used to apply to each "node" or subarea of the vehicle surface to determine a local thickness according to the local heat load. These local values were converted to masses and summed to give the total TPS mass. Ablative materials were considered only for one-pass missions, i.e., they are not reusable.

For the carbon-carbon material no detailed thermal analyses were conducted since this material is quite heavy and very expensive. The cost is discussed later in this section. However, this material was considered initially due to its reusability at extremely high temperature for areas such as a nose cap or leading edge.

Results of the TPS analyses showed that a one-pass mission using the Langley low-density ablator would give the lightest TPS mass. Table 9 shows the ablative TPS masses for various trajectories for HB and 5B configurations. These masses are for the windward side only. These masses do not include the trim flap TPS masses. For the HB and 5B the flap TPS masses are 16 kg (35.2 lb) and 15.2 kg (33.4 lb), respectively, for the worst case trajectory. The masses given in Table 9 include an additional 10% for closeouts around doors, access hatches, etc., and 0.74 kg/m^2 (0.15 lb/ft^2) for sealer and bonding agents. These numbers are from Apollo TPS experience.

Results of the lee-side TPS analysis showed that the minimum thickness required for manufacturing purposes of 0.25 cm (0.1 in.) would be sufficient for thermal protection. This yielded a mass per unit area of 0.570 kg/m^2 (0.117 lb/ft^2).

Figure 50 presents results of a comparison of LI-900 material and the Langley low-density ablator. The curves shown are for mass per unit area versus total heat load. As seen the LI-900 is about 50% heavier.

Since cost is to be an important consideration in the AMOOS program, it was felt that it might be worthwhile to consider a heavier TPS if a significant cost reduction could be obtained. It was felt that a cost analysis might show that the reusable materials were cheaper. Therefore, a TPS cost analysis was conducted with the following ground rules:

- 25-pass limit on LI-900
- 1650°K (2500°F) maximum temperature limit on LI-900
- 1650°K (2500°F) maximum temperature limit on coated Columbium
- Use worst case trajectories only
- Ablators considered for one-pass only
- Total of 20 AMOOS flights
- Neglect nose cap problem
- Use superalloys in areas below 1250°K (1800°F)
- Coated Columbium is good for 100 passes
- Carbon/carbon good for number of passes according to maximum temperature experienced per Fig. 51(from Ref. 17, p. 347)
- Material and refurbishment costs as shown in Table 10
- Compare cost on a per flight basis.

Most of the cost data and ground rules are taken from "Apollo-era" technology as presented in the appropriate Shuttle Technology Conferences documents and data.

Using these ground rules, TPS costs were computed for 1, 2, 3, 5 and 10 pass missions. The appropriate materials were applied to each area of the vehicle according to its temperature limit for each mission/trajectory. The areas were computed and converted to costs. Refurbishment costs were computed as required in accordance with the ground rules.

Results of the study are shown in Table 11. A range of values is shown in the cost column due to the range of refurbishment costs as presented in

Ref. 17. As shown by Table 11, the one-pass ablative-superalloy TPS approach provided the cheapest system. However, this system is much heavier than the ablator-ablator system. The next cheapest is the ablator-LI-900 approach. However, it is also heavier than the ablator-ablator approach. Because of this the ablator-ablator system is recommended for the AMOOS vehicle.

2.5.3 Structural Analysis Summary

The primary structure of the 5B and HB AMOOS configurations are typical shell structures stiffened internally by stringers and ring frames. The aft body flap is also a skin structure stiffened by frame members. The cargo bay doors are considered to be non-structural for load-carrying capability but must withstand a pressure differential at various times during the typical mission cycle.

The TPS is bonded to the external surface of the skin and is removed whenever refurbishment is necessary. This operation plus the use of standard gages for practical manufacturing considerations resulted in the selection of a minimum skin gage thickness of t = 0.981 mm (.032 in.). This is not an optimum value based on minimum weight-stiffened cylindrical shell design criteria but is a realistic, practical minimum gage for metallic materials. The ring and stringer spacings are determined by local and general instability, in most cases, rather than by material strength limitations.

Layout drawings for the 5B and HB small payload bay configurations are shown in Figs. 52 and 53, respectively. The HB aft payload bay configuration is shown in Fig. 54. Location and arrangement of the major vehicle components are shown. The interface attachment points to the Space Shuttle orbiter for the 5B vehicle are at the 7 and 17 m stations for the vertical and longitudinal supports, and the 7 m and 15 m stations for the lateral support. The interface attachment points for the HB vehicle are located at the 5 and 17 m stations for the longitudinal and vertical supports, and the 5 and 15 m stations for the lateral support. In addition a hinge line attachment is located at the lower rear of the AMOOS vehicle, at the aft flap hinge line. It is used

as a pivot point to rotate the vehicle in-and-out of the shuttle cargo bay. The vertical and longitudinal load attachment points are on the outside surface of the shell structure and are located on the vehicle centerline. The lateral support points are on the top of the AMOOS vehicle and are located on the centerline. Both AMOOS configurations are rotated 180 deg about the longitudinal axis and rotated 180 deg about the vertical axis for installation in the Space Shuttle cargo bay, Fig. 55. This is necessitated by the location of the lateral attachment points in the Space Shuttle vehicle. If the AMOOS lateral attachment points were located on the underside of the vehicle, they would be exposed to a higher temperature environment during the AMOOS reentry flight.

The criteria used in the structural design were: (1) the vehicle center of gravity and mass has to fall within the Space Shuttle payload center of gravity envelope; (2) acceptable center-of-gravity location and range for the vehicle mission profile; (3) the structure is thermally protected so that it does not exceed a uniform temperature of 589°K (600°F); and (4) the critical load occurs during the AMOOS pass through the atmosphere or during the Space Shuttle flight environment.

Four candidate materials were selected for the primary structure, three metallic and one non-metallic. All four meet the maximum temperature requirement. The metallic materials are titanium (Ti-6Aℓ-4V), beryllium-aluminum, (Be-38% Aℓ) and magnesium (HM21A-T8). The properties for these three metallic materials for room temperature and the 589°K (600°F) temperature level are given in Table 12. Values are given in Table 13 for a series of structural tests for graphite/polyimide (Gr/Pi) specimens. Data are still limited for Gr/Pi. Most strength properties given are average test values and do not correspond to the "A" or "B" values given in MIL-HDBK-5 that are required for structural design. Hence conservatism, such as larger safety factors and/or larger margins of safety, must be used in any Gr/Pi design at the present time.

The mass distributions established in the Phase I study were refined for the two AMOOS configurations based on the latest loads, TPS requirements

and structural material. The mass distributions for both the 5B and HB configurations are given in Figs. 56 and 57, respectively. The distribution for the orbiter launch, AMOOS reentry and orbiter reentry masses are given for the Be-38% Aℓ configurations. The center-of-gravity ranges for these conditions are given in Table 14. The possible AMOOS center-of-gravity range in the Shuttle cargo bay is shown in Fig. 58. The full and purged fuel tank conditons are shown. These correspond to the orbiter launch and reentry and landing configurations. The three selected AMOOS payload missions are shown. The three missions are: (1) Baseline – 1360 kg delivered to orbit and returned to earth; (2) Alternate A – 3660 kg delivered to orbit; and (3) Alternate B – 1886 kg returned from orbit to earth. Values are shown for the Be-38 Aℓ vehicles only since they are the lightest of the four candidate materials.

A dry mass breakdown for the two Be-38 Aℓ configurations is given in Table 15. The Gr/Pi 5B configuration mass value is also given. This vehicle is over the 4247 kg dry mass allowable for Alternate A mission but is still under the maximum allowables for the Baseline and Alternate B missions. This mass is conservative due to the small amount of test data available for design purposes and also due to the low shear strength exhibited by the panels tested so far (Ref. 18). Different orientations of the graphite fibers may possibly increase this strength property. Laminate separation is also another problem area but this is usually caused by voids in the composite and not necessarily a material strength failure. Additional research and testing of Gr/Pi and other similar composites in the next few years will probably make Gr/Pi a very competitive AMOOS structural material.

Honeycomb construction was not considered in this phase study due to the 589°K (600°F) structure temperature requirement. This temperature level would result in degradation in most honeycomb braze materials. The temperature level would also require the core material to be Be-Aℓ or Ti.

The critical load condition was assumed to occur during the AMOOS reentry to the atmosphere or during a Space Shuttle flight environment. A list of the payload bay limit load factors for the Space Shuttle flight environment is given in Table 16. The maximum combination of load factors occurs in the orbiter end burn condition during which the AMOOS is at maximum weight.

Aerodynamic normal and axial force distributions, combined with the mass distribution, were analyzed to determine the maximum vehicle bending moments, axial loads and shear loads during AMOOS reentry. The aerodynamic force distributions for both AMOOS configurations are given in Appendix C. The maximum flight loads occurred at a dynamic pressure of 5920 N/m^2 for the 5B and 5038 N/m^2 for the HB configuration. The resultant vehicle bending moment, axial load and shear load distributions are given in Appendix C.

The limit compressive load, N, in the stiffened shell was determined by the equation,

$$N = \frac{P}{2\pi R} + \frac{M}{\pi R^2}$$

The maximum combination of bending moment and axial load was found to occur during the Space Shuttle Orbiter end burn for both vehicles. The design load, N_D, equals the limit load N multiplied by the factor of safety f = 1.25

$$N_D = f \cdot N$$

Design load value for the forward cylindrical section of the 5B vehicle, Station 5.3 – 9.1 m, is 65,500 N/m (374 lb/in.). A design load of 38,705 N/m (221 lb/in.) was used for the remainder of the vehicle. Based on these load values skin thicknesses and stringer spacing were determined. Standard gage thicknesses only were considered in selecting the skin. Analyses were performed to ensure that local and general instability would not occur for the above design load values. Skin panel buckling between stiffeners was not allowed as this would cause failure of the TPS bond.

Design load values for the HB configuration are: N_D = 45,009 N/m (257 lb/in.) for the nose and forward body section, Station 0.0 – 7.6 m, and N_D = 16,638 N/m (95 lb/in.) for the remainder of the body. Typical cross-sectional dimensions are given in Table 17 for both of the Be-38 Al configurations.

The aft body flap is a flat panel with I-beam stiffeners on the leeward side. The stiffeners were sized to carry the bending moment resulting from the normal force without local or general instability occurring.

Preliminary cost data were obtained for the Beryllium-Aluminum, titanium, magnesium and Gr/Pi materials. The total cost per pound for the stiffened shell structure is considerably different for the different materials. There are also major differences in the material and fabrication costs among the four.

The material cost for the Be-38 Al is approximately $990 per kg for thin sheet and extrusions. This material is a low quantity production item, resulting in high foundry prices. The fabrication cost for a typical stiffened panel is approximately $400 per kg. Hence, a total cost per kg of $1390 ($630 per pound).

The material costs for titanium (Ti-6 Al-4V) and magnesium (HM21A-T8) are approximately $15 and $4.50 per kg, respectively, for thin sheets and extrusions. Typical fabrication costs for either material would be $13 per kg. Therefore, the total cost per kg is $28 ($13 per pound) and $17.50 ($8 per pound) respectively.

The material cost for the Gr/Pi is approximately $375 per kg with a fabrication cost of roughly three times that amount, namely $1125 for stiffened panel type construction. This gives a total cost of approximately $1500 per kg ($680 per pound).

The fabrication cost for the HB configuration will be much higher than the 5B due to the tapered elliptical shape. Tooling costs are greatly increased, especially for the Gr/Pi vehicle, due to the non-standard shape and non-symmetrical panels throughout the vehicle length. A 100% increase in fabrication cost for the HB over the 5B should be used and as much as 200 to 300% for the Gr/Pi structure.

Although the above values are preliminary, they do offer an approximate estimate of the comparative cost differences between the possible material and vehicle shape combinations. Using the above values the 5B magnesium vehicle should be the least costly of the possible combinations.

2.6 VEHICLE DESIGN DATA PARAMETERS FOR THE BALLUTE CONFIGURATION

The ground rules, sources and methods used for estimating the aerodynamic parameters, heating rates, TPS and masses are given in this section for the ballute high-drag device. The ballute was assumed to be towed behind the HB vehicle at zero lift angle of attack for the purpose of estimating the TPS requirements for the spacecraft.

2.6.1 Ballute Aerodynamic Analysis Summary

The aerodynamic drag coefficient was computed for the ballute configuration shown in Fig. 7. The Hypersonic Arbitrary-Body Program was utilized with a Newtonian flow assumption. The ballute was assumed to be flying at zero angle of attack. Various drag coefficients were obtained by ratioing up the coefficients as a function of cross-sectional area. This enabled quick computation of C_D for various sizes of ballutes.

2.6.2 Ballute Thermodynamic Analysis Summary

Heating rates for the ballute configuration were calculated using the method of Vaglio-Laurin (Ref. 19) for an unyawed cone. This method is known as the streamline divergence method. In this method a modified characteristic length calculation is made for use in the Blasius incompressible flow solution modified for compressible flow using Eckert's reference enthalpy to obtain fluid properties. A typical ballute heating rate curve is shown in Fig. 59.

The temperature limit on protected fabric made from Goodyear Fiber B is 1367°K (2000°F). A study was conducted to determine what size ballute would be required to keep the surface temperature below this value. In this

study, the ballute diameter was increased from 15.2 to 60.4 m and temperatures calculated for three locations on the conical surface.

Results of the ballute analyses are shown in Table 8. Various ballute diameters were tried and the resulting heating rates and radiative equilibrium temperatures were calculated. As seen from Table 8, the temperature values are above those allowed for normal organic materials, i.e., approximately $590^{o}K$ ($600^{o}F$).

The peak temperatures on the basic AMOOS vehicle were also estimated and shown to be such that a TPS, although reduced, was still required. The heating rates and TPS mass are given in Table 18.

2.6.3 Ballute Structural Analysis Summary

A ballute fabric mass of 1820 kg (4000 lb), a storage volume requirement of 719 kg/m^3 (45 lb/ft^3) and a g-loading of 3 during AMOOS reentry to the atmosphere were the ballute data supplied for structural and mass analysis.

Based on the storage requirement a total volume of 2.53 m^3 (89 ft^3) is required for the ballute fabric. An additional 10% volume was assumed for the vables, deployment mechanism, etc., resulting in a total storage volume requirement of 2.84 m^3 (100 ft^3). This volume can be packaged in a cylinder with a diameter of 1.83 m by 0.914 m length (6 x 3 ft). Adequate volume is available in the nose section of the small cargo bay vehicles for this packaging. However, this volume is not available for this packaging on the aft cargo bay vehicles.

A total cable length of four vehicle lengths was assumed, ℓ = 72 m (240 ft). The cable loading was determined based on the AMOOS reentry weight of 8380 kg (18,500 lb) and the 3-g factor.

$$P = (3)(8380) = 25{,}140 \text{ kg } (55{,}500 \text{ lb})$$

A working stress level of 1.378×10^{8} N/m^2 (20,000 psi) is used for the cable. This is a conservative value corresponding to a safety factor of 5. Failure of the cable would result in loss of the vehicle. The required cable area is

$$A_{req} = P/\sigma = 1.79 \times 10^{-3} \text{ m}^2 \ (2.77 \text{ in}^2)$$

The mass for the cable, assuming steel cable, is

$$wt = (A_{req})\,(\ell)\,(\rho) = 1045 \text{ kg } (2310 \text{ lb})$$

Assume mass values of 91 kg (200 lb) for the deployment mechanism; 23 kg (50 lb) additional structure for mounting hardware; and 23 kg (50 lb) for the ballute storage package. Hence the total ballute system mass is

Ballute	1815 kg (4000 lb)
Cable	1048 kg (2310 lb)
Deployment Mech.	91 kg (200 lb)
Mounting Hardware	23 kg (50 lb)
Package	23 kg (50 lb)
	3000 kg (6610 lb)

The mass saved in the AMOOS from the items no longer required would be:

External TPS	493 kg (1087 lb)
Internal TPS	155 kg (343 lb)
Body Flap	102 kg (225 lb)
	750 kg (1655 lb)

No additional structural mass would be saved with the present configurations since the body shell sizing is determined by the orbiter launch environment.

The ballute would result in a net mass gain of:

Added Mass	3000 kg
Saved Mass	750 kg
Net Mass Gain	2250 kg (4960 lb)

No savings can be shown with the present configuration for the addition of the ballute system. The effect of this system on the center-of-gravity location and range was not determined. A forward center-of-gravity shift would be experienced due to the location of the system in the nose.

The intent of the ballute is to remove the requirement for a TPS from the vehicle. However, even with the 60.4 m (198 ft) diameter ballute an unprotected shell structure is not possible even with the structural materials considered. It should be noted that, even if an aluminum skin could be used, a structural mass savings could not be obtained since the material properties to density ratio of beryllium-aluminum is superior to conventional aluminum alloys. The use of a less exotic material could result in a material cost saving. However, neither aluminum nor titanium can be used without a TPS.

2.7 TRADE AND OPTIMIZATION STUDIES

These studies encompassed fundamental trades between aeromaneuvering techniques such as the ballute versus the ablative TPS and detail trades between specific ablative TPS vehicles.

2.7.1 Ballute vs Ablative TPS Vehicles

The basic drawback to the ballute stems from the large ballute diameter required to effect an appreciable surface temperature reduction on the spacecraft and the ballute itself. A ballute diameter of approximately 60 m is required to reduce the surface temperatures to the acceptable level of 1367°K (2000°F). As Table 8 shows the peak surface temperature on the ballute decreases slowly with increases in ballute diameter. Similarly, the surface temperature on the spacecraft decreases slowly with increases in ballute diameter. This results in a TPS being required for the spacecraft and internal stowage for the return payload even for large diameters of the ballute. The trade between ballute mass and savings in TPS and structural mass proves, therefore, to be unfavorable. The position of the ballute is further degraded when cable mass and attachment points are considered.

The problems associated with off-nominal atmospheric density and trajectory conditions have been discussed in Section 2.2.4. The conditions imposed on the guidance and targeting system during atmospheric flight allow for no amelioration effects on the thermal environment as do the possible guidance schemes for the ablative TPS vehicle.

The spacecraft creates a shadowing effect on the ballute which makes accurate drag estimation difficult on the ballute or combined configuration. Also shock cone impingement on the ballute is a possibility at the very high Mach numbers encountered. This impingement problem can, of course, be overcome by choice of a sufficiently long cable, which, in turn, increases the mass of the ballute system.

2.7.2 5B and HB Aerodynamics

From a performance standpoint, the 5B vehicle is the better of the two vehicles because of its larger lift-to-drag ratio (Fig. 36). The difference in C_D between the two vehicles was found not to be significant from a trajectory standpoint.

From a stability standpoint, the HB is more stable than the 5B about all three axes. However, since no stability criteria have been established except for stability about all three axes, either vehicle might fulfill the final requirements.

2.7.3 5B and HB Trim Flap

From a trimmed center-of-gravity range standpoint, both vehicles are capable of being trimmed throughout the expected center-of-gravity range with either the expansion or ramp flap. Of course, the ramp flap has a larger trim range capability. Since the compression flap failed to give the required trim capability it was eliminated.

The three candidate flap configurations were evaluated as to potential TPS requirements. The ramp flap proved to be equally acceptable as the compression flap. The expansion flap without the ramp presents problems. These problems arise from the gap between the rear of the AMOOS vehicle and the exposure of the outboard leading edges when in use. As a result, the upper surface of the flap would require a TPS as well as the under surface. Furthermore, the configuration is difficult to analyze accurately so that either considerable testing or a conservative TPS would be required.

Since the ramp flap was acceptable after both aerodynamic and thermal evaluation it was chosen over the expansion flap.

2.7.4 Structural Materials

Four candidate materials were investigated for the vehicle body shell. These were: (1) titanium, Ti-6 Aℓ-4V alloy; (2) beryllium-38% aluminum (Be-38Aℓ); (3) magnesium (HM21A-T8) and (4) a non-metallic material, graphite/polyimide. The densities of the Be-38 Aℓ, HM21A-T8 and Gr/Pi are 47, 40 and 31%, respectively, of that of titanium and all four are adequate strengthwise throughout the required temperature range.

The titanium vehicle mass exceeded the budgeted dry mass of 4247 kg (9363 lb). The Gr/Pi vehicle was over the allowable for the Alternate A mission but was well within the allowables for the other two missions used as design criteria. This mass value is conservative due to the small amount of test data for Gr/Pi and the problems encountered with laminate separation. The Be-38 Aℓ vehicle was well within the dry mass budget as was the magnesium vehicle.

On a cost basis the Be-38 Aℓ and Gr/Pi 5B vehicle structure cost approximately the same considering the total material cost and fabrication cost on a per kg basis. The mass difference in the two would make the Gr/Pi vehicle total cost larger at this time. The titanium and magnesium structures would be considerably cheaper than either the Be-Aℓ or the Gr/Pi. The cost difference between titanium and magnesium is minimal. The HB vehicle

structure manufacturing cost is at least 100% more than the 5B due to the tapered elliptical body shape. This shape requires additional complex tooling forms.

Currently, the materials trade appears to be between Be-Al with a higher payload and cost and magnesium with a slightly lower payload and considerably lower cost. At this time the magnesium structure would be preferred since on a first unit cost basis it yields a slightly better payload per dollar figure.

2.7.5 TPS Materials

The Langley low density ablator has been selected over other TPS materials. Trade studies between this material and other ablative or insulative materials showed this ablator to yield the lowest TPS mass. The mass trades are summarized in Table 9 and Fig. 50. The cost trades are discussed in more detail in Sections 2.5.2 and 2.9.

2.7.6 Mixed Atmospheric and Propulsive Braking Maneuver

The possibility of reducing the severity of the flight environment by a mixed atmospheric and propulsive braking maneuver was studied. In this mode, a portion of the braking Δv required at the perigee of the transfer ellipse (a return from geosynchronous orbit was assumed for this study) would be performed propulsively. The resulting reduction in aeromaneuvering Δv allows the aeromaneuver to be performed at a higher altitude which in turn results in lower heating rates and heat loads and thus a possible reduction in TPS mass. The trade involved in these studies is one of additional propellant mass versus savings in TPS mass. Other masses involved, namely structure, avionics, etc., are almost independent of the type of aeromaneuver performed and are thus omitted from the trade study.

A one-pass mission with the ablative TPS concept was investigated. The return from a geosynchronous orbit mission was assumed. Figure 60 shows

TPS and propellant mass versus the portion of the total braking Δv which is performed propulsively. For the given mission the total braking Δv at the perigee of the transfer ellipse is 2300 m/s. The ablator TPS mass for propulsive Δv values below 1000 m/s remains almost constant, while the propellant mass required for a propulsive Δv of 500 m/s already exceeds the total TPS mass. The curve showing the sum of the propellant and ablator mass has its minimum at zero propulsive Δv. The trade is thus clearly in favor of the pure aerobraking mode.

2.7.7 Propulsive Compensation for Off-Nominal Trajectory and Atmospheric Conditions

The cost of thrusting to compensate for off-nominal trajectory and atmospheric conditions was evaluated. It was assumed that the thrust vector to compensate for off-nominal conditions is perpendicular to the velocity vector and thus is essentially acting like a lift force. It was further assumed that this concept is feasible. A potential problem is the main engine burn during atmospheric flight. This requires protection of the nozzle from the flight environment, resulting in additional structural and TPS mass.

The return from a geosynchronous mission orbit in one atmospheric pass was investigated. Figure 61 shows the propellant mass required if thrust is used to compensate for off-nominal conditions as a function of the ratio of effective density to nominal density. The difference between effective density and nominal density represents the combined effects of navigation errors and atmospheric density variations. See Section 2.2.1 for a more detailed discussion of the meaning of the effective density.

Combining the effect of a trajectory whose target perigee is 3.5 km higher than nominal with an atmospheric density variation of -35% from nominal, using the RSS method, results in a $\rho_E/\rho_{nom} = 0.48$. The additional propellant required is obtained from Fig. 61 as 770 kg.

It is concluded that this type of compensation for off-nominal conditions is not economical due to the excessive propellant requirements and the need to protect the main engine nozzle from the flight environment, especially because the same compensation capability can be obtained by using aerodynamic lift forces.

2.7.8 Propellant Saved as a Function of Aeromaneuvering Plane Change

The aerodynamic lift forces of the AMOOS vehicle can be employed to perform part of an inclination change during the atmospheric flight. This results in a savings in propellant mass. The Space Tug Baseline mission (i.e., equatorial geosynchronous orbit mission involving a 28.5-deg inclination change) was analyzed to determine the propellant savings and the optimal split in inclination change between geosynchronous orbit and low earth orbit.

The AMOOS vehicle HB has a 7.4-deg inclination change capability for the analyzed mission in its no flap configuration. It was assumed that this 7.4-deg inclination change could be achieved to within 1 deg due to uncertainties in the atmospheric density, navigation errors and guidance system limitations. This results in a 50 kg propellant mass contingency for the aeromaneuvering inclination change.

The inclination change at geosynchronous orbit is combined with the deorbit ellipse insertion burn. Only the additional fuel required for the inclination change was considered in this analysis.

Figure 62 shows the propellant mass for the inclination change in low earth orbit, at geosynchronous altitude and the total as a function of the fraction of the 28.5-deg inclination change performed in low earth orbit. The propellant required for the inclination change in low earth orbit consists of the 50 kg contingency for the aeromaneuvering inclination change up to 7.4 deg and increases

rapidly for larger angles due to the fuel required for the propulsive portion of the inclination change. The propellant mass shown in Fig. 62 for the inclination change at geosynchronous orbit is for an angle of 28.5 deg minus the inclination change in low earth orbit. The total propellant used to accomplish a 28.5-deg inclination change consists of the sum of the propellants used for the partial inclination changes in low earth orbit and at geosynchronous altitude. The curve showing the total propellant has a distinct minimum at 7.4-deg inclination change in low earth orbit, which indicates that the full aeromaneuvering inclination change capability of the vehicle should be utilized. The propellant saved via aeromaneuvering inclination change is about 300 kg as compared to a purely propulsive inclination change.

2.7.9 *Sensitivity Analysis*

A sensitivity analysis was performed to determine the effect of AMOOS total mass delivered to orbit by the EOS, the AMOOS dry mass and the specific impulse of the main engine on the AMOOS payload mass capability. A comparison of the sensitivities of the AMOOS payload to the sensitivities of the Space Tug payload is given in Table 19 for the missions to equatorial geosynchronous orbit. The smaller absolute values of these sensitivities means that AMOOS will experience a smaller percentage change in payload for a given change in each of the above parameters than will the Space Tug.

The sensitivities are presented in Figs. 63, 64 and 65 as a function mission orbit altitude. A circular mission orbit was assumed. Missions were considered requiring no orbit inclination change as well as 28.5-deg inclination change. Also considered were missions involving deployment and retrieval of the same payload mass, deployment only and retrieval only. The partial derivatives were evaluated for a total AMOOS mass delivered to orbit by the EOS of 28,848 kg, an AMOOS dry mass of 4247 kg and a specific impulse of 470 s. The partial derivatives are functions of AMOOS delivered mass, dry mass and specific impulse (as well as other parameters not mentioned here) and are therefore valid only for small changes around the parameter values used to compute the partial derivatives.

The mission involving retrieval of a payload tends to have a large sensitivity with respect to all parameters considered. This large sensitivity is not of great significance since there exists a large contingency in payload mass capability for this particular mission.

2.8 OPERATIONS ANALYSIS

This analysis is based on the operational functions of North American Rockwell's point design Space Tug containing a 44,500N (10,000) thrust advanced LOX-LH_2 main engine (Ref. 3). Described below is an overview of operations common to both vehicles plus additional functions that are peculiar to AMOOS.

A functional flow block diagram (FFBD) of the major functions to be performed for the baseline mission is shown in Fig. 66. The baseline mission is delivering a 1360 kg payload to geosynchronous orbit and retrieving a 1360 kg payload from geosynchronous orbit.

In FFB1 the ground support equipment is connected to AMOOS for systems checkout. The payload is installed in AMOOS and AMOOS/payload is installed in the orbiter. AMOOS is loaded with propellant while in the EOS.

In FFB2 the orbiter/AMOOS is launched with AMOOS propellant gases vented through the orbiter system. The orbiter injects into initial orbit and finally into the operations orbit.

In FFB3 the orbiter activates and deploys AMOOS with its pole arm.

In FFB4 AMOOS coasts in orbit and then burns to mission transfer orbit. During the coasting AMOOS aligns its IMU, updates its state vector and checks accuracy of state vector with orbiter furnished data. AMOOS then computes the burn parameters for mission transfer orbit insertion, places itself into burn attitude and makes the burn. After the burn the IMU is aligned and the state vector is updated. The above procedure is essentially the same for any orbit insertion. A midcourse correction is performed if so required.

In FFB5 synchronous orbit insertion is performed and correction for off-nominal course is executed.

In FFB6 the payload is deployed and is checked for proper opperation if necessary.

In FFB7 the rendezvous phasing orbit burn for payload retrieval is accomplished.

In FFB8 the burn for rendezvous with payload is done. The payload is locked onto with the laser radar. AMOOS is maneuvered to rendezvous with the payload, and the docking maneuvers are executed. The payload is then attached to AMOOS and stowed.

In FFB9 AMOOS phase coasts to insertion burn to aeromaneuvering orbit. The transfer burn is done and then a midcourse correction burn to hit the aeromaneuvering reentry corridor is executed.

In FFB10 aeromaneuvering is done to reach phasing orbit plane and apogee. Immediately before reentry into the earth's atmosphere a state vector update from ground or onboard sensors is performed.

In FFB11 a burn to achieve phasing orbit perigee is accomplished.

In FFB12 a burn to drop to EOS rendezvous orbit is done.

In FFB13 the orbiter locates, intercepts and docks with AMOOS. AMOOS is the passive element unless an emergency situation occurs whereupon it takes on an active role.

In FFB14 when the orbiter deorbits, reenters, and lands, AMOOS is essentially dormant.

In FFB15 AMOOS is checked out with ground support equipment and required maintenance and repair is carried out. Ablative TPS refurbishment must be performed after each mission. AMOOS is then stored until needed.

In FFB16 whatever operations that need to be done to get back to the orbiter are executed assuming AMOOS is capable of performing such operations.

In FFB17 abort operations are performed according to where the orbiter and AMOOS are in their mission.

For further details on operations analysis see Appendix E.

2.9 ECONOMICS ANALYSIS

A listing of the costs is presented in this section. These costs are merely estimates and are not to be construed as the results of a detailed analysis based on AMOOS subsystems. Costing data and methodology are based on North American Rockwell's point design study document (Ref. 3), Aerospace Corporations STS cost methodology documents (Refs. 20 and 21), and an IBM Tug avionics document (Ref. 6).

Costs are broken down into four categories: Design, Development, Test and Evaluation (DDT&E); First Production Unit; Technological Advancement; and Maintenance and Refurbishment Costs per Flight.

Design, Development, Test and Evaluation includes: design and development of new hardware; systems engineering and integration; design and development of tooling, special test equipment and ground support equipment; ground and flight testing; and program management.

First Production Unit includes: procurement, fabrication, assembly and checkout of vehicle hardware; spares and tooling maintenance; and program management associated with first unit production.

Technological Advancement costs identify areas that are not state of the art and what it will cost to make these areas state of the art.

Maintenance and Refurbishment Costs per Flight concern three major areas: manhours involved in maintenance, installation and checkout of replacement hardware and average costs per flight which are based on estimates of the amount of hardware that must be replaced during the life of one vehicle.

Cost listings are given in Tables 20 through 25. For a breakdown of individual cost items and masses used for costing refer to Appendix F.

The HB and 5B vehicles are costed with a primary structure of Be-38Aℓ. The graphite-polyimide primary structure at the present time is heavier and much more expensive than one made of Be-38Aℓ. Consequently, no costs are shown for graphite polyimide. The graphite polyimide DDT&E costs are much higher due to high mass and lack of technology. As graphite polyimide technology increases, costs and mass will accordingly decrease.

In addition the 5B vehicle cost listings with primary structures of titanium and magnesium are given. For the magnesium structure the SLA 561 Martin Marietta-developed ablator TPS is costed. The rest of the cost listings have a Langley Research Center ablator TPS. However, either ablator may be used with any of the primary structure materials. It is to be noted here that the Martin ablator is shown to cost more than the Langley ablator. This is not necessarily the case since the costing equation for the ablator subsystem uses ablator mass as the independent variable and so only indicates the additional cost created by the need for a TPS.

2.10 TECHNOLOGY IDENTIFICATION

The AMOOS concept as depicted in the 5B and HB configurations uses the technology that is expected to be available by 1976. At this time, this technology appears adequate except in the area of autonomous navigation, however, should the mass contingencies, which currently total more than

10% of the dry mass be used then the realization of the graphite-polyimide structural capabilities would be required to reduce the dry mass to maintain feasibility. No advancement in aerodynamic coefficient prediction or experimental techniques is considered necessary. The other three areas, namely thermal, structures and trajectory analysis, are considered worthy of some discussion.

The TPS currently proposed consists of a Langley-developed light weight ablator bonded directly onto the load bearing skin. The formulation for the "Langley Low Density" ablative TPS material is well established. Some arc-jet testing of this material has been conducted. The data and results of this ablation performance testing were used in the AMOOS TPS analyses presented in this report. However, this material has not yet been flight qualified, that is, it has never been flown on an actual vehicle. Therefore, before being used in the final AMOOS design, an additional testing and development program will be required. Ablation data should be gathered from several facilities and the results compared. A carefully planned test program should be carried out with proper interpretation and analysis of the data. This will greatly enhance the confidence level in this material and in the required thickness calculations. The result will be a less conservative and more reliable TPS design.

There will also be a need for TPS development along the lines of scale manufacturing techniques, application to the vehicle, and refurbishment procedures. None of these are expected to present any severe problem areas but will require time, money and good design engineering.

Since dry mass has a habit of increasing during the development of a project it is well to establish a few contingencies. Currently, the AMOOS concept has at least a 486 kg contingency for dry mass in access of the 5% allowed in the dry structural mass estimation. Should this be used then a graphite-polyimide structure would be required to maintain the alternate mission A payload of 3660 kg. In order to use the full potential of graphite-polyimide as a structural material considerable testing would be required above that currently (1973) performed. Since this is a material with outstanding potential it is probable that considerable testing is planned for the near future under other programs.

Current autonomous navigation systems are apparently incapable of placing a payload in geosynchronous orbit with an accuracy sufficient to give a drift rate of less than 1 deg/year. Three alternatives exist: (1) use a ground based update; (2) advance the state-of-the-art of autonomous navigation systems; and (3) use an existing spacecraft already in geosynchronous orbit to obtain a navigation update. This third alternative may not be always available. Alternatives 1 and 3 are state of the art. The navigational accuracy on the return to EOS phasing transfer orbit is marginal even with a landmark tracker. The development of an all-weather increased range landmark tracker would provide sufficient accuracy. However, at this time relaxing the autonomous requirement and so allowing a ground based update would appear the best solution. The above remarks apply, in general, to the Space Tug. However, since the Space Tug burns directly into the phasing orbit, the precision of this orbit can be traded against high altitude navigation accuracy.

The guidance strategy proposed for the AMOOS vehicles HB and 5B during atmospheric passage is based on lift vector modulation. This involves relative rapid changes in the vehicle attitude. An estimate of the size of the attitude control thrusters was obtained by considering: (1) the pitching moment induced by the rotation of the vehicle ($20^{o}/s$) about its velocity vector at 45-deg angle of attack, and (2) by the roll acceleration of $1.1^{o}/s^{2}$. It was found that case (1) above determines the thruster size. Assuming two thrusters, one on each end of the vehicle at opposite sides and allowing for 50% contingency, results in 1000N (220 lb) thrust per thruster. These thrusters must be able to operate during the pass through the atmosphere. The operation and protection of these thrusters may require limited development.

Section 3
CONCLUSIONS

The more detailed analyses of the 5B and HB configurations have further established the feasibility of the one-pass, ablative TPS AMOOS concept. The HB configuration appears the more practical at this time since it will prove the easier to modify to the modular concept. The ballute configuration results in a heavy dry mass relative to the 5B and HB configurations because of the large diameter of 60 m required for the ballute to bring the ballute surface temperatures below the 1367°K (2000°F) maximum allowable for protected Goodyear Fiber B. Even for the above ballute size a TPS is required for the spacecraft. This results in negligible savings in dry mass.

Specific conclusions from the multi-disciplined study of the 5B and HB configurations and the deployable ballute are:

- The AMOOS vehicle is practical and is well within present state-of-the-art technology using magnesium (HM21A-T8) or beryllium-aluminum (Be-38Aℓ) material for the primary shell structure. The vehicle mass is below the dry mass allowable with some growth contingency possible. The present small cargo bay HB configuration has sufficient internal volume to adequately accommodate all of the required vehicle components while maintaining a desirable center-of-gravity range. The HB vehicle is readily adaptable to the EOS cargo bay and is within the required EOS payload c.g. -weight envelope. A cursory analysis showed that the aft cargo bay HB configuration also yields an acceptable range of c.g. locations.

- The operation of the AMOOS vehicle would differ from the purely propulsive concept in the areas of refurbishment and, of course, in transfer to phasing orbit.

- The aerobraking concept is feasible for the 5B and HB vehicles over a wide range of mission altitudes. Extrapolation of the results from geosynchronous transfer orbits to higher energy transfer orbits indicates that

aerobraking is feasible on return from lunar and planetary missions. Missions to Mars and Venus yield high payloads to orbits about the respective planet.

- The AMOOS concept is most advantageous for high-altitude mission orbits where the propellant savings are largest as a result of aerobraking. This advantage is reduced for lower mission orbits and for mission altitudes below approximately 10,000 km the purely propulsive tug has a larger payload mass capability than an AMOOS vehicle for a round-trip payload mission with a 28-deg plane change.

- The lightweight nylon-phenolic/microballoon ablative material developed at Langley Research Center proved to be the best TPS material although the Martin-developed SLA 561 ablator proved a good alternative. The selection of an ablative material over other forms of TPS was due in part to the high temperatures encountered even during multi-pass maneuvers. Recall that the number of passes per maneuver is restricted to 10 due to the six-day on orbit lifetime guideline for AMOOS, and an equivalent seven-day lifetime guideline for the EOS.

- Studies of insulative TPS, reradiative TPS and either of the preceding patched with ablator at the hot spot showed such systems to be very heavy relative to ablative TPS.

- The use of a ballute high drag device in conjunction with AMOOS was shown to be heavy relative to ablative TPS resulting in a reduced payload capability. The general lack of vertical maneuverability requires either drag modulation or modulation of the number of passes per maneuver to compensate for off-nominal conditions. Neither appear practical because of the approximate tenfold variation in atmospheric density predicted at target perigee.

- A survey of the navigation literature showed that the autonomous system would probably not have sufficient accuracy for insertion into geosynchronous orbit (< 1 deg/yr drift rate) nor for return transfer orbit navigation. Three alternatives exist: (1) use a ground based update; (2) advance the state-of-the-art of autonomous navigation systems; and (3) use an existing spacecraft already in geosynchronous orbit to obtain a navigation update. This third alternative may not be always available. Alternatives 1 and 3 are state of the art. The navigational accuracy on the return to EOS phasing transfer orbit is marginal even with a landmark tracker. The development of an all-weather increased range landmark tracker would provide sufficient accuracy. However, at this time relaxing the autonomous requirement and so allowing a ground based update would appear the best solution.

- Studies of off-nominal trajectory conditions substantiated that trajectory corrections were necessary during atmospheric passage to avoid reentry or an inordinate increase in the number of passes for the maneuver. The most economic method of achieving the trajectory correction is by using aerodynamic lift forces. Drag modulation, modulation of the number of passes and thrusting were investigated and found either impractical or too expensive in consumables.

- A cursory study of the RCS sizing revealed that approximately 1000N (220 lb) thrusters would be needed in pitch and yaw. The roll RCS could be considerably smaller, say 500N (110 lb). The RCS must be capable of operating in the atmosphere.

- The large payload bay configuration is capable of performing 100% of the projected non-expendable Space Tug missions on the basis of payload length and diameter. Only non-Dod missions were available for analysis. The configuration, which was derived from the HB, also has considerable potential for development as a modular vehicle. Further evaluation of the modular concept is required since it can result in large variations in vehicle length and in center-of-gravity position and travel.

- Performance analysis has shown that AMOOS has payload capabilities to high energy orbits well in excess of the Space Tug. Both the 5B and HB AMOOS vehicles are capable of performing 100% of the projected non-expendable Space Tug missions on the basis of payload mass. Three missions (2% of the total missions) require an expendable tug due to large incremental velocity requirements. These incremental velocities are beyond the propulsive capability of the 5B or HB AMOOS vehicles. Only non-DoD missions were available for analysis.

- A cursory extension of the performance analysis to interplanetary and lunar missions further enhances the position of AMOOS relative to the Space Tug-type vehicle. Slingshotting around the Moon and a kick stage holds the potential for performing the 2% of the missions which require and expendable Tug. Furthermore, inserting AMOOS on a free return trajectory around the moon would allow the recovery of AMOOS on these missions.

- The relatively large payload capability with a totally enclosed payload bay offers the potential for manned spaceflight including further lunar explorations.

- The AMOOS vehicle is, in general, less sensitive (than the Space Tug) to variations in I_{sp}, mass delivered to low earth orbit and structural mass. This is due to the smaller Δv requirement for AMOOS which allows a higher inert mass.

The AMOOS vehicles are, therefore, less sensitive to design and development changes and so more likely to meet their estimated payload capabilities than the Space Tug.

- The analysis showed that the ablative TPS would be more practical than other materials. The preferred structural material would be magnesium (HM21A-T8) from purely cost considerations. However, certain properties of magnesium make the beryllium-aluminum (Be-38Aℓ) structure attractive. The manufacturing costs for the 5B configuration would probably be cheaper than the HB configuration.

- Titanium and graphite/polyimide are also suitable materials for the AMOOS primary structure. However, both result in somewhat overweight vehicles which causes a reduction in the alternate mission A payloads. Neither material should be completely ruled out at this time since more sophisticated design and, in the case of graphite/polyimide, more testing and manufacturing technique development may result in dry masses within budget. Titanium is particularly attractive from cost and material properties considerations.

- The aeromaneuvering plane change capability of the 5B and HB vehicles on return from geosynchronous altitude missions is approximately 7 deg. This capability increases rapidly with mission altitude. In order to minimize propellant requirements the optimum procedure for plane change is to perform up to the aeromaneuvering capability during atmospheric passage and perform the remainder at mission altitude during the burn to transfer orbit. Considerations of the need for aeromaneuvering for trajectory correction modifies this slightly so that about one degree more is performed at mission altitude and a propulsive correction made during the burn at phasing orbit apogee after the atmospheric passage.

- Further investigations substantiated that the mixed mode of operation was impractical. In the mixed mode, the energy dissipation necessary to attain phasing orbit is divided between a propulsive and aerobraking maneuver.

- The differences in the aerodynamic drag coefficients for the 5B and HB vehicles are considered negligible since the effects on the thermal environment are negligible. Both vehicles satisfy the requirement of static stability about all axes. To date, no quantitative stability requirements have been established. Therefore the differences in static stability cannot be evaluated.

- The expansion flap faired into the aft end of the body by a ramp was selected over the compression flap and the unfaired expansion flap for reasons of performance and thermal considerations, respectively.

Page intentionally left blank

Section 4
RECOMMENDATIONS

The results of this study have demonstrated the general feasibility of the AMOOS concept and the specific feasibility of the 5B and HB configurations. However, these studies have also identified areas which require additional investigation to establish the practicability of the AMOOS concept. The primary areas requiring further investigation are vehicle internal heating and structural analysis, extension of mission profile to planetary and lunar missions, and vehicle navigation, guidance, stability and control.

Task 1 — Thermal and Structural Analysis

Within the ranges of mission extremes, guidance and control strategy and flight environment, perform the following subtasks in the areas of thermodynamics and structural analysis to supplement or modify existing vehicle design data.

1. Review TPS selection using 1984 technology. The review should include single pass and multi-pass aeromaneuvers with all types of TPS. The use of synergetic plane change in the ascent to mission altitude maneuvers should also be reevaluated.

2. Investigate the effects of heat soak into the interior of the AMOOS vehicles after exiting the atmosphere. The effects of solar radiation on internal temperatures and cryogenic storage should also be investigated. If necessary, determine thermal protection necessary for internal components, in particular cryogenics tanks, astrionics and return payload. Thermal aspects of the common bulkhead between the LOX and LH_2 tanks should be investigated.

3. Conduct detailed analysis of vehicle leeside thermal protection system (TPS) requirements. Investigate various candidate materials to optimize vehicle structure and minimize weight.

4. Investigate vehicle base heating to determine the degree of thermal protection required.

5. Determine TPS requirements and weights as required for modified trim devices.

6. Conduct an experimental (wind tunnel) test program to verify aerothermal analytical results.

7. Determine external temperature of AMOOS at the time of docking with the Space Shuttle. Investigate the effects of these temperatures on the Space Shuttle cargo bay.

8. Determine the effect of the revised environmental analysis of Task VIII on vehicle TPS and structural weight.

9. Perform an analysis to determine the effect of combined thermal gradients and internal load distributions on the structural design and weight of the vehicle.

10. Perform structural dynamic analysis of the vehicle to determine compatibility with the Space Shuttle and to size vehicle RCS.

11. Update structural mass, c.g. range and structural design to incorporate the latest TPS and aerodynamic requirements.

Task II – Systems Analysis

1. Determine the interface requirements between AMOOS and its payload and AMOOS and the EOS. In particular emphasis should be placed on the study of those interfaces peculiar to AMOOS and distinct from the Space Tug. Interfaces common to both AMOOS and the Space Tug should be studied sufficiently to establish the validity of the application of these Space Tug study results to AMOOS.

2. Establish the impact of the mission spectrum on the subsystems requirements. The mission spectrum should include the current Space Tug mission spectrum and lunar and planetary missions. The subsystem requirements should be evaluated against 1984 technology. The impact of manned missions on the AMOOS should be considered.

3. Develop layouts of possible AMOOS configurations which will enhance the flexibility of the AMOOS concept. In particular maximum geometric payload dimensions should be given equal weight with payload mass.

Task III – Navigation

Determine navigation accuracy requirements in high and low altitude orbits and transfer orbits from EOS parking orbit and to the EOS phasing orbit. These navigation accuracy requirements should be given as 1σ errors in three components of position and three components of velocity. Determine the navigation system necessary to produce these accuracies. Compare the performance of the best autonomous system available by 1984 to the requirements and determine penalties of using the autonomous system. Special emphasis will be placed on navigation accuracy requirements and capabilities on the return transfer orbit immediately prior to the aerobraking maneuver.

The accuracy with which vacuum perigee can be estimated prior to atmospheric entry will largely determine the sophistication of the guidance scheme. It should be noted that a vacuum perigee one kilometer below target perigee will, if uncorrected, cause reentry instead of an aerobraking pass. A recently developed, Lockheed sponsored, preliminary guidance scheme (Ref. 22) is capable of guiding AMOOS to a successful phasing orbit over navigation errors of $\pm$ 3.5 km combined with -50 and +100% unpredictable atmospheric density variation, or equivalently, $\pm$ 6 km entry corridor combined with a -35 and + 40% atmospheric density variation. Accurate knowledge of position within the entry corridor of $\pm$ 3.5 km will reduce considerably the unpredictable variation in atmospheric density. This, in turn, will decrease the complexity of the guidance scheme since smaller random errors will need to be corrected. Currently, a landmark tracker is the only autonomous system that can yield the navigation accuracy necessary for the midcourse correction. Since its range capability is limited the midcourse correction must be made close to the earth and is, therefore, relatively expensive in propellant. Furthermore, the proximity to atmospheric entry may preclude recycling the midcourse maneuver should it fail on first attempt. The Space Tug does not need such navigational accuracy to achieve an acceptable phasing orbit. In fact, a midcourse correction may not even be necessary for the Space Tug since apparently both 315 km x 720 km and 520 km circular phasing orbits are acceptable and so potentially anything in between.

The navigation study shall include the use of fully autonomous, cooperative and ground based systems. The specific equipment studied shall include: inertial measuring unit, star tracker, horizon sensor, landmark tracker, sun sensor, ground based beacon, and ground based tracker. The latter will include range, range rate and two angular measurements.

Task IV – Guidance

1. Exoatmospheric Guidance and Targeting

Develop guidance and targeting laws applicable over all mission altitudes. Optimize the midcourse correction maneuver(s). Determine the errors resulting from the midcourse correction maneuver. Propagate these errors to atmospheric entry and vacuum perigee. Determine the 3σ entry corridor width. The determination of the exact corridor width for given navigation and exoatmospheric guidance schemes is most important due to the sensitivity of the AMOOS trajectory and phasing orbit apogee to atmospheric density and actual vacuum perigee.

2. Atmospheric Guidance and Targeting

Develop a technique for detecting non-predictable atmospheric densities. These off-nominal densitites may be due to unknown density variations with altitude or due to navigation errors. Develop a guidance law for atmospheric flight. At least one candidate law studied will use lift vector modulation. Study methods of lift vector modulation. These methods shall include:

a. Continuous rotation of 360 deg about the velocity vector with the rotation rate modulated to modulate the resultant lift vector.

b. The bank angle changed by 180 deg at some point on the trajectory.

c. Flight along a constant altitude arc.

d. Modulate the bank angle about the maximum plane change value.

Losses in plane change capability will be compensated with a small propulsive plane change maneuver. Studies to date have shown that the resulting plane change requirement is about one degree.

The atmospheric flight guidance requirements are distinct from the Apollo, Space Shuttle or skip-type reentry guidance for several reasons. First, AMOOS must leave the atmosphere with a relatively precise velocity to give an acceptable phasing orbit, therefore guidance laws based on heat loads or heating rates are not applicable. This is so since such laws could result in a combination of flight path angle, atmospheric density and velocity that would allow early escape from the atmosphere and hence a too high velocity. Reentry is also a possibility with such a scheme. Rather, what must be done is to guide to yield the desired exit velocity and design the TPS to accept the resulting heating rates and heat loads. This does not mean that these rates and loads cannot be minimized in the technical sense of the word. Furthermore, the guidance scheme must differ from skip entry since AMOOS leaves with an energy in excess of that required for circular orbit. This means that inertial and gravitational forces determine the exit of a successful AMOOS atmospheric pass. On the other hand, if the velocity is slowed to near, but sub, orbital speeds as is done with a skip-type reentry guidance, flight path angle and hence egress can be effectively controlled with the use of aerodynamic lift. Vehicles with L/D ratios comparable to the AMOOS 5B and HB configurations have sufficient maneuverability to perform such a maneuver. However, the resulting exoatmospheric flight is only a few thousands of kilometers instead of being almost one revolution as in the case of the AMOOS vehicle without an apogee burn.

The AMOOS guidance problem is further complicated by the rise of v and Δv versus time, after some threshold level indicating atmospheric entry, being indistinguishable for a wide range of maximum atmospheric densities until near peak penetration of the atmosphere. At this time, the lift force and the time available are insufficient to make the necessary corrections. The use of flight path angle offers an attractive alternative to time provided

it can be measured to an accuracy of approximately 0.2 deg. This figure is an estimate and requires considerable effort to justify.

One problem that plagues all atmospheric flight is the difficulty of obtaining an analytical solution of sufficient accuracy to yield a good first estimate and provide a rapid trajectory convergence scheme. This applies particularly to AMOOS guidance where, on a successful pass, the aerodynamic forces are large modifiers of the basic two-body motion. The result is that none of the usual assumptions such as constant velocity, constant altitude, small flight path angle, etc., are applicable. The literature on synergetic maneuvering contains several approximate analytical solutions which have been shown to be in considerable error when compared to integrated trajectories. Synergetic maneuvering guidance is also not applicable to AMOOS since it invariably attempts to minimize energy loss. In the AMOOS problem a precise, fixed energy increment must be dissipated for a given mission altitude and phasing orbit apogee.

3. Guidance Update Requirements

Determine the allowable errors in phasing orbit apogee altitude. Using these allowable errors determine the required guidance cycle time. Determine the computational requirements and compare these requirements with current and 1984 computer technology.

4. Guidance Law Trades

By the use of a three-degree-of-freedom simulation, demonstrate the practicability of the guidance schemes. The simulation shall include all guidance and targeting parameters. The response of the vehicle to control forces and perturbations shall not be simulated. The simulation shall be used to determine the optimum guidance system taking into account the exo-atmospheric and atmospheric modes and the navigation system.

Task V – Trajectory Optimization

The propulsive maneuvers will be optimized upon considerations of engine thrust, propellant, start and stop losses, use of main engine full thrust, main engine throttled and RCS. Determine the best compromise between aeromaneuvering, TPS, guidance and navigation. Current technology will be used as well as 1984.

Task VI – Flight Control

Size the RCS for both atmospheric flight and exoatmospheric flight from consideration of the rates required to change the attitude of the vehicle. Estimate the propellant requirements of the various guidance schemes. Consider the effects of stable, neutrally stable and unstable vehicles on propellant requirements.

Task VII – Mission Analysis

The mission profile will be extended from previous studies to include lunar and planetary missions. Propulsive as well as aeromaneuvering requirements will be determined.

Task VIII – Analysis of Flight Environments

Perform detailed analysis of flight environments within the operation ranges defined in Task VII. The analysis will include aerodynamic and thermodynamic loading, performance and flight mechanics studies.

Task IX – Vehicle Design Data

Within the ranges of mission extremes, control strategy and flight environment, perform the following subtasks in the areas of aerodynamics, to supplement or modify existing vehicle design data.

1. Utilize the Hypersonic Aerodynamic program to obtain dynamic aerodynamic data, and perform a dynamic stability analysis.

2. Perform wind tunnel testing in the form of pressure, heat transfer, six-component and dynamic tests. Oil flows and shadowgraphs should be obtained. Both the HB and 5B with the ramp flap should be tested.

3. Optimize the flap area to the center-of-gravity range as provided by the structures discipline.

4. Investigate other theoretical computation techniques which might better match the experimental data.

5. Support other disciplines in the areas of configuration change and possible new aerodynamics.

Task X – Operations

Revise the operational functions of the AMOOS as required, based on the results of Tasks I through IX. Identify potential problem areas and discuss probable solutions.

Task XI – Economics

Revise previous cost estimates as required based on the results of Tasks I through X. Within the scope of Tasks I through X, perform an economic analysis of the Space Tug and AMOOS concepts.

Task XII – Technology Identification

Identify and discuss technology areas that may require development and/or advancement to be applicable to AMOOS.

Section 5
REFERENCES

1. Andrews, C. D., "Feasibility and Tradeoff Study of an Aeromaneuvering Orbit-to-Orbit Shuttle (AMOOS)," LMSC-HREC TR D306600, Lockheed Missiles & Space Company, Huntsville, Ala., June 1973.

2. National Aeronautics and Space Administration, "Baseline Tug Definition Document, Revision A," PD-DO-SI(72-56), Marshall Space Flight Center, Ala., 26 June 1972.

3. Greeg, C., "Space Tug Point Design Study, Final Report," SO72-SA-0032, North American Rockwell Corp., Downey, Calif., 11 February 1972.

4. McMillan, William III, and David G. Hull, "Hypersonic Bodies of Maximum Drag for a Given Lift-to-Drag Ratio," J. Astronaut. Sci., Vol. XIX, No. 2.

5. Letter from Goodyear Aerospace Corporation to Lockheed-Huntsville, 27 September 1973.

6. IBM Huntsville, "Astrionic System Optimization and Modular Astrionics for NASA Missions After 1974, Preliminary Definition of Astrionic System for Space Tug Mission Vehicle Payload (MVP) Progress Report," IBM No. 69-K44-0006H, Contract No. NAS8-14000, IBM Federal Systems Division, Electronics System Center, Huntsville, Ala., 16 June - 15 August 1970.

7. Corso, C. J. et al., "Space Tug Aerobraking Study," Boeing Document No. D5-17142, The Boeing Co., Huntsville, Ala., 12 April 1972.

8. National Aeronautics and Space Administration, "Traffic Model for the Space Shuttle," NASA TM X 64717, January 1973.

9. Gentry, A. E., and D. N. Smyth, "Hypersonic Arbitrary-Body Aerodynamic Computer Program, Mark III Version," Vols. 1 and 2, DAC 61552, Douglas Aircraft Co., Santa Monica, Calif., April 1968.

10. Ketter, F. C., "Results of Tests to Determine the Aerodynamic Characteristics of Two Potential Aeronaneuvering Orbit-to-Orbit Shuttle (AMOOS) Vehicle Configurations in the NASA-AMES 3.5-Foot Hypersonic Wind Tunnel – Final Report," LMSC-HREC TR D306979, Lockheed Missiles & Space Company, Huntsville, Ala., May 1974.

11. Engel, C. D., "Aeroheating Correlations for Noncontinuum Hypersonic Flight," RT R-008-2, REMTECH, Inc., Birmingham, Ala., December 1972.

12. Perrine, C., "Estimation of Maximum Heating Rates and Total Heat Load During Supercircular Reentry," The Martin Company, MVL TechnicalNote 10 (undated).

13. Thomas, A. C., A. Perlbachs and A. L. Nagel, "Advanced Reentry Systems Heat Transfer Manual for Hypersonic Flight," AFFDL TR-65-195, Wright-Patterson AFB, Ohio, October 1966.

14. Stevens, R. A. et al., "Reentry Heat Transfer to a Delta Wing Space Shuttle Booster at High Angles of Attack," FZA-452, General Dynamics, Convair Division, Fort Worth, Texas, March 1971.

15. Lovin, J. K., "Lockheed-Huntsville Thermal Analyzer," LMSC-HREC D225095, Lockheed Missiles & Space Company, Huntsville, Ala., April 1971.

16. Curry, D. M., "An Analysis of a Charring Ablation Thermal Protection System," NASA TN D-3150, December 1965.

17. Space Shuttle Technology Conference – Structures and Materials, NASA TM X-2570, San Antonio, July 1972.

18. General Dynamics, "Development of Design Data for a Graphite Reinforced Epoxy and Polyimide Composite – Vol. 1 – Final Report," GDC-DBG70-005, Convair Aerospace Div., San Diego, December 1973.

19. Vaglio-Laurin, R., "Laminar Heat Transfer on Blunt Nosed Bodies in Three-Dimensional Hypersonic Flow," WADC TN 58-147, Wright-Patterson AFB, Ohio, May 1958.

20. Aerospace Corporation, "STC Cost Methodology Book," Vol. II, TDR-0059 (6758-04)-1, 31 August 1970.

21. Grace, George J., and James B. Carey, "STC Cost Model, Volume I, Computer Program Description," TDR-0059 (6758-04)-1, Aerospace Corporation, Systems Engineering, El Segundo, Calif., March 1971.

22. White, J. and A. Wernli, "Guidance Concepts for the Aeromaneuvering Orbit-to-Orbit Shuttle," LMSC-HREC TM D306356, Lockheed Missiles & Space Company, Huntsville, Ala., August 1974.

Table 1

AMOOS Δv BUDGET (m/s)

Event	Main Engine	Orbital Maneuver	RCS
Separate from EOS			3
Perigee Burn for Transfer Orbit Injection	2448		
Gravity Loss	94		
Midcourse Correction			15
Apogee Burn to Circularize	1786		
Gravity Loss	3		
Station Keeping			9
Deploy Payload			3
Phasing Orbit Insertion		30	
Retrieve Payload		30	5
Deorbit to Transfer Orbit Injection	1841		
Gravity Loss	3		
Midcourse Correction			15
Aeromaneuvering		30	
Adjust to 315 x 720km		61	
Circularization Burn into 315 km	112		
Terminal Rendezvous		30	5
Dock with EOS			3
2% Contingency	126		
Total	6413	181	58

Table 2
SPACE TUG Δv BUDGET (m/s)

Event	Main Engine	Orbital Maneuver	RCS
Separate from EOS			3
Perigee Burn for Transfer Orbit Injection	2448		
Gravity Loss	94		
Midcourse Correction			15
Apogee Burn to Circularize	1786		
Gravity Loss	3		
Station Keeping			9
Deploy Payload			3
Phasing Orbit Insertion		30	
Retrieve Payload		30	5
Deorbit to Transfer Orbit Injection	1784		
Gravity Loss	3		
Midcourse Correction			15
Perigee Burn to Inject into 315 x 720km	2331		
Gravity Loss	8		
Circularization Burn into 315 km	112		
Terminal Rendezvous		30	5
Dock with EOS			3
2% Contingency	171		
Total	8740	90	58

Table 3

AMOOS MASS SUMMARY AND PAYLOADS FOR EQUATORIAL GEOSYNCHRONOUS MISSIONS

					Baseline Mission (Deliver and Retrieve Payload)		Alternate Mission A (Deliver Payload)		Alternate Mission B (Retrieve Payload)	
					kg	lb	kg	lb	kg	lb
AMOOS Mass at EOS Separation					28838	63600	28848	63600	27488	60600
Baseline Payloads					1360	3000	3660	8060	1883	4150
Consumables (Baseline Payloads)					22465	49527	20946	46177	21549	47507
Maximum Allowable Dry Mass for Baseline Payloads					5033	11073	4247	9363	9363	12093
Payloads for Structural Material Options										
Config.	Structure	Ablator	Dry Mass kg	Dry Mass lb						
5B	HM218-T8	SLA-561	3923	8648	2462	5416	4181	9198	6045	13299
5B	Be-38Al	LRC	3859	8490	2552	5614	4296	9451	6236	13719
5B	Titanium	SLA-561	4921	10848	1462	3216	2578	5672	3390	7458
5B	Gr/Pi	LRC	4589	10104	1800	3960	3120	6864	4287	9431
HB	Be-38Al	LRC	3774	8291	2642	5812	4440	9768	6475	14245

Table 4

PHASE II CANDIDATE CONFIGURATIONS AND CHARACTERISTICS

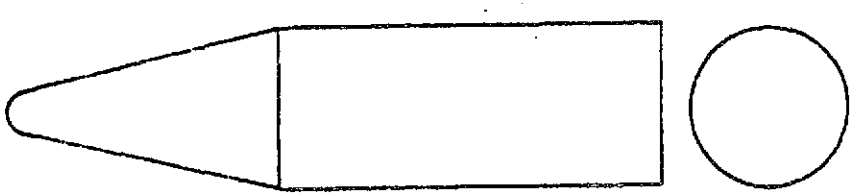

AMOOS 1

AMOOS 5

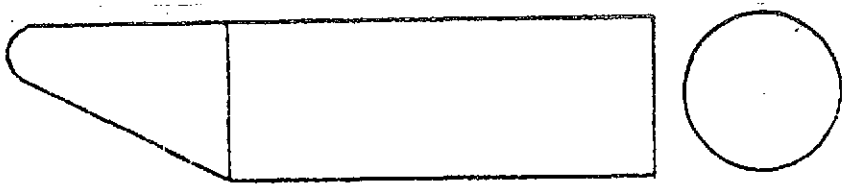

AMOOS 5B

AMOOS HB

AMOOS Conf.	$(L/D)_{max}$	L/D at $C_{L_{max}}$	C_{M_α} at $C_{L_{max}}$	$C_{L_{max}}$	α at $C_{L_{max}}$	C_D at $C_{L_{max}}$	C_{Y_β} at $C_{L_{max}}$	C_{n_β} at $C_{L_{max}}$	C_{ℓ_β} at $C_{L_{max}}$	Dry Mass (kg)
1	1.615	0.650	-0.0055	2.080	50°	3.170	-0.086	0.00008	0.0	3311
5	1.490	0.698	-0.0013	2.240	53°	3.220	-0.090	-0.00142	0.00096	3356
5B	1.042	0.603	-0.0105	1.979	45°	3.285	-0.085	0.00202	-0.00109	3356
HB	0.788	0.517	-0.0147	2.003	45°	3.874	-0.070	0.0079	-0.00165	3572

Table 5

COMPARISON OF AMOOS AND SPACE TUG PAYLOAD CAPABILITY FOR INTERPLANETARY AND LUNAR MISSIONS

I_{sp} (s)			470		465		460	
			kg	lb	kg	lb	kg	lb
Mars	Deliver to Orbit About Mars	AMOOS	11318	24900	11214	24670	11114	24450
		Space Tug	6836	15040	6736	14820	6636	14600
Venus	Deliver to Orbit About Venus	AMOOS	11318	24900	11214	24670	11114	24450
		Space Tug	5491	12080	5400	11880	5295	11650
Moon	Deliver to and Retrieve from Orbit About Moon	AMOOS	8558	18828	8455	18601	8351	18372
		Space Tug	4407	9695	4322	9508	4237	9321

Table 6

EFFECTS OF ENTRY ATTITUDE AND ATMOSPHERIC DENSITY VARIATIONS ON TOTAL HEAT LOAD FOR HB, 5B AND HB WITH BALLUTE CONFIGURATIONS (ONE-PASS MISSION ONLY)

Config.	Trajectory Description		Flight Time (s)	Heat Load on Stag Point of 1-m Radius Sphere (J/m^2)
HB	RHOFAC = 1.0	Nominal Entry	405	2.9×10^8
	RHOFAC = 2.0	Nominal Entry	323	1.8×10^8
	RHOFAC = 2.0	3.5 km Low Entry	279	1.7×10^8
	RHOFAC = 0.5	Nominal Entry	564	4.9×10^8
	RHOFAC = 0.685	3.5 km High Entry	642	4.4×10^8
5B	RHOFAC = 1.0	Nominal Entry	406	3.2×10^8
	RHOFAC = 2.0	Nominal Entry	324	2.0×10^8
	RHOFAC = 2.0	3.5 km Low Entry	285	1.9×10^8
	RHOFAC = 0.5	Nominal Entry	559	5.3×10^8
	RHOFAC = 0.606	3.5 km High Entry	643	5.3×10^8

Table 7

PEAK HEATING RATES AND TOTAL HEAT LOADS FOR AMOOS CONFIGURATION HB FOR MULTIPLE PASS MISSIONS

Total Time of Pass (s)	Mission	Pass No.	Peak Heating Rate to 1-m Radius Sphere (W/m^2)	Heat Load on Stagnation Point of 1-m Radius Sphere (J/m^2)
238	2-Pass	1	1.9×10^6	2.06×10^8
432	(Nominal)	2	1.5×10^6	2.46×10^8
200	3-Pass	1	1.6×10^6	1.67×10^8
278	(Nominal)	2	1.4×10^6	1.7×10^8
480		3	1.5×10^6	2.16×10^8
210	5-Pass	1	1.26×10^6	1.2×10^8
236	(Nominal)	2	1.14×10^6	1.23×10^8
264		3	1.05×10^6	1.27×10^8
312		4	$.96 \times 10^6$	1.35×10^8
512		5	$.87 \times 10^6$	1.81×10^8
200	10-Pass	1	8.5×10^5	8.09×10^7
203	(Nominal)	2	8.3×10^5	7.6×10^7
220		3	7.9×10^5	7.9×10^7
222		4	7.6×10^5	7.7×10^7
236		5	7.3×10^5	8.3×10^7
264		6	5.9×10^5	5.2×10^7
272		7	6.8×10^5	8.5×10^7
309		8	6.5×10^5	9.1×10^7
366		9	6.3×10^5	1.0×10^8
558		10	6.1×10^5	1.5×10^8

Table 7 (Concluded)

PEAK HEATING RATES AND TOTAL HEAT LOADS FOR AMOOS CONFIGURATION HB FOR MULTIPLE PASS MISSIONS

Total Time of Pass (s)	Mission	Pass No.	Peak Heating Rate to 1-m Radius Sphere (W/m^2)	Heat Load on Stagnation Point of 1-m Radius Sphere (J/m^2)
210	2-Pass	1	1.8×10^6	1.66×10^8
332	(3.5 km Low)	2	1.3×10^6	1.61×10^8
196	3-Pass	1	1.6×10^6	1.34×10^8
236	(3.5 km Low)	2	1.3×10^6	1.27×10^8
344		3	1.1×10^6	1.31×10^8
192	5-Pass (3.5 km Low)	1	1.3×10^6	1.05×10^8
188	10-Pass (3.5 km Low)	2	9.9×10^5	8.59×10^7

Table 8

BALLUTE ANALYSIS RESULTS

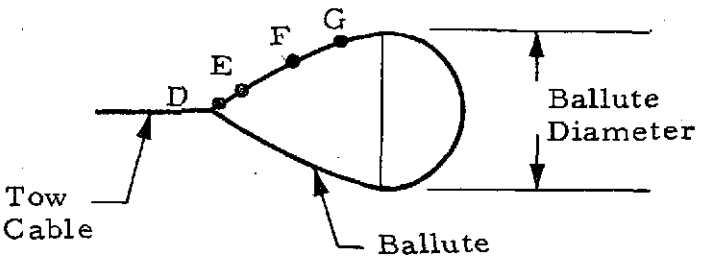

Ballute Diameter (m)	Reference Points	Distance from Apex (m)	$\dot{q}$ (W/m^2)	Radiative Equilibrium Temperature (^oK)
15.24	D	.3	86.9×10^4	2092
3.5 km	E	4.25	23.3×10^4	1504
High	F	6.73	18.5×10^4	1420
Entry	G	10.3	15.0×10^4	1348
15.24	D	.3	137.5×10^4	2346
3.5 km	E	4.25	36.8×10^4	1687
Low	F	6.73	29.3×10^4	1593
Entry	G	10.3	23.7×10^4	1512
30.2	D	.3	27.8×10^4	1572
3.5 km	E	8.42	5.3×10^4	1038
Low	F	13.35	4.2×10^4	980
Entry	G	20.4	3.4×10^4	929
45.3	D	.3	18.8×10^4	1427
3.5 km	E	12.6	2.9×10^4	896
Low	F	20.0	2.3×10^4	846
Entry	G	30.6	1.9×10^4	801
60.4	D	.3	14.0×10^4	1324
3.5 km	E	16.9	1.9×10^4	801
Low	F	26.7	1.5×10^4	756
Entry	G	40.7	1.2×10^4	717

Table 9

AMOOS TPS MASS SUMMARY

Config.	Traj. No.	Trajectory Description		Ablator TPS Mass* (kg)
HB	1	RHOFAC = 1.0	Nominal Case	389.4
	2	RHOFAC = 2.0	Nominal Entry	345.5
	3	RHOFAC = 2.0	3.5 km Low Entry	340.8
	4	RHOFAC = 0.5	Nominal Entry	453.5
	5	RHOFAC = 0.685	3.5 km High Entry	438.9
5B	1	RHOFAC = 1.0	Nominal Case	372.1
	2	RHOFAC = 2.0	Nominal Entry	328.8
	3	RHOFAC = 2.0	3.5 km Low Entry	323.9
	4	RHOFAC = 0.5	Nominal Entry	431.9
	5	RHOFAC = 0.606	3.5 km High Entry	430.9

*windward side only. Masses include an additional 10% for closeouts around doors, hatches, etc., and 0.74 kg/m^2 for sealer and bonding agents (from Apollo experience).

Table 10

TPS MATERIAL AND REFURBISHMENT UNIT COSTS

Material or TPS Type	Material		Refurbishment	
	($/m^2)	($/ft^2)	($/m^2)	($/ft^2)
Superalloys	2152	200	88.00 to 659.70	8.18 to 61.32
LI-900	4303 to 8607	400 to 800 (Avg 600)	65.90 to 811.60	6.13 to 75.44
Carbon/Carbon	43,030	4000	65.90 to 811.60	6.13 to 75.44
Ablators	538	50	65.90 to 1013.44	6.13 to 94.20
Coated Columbium	10,758	1000	88.00 to 659.70	8.18 to 61.32

Table 11

AMOOS CONFIGURATION HB CONFIGURATION TPS COST ANALYSIS BASED ON 20 MISSIONS

Mission Type	TPS Materials	TPS Cost/Mission (Material and Refurbishment)
1-Pass	Ablator – Superalloy Ablator – Ablator Ablator – LI-900	$ 71,500 - 168,200 112,400 - 282,200 88,850 - 186,200
2-Pass	C/C – LI-900 – Superalloy C/C – Columbium – Superalloy	715,200 - 734,200 711,700 - 729,300
3-Pass	C/C – LI-900 – Superalloy C/C – Columbium – Superalloy	408,400 - 421,100 392,400 - 402,200
5-Pass	C/C – Columbium – Superalloy	151,300 - 165,300
10-Pass	C/C – Columbium – Superalloy	$164,600 - 190,600

Notes:

1. Material, fabrication and refurbishment costs calculated based on a total of 20 missions.
2. Does not include between missions inspection costs for ceramic and metallic TPS.
3. TPS cost for the nose section not included.
4. TPS materials and their applicable areas determined from radiation equilibrium surface temperatures obtained using nominal trajectories.
5. C/C – Carbon/Carbon

Table 12

MATERIAL PROPERTIES

Mechanical Properties Basis	Titanium T_i - 6 Al - 4V (Sheet, Annealed) A	Beryllium-Aluminum Be-38 Al (Sheet, Annealed) A	Magnesium HM 21A-T8 (Sheet) A
F_{tu}, MN/m^2 (ksi):			
294°K (70°F)	924 (134)	303 (44)	228 (33)
589°K (600°F)	724 (105)	179 (26)	76 (11)
F_{ty}, MN/m^2 (ksi):			
294°K (70°F)	869 (126)	214 (31)	124 (18)
589°K (600°F)	586 (85)	152 (22)	55 (8)
F_{cy}, MN/m^2 (ksi):			
294°K (70°F)	910 (132)	193 (28)	103 (15)
589°K (600°F)	921 (90)	124 (18)	69 (10)
F_{su}, MN/m^2 (ksi):			
294°K (70°F)	545 (79)	159 (23)	145 (21)
589°K (600°F)	400 (58)	97 (14)	48 (7)
E, GN/m^2 (10^3 ksi:)			
294°K (70°F)	110 (16)	193 (28)	45 (6.5)
589°K (600°F)	90 (13)	172 (25)	36 (5.2)
μ	.31	.14	.35
Physical Properties			
ρ, kg/m^3 (lb/in^3)	4430(.16)	2080(.075)	1770(.064)

Ref: Ti-6Al-4V, MIL-HDBK-5, Sept. 1971
Be-38Al, LMSC Report 679606, Oct. 17, 1967
HM 21A-T8, MIL-HDBK-5, Sept. 1971

Table 13

DESIGN PROPERTIES OF HT-S/710 COMPOSITES (0, ± 45 DEGREES, 90)
(GRAPHITE/POLYIMIDE)

Test Temperature °K (°F)	Post-cure Cycle	Laminate Orientation (deg)	Test Orientation (deg)	Tensile Strength MN/m² (ksi)	Tensile Modulus GN/m² (psi × 10⁶)	Strain to Failure (in./in. × 10⁻⁶)	Compression Strength MN/m² (ksi)	Compression Modulus GN/m² (psi × 10⁶)	Strain to Failure (in./in. × 10⁻⁶)	Flexural Strength MN/m² (ksi)	Flexural Modulus GN/m² (psi × 10⁶)	Short Beam Shear Strength MN/m² (ksi)
77 (-320)	1	$(0, \pm 45, 90)_{2s}$	0	346 (50.4)	33 (4.8)	(4200)	444 (63.9)	56.7 (8.22)	(8000)	353 (50.6)	29.4 (4.26)	25.5 (3.70)
				290 (42.0)	59 (8.5)	-	423 (61.4)	55.3 (8.02)	(9600)	367 (53.2)	27.9 (4.04)	30.5 (4.42)
				311 (45.0)	68 (9.9)	-	367 (53.2)	46.4 (6.73)		388 (56.3)	30.1 (4.36)	33.5 (4.5)
				304 (43.8)	66 (9.6)	-	325 (47.0)	34.9 (5.07)	(10500)	304 (44.1)	- -	20.8 (3.02)
				262 (38.4)	47 (6.8)	-	339 (49.2)	61.2 (8.88)	(9800)	339 (48.9)	- -	24.4 (3.54)
				290 (41.7)	43 (6.3)	-	360 (52.2)	56.6 (8.20)	(10400)	367 (52.6)	28.8 (4.18)	23.2 (3.36)
			Average	301 (43.6)	53 (7.7)	(4200)	376 (54.5)	51.8 (7.52)	(9800)	353 (51.0)	29.1 (4.22)	26.3 (3.82)
297 (75)	1	$(0 \pm 45, 90)_{2s}$	0	276 (39.6)	53 (7.7)	-	374 (53.7)	60.0 (8.70)	(6700)	458 (65.5)	25.2 (3.66)	23.2 (3.37)
				283 (40.9)	59 (8.5)	(3140)	353 (51.4)	60.2 (8.73)	(7600)	388 (55.7)	24.1 (3.50)	24.5 (3.5)
				297 (43.2)	59 (8.6)	(5200)	360 (51.8)	53.5 (7.76)	(7700)	367 (52.9)	24.8 (3.59)	24.7 (3.58)
				339 (48.9)	66 (9.6)	(5320)	304 (43.7)	59.2 (8.58)	(7900)	353 (50.9)	24.5 (3.55)	19.7 (2.86)
				311 (44.7)	50 (7.2)	(7660)	311 (45.1)	46.5 (6.74)	(8200)	353 (51.3)	24.0 (3.48)	19.7 (2.85)
				283 (41.4)	57 (8.2)	(4200)	283 (41.0)	48.8 (7.07)	(7800)	402 (58.4)	26.2 (3.80)	20.3 (2.82)
			Average	298 (43.1)	57 (8.3)	(5100)	331 (47.8)	54.7 (7.93)	(7700)	387 (55.8)	24.8 (3.60)	21.9 (3.17)
589 (600)	1	$(0, \pm 45, 90)_{2s}$	0	374 (53.5)	48 (7.0)	(6620)	283 (41.1)	24.6 (3.57)	(11600)	283 (41.0)	17.7 (2.56)	20.7 (3.00)
				325 (46.9)	46 (6.6)	(6600)	255 (37.2)	24.3 (3.53)	(9300)	227 (33.1)	16.1 (2.34)	21.7 (3.14)
				318 (46.3)	46 (6.6)	(5950)	234 (34.4)	24.8 (3.60)	(9700)	255 (37.0)	15.5 (2.25)	21.1 (3.06)
				325 (47.2)	42 (6.1)	(7320)	241 (35.0)	25.4 (3.68)	(10200)	255 (36.6)	17.6 (2.55)	23.9 (3.46)
				290 (42.3)	66 (9.5)	(5040)	262 (37.5)	22.9 (3.33)	(12100)	311 (44.5)	- -	22.3 (3.24)
				304 (43.9)	48 (6.9)	(5660)	255 (37.2)	21.2 (3.04)	(11600)	290 (42.4)	- -	21.2 (3.13)
			Average	323 (46.7)	49 (7.1)	(6200)	255 (37.1)	23.9 (3.46)	(10800)	270 (39.1)	16.8 (2.43)	21.9 (3.17)
297 (75)	2	$(0, \pm 45, 90)_{2s}$	0	332 (48.4)	70 (10.2)	(4400)	360 (51.9)	66 (9.6)	(7890)	318 (46.3)	32.4 (4.70)	22.3 (3.24)
				290 (42.1)	50 (7.2)	(4800)	395 (57.0)	55 (8.0)	(10000)	297 (43.1)	28.3 (4.10)	26.1 (3.78)
				339 (49.3)	74 (10.8)	(4800)	332 (48.0)	58 (8.4)	(8220)	290 (41.5)	26.9 (3.90)	24.6 (3.56)
				269 (39.2)	51 (7.4)	(5900)	332 (47.5)	54 (7.9)	(10000)	276 (39.8)	22.3 (3.23)	31.5 (4.57)
				283 (41.4)	66 (9.6)	(6100)	332 (47.9)	41.1 (6.0)	(11550)	234 (34.1)	23.4 (3.40)	37.7 (5.47)
				339 (49.3)	48 (6.9)	(4000)	381 (54.6)	43.3 (6.3)	(11100)	283 (41.0)	21.0 (3.05)	35.6 (5.16)
			Average	309 (45.0)	60 (8.7)	(5000)	355 (51.2)	53 (7.7)	(11300)	283 (41.0)	25.7 (3.73)	29.6 (4.30)

Table 14

AMOOS VEHICLE CENTER-OF-GRAVITY RANGE
(PERCENT VEHICLE LENGTH)

Condition	AMOOS Be-38 Aℓ Vehicle	
	5B	HB
Orbiter Launch		
Baseline	37.40 → 38.03	32.07 → 32.68
Alt. A	39.91 → 41.55	34.63 → 36.27
Alt. B	35.98	30.62
AMOOS Reentry		
Baseline	49.43 → 51.73	45.28 → 47.62
Alt. A	45.81	41.8
Alt. B	50.48 → 53.47	46.30 → 49.32
Orbiter Reentry		
Baseline	56.30 → 59.57	53.08 → 56.43
Alt. A	53.05	50.40
Alt. B	57.13 → 61.25	53.77 → 57.82

Note: Vehicle center-of-gravity range obtained by varying the payload center-of-gravity from 1/4 cargo bay to 3/4 cargo bay length.

Table 15

AMOOS DRY MASS BREAKDOWN

Components	Mass (kg)	Be-38 Aℓ Structure HB Mass (kg)	Be-38 Aℓ Structure 5B Mass (kg)	Graphite/ Polyimide Structure 5B Mass (kg)
Structure				
Propellant Tanks	301.3			
Tank Supports	67.0			
Thrust Structure	30.8			
Docking Mechanisms, Payload and Tug/EOS	48.0			
Primary Structure		1052	1158	1888
Mounting Hardware, Meteoroid Shield, Umbilicals	73.0			
Expansion Flap		102	102	102
Thermal Control System				
Tank Insulation	118.7			
Purge Bag, Valves and Lines	35.8			
Thermal Control System	34.0			
Ablator Bond and Sealer		515	494	494
Internal Insulation of Astrionics and Internal Batten	200.3			
Astrionics (from Boeing Space Tug Aerobraking Study)				
Data Management	204.8			
Navigation	94.2			
Electrical Power	233.3			
Communications	59.8			
Instrumentation	22.7			
Propulsion (from MSFC Baseline Tug Definition Document)				
Main Engine	135.0			
Feed, Fill, Drain and Vent Systems	117.3			
Gimbal Actuation System	15.4			
Attitude Control System	257.3			
Propellant Utilization System	15.7			
Helium Purge System	40.8			
Dry Mass (Less Primary Structure and TPS)	2105.2	2105	2105	2105
Total Dry Mass		3774	3859	4589

Table 16

SHUTTLE PAYLOAD BAY LIMIT LOAD FACTORS

Condition*	Longitude (+ Aft) x	Latitude (+ Right) y	Vertical (+ Up) z
Lift-off**	-1.7 ± 0.6	± 0.3	-0.8 -0.2
High Q Boost	-1.9	± 0.2	+0.2 -0.5
Booster End Burn	-3.0 ± 0.3	± 0.2	-0.4
Orbiter End Burn	-3.0 ± 0.3	± 0.2	-0.5
Space Operations	-0.2 +0.1	± 0.1	±0.1
Entry	±0.25	± 0.5	+3.0 -1.0
Subsonic Maneuvering	±0.25	± 0.5	+2.5 -1.0
Landing and Braking	±1.5	± 1.5	+2.5
Crash***	+9.0 -1.5	± 1.5	+4.5 -2.0

*Positive x, y, z directions equal aft, right and up. Load factor carries the sign of the externally applied load.

**Crash load factors are ultimate and only used to design payload support fittings and payload attachment fasteners. Crash load factors are for the nominal payload of 29,480 kg(65,000lb). Longitudinal load factors are directed in the forward asimuth within 20 deg of the orbiter longitudinal axis. The specified load factors operate separately.

***These factors include dynamic transient load factors at liftoff.

Table 17

TYPICAL CROSS-SECTION OF Bc-38 Al AMCOS CONFIGURATIONS

Note:

Subscripted x = r denotes ring

x = s denotes stringer

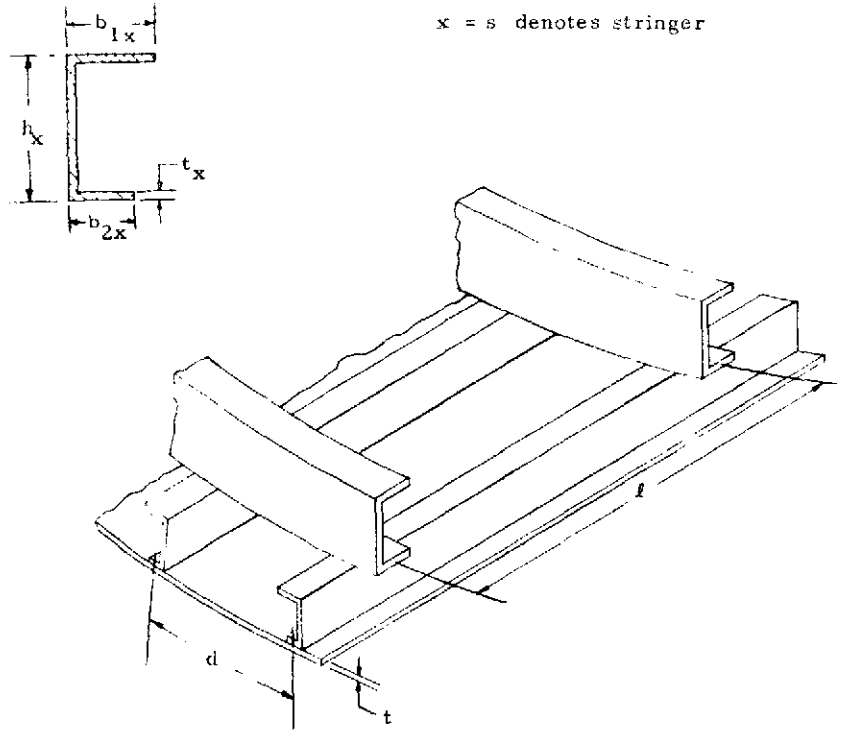

	HB		5B		
	Fwd Sec	Aft Sec	Nose	Fwd Cyl	Aft Cyl
Station cm.	0.0-726	726-1781	0-533	533-914	914-1781
Station in.	(0.0-300)	(300-701)	(0-210)	(210-360)	(360-701)
t	0.127(0.050)	0.081(0.032)	0.102 (0.040)	0.127 (0.050)	0.102 (0.040)
d	13.9 (5.47)		12.7 (5.0)		
t_s	0.081 (0.032)		0.081 (0.032)		
h_s	7.62 (3.0)		7.62 (3.0)		
b_{1_s}	3.81 (1.5)		3.81 (1.5)		
b_{2_s}	3.81 (1.5)		3.81 (1.5)		
ℓ	228.6 (90.0)		127.0 (50.0)		
t_r	0.165 (0.065)		0.165 (0.065)		
h_r	10.2 (4.0)		10.2 (4.0)		
b_{1_r}	5.08 (2.0)		5.08 (2.0)		
b_{2_r}	5.08 (2.0)		5.08 (2.0)		

NOTE: All values in cm (in).

Table 18
EFFECTS OF ENTRY ATTITUDE AND ATMOSPHERIC DENSITY VARIATIONS ON TOTAL HEAT LOAD AND ABLATOR TPS MASS FOR HB WITH BALLUTE CONFIGURATIONS
(ONE-PASS MISSION ONLY)

Config.	Trajectory Description	Flight Time (s)	Heat Load on Stag Point of 1-m Radius Sphere (J/m^2)	Ablator TPS Mass* (kg)
HB with Ballute	RHOFAC = 0.5 3.5 km High Entry	406	2.7×10^8	406.0
	RHOFAC = 2.0 3.5 km Low Entry	440	4.4×10^8	440.0

*windward side only. Masses include an additional 10% for closeouts around doors, hatches, etc., and 0.74 kg/m^2 for sealer and bonding agents (from Apollo experience).

Table 19

COMPARISON OF SENSITIVITIES OF PAYLOAD TO SPECIFIC IMPULSE, DRY MASS AND DELIVERED MASS (%/%)

Conditions	I_{sp}		M_{dry}		M_{del}	
	AMOOS	Space Tug	AMOOS	Space Tug	AMOOS	Space Tug
Baseline	1.70	2.62	-1.60	-1.74	2.70	3.05
Deploy	1.48	2.15	-1.50	-1.90	2.63	3.01
Retrieve	2.16	3.45	-1.72	-2.06	3.01	3.68

Table 20

COST LISTING FOR AMOOS 5B WITH LRC ABLATOR AND A PRIMARY STRUCTURE OF Be-38 Al (M, Millions of Dollars)

Cost Item (1970$)	($M)DDT+E	($M) First Unit Cost
Total Structure	35.442	2.711
Body Structures	16.847	1.982
Main Tanks	13.391	.444
Docking	5.204	.285
Propulsion	154.124	5.072
Main Engine	130.000	.700
APS	21.390	3.877
Press., Feed + Vent	2.734	.495
Avionics	73.284	9.624
Data Management	16.027	2.425
GN+C	20.066	3.061
Communications	30.079	2.483
Instrumentation	.437	.120
El Pwr Distr	6.676	1.535
Thermal Protection	33.426	3.147
Hi-Perf Insulation	10.911	.281
Insulation Purge	.600	.130
Thermal Control	.891	.089
External TPS	21.024	2.647
Power	13.700	.477
Fuel Cell	13.226	.427
Hydraulics	.474	.050
EOS Interface	3.284	.351
Testing	140.811	.000
Grd. Test Ops.	20.002	.000
Flt. Test Ops.	28.844	.000
Test Hdwre	89.160	.000
Wind Tunnel Testing	2.805	.000
GSE	13.699	.000
Initial Tooling + Ste.	24.740	1.861
Logistics + Spares	.000	1.861
Training	6.351	.000
Systems Engineering + Integration	13.891	2.669
Installation, Assembly + Checkout	.000	2.394
Contractor Program Management	30.620	1.327
Total	543.372	31.514

Table 20 (Concluded)

Cost Item (1970$)	($M)Main+Refurb/Flight
Hardware	.640
Structures	.217*
Propulsion	5.782
Thermal Protection	.706
Data Management	.606
GN+C	.765
Fuel Cell	.450
El.Pwr. Distr.	.767
EOS Interface	.527
Communications	.621
Maintenance	.032
Installation + Checkout	.441
Total	1.113

* Costs in this column are for 20 missions. These costs are divided by 20, and $M. 1176 is added for TPS costs to yield cost per mission and entered in right hand column.

Table 21

COST LISTING FOR AMOOS HB WITH LRC ABLATOR AND A PRIMARY STRUCTURE OF Be-38 Al

Cost Item (1970$)	($M)DDT+E	($M)First Unit Cost
Total Structure	38.637	3.087
Body Structures	20.042	2.358
Main Tanks	13.391	.444
Docking	5.204	.285
Propulsion	154.124	5.072
Main Engine	130.000	.700
APS	21.390	3.877
Press., Feed + Vent	2.734	.495
Avionics	73.284	9.624
Data Management	16.027	2.425
GN+C	20.066	3.061
Communications	30.079	2.483
Instrumentation	.437	.120
El Pwr Distr	6.676	1.535
Thermal Protection	33.912	3.206
Hi-Perf Insulation	10.911	.281
Insulation Purge	.600	.130
Thermal Control	.891	.089
External TPS	21.510	2.706
Power	13.700	.477
Fuel Cell	13.226	.427
Hydraulics	.474	.050
EOS Interface	3.284	.351
Testing	142,872	.000
Grd.Test Ops.	20.328	.000
Flt.Test Ops.	28.844	.000
Test Hdwre	90.895	.000
Wind Tunnel Testing	2.805	.000
GSE	13,876	.000
Initial Tooling + Ste.	25.237	1.901
Logistics + Spares	.000	1.901
Training	6,414	.000
Systems Engineering + Integration	14,143	2.745
Installation, Assembly + Checkout	.000	2,422
Contractor Program Management	31.159	1.354
Total	550.642	32.140

Table 21.(Concluded)

Cost Item (1970$)	($M)Main+Refurb/Flight	
Hardware		.641
Structures	.247*	
Propulsion	5.782	
Thermal Protection	.706	
Data Management	.606	
GN+C	.765	
Fuel Cell	.450	
El.Pwr. Distr.	.767	
EOS Interface	.527	
Communications	.621	
Maintenance		.032
Installation + Checkout		.441
Total		1.114

*Costs in this column are for 20 missions. These costs are divided by 20, and $M. 1176 is added for TPS costs to yield cost per mission and entered in right hand column.

Table 22

COST LISTING FOR AMOOS 5B WITH LRC ABLATOR AND A PRIMARY STRUCTURE OF TITANIUM

Cost Item (1970$)	($M)DDT+E	($M) First Unit Cost
Total Structure	19.189	.799
Body Structures	.594	.070
Main Tanks	13.391	.444
Docking	5.204	.285
Propulsion	154.124	5.072
Main Engine	130.000	.700
APS	21.390	3.877
Press., Feed + Vent	2.734	.495
Avionics	73.284	9.624
Data Management	16.027	2.425
GN+C	20.066	3.061
Communications	30.079	2.483
Instrumentation	.437	.120
El. Pwr. Distr.	6.676	1.535
Thermal Protection	33.426	3.147
Hi-Perf. Insulation	10.911	.281
Insulation Purge	.600	.130
Thermal Control	.891	.089
External TPS	21.024	2.647
Power	13.700	.477
Fuel Cell	13.226	.427
Hydraulics	.474	.050
EOS Interface	3.284	
Testing	131.867	
Grd. Test Ops.	18.587	.000
Flt. Test Ops.	28.844	.000
Test Hardware	81.631	.000
Wind Tunnel Testing	2.805	.000
GSE	13.049	.000
Initial Tooling + Ste.	22.546	1.689
Logistics + Spares	.000	1.689
Training	6.080	.000
Systems Engineering + Integration	12.787	2.440
Installation, Assembly + Checkout	.000	2.298
Contractor Program Management	28.267	1.210
Total	511.603	29.796

Table 22 (Concluded)

Cost Item (1970$)	($M)Main+Refurb/Flight	
Hardware		.632
Structures	.064*	
Propulsion	5.782	
Thermal Protection	.706	
Data Management	.606	
GN+C	.765	
Fuel Cell	.450	
El. Pwr. Distr.	.767	
EOS Interface	.527	
Communications	.621	
Maintenance		.032
Installation + Checkout		.438
Total		1.102

* Costs in this column are for 20 missions. These costs are divided by 20, and $M. 1176 is added for TPS costs to yield cost per mission and entered in right hand column.

Table 23

COST LISTING FOR AMOOS 5B WITH LRC ABLATOR AND A PRIMARY STRUCTURE OF MAGNESIUM

Cost Item (1970$)	($M)DDT+E		($M) First Unit Cost	
Total Structure		18.770		.750
Body Structures	.175		.021	
Main Tanks	13.391		.444	
Docking	5.204		.285	
Propulsion		154.124		5.072
Main Engine	130.000		.700	
APS	21.390		3.877	
Press., Feed + Vent	22.734		2.734	.495
Avionics		73.284		9.624
Data Management	16.027		2.425	
GN+C	20.066		3.061	
Communications	30.079		2.483	
Instrumentation	.437		.120	
El. Pwr. Distr.	6.676		1.535	
Thermal Protection		33.426		3.147
Hi-Perf. Insulation	10.911		.281	
Insulation Purge	.600		.130	
Thermal Control	.891		.089	
External TPS	21.024		2.647	
Power		13.700		.477
Fuel Cell	13.266		.427	
Hydraulics	.474		.050	
EOS Interface		3.284		.351
Testing		131.636		.000
Grd. Test Ops.	18.550		.000	
Flt. Test Ops.	28.844		.000	
Test Hardware	81.437		.000	
Wind Tunnel Testing	2.805		.000	
GSE		13.033		.000
Initial Tooling + Ste.		22.489		1.685
Logistics + Spares		.000		1.685
Training		6.073		.000
Systems Engineering + Integration		12.758		2.434
Installation, Assembly + Checkout		.000		2.296
Contractor Program Management		28.206		1.207
Total		510.783		28.728

Table 23 (Concluded)

Cost Item (1970$)	($M)Main+Refurb/Flight	
Hardware		.632
Structures	0.60*	
Propulsion	5.782	
Thermal Protection	.706	
Data Management	.606	
GN+C	.765	
Fuel Cell	.450	
El. Pwr. Distr.	.767	
EOS Interface	.527	
Communication	.621	
Maintenance		.032
Installation + Checkout		.438
Total		1.102

* Costs in this column are for 20 missions. These costs are divided by 20, and $M.1176 is added for TPS costs to yield cost per mission and entered in right hand column.

Table 24

COST LISTING FOR AMOOS 5B WITH MARTIN ABLATOR AND A PRIMARY STRUCTURE OF MAGNESIUM

Cost Item (1970$)	($M)DDT+E		($M) First Unit Cost	
Total Structure		18.770		.750
Body Structures	.175		.021	
Main Tanks	13.391		.444	
Docking	5.204		.285	
Propulsion		154.124		5.072
Main Engine	130.000		.700	
APS	21.390		3.877	
Press., Feed + Vent	2.734		.495	
Avionics		73.284		9.624
Data Management	16.027		2.425	
GN+C	20.066		3.061	
Communications	30.079		2.483	
Instrumentation	.437		.120	
El. Pwr. Distr.	6.676		1.535	
Thermal Protection		34.690		3.300
Hi-Perf. Insulation	10.911		.281	
Insulation Purge	.600		.130	
Thermal Control	.891		.089	
External TPS	22.288		2.800	
Power		13.700		.477
Fuel Cell	13.226		.427	
Hydraulics	.474		.050	
EOS Interface		3.284		.351
Testing		132.421		.000
Grd. Test Ops.	18.674		.000	
Flt. Test Ops.	28.844		.000	
Test Hardware	82.098		.000	
Wind Tunnel Testing	2.805		.000	
GSE		13.159		.000
Initial Tooling + Ste.		22.660		1.699
Logistics + Spares		.000		1.699
Training		6.096		.000
Systems Engineering + Integration		12.848		2.454
Installation, Assembly + Checkout		.000		2.319
Contractor Program Management		28.403		1.217
Total		513.439		28.962

Table 24 (Concluded)

Cost Item (1970$)	($M)Main+Refurb/Flight	
Hardware	*	.632
Structure	.060	
Propulsion	5.782	
Thermal Protection	.706	
Data Mangement	.606	
GN+C	.765	
Fuel Cell	.450	
El. Pwr. Distr.	.767	
EOS Interface	.527	
Communication	.621	
Maintenance		.032
Installation + Checkout		.438
Total		1.102

* Costs in this column are for 20 missions. These costs are divided by 20, and $M. 1176 is added for TPS costs to yield cost per mission and entered in right hand column.

Table 25

COST LISTING OF TECHNOLOGICAL ADVANCEMENT FOR 5B AND HB WITH A PRIMARY STRUCTURE OF Be-38 Al*

	($M) Cost
Fracture Mechanics for Thin Wall Tanks	0.980
High Performance Insulation (MLI)	1.000
Payload/EOS Docking	0.700
Zero-g Propellant Management	0.780
APS Propellant Conditioning Unit	4.000
APS/Propellant Slosh Interaction	0.150
Rendezvous Laser Radar	0.200
Computer Software	0.120
AMOOS/EOS Integration	0.170
Total	8.100

*from Ref. 3.

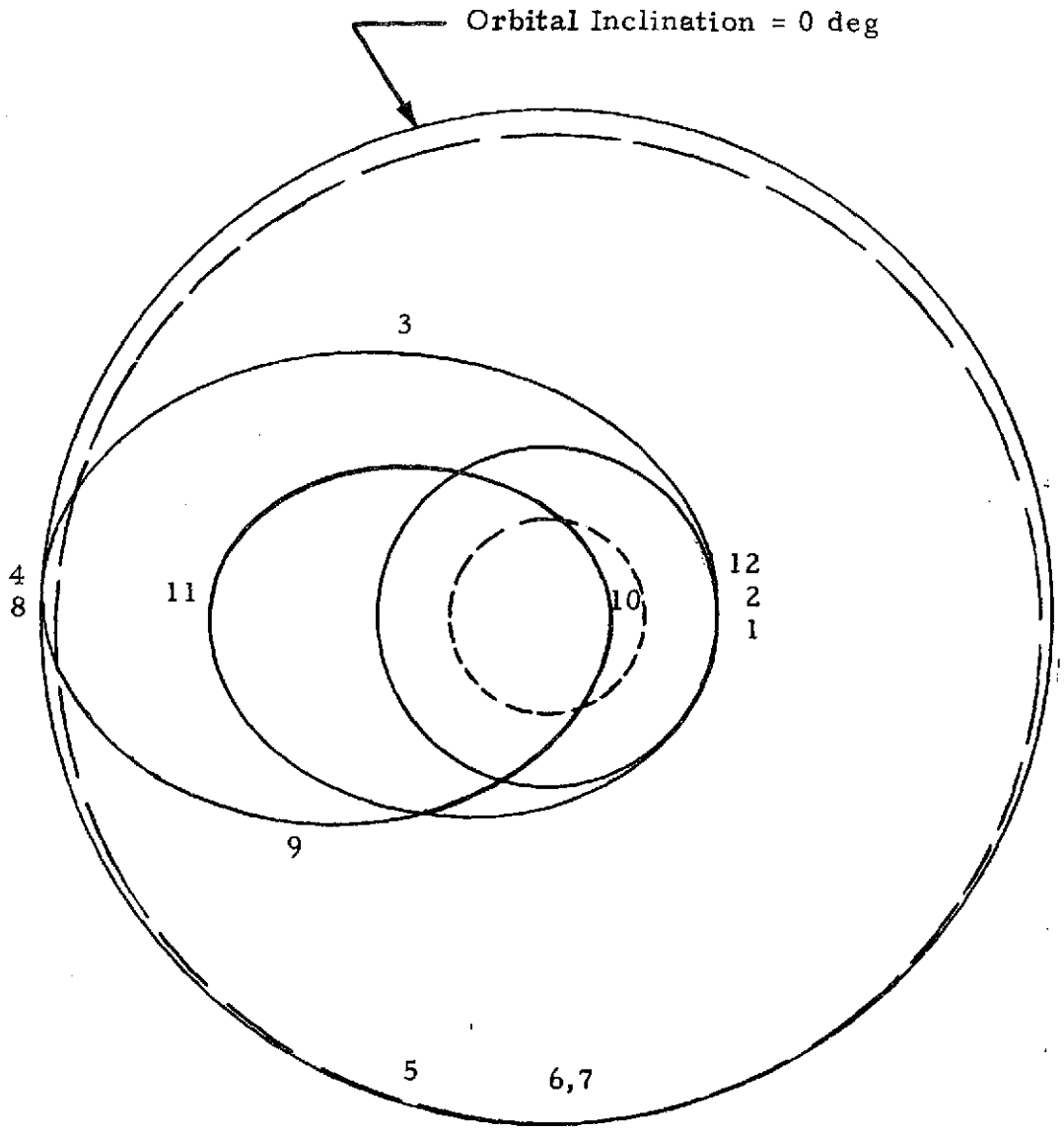

1. Delivered to 296 km Circular Orbit by the EOS
2. Burn to Mission Transfer Orbit
3. Midcourse Correction
4. Burn-to-Mission Orbit
5. Deliver Payload
6. Burn-to-Phasing Orbit for Rendezvous with Return Payload
7. Rendezvous and Dock with Return Payload
8. Burn-to-Transfer to Aeromaneuvering Orbit*
9. Midcourse Correction*
10. Aeromaneuver to Phasing Orbit Plane and Apogee*
11. Burn-to-Achieve Phasing Orbit Perigee*
12. Burn-to-EOS Rendezvous Orbit

*Denotes AMOOS Maneuvers Distinct from Space Tug Maneuvers.

Fig. 1 - AMOOS Mission Profile

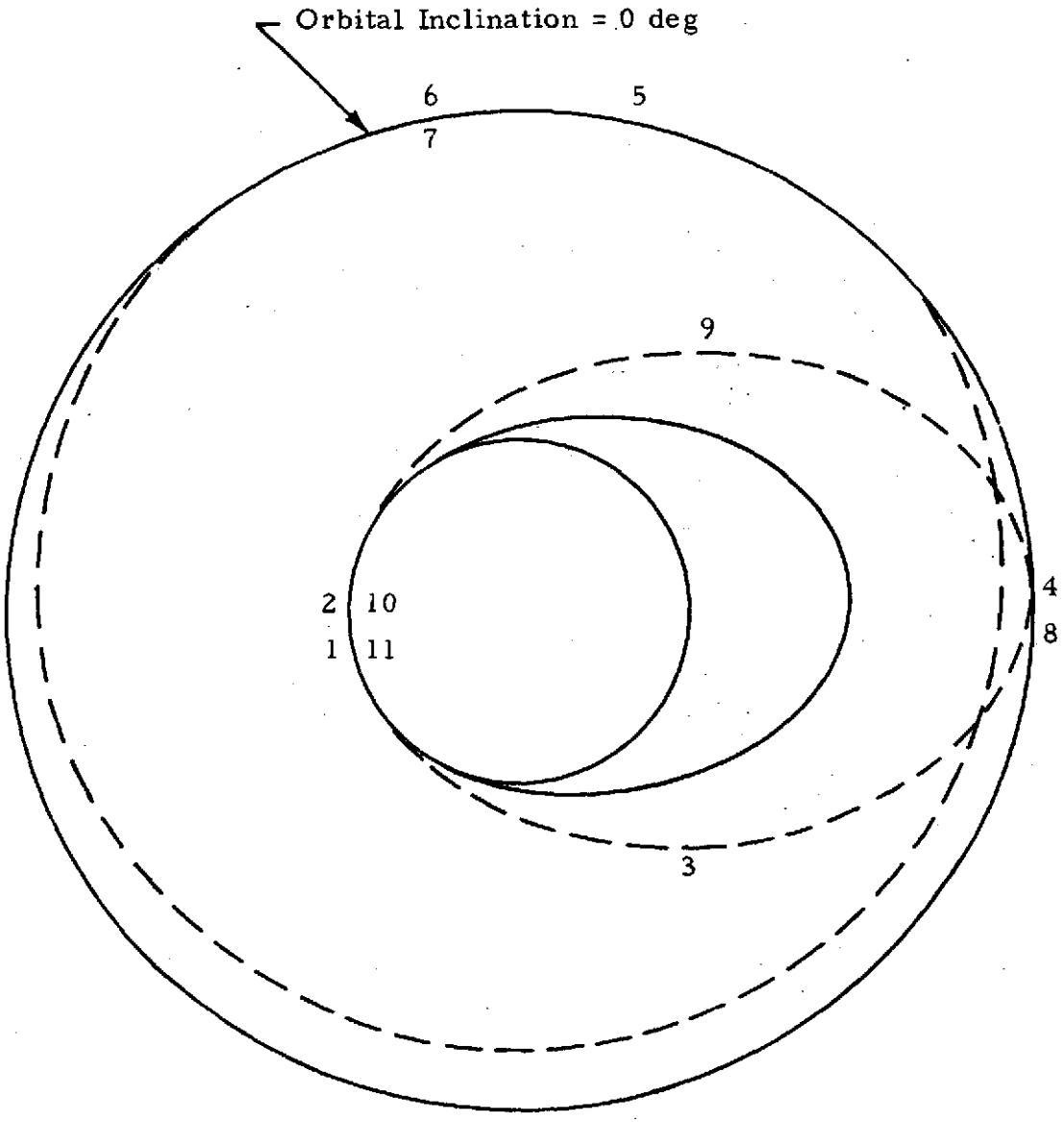

1. Delivered to 296 km Circular Orbit by the EOS
2. Burn to Mission Transfer Orbit
3. Midcourse Correction
4. Burn-to-Mission Orbit
5. Deliver Payload
6. Burn-to-Phasing Orbit for Rendezvous with Return Payload
7. Rendezvous and Dock with Return Payload
8. Burn-to-Transfer Orbit
9. Midcourse Correction
10. Burn to Achieve Phasing Orbit Apogee
11. Burn-to-EOS Rendezvous Orbit

Fig. 2 - Space Tug Mission Profile

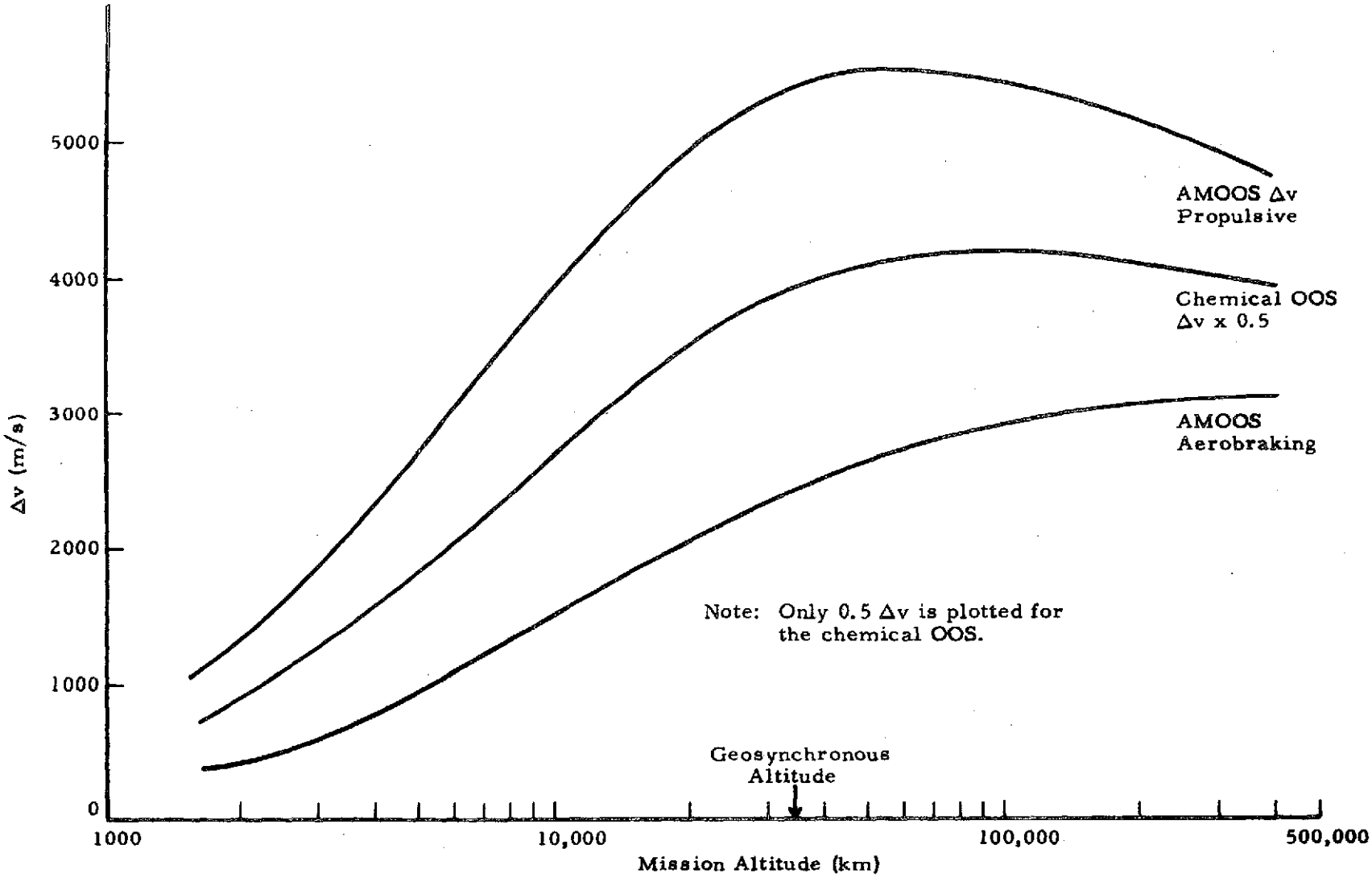

Fig. 3 - Incremental Velocity Requirements

Example: Max. Length, L = 18.3 m

LH_2 = 3,184 kg

LO_2 = 19,105 kg

22,289 kg

NOTE: All dimensions in meters

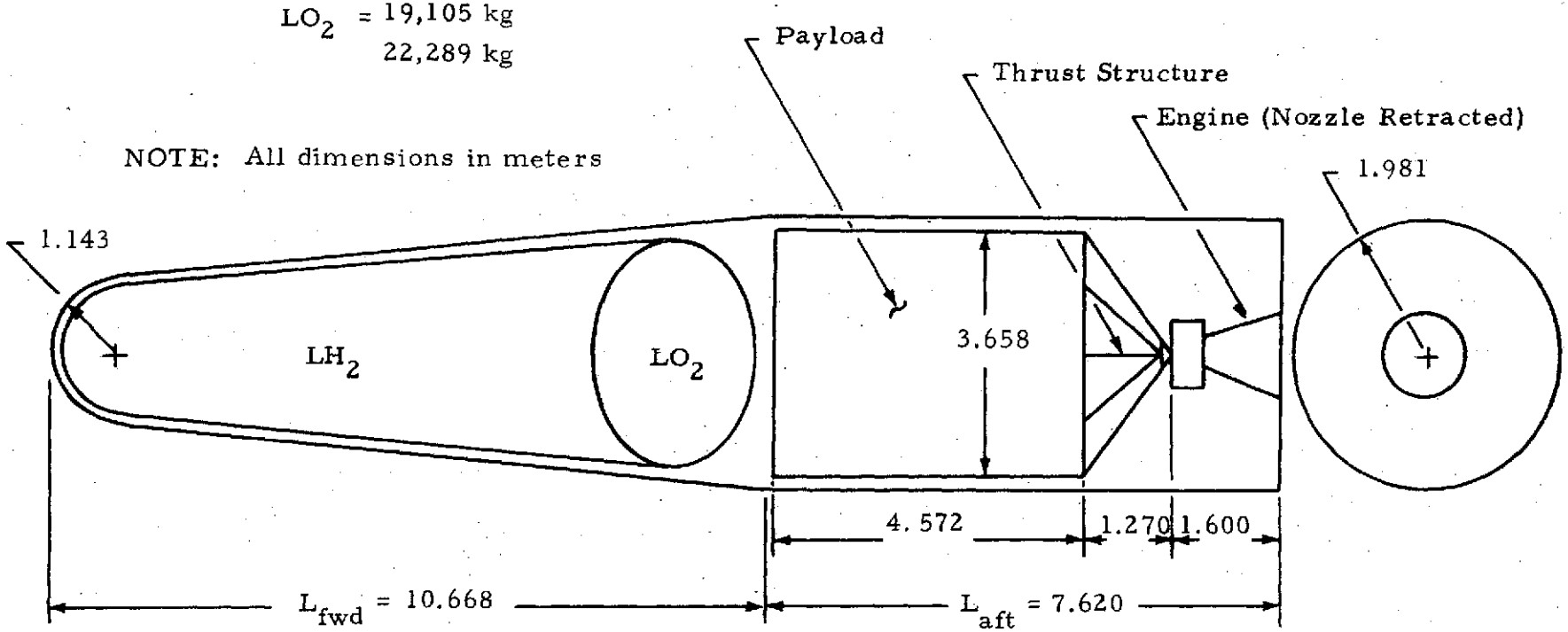

V_{fwd} = 77.220 m^3

V_{aft} = 93.927 m^3

Minimum V_{tot} = 171.147 m^3

Fig. 4 - Representative AMOOS Packaging

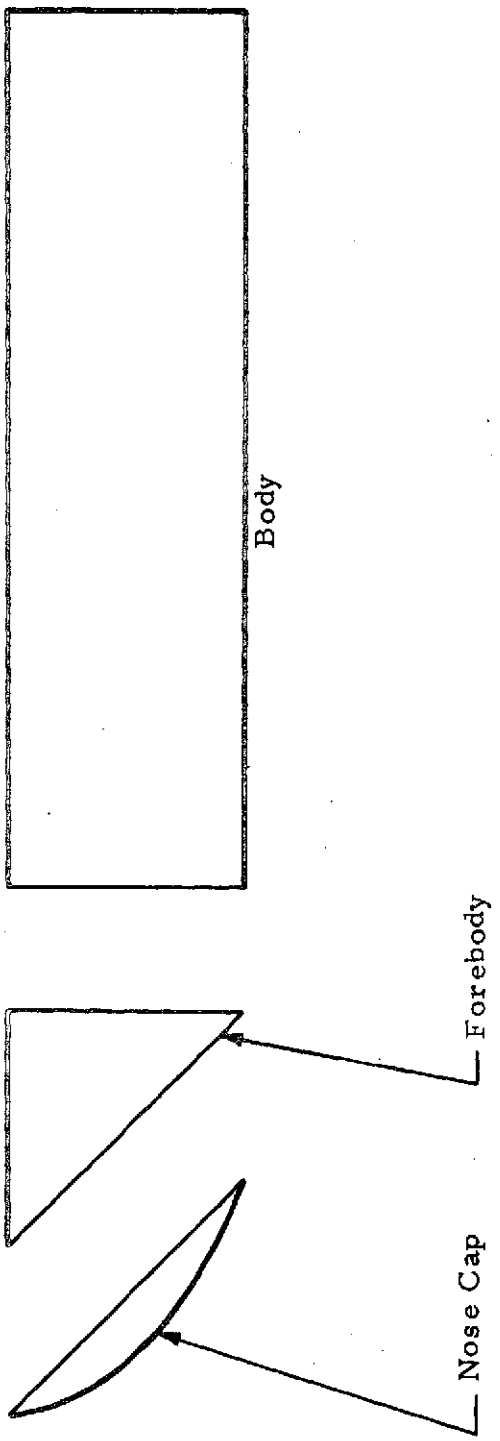

Fig. 5 - Components of the HB Configuration

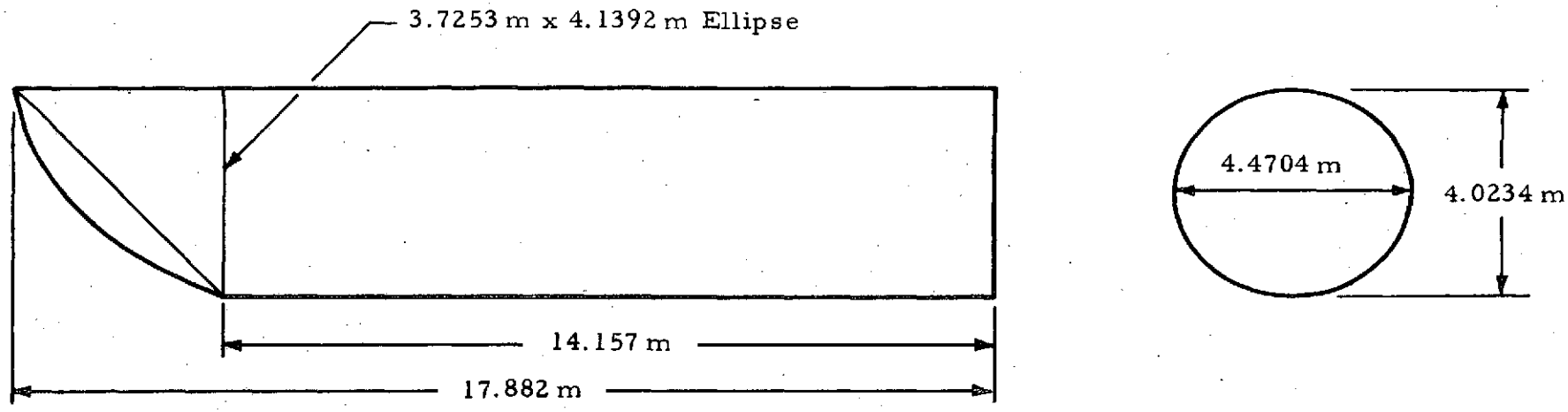

AMOOS Configuration HB

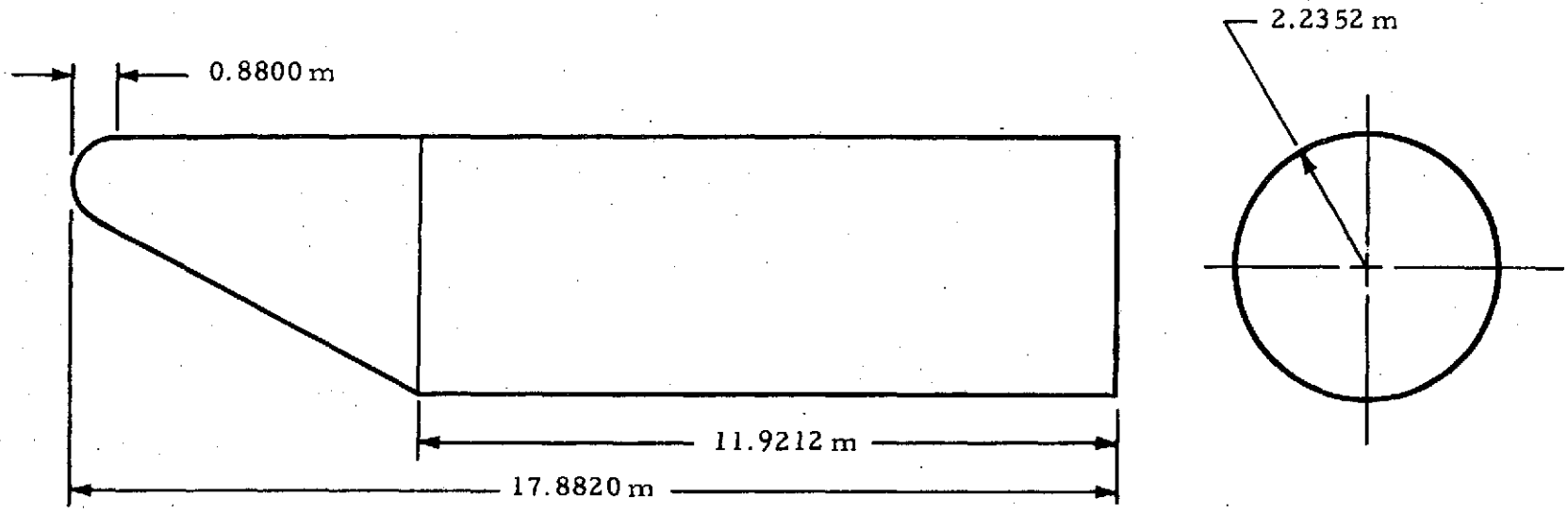

AMOOS Configuration 5B

Fig. 6 - Configurations for Detailed Study During Phase II

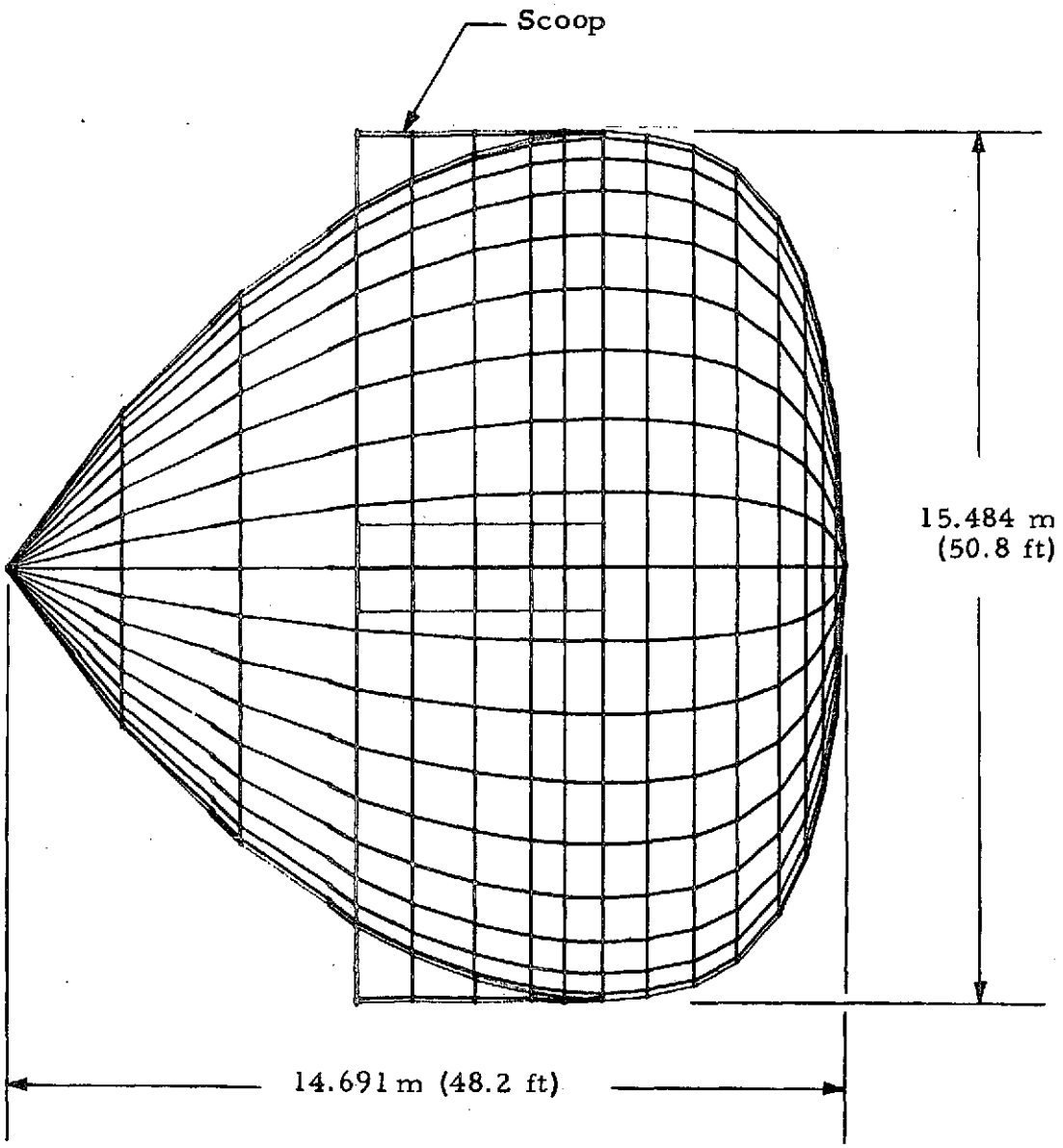

Fig. 7 - Trailing Ballute for A High Drag Concept for AMOOS

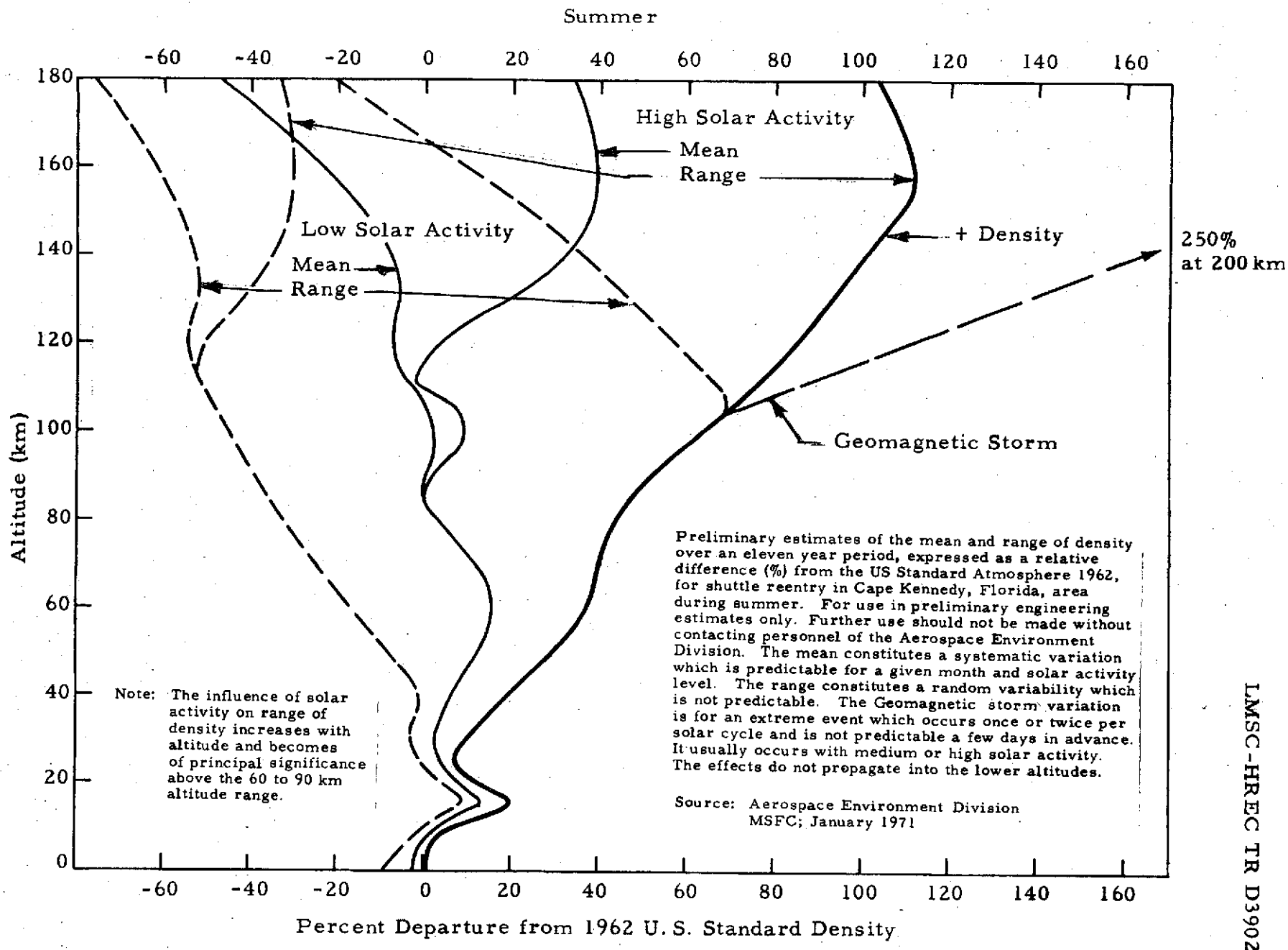

Fig. 8 - Atmospheric Density Dispersions Based on 1962 US Standard Atmosphere – Summer

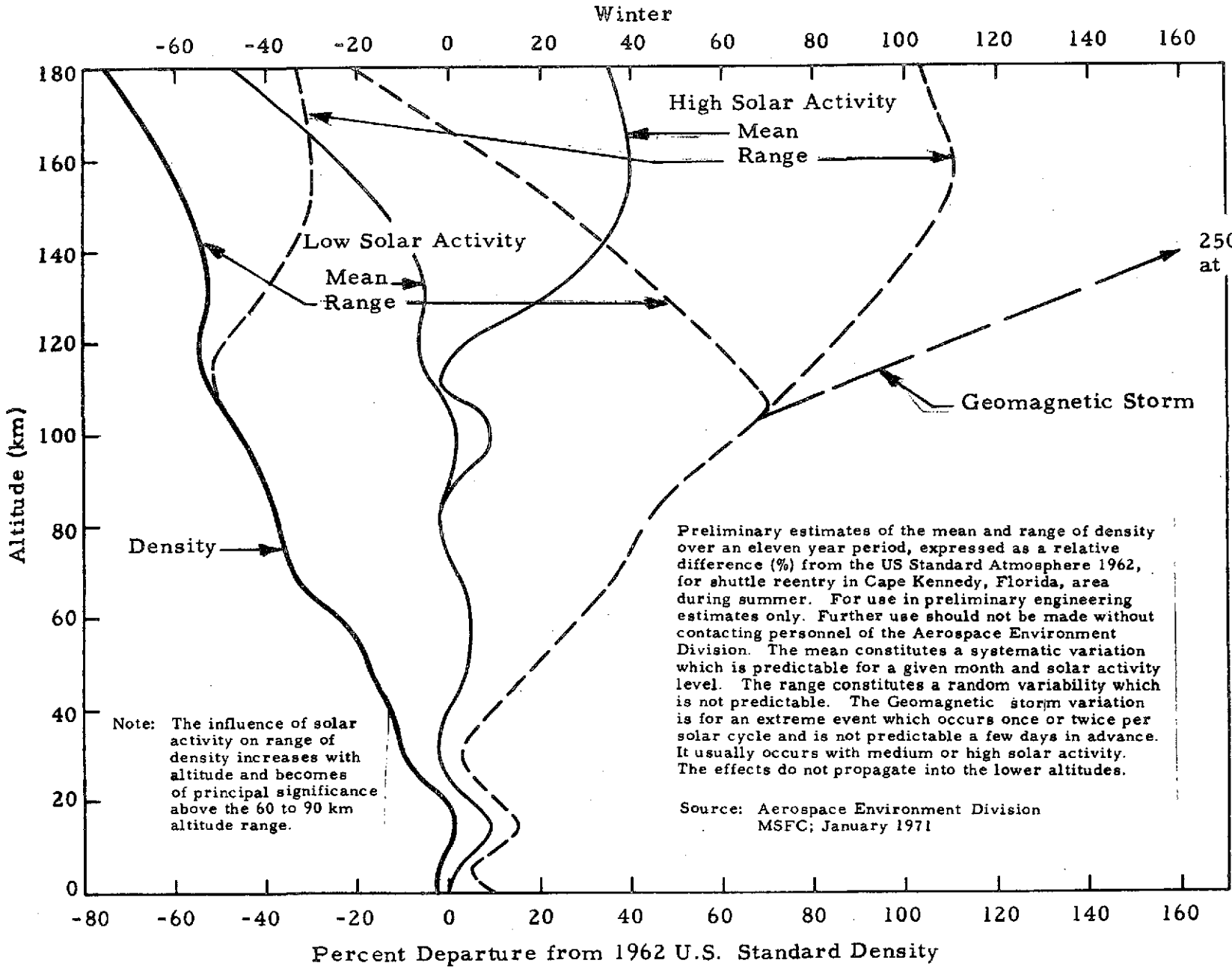

Fig. 9 - Atmospheric Density Dispersions Based on 1962 US Standard Atmosphere — Winter

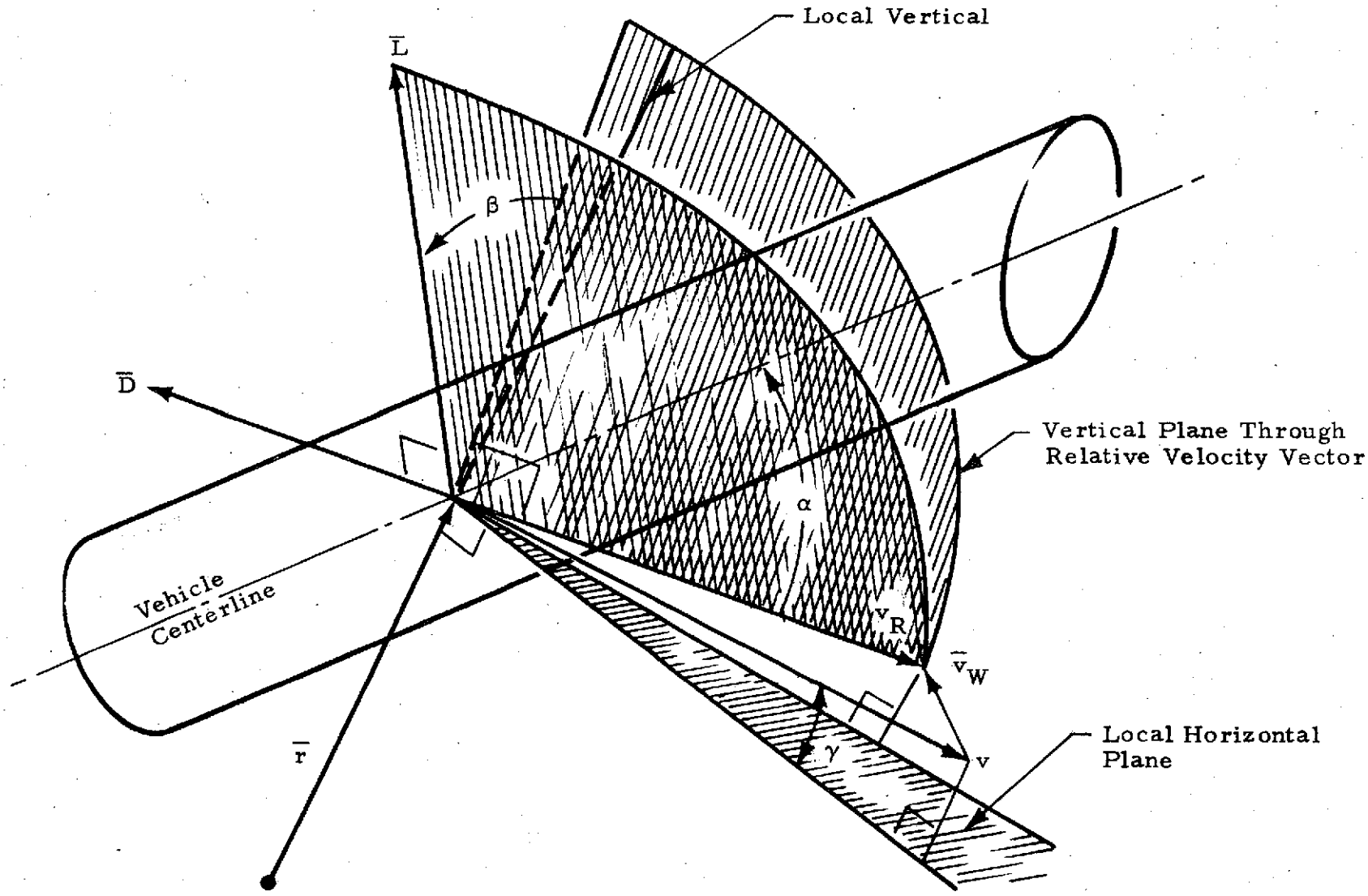

Fig. 10 - Definition of Angle of Attack, Bank Angle and Flight Path Angle

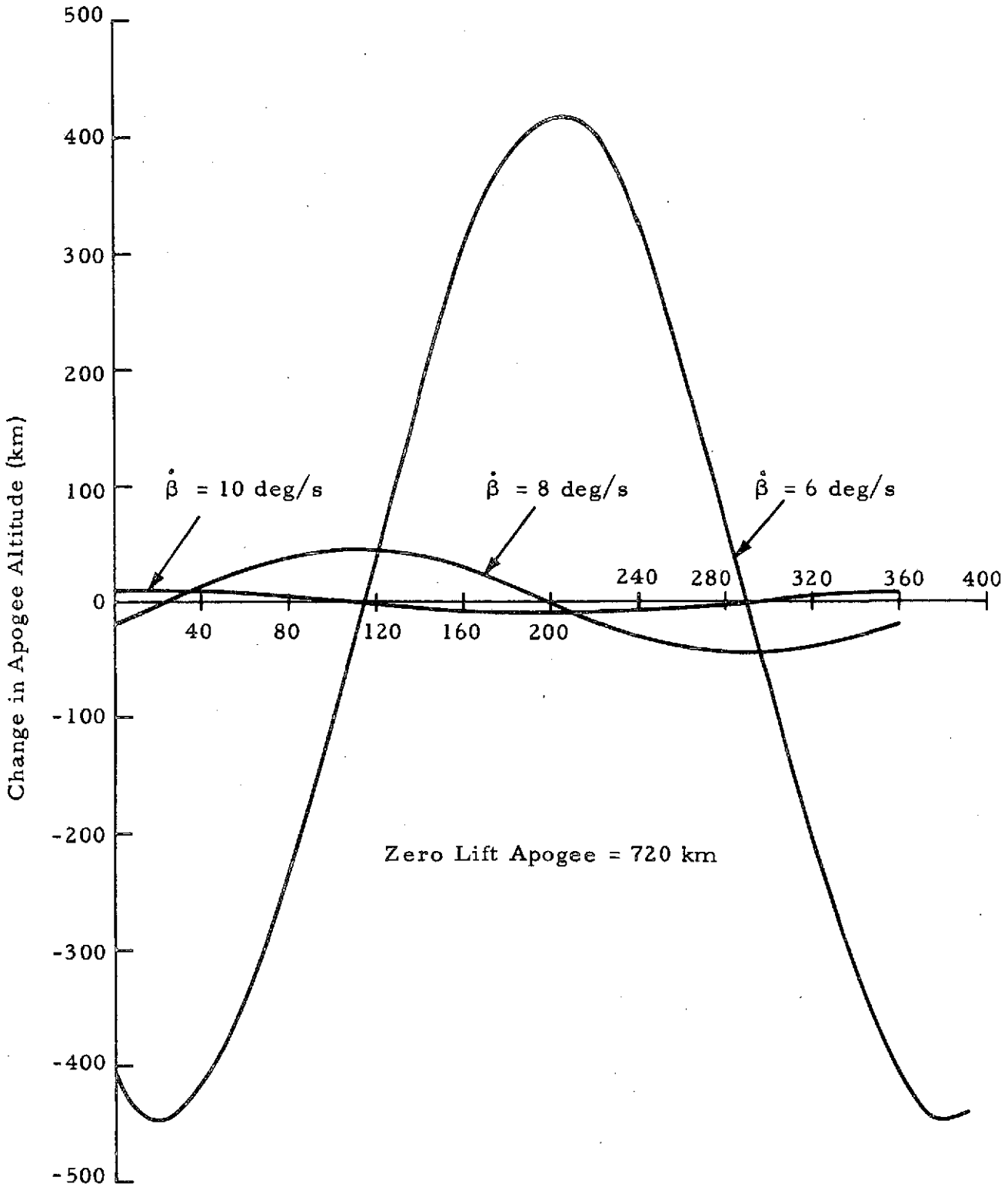

Fig. 11 - Change of Apogee Altitude as a Function of Initial Bank Angle at Atmospheric Entry for $\dot{\beta}$ of 6, 8, 10 deg/s. Vehicle HB, C_L = 1.753, C_D = 3.613, Vehicle Mass = 10,000 kg. Return from Geosynchroneous Orbit

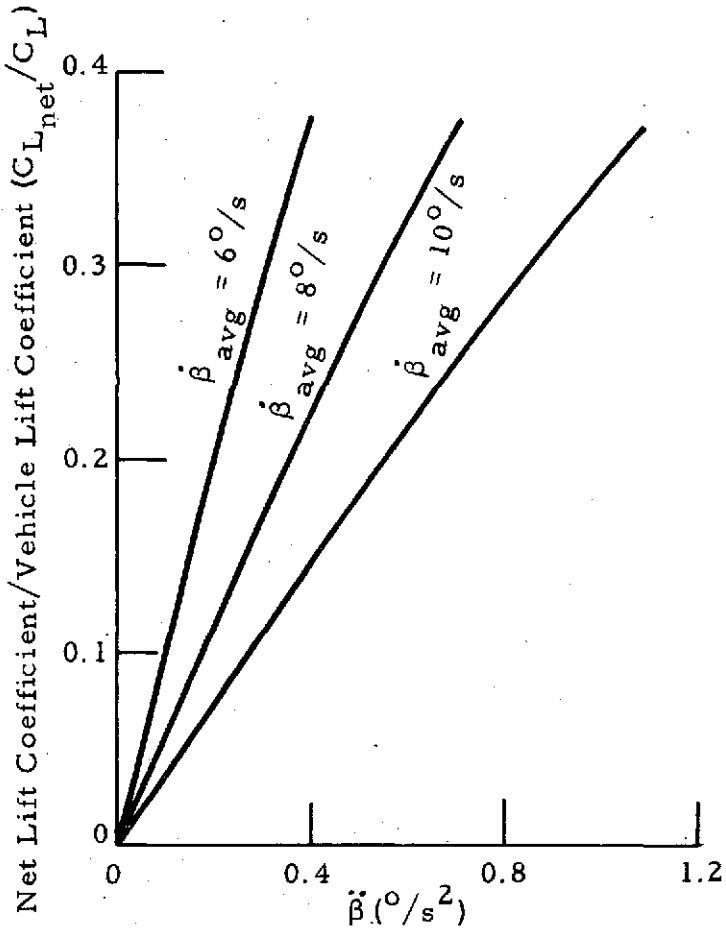

Fig. 12 - $C_{L_{net}}/C_L$ vs $\ddot{\beta}$

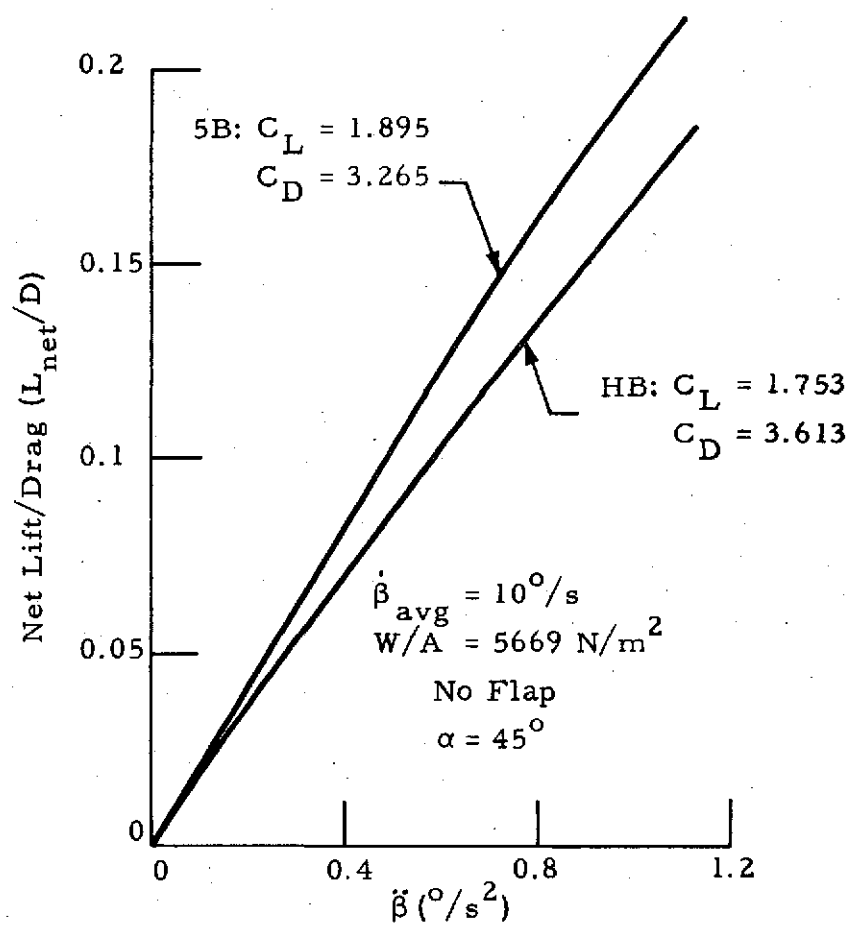

Fig. 13 - L_{net}/D vs $\ddot{\beta}$ for Vehicles HB and 5B

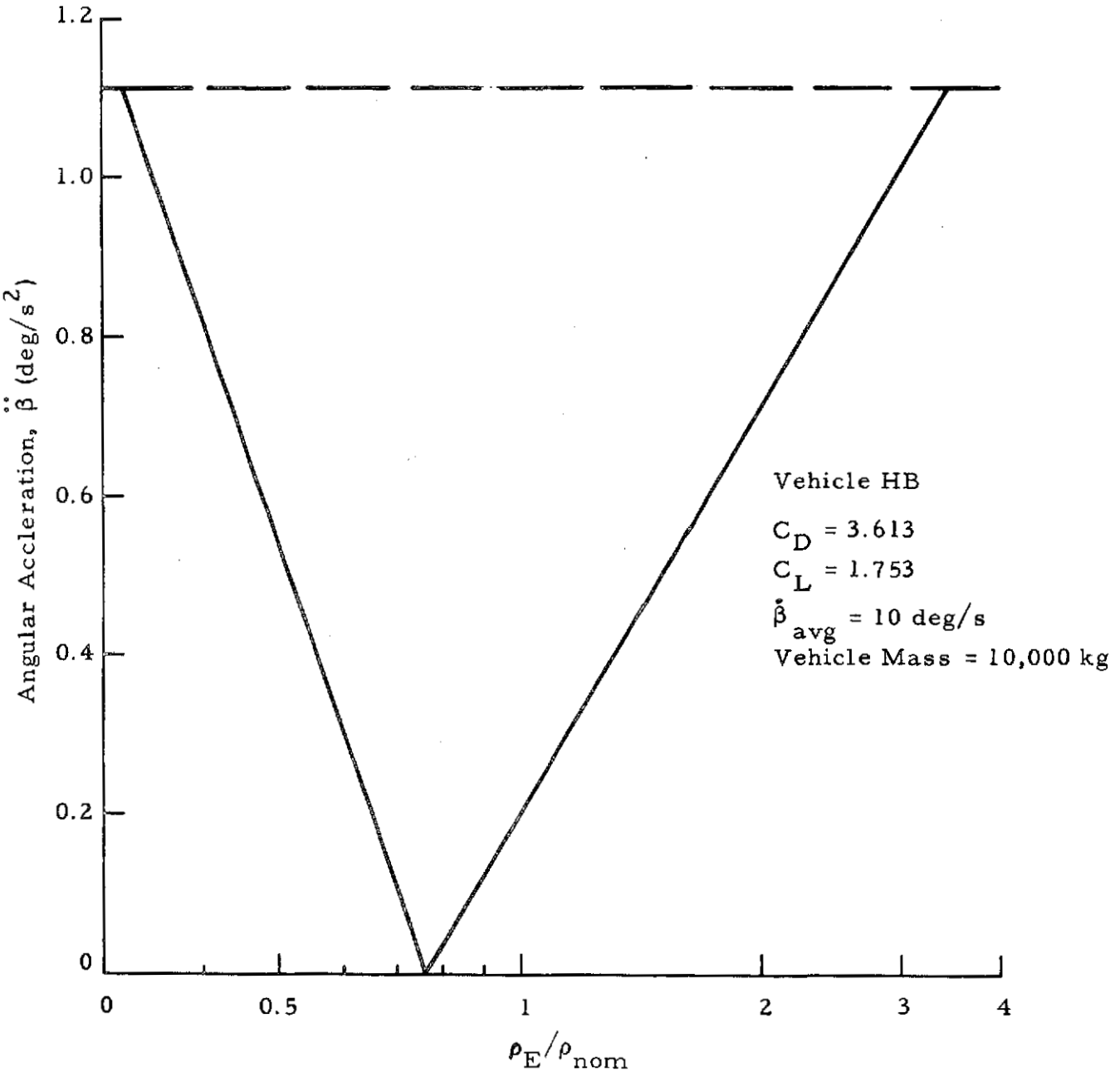

Fig. 14 - Angular Acceleration vs Ratio of Effective Density to Nominal Density for Return from Geosynchronous Orbit in One Atmospheric Pass

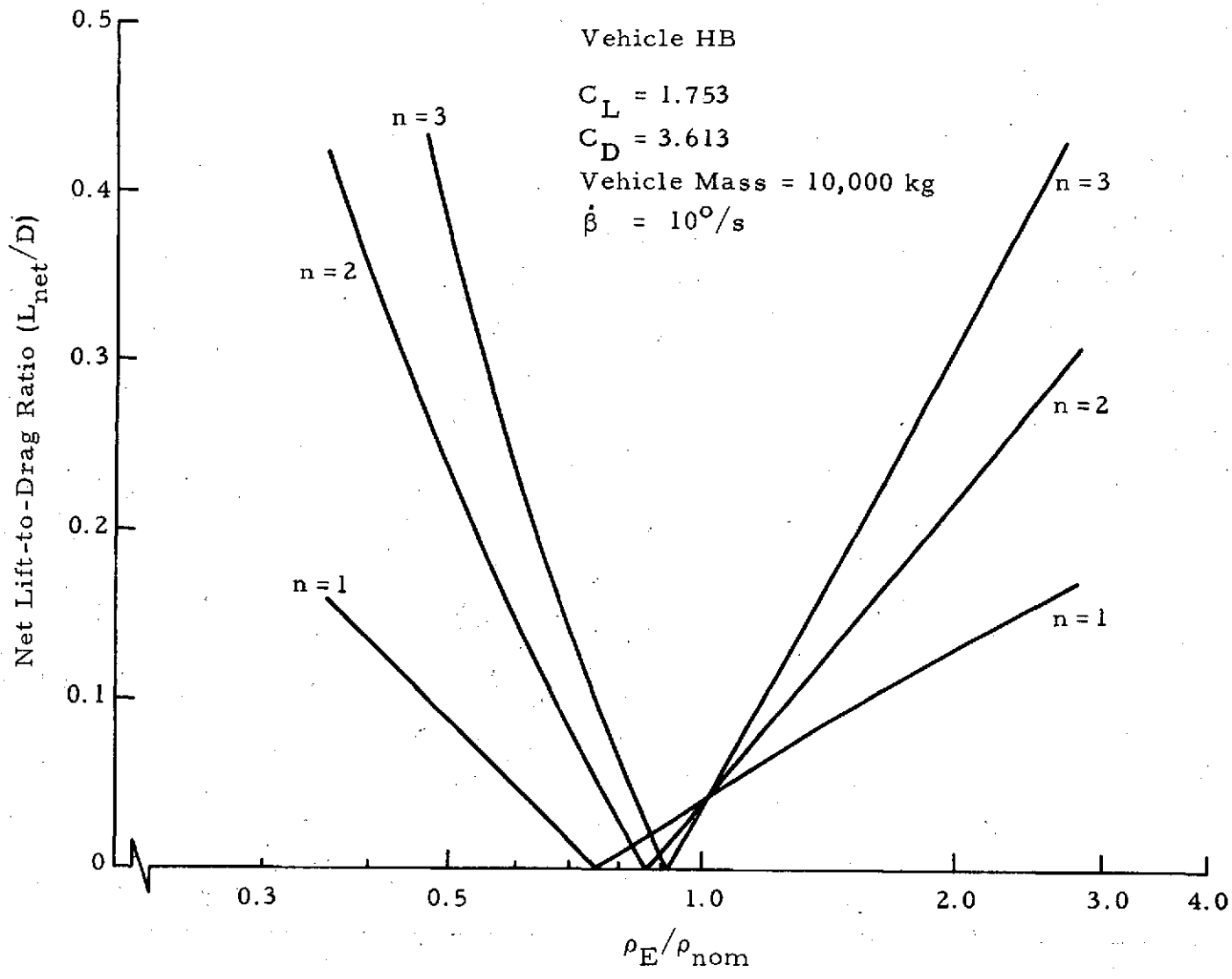

Fig. 15 - Lift-to-Drag Ratio Required vs Ratio of Effective Density to Nominal Density for Return from Geosynchronous Mission Orbit for 1, 2 and 3 Atmospheric Passes

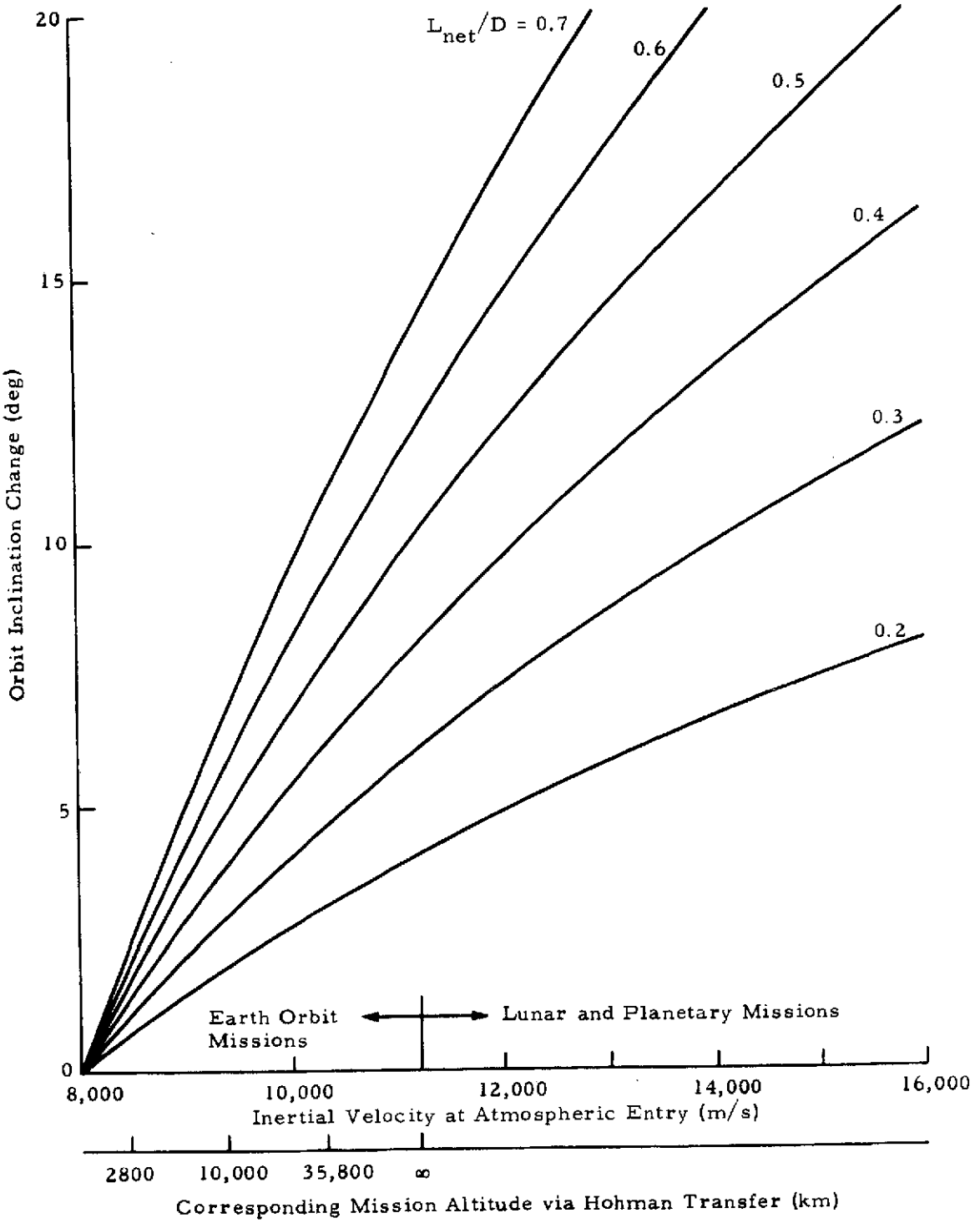

Fig. 16 - Inclination Change Capability for Nominal Atmospheric Conditions vs Inertial Velocity at Atmospheric Entry (120 km Altitude) for 1 to 10 Atmospheric Passes

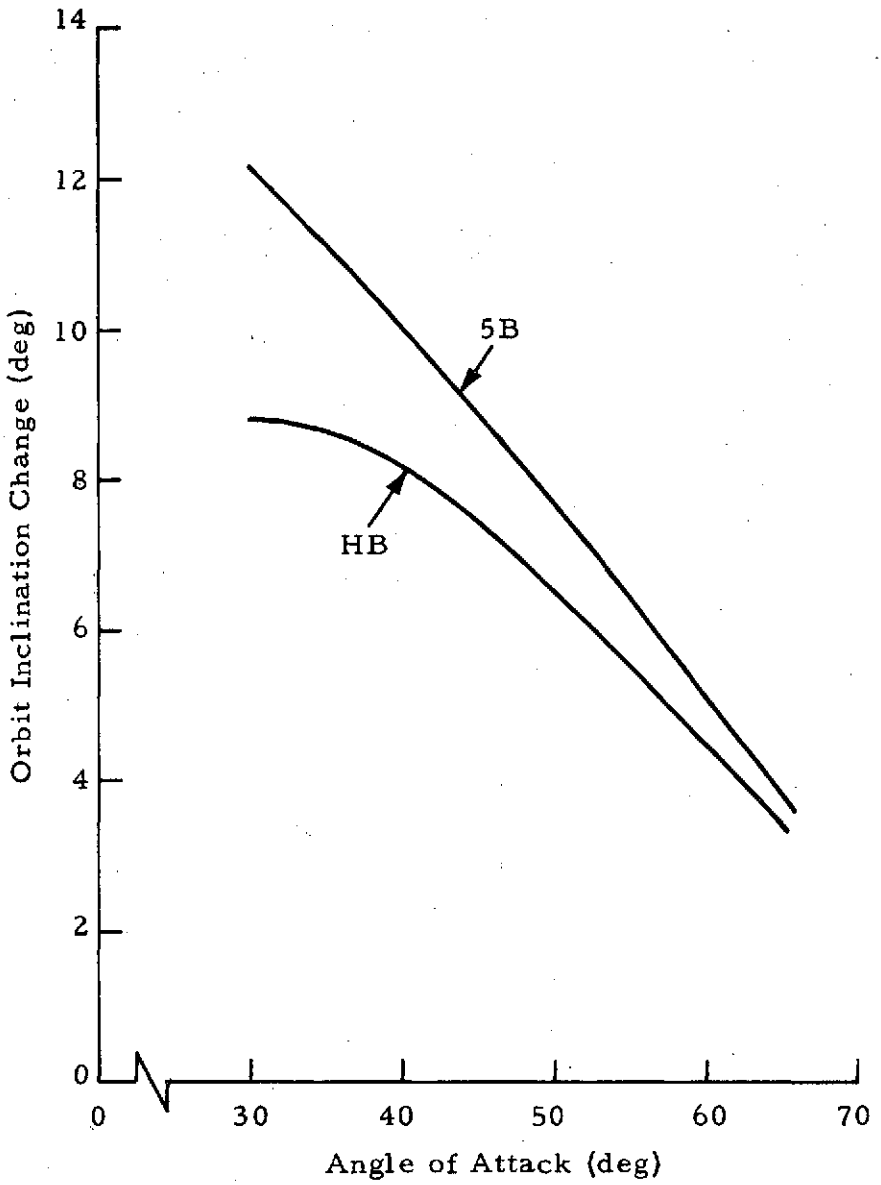

Fig. 17 - Orbit Inclination Change vs Angle of Attack for Return from Geosynchronous Mission Orbit and for any Number of Atmospheric Passes (Nominal atmospheric density and no navigation errors. Both vehicles without flap)

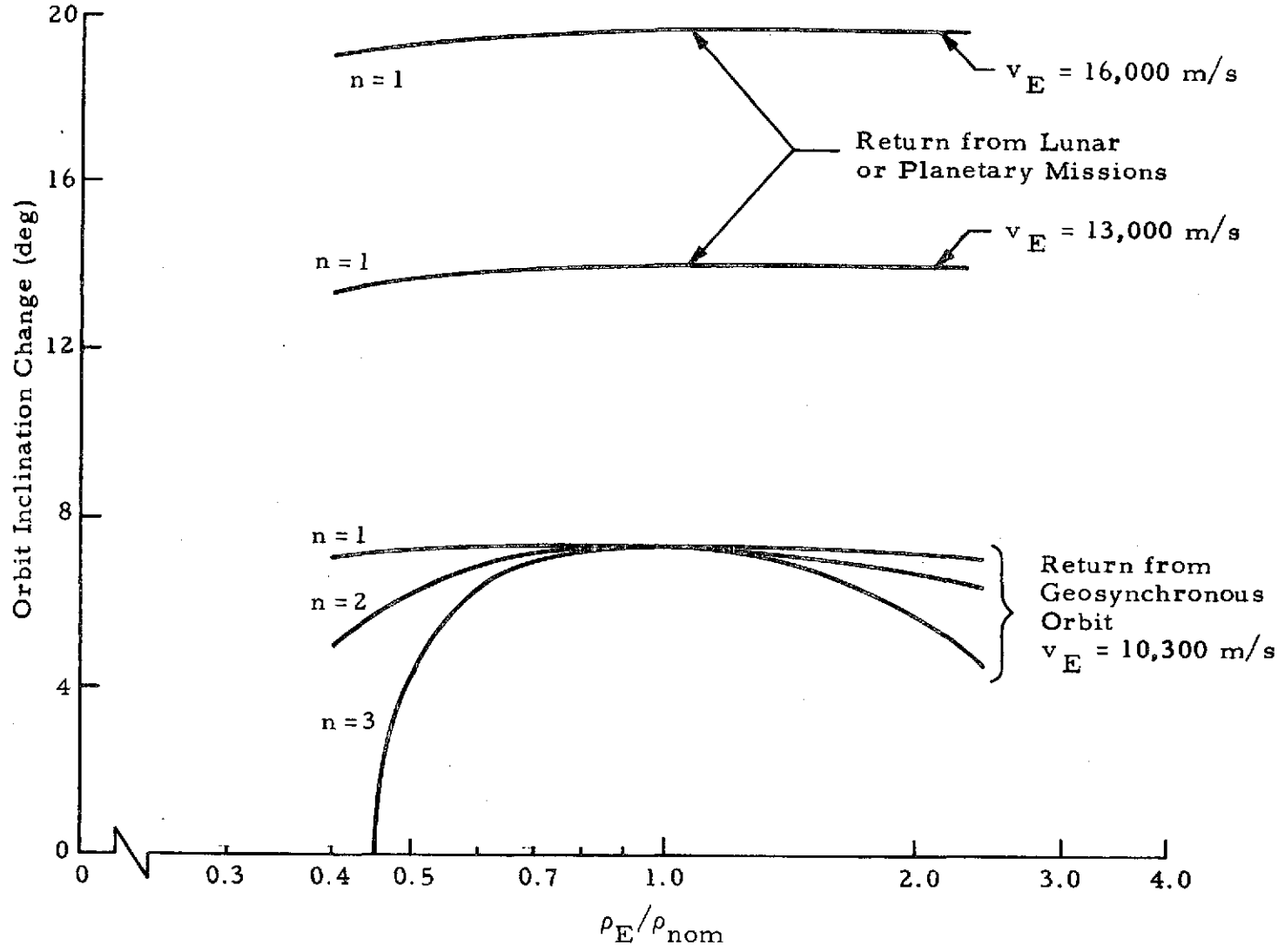

Fig. 18 - Orbit Inclination Change Capability vs Ratio of Effective Density to Nominal Density (The deviation of effective density from the nominal density represents atmospheric density variations and the effect of navigation errors for which a portion of the lift force is used to compensate for V_E is the inertial velocity at atmsopheric entry at 120 km altitude. HB vehicle, C_L = 1.753, C_D = 3.613, vehicle mass = 10,000 kg.)

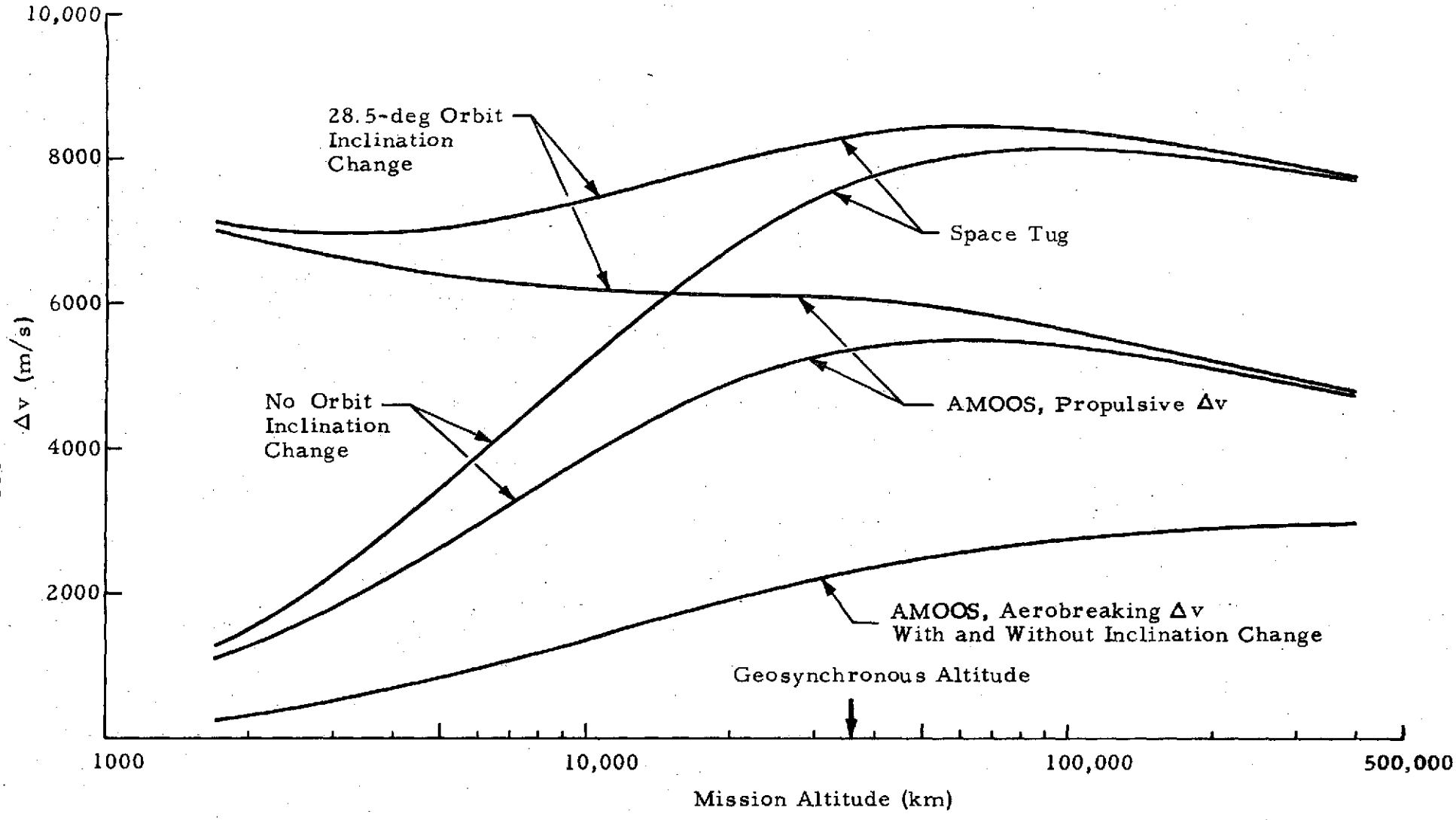

Fig. 19 - Incremental Velocity Requirements vs Mission Altitude With and Without Orbit Inclination Change (Gravity losses, contingency and Δv for orbital maneuvers not included)

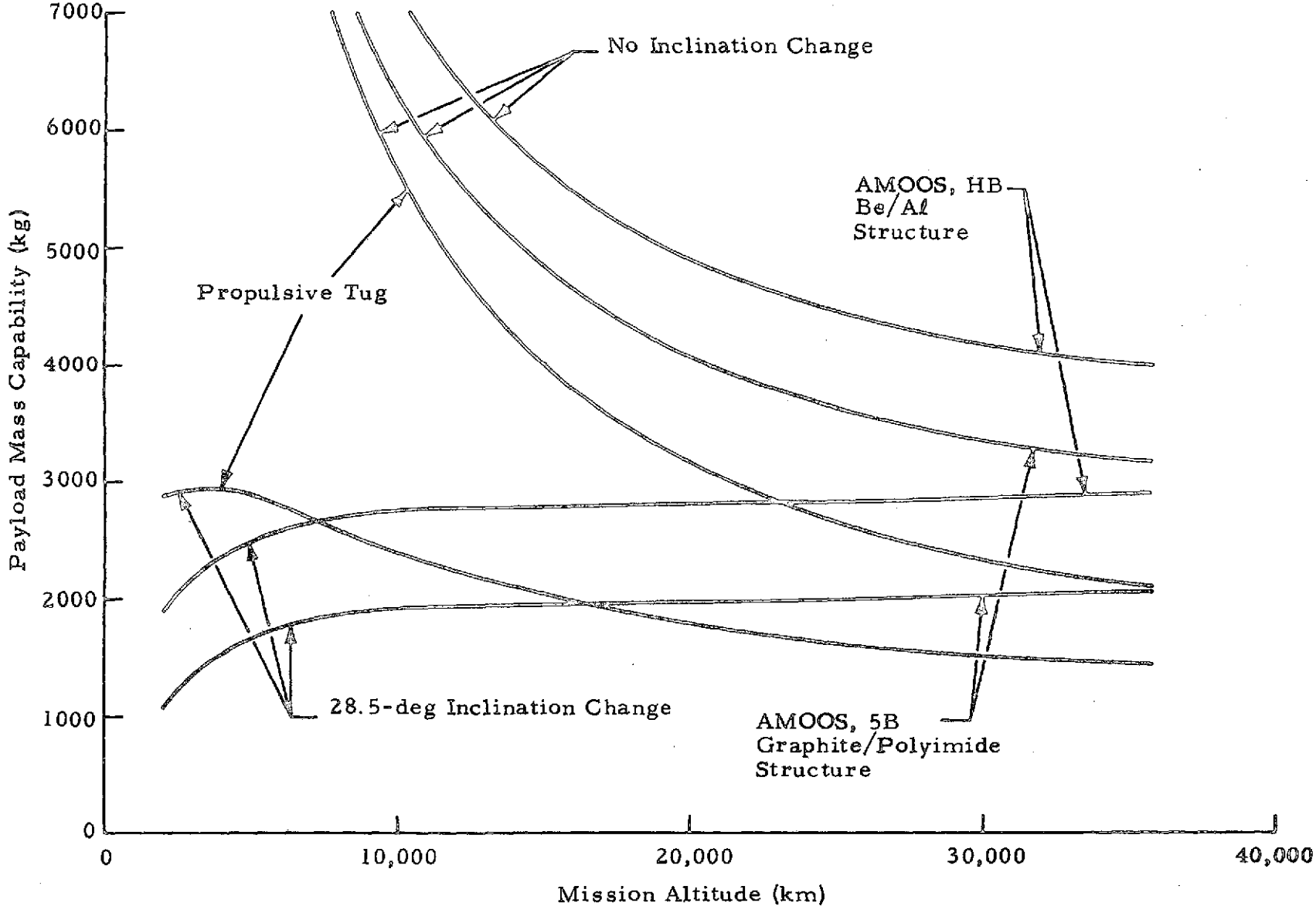

Fig. 20 - AMOOS Payload Mass Capability for Baseline Mission (Deliver and Retrieve Same Payload Mass)

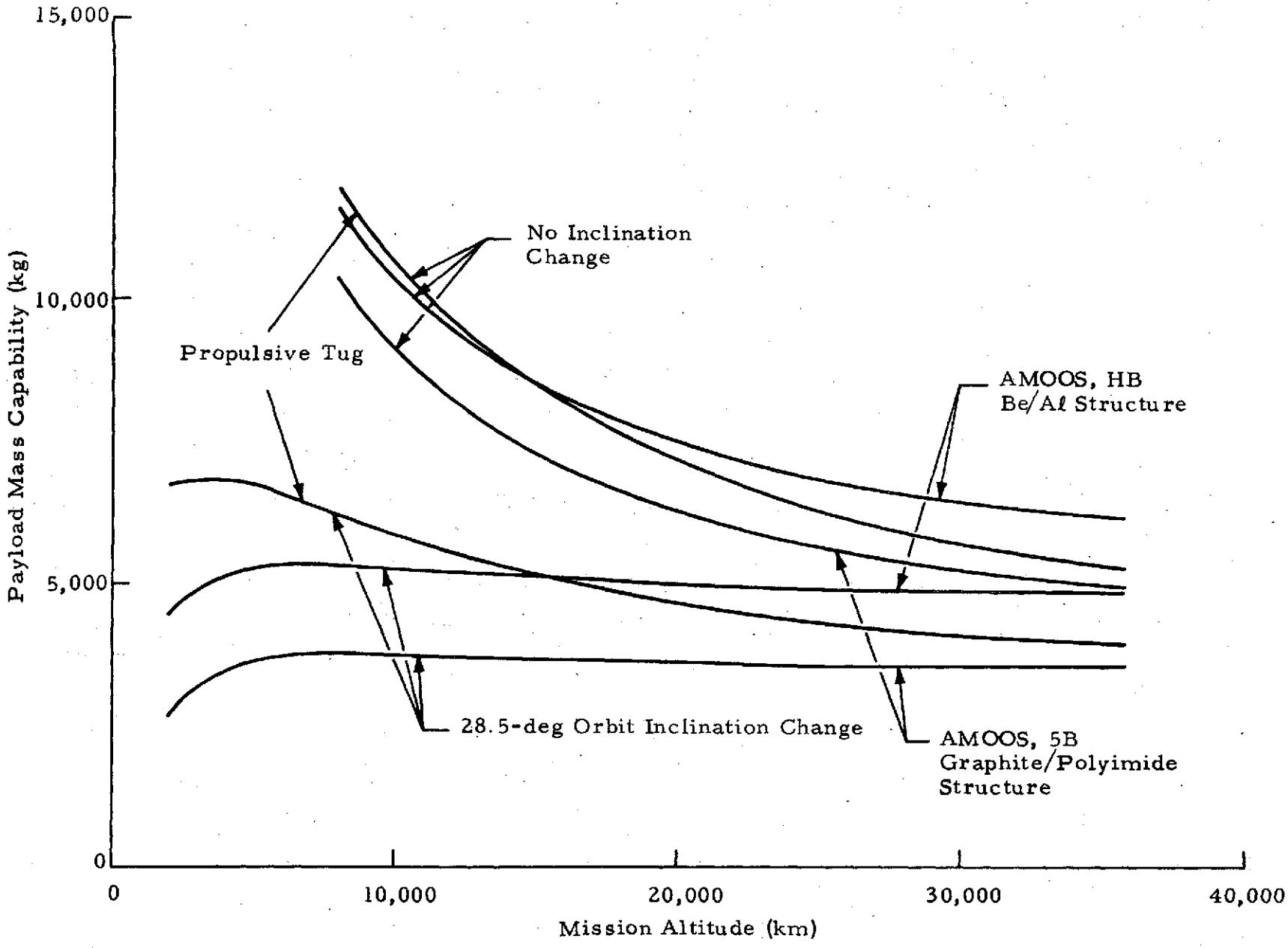

Fig. 21 - AMOOS Payload Mass Capability for Alternate Mission A (Payload Delivery Only)

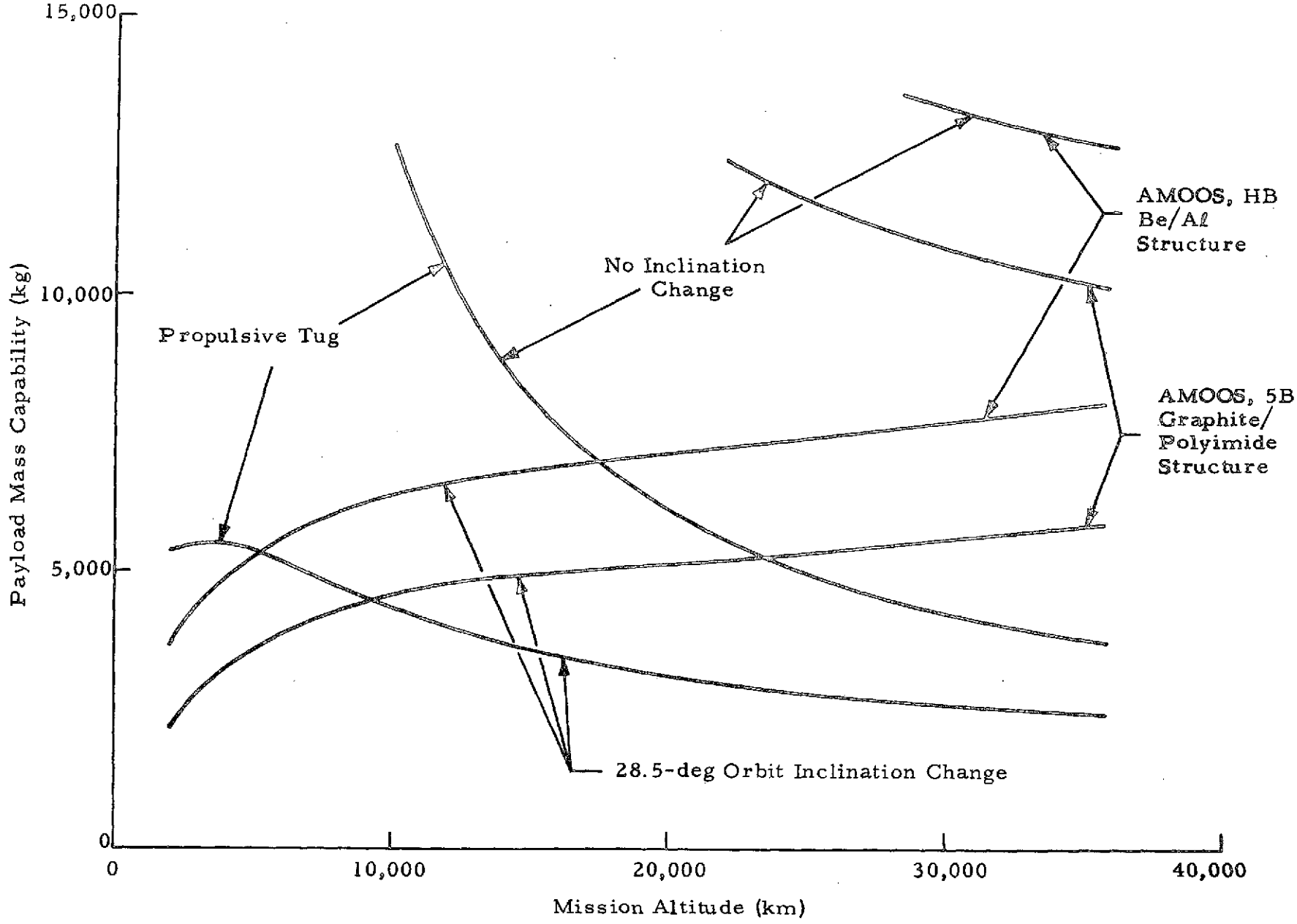

Fig. 22 - AMOOS Payload Mass Capability for Alternate Mission B (Payload Retrieval Only)

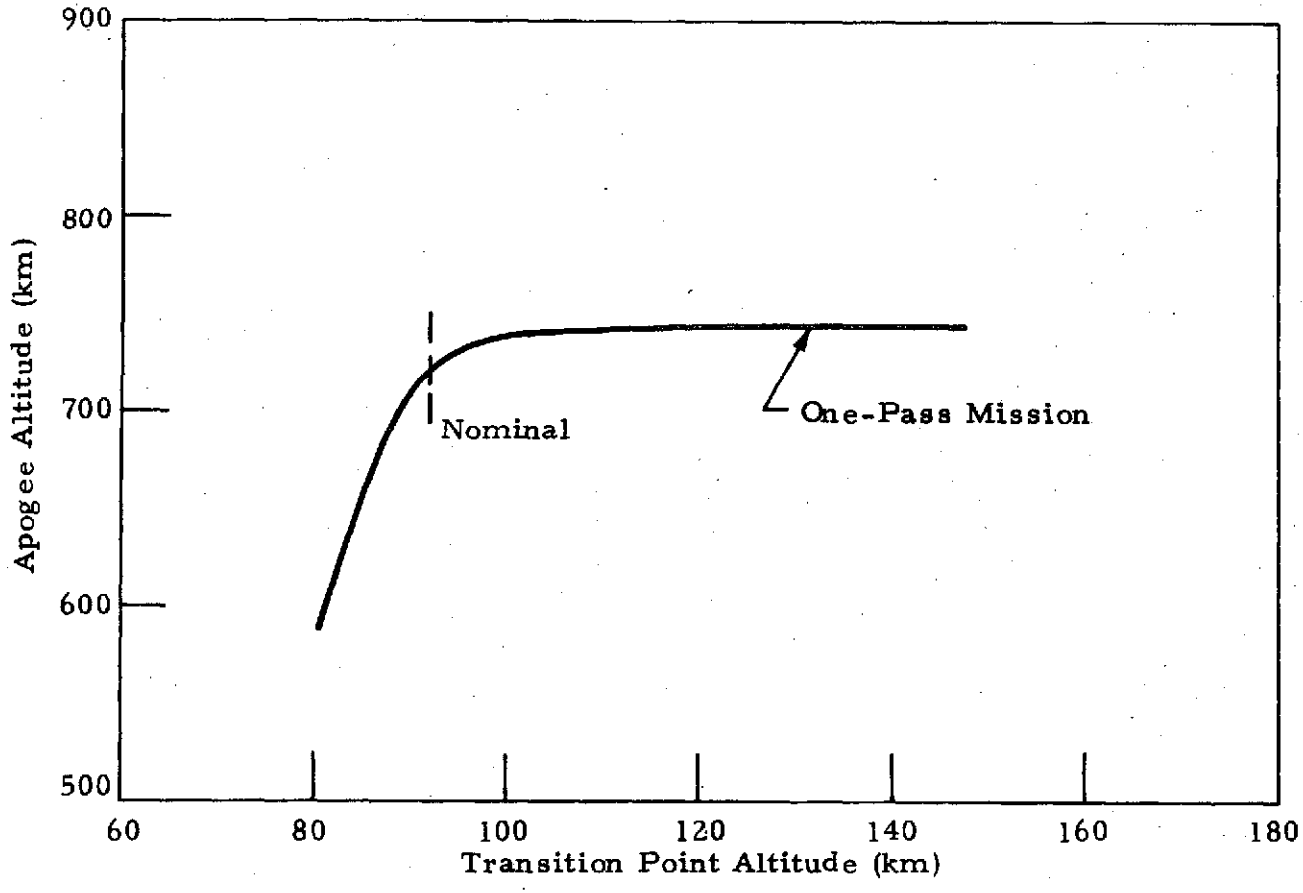

Fig. 23 - Flow Transition Point Effect on AMOOS 5B Apogee Altitude (Continuum to Transitional Flow)

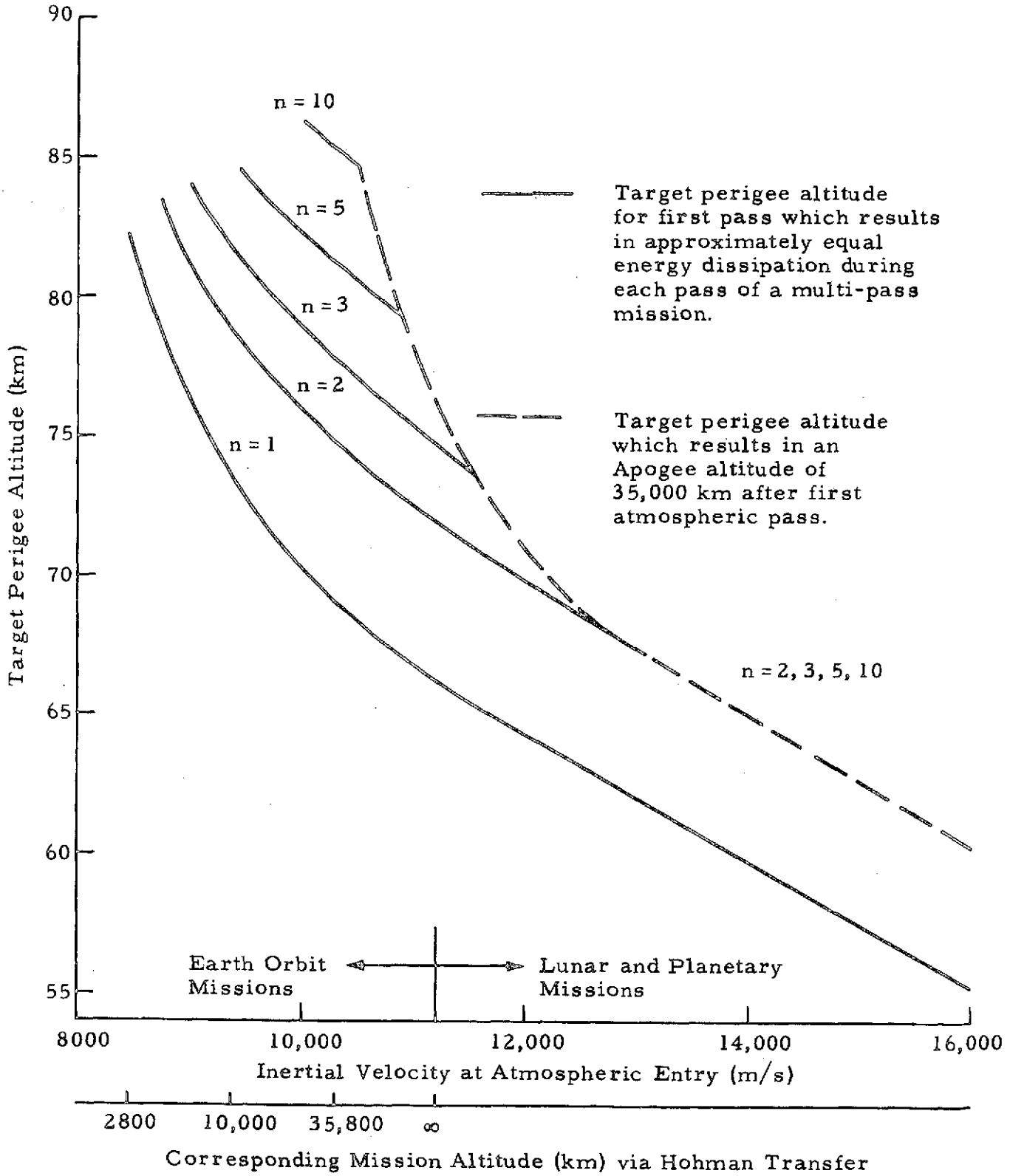

Fig. 24 - Target Perigee Altitude for Nominal Atmospheric Conditions vs Inertial Velocity at Atmospheric Entry for Single and Multi-Pass Aeromaneuvers Vehicle HB, C_L = 1.753, C_D = 3.613, Vehicle Mass = 10,000 kg

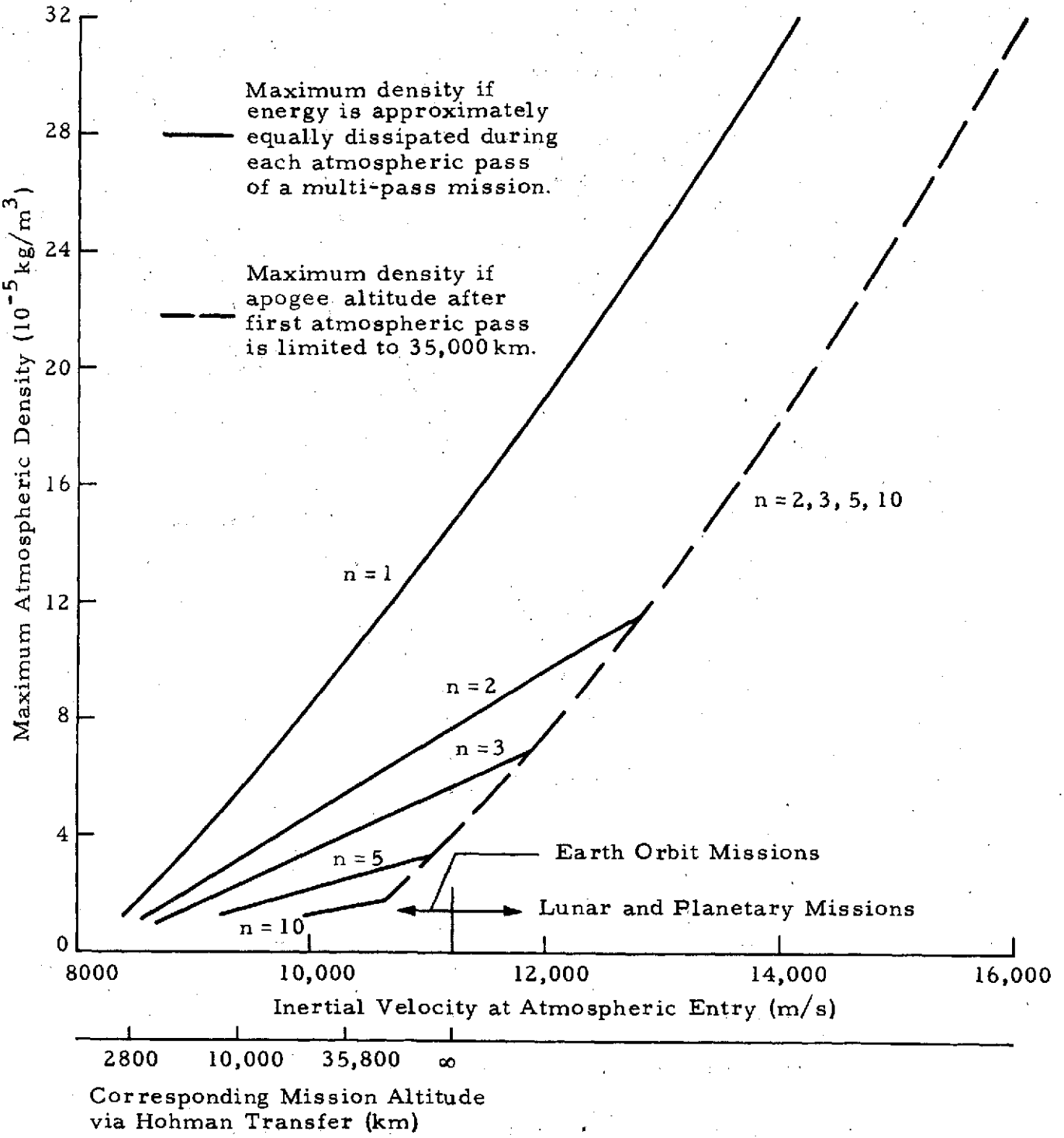

Fig. 25 - Maximum Atmospheric Density for Nominal Atmospheric Conditions vs Inertial Velocity at Atmospheric Entry (120 km Altitude) for Single and Multi-Pass Aeromaneuvers, Vehicle HB, C_L = 1.753, C_D = 3.613, Vehicle Mass = 10,000 kg

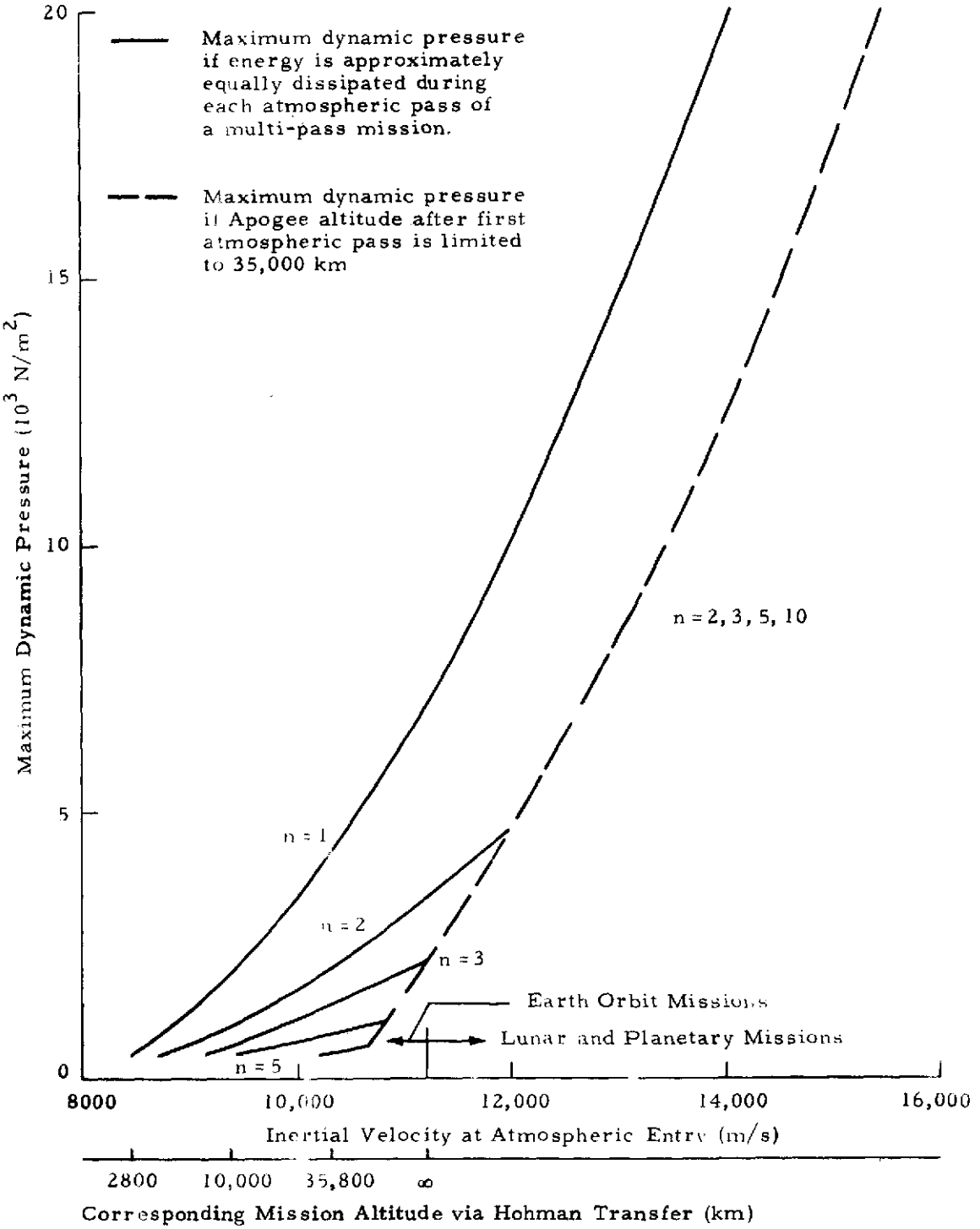

Fig. 26 - Maximum Dynamic Pressure for Nominal Atmospheric Conditions vs Inertial Velocity at Atmospheric Entry (120 km Altitude) for Single and Multi-Pass Aeromaneuvers (Vehicle HB, C_L = 1.753, C_D = 3.613, Vehicle Mass = 10,000 kg)

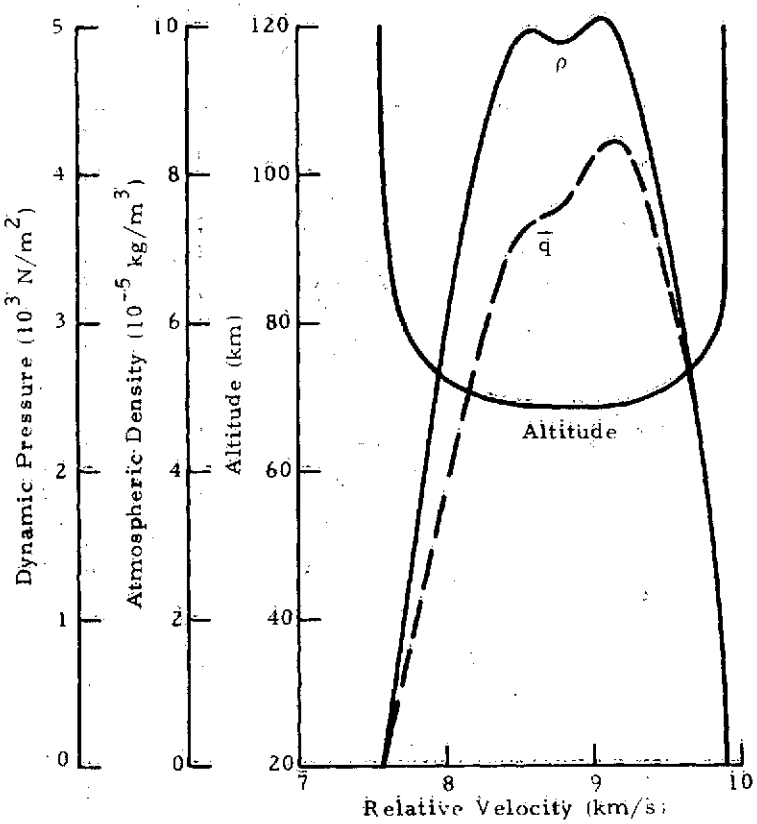

Fig. 27 - Nominal Trajectory for Return from Geosynchronous Orbit in One Atmospheric Pass (Vehicle HB, C_D = 3.613, C_L = 1.753, Vehicle Mass = 10,000 kg)

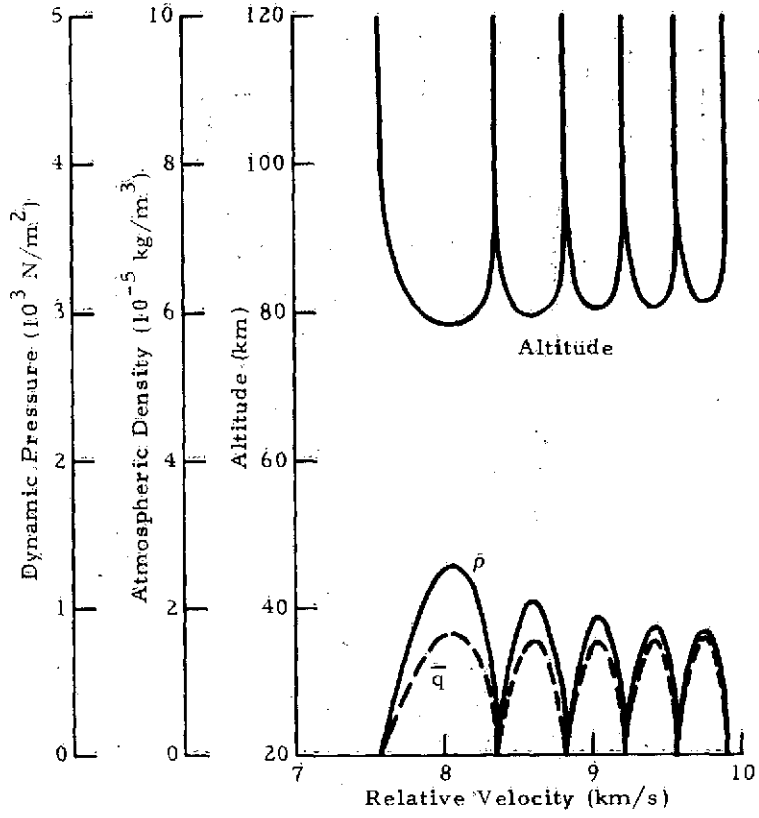

Fig. 28 - Nominal Trajectory for Return from Geosynchronous Orbit in Five Atmospheric Passes (Vehicle HB, C_D = 3.613, C_L = 1.753, Vehicle Mass = 10,000 kg)

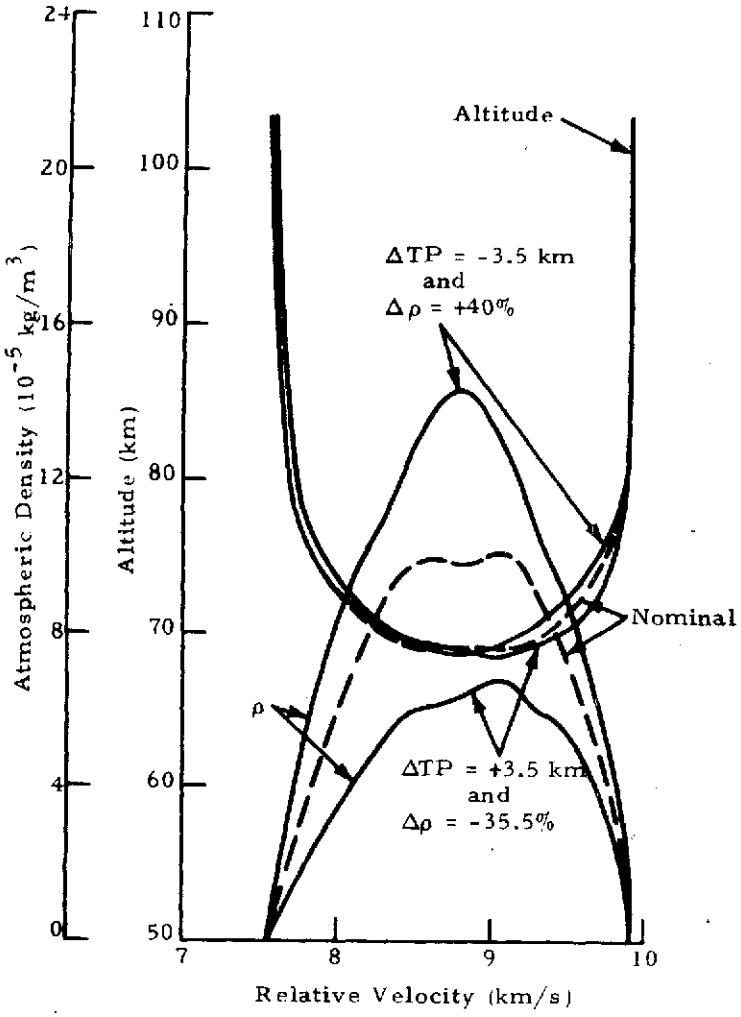

Fig. 29 - Density and Altitude Variations for a Return from Geosynchronous Orbit in One Atmospheric Pass. ΔTP = Variation of Target Perigee from Nominal Δρ = Variation of Atmospheric Density from Nominal Vehicle HB, C_D = 3.613, C_L = 1.753, Vehicle Mass = 10,000 kg

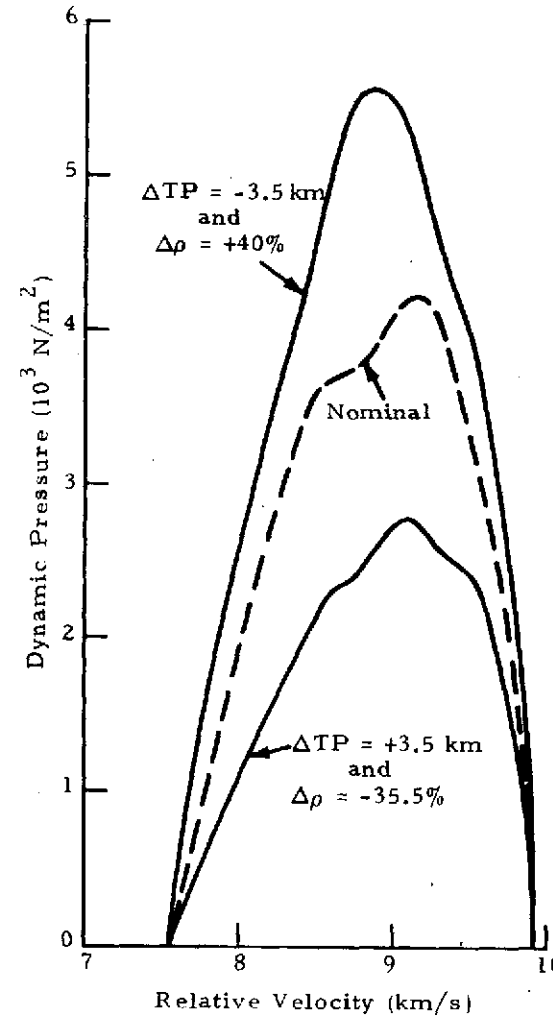

Fig. 30 - Pressure Variation for a Return from Geosynchronous Orbit in One Atmospheric Pass. ΔTP = Variation of Target Perigee from Nominal Δρ = Variation of Atmospheric Density from Nominal Vehicle HB, C_D = 3.613, C_L = 1.753, Vehicle Mass = 10,000 kg

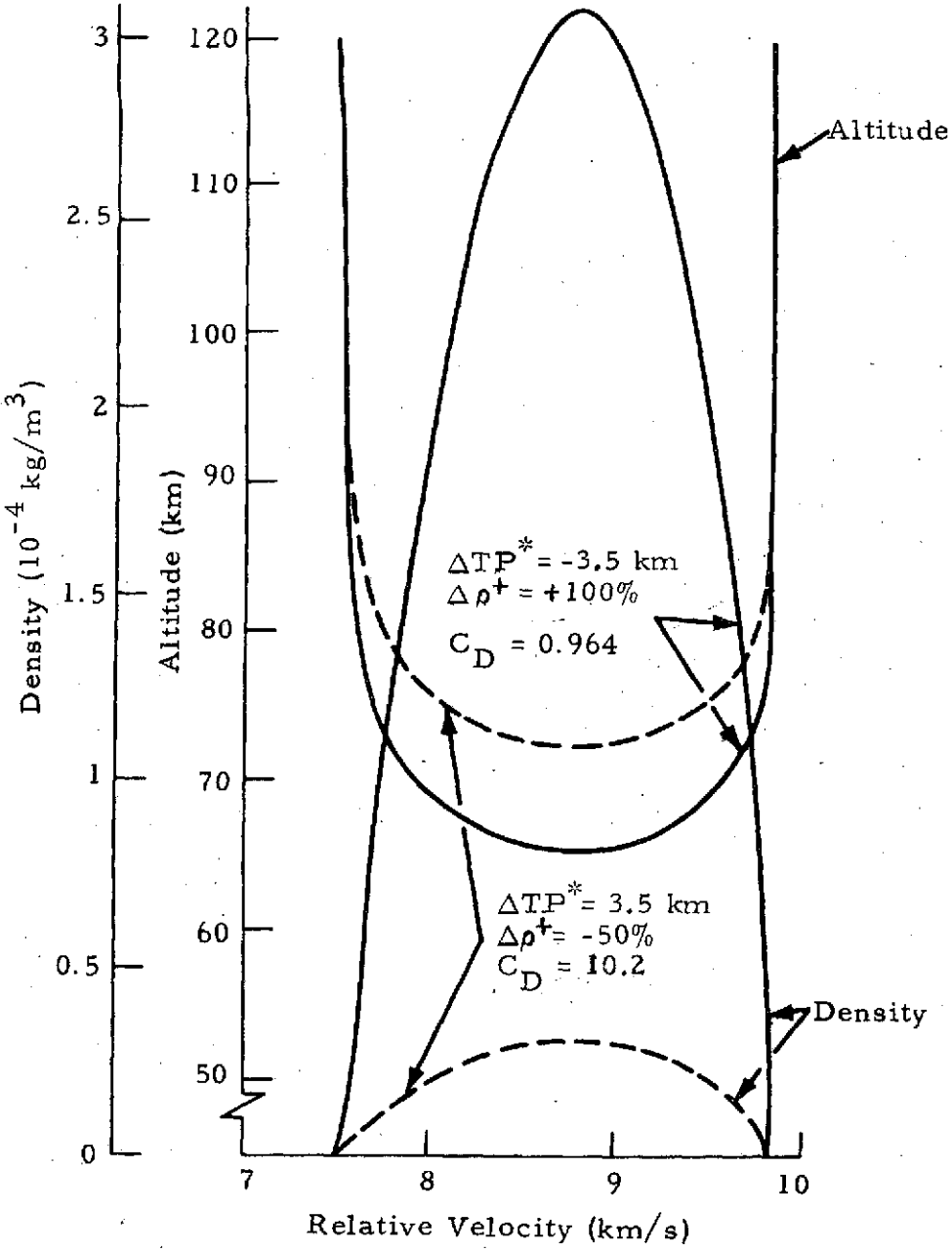

Fig. 31 - Density and Altitude Variations for Vehicle with High Drag Device (Ballute) for Return from Geosynchronous Orbit

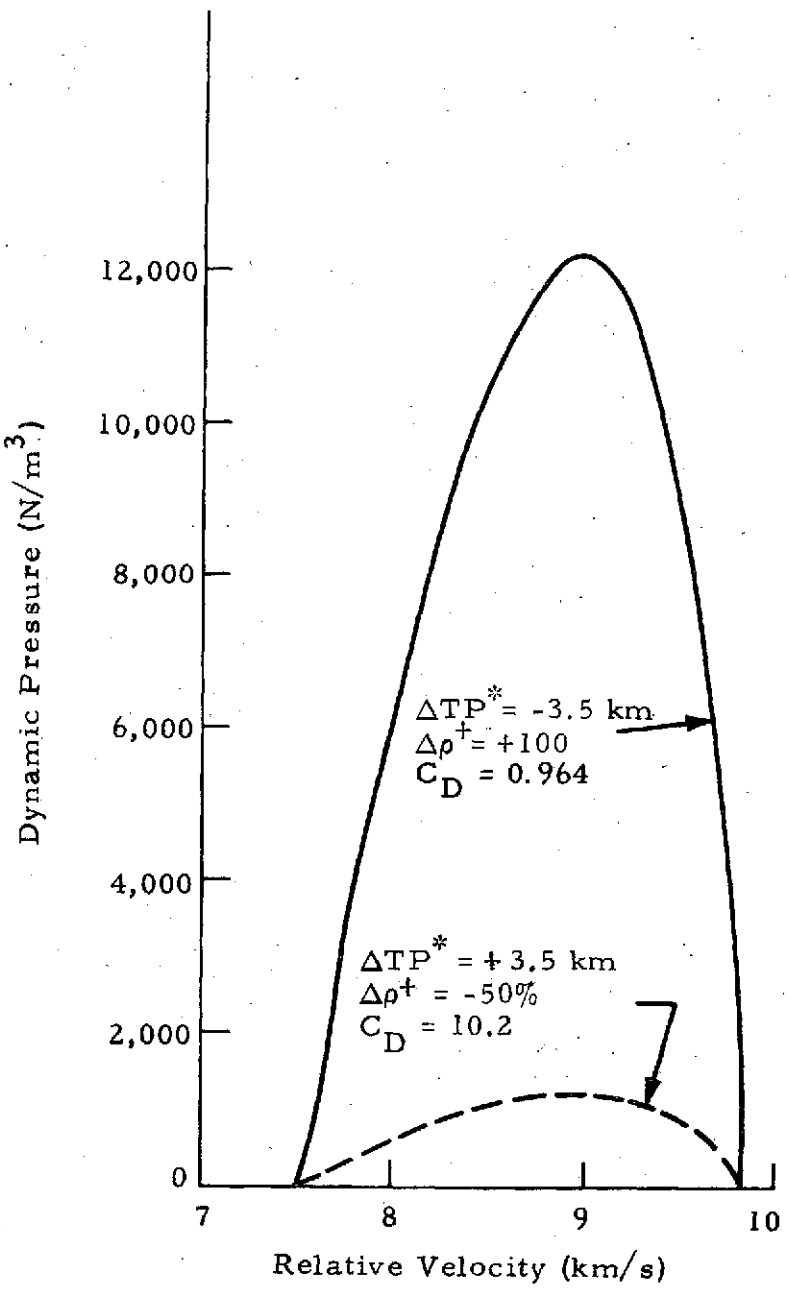

Fig. 32 - Dynamic Pressure Variation for Vehicle with High Drag Device (Ballute) for Return from Geosynchronous Orbit

*ΔTP = Variation of Target Perigee for Nominal; $^+\Delta\rho$ = Variation of Atmospheric Density from Nominal

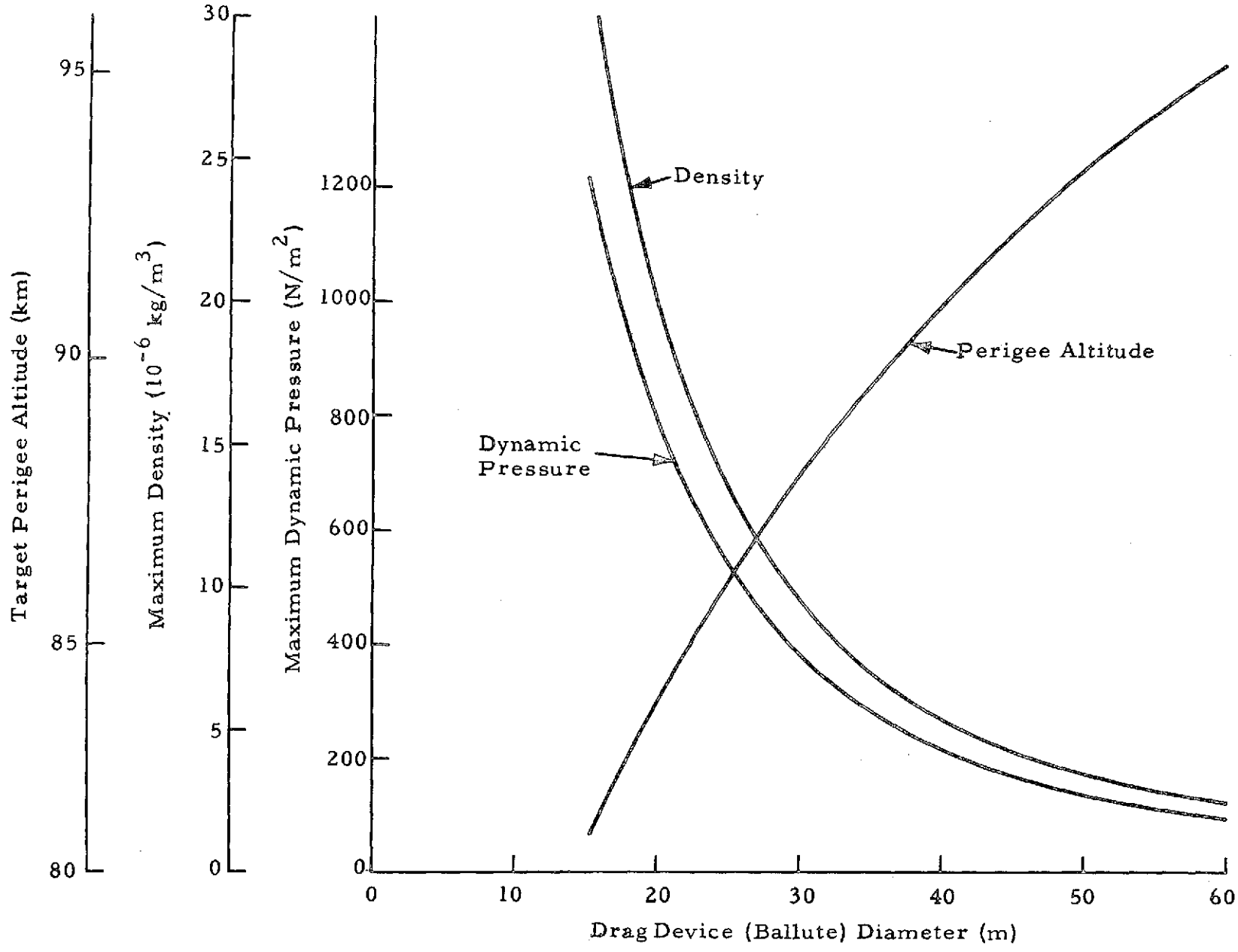

Fig. 33 - Target Perigee Altitude, Maximum Atmospheric Density and Maximum Dynamic Pressure vs Drag Device (Ballute) Diameter for One Atmospheric Pass and for Return from a Geosynchronous Orbit Mission (Vehicle Mass = 10,000 kg)

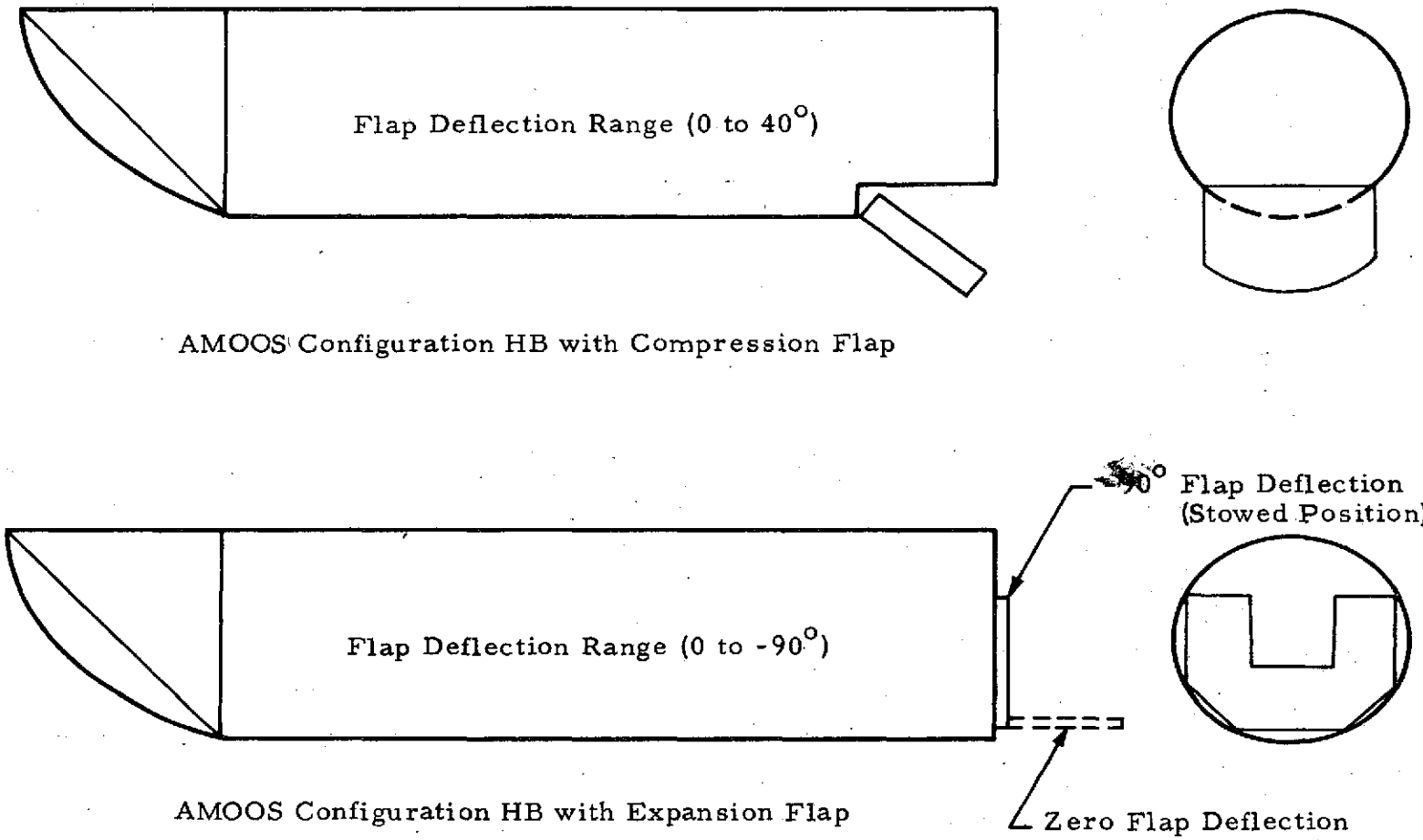

Fig. 34 - AMOOS Configuration HB with Compression and Expansion Flap

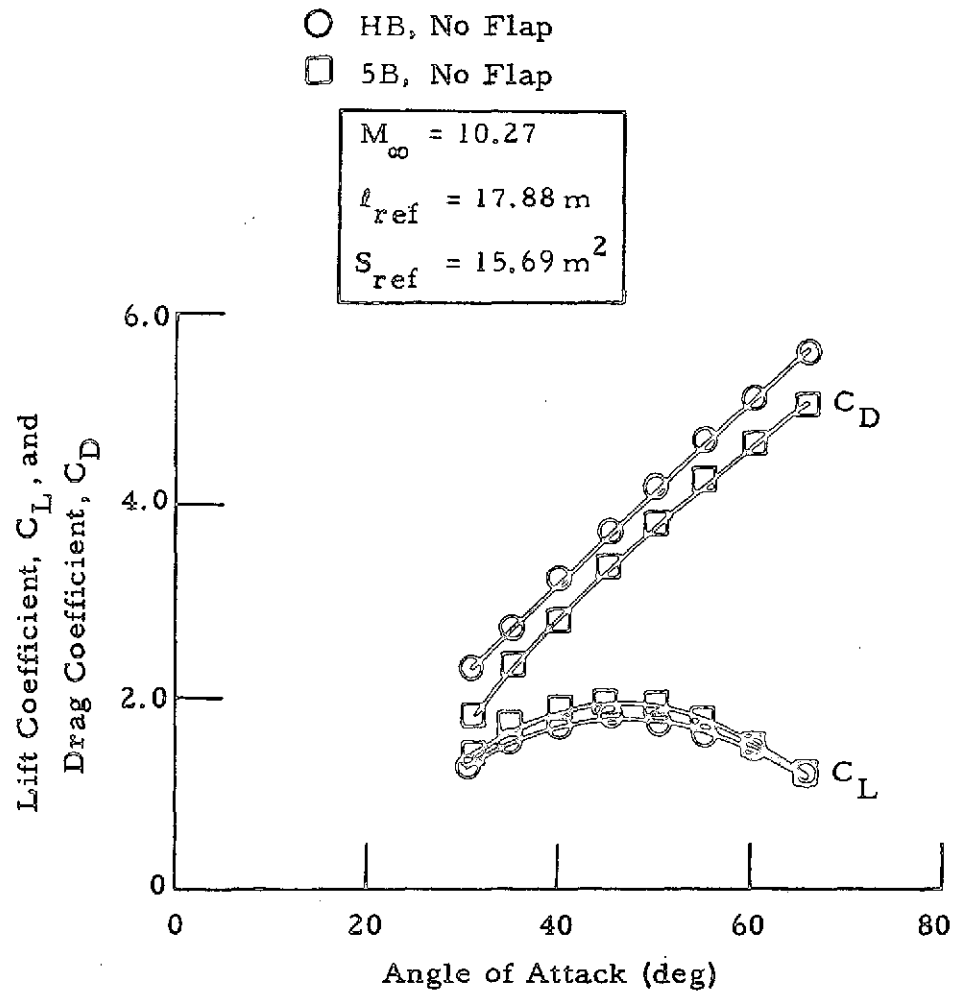

Fig. 35 - Comparison of AMOOS 5B and HB Performance Parameters

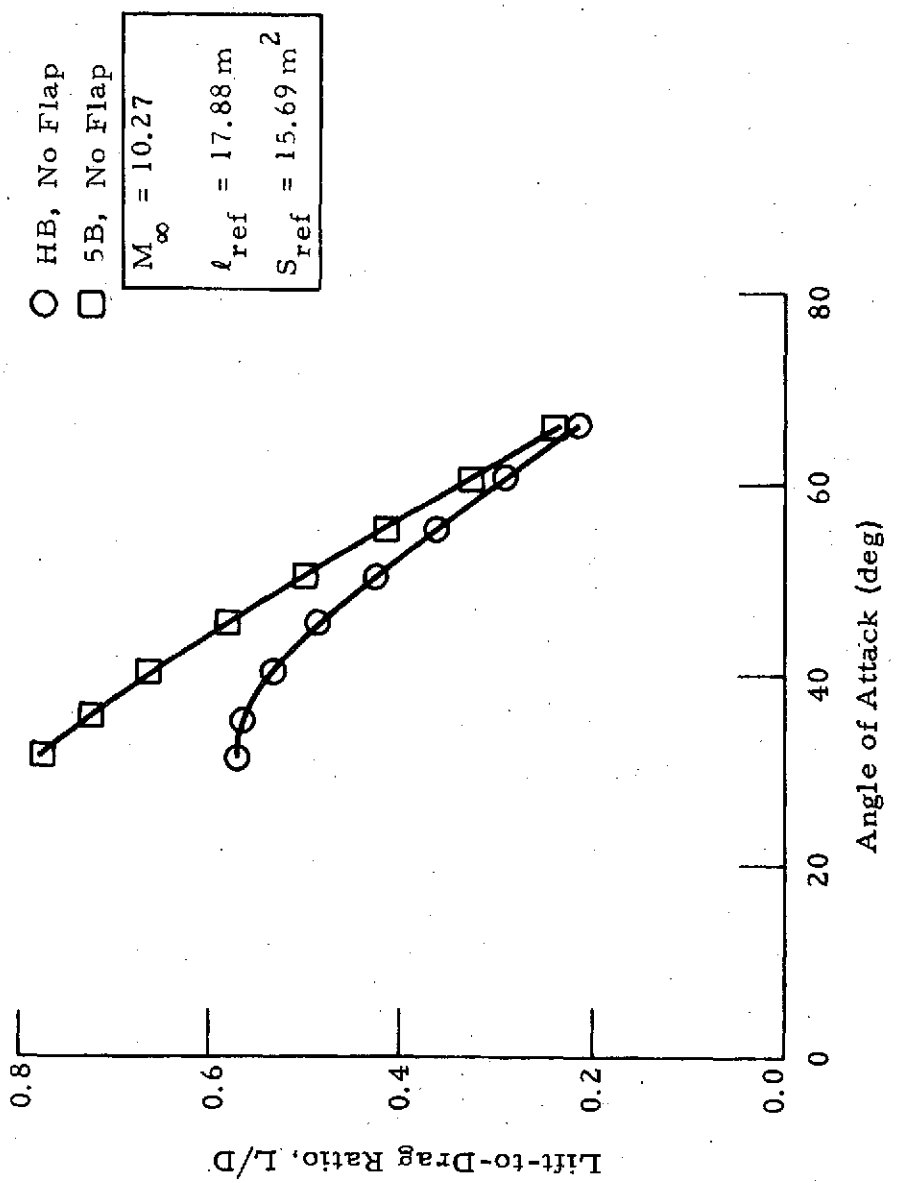

Fig. 36 - Comparison of AMOOS 5B and HB Lift-to-Drag Ratios

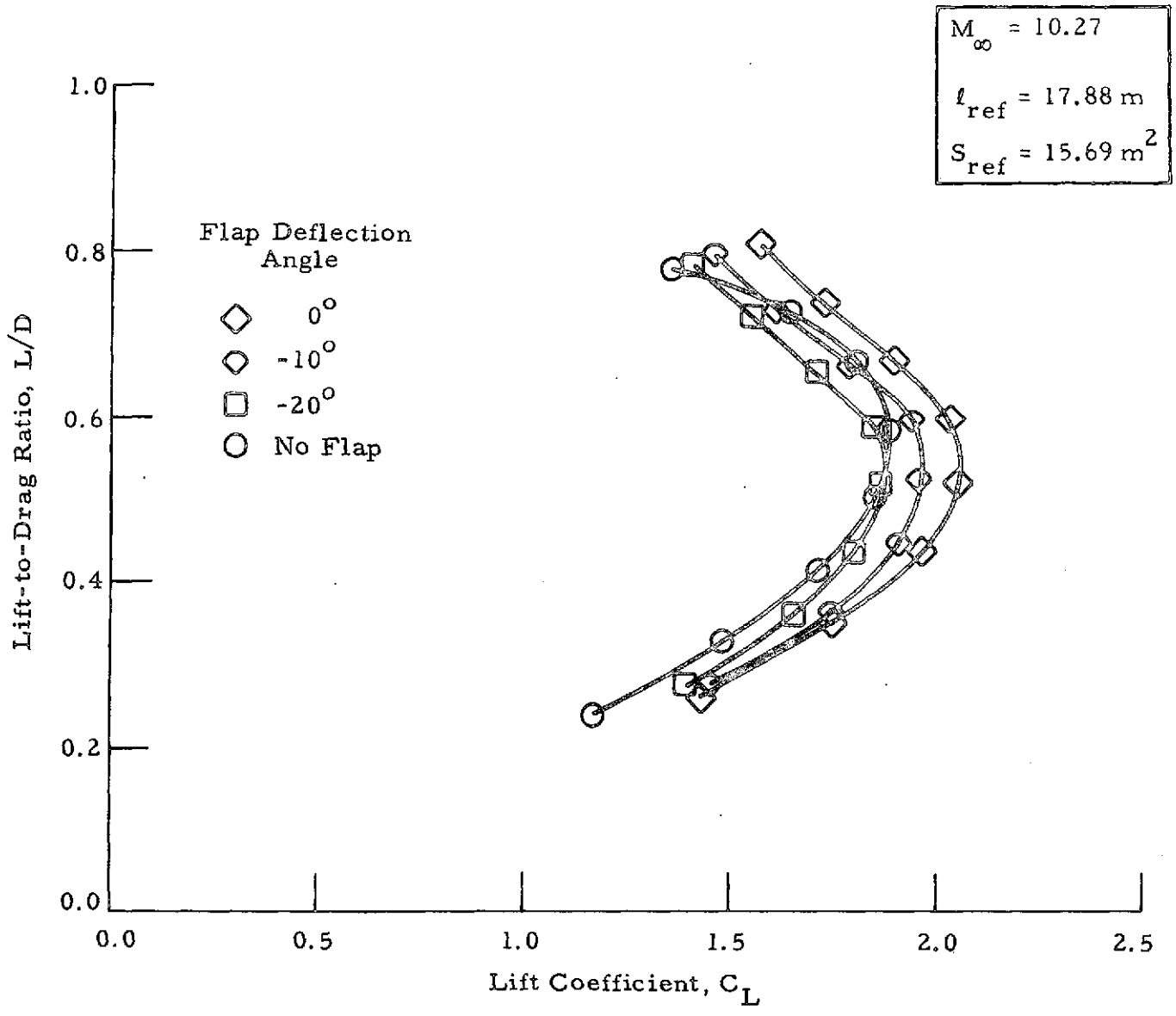

Fig. 37 - Variation of AMOOS 5B L/D with Expansion Flap Deflection

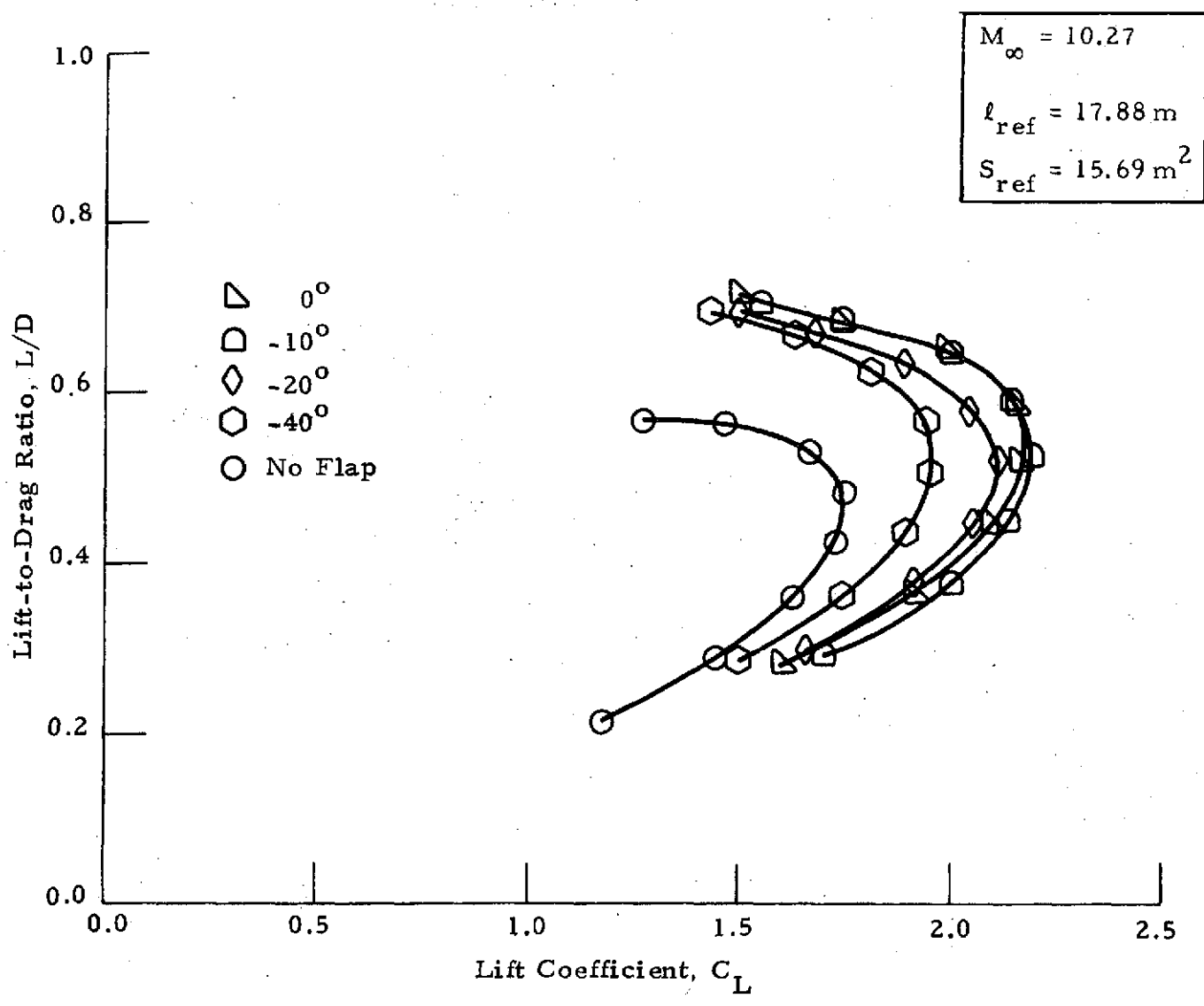

Fig. 38 - Variation of AMOOS HB L/D with Expansion Flap Deflection

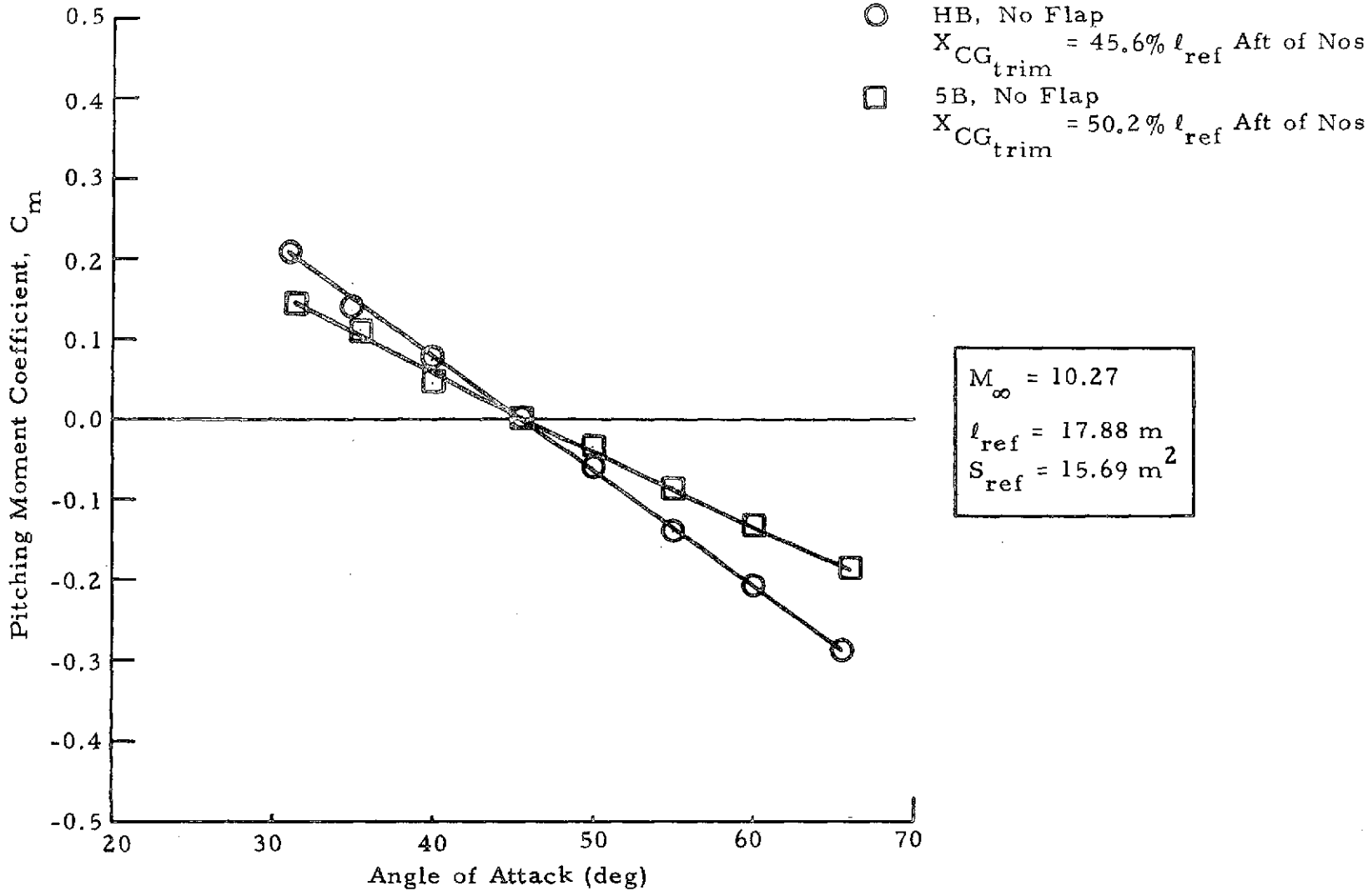

Fig. 39 - Comparison of AMOOS 5B and HB Trimmed Pitching Moments

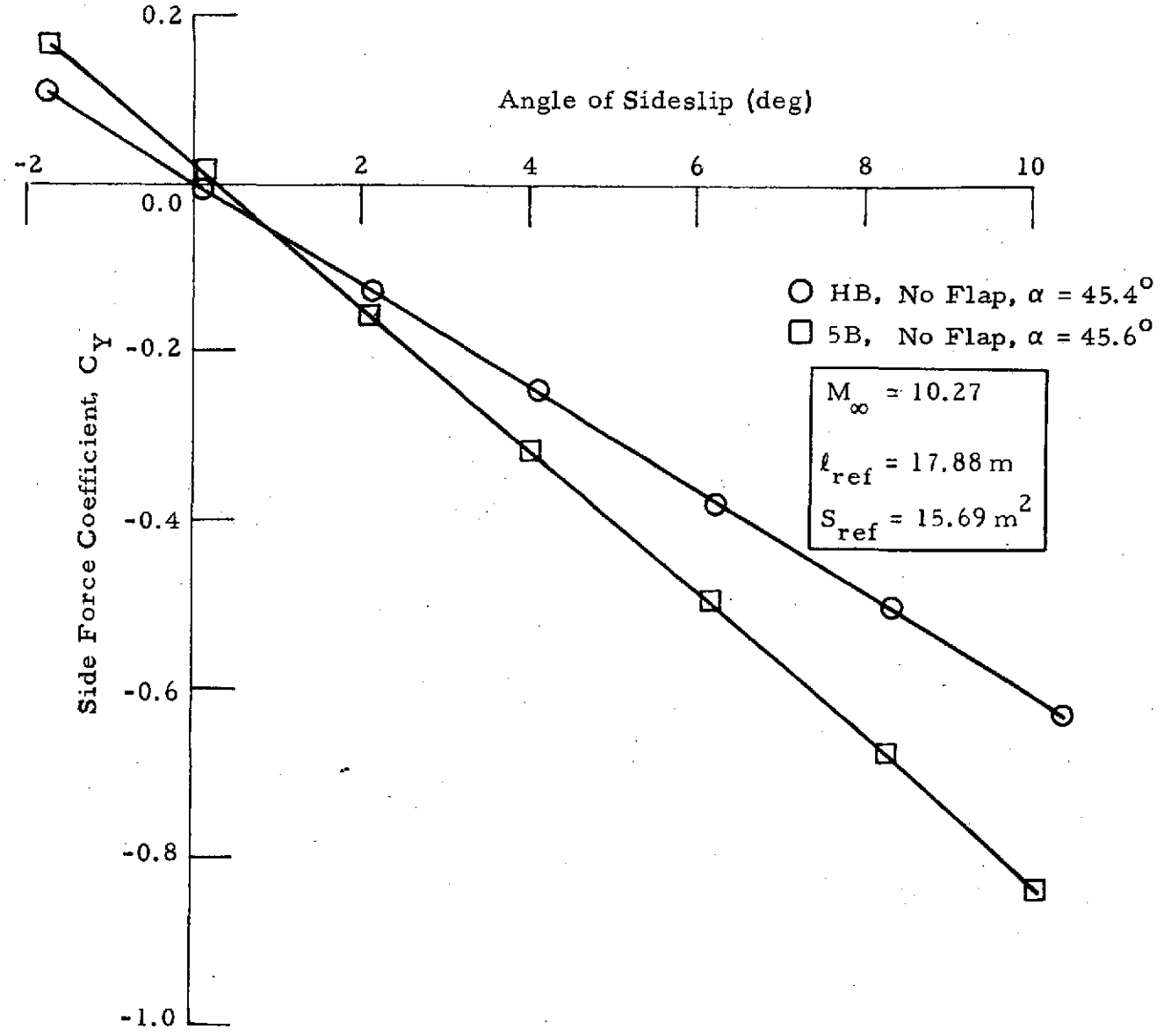

Fig. 40 - Comparison of AMOOS 5B and HB Side Force Coefficients

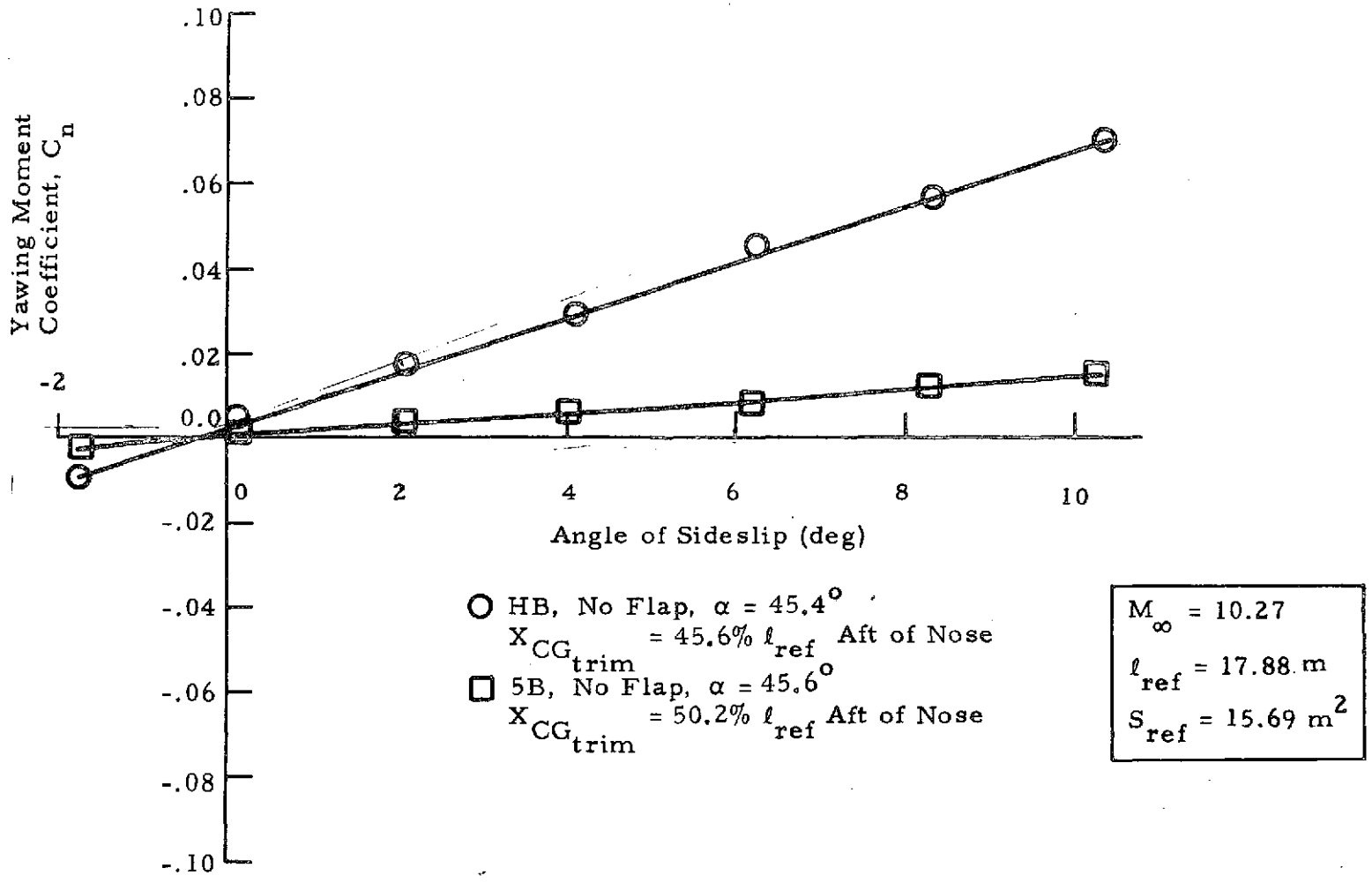

Fig. 41 - Comparison of 5B and HB Yawing Moment Coefficients

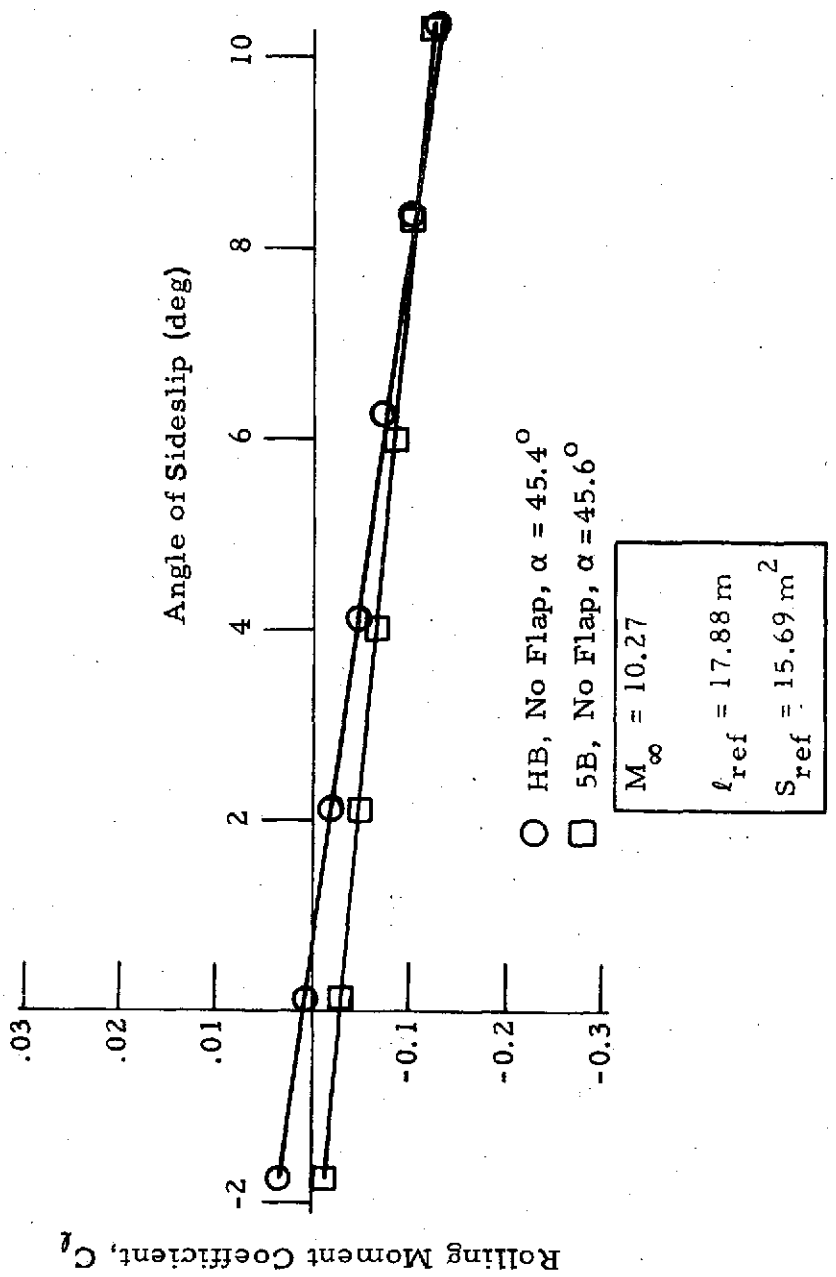

Fig. 42 - Comparison of AMOOS 5B and HB Rolling Moment Coefficients

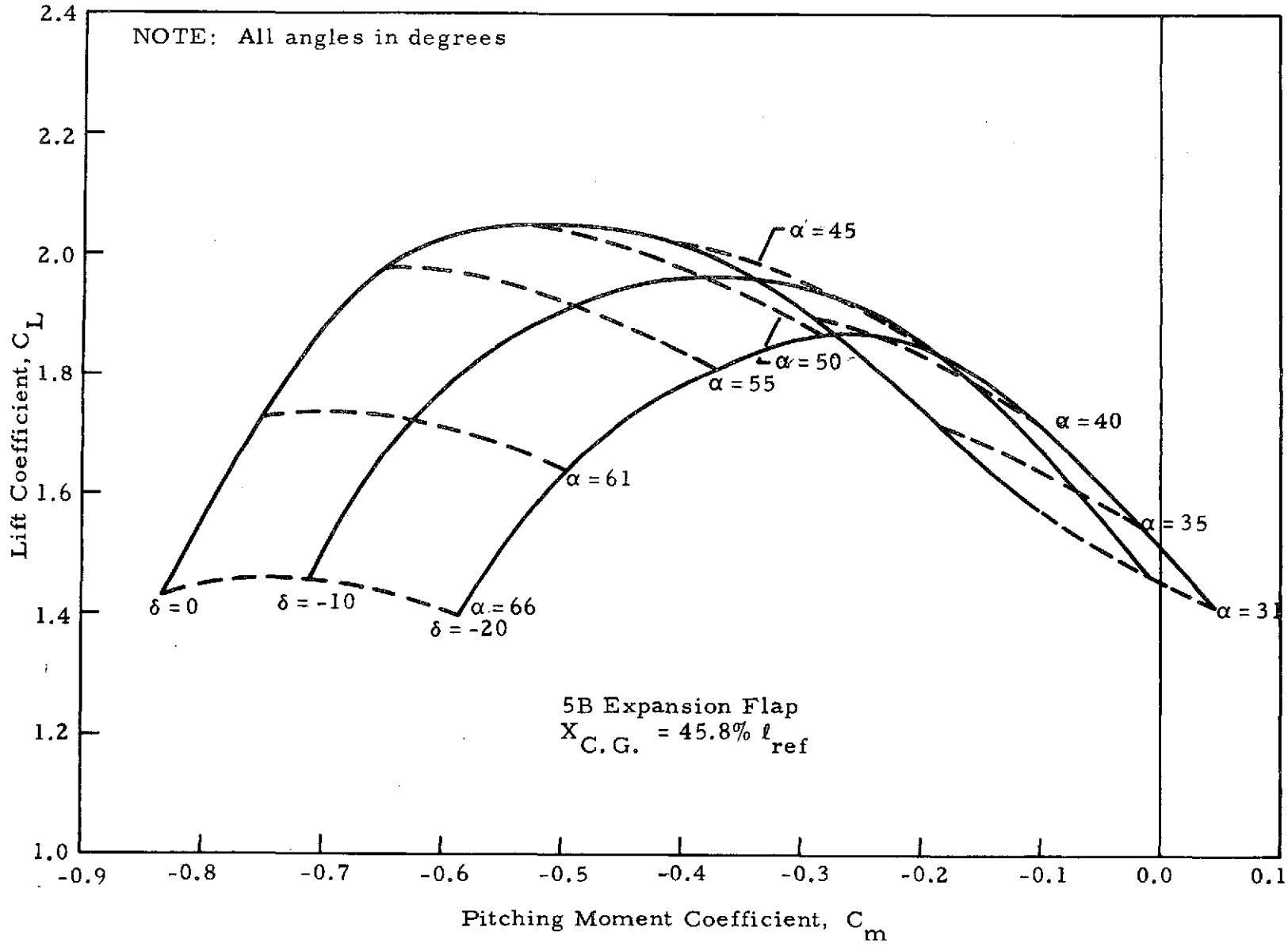

Fig. 43 - Trim Characteristics of AMOOS 5B at Forward C.G.

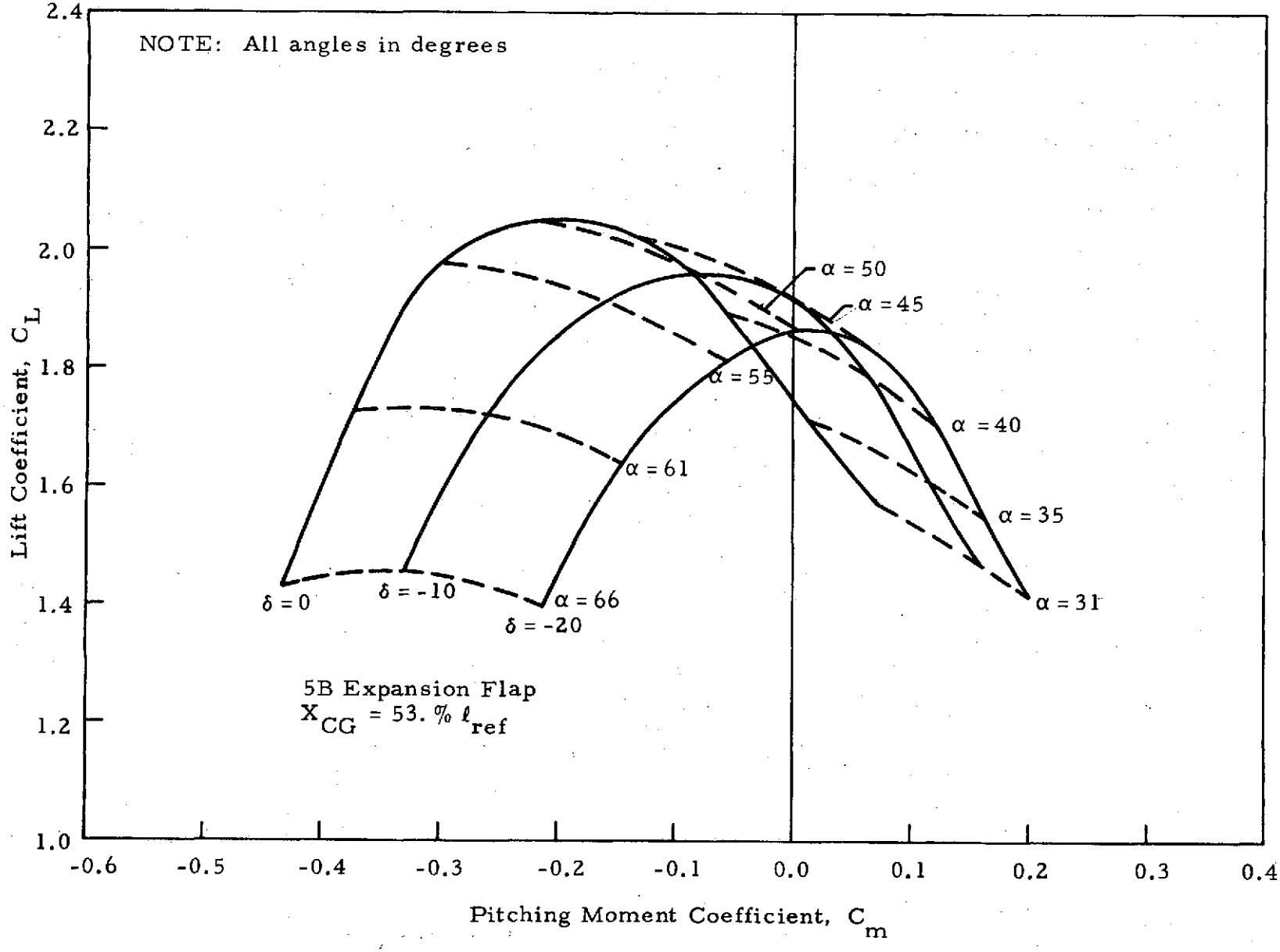

Fig. 44 - Trim Characteristics of AMOOS 5B at Aft C.G.

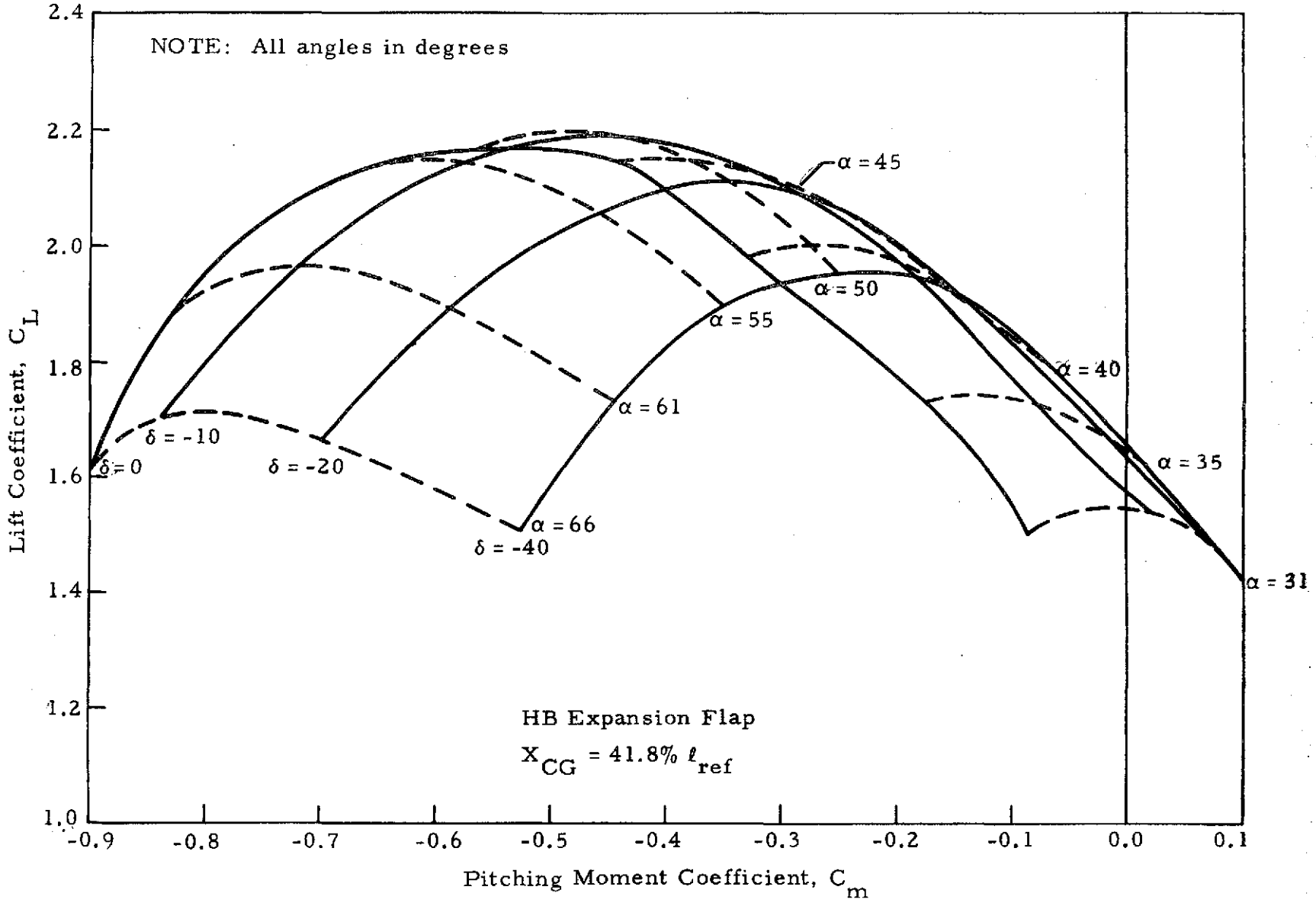

Fig. 45 - Trim Characteristics of AMOOS HB at Forward C.G.

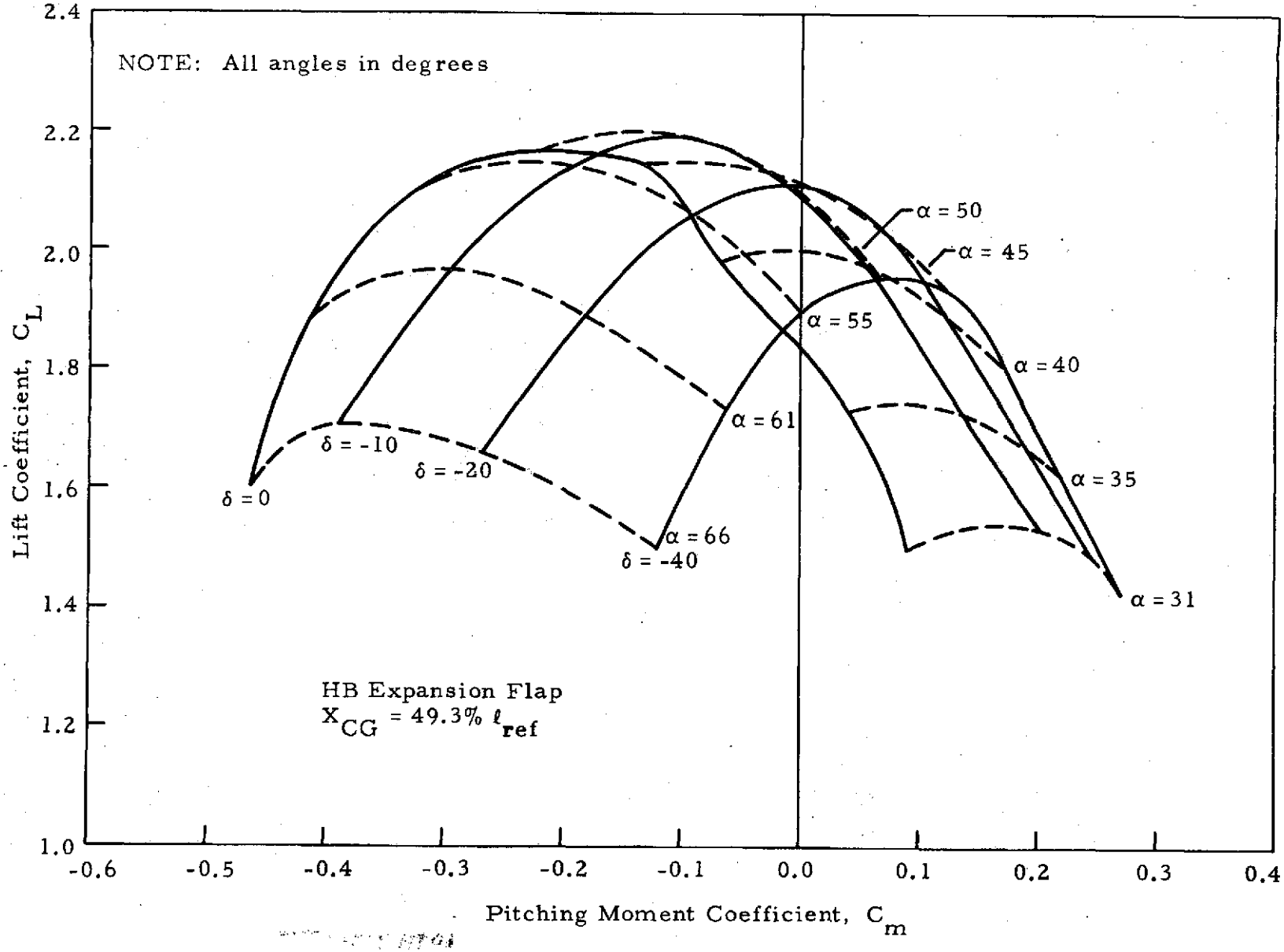

Fig. 46 - Trim Characteristics of AMOOS HB at Aft C. G.

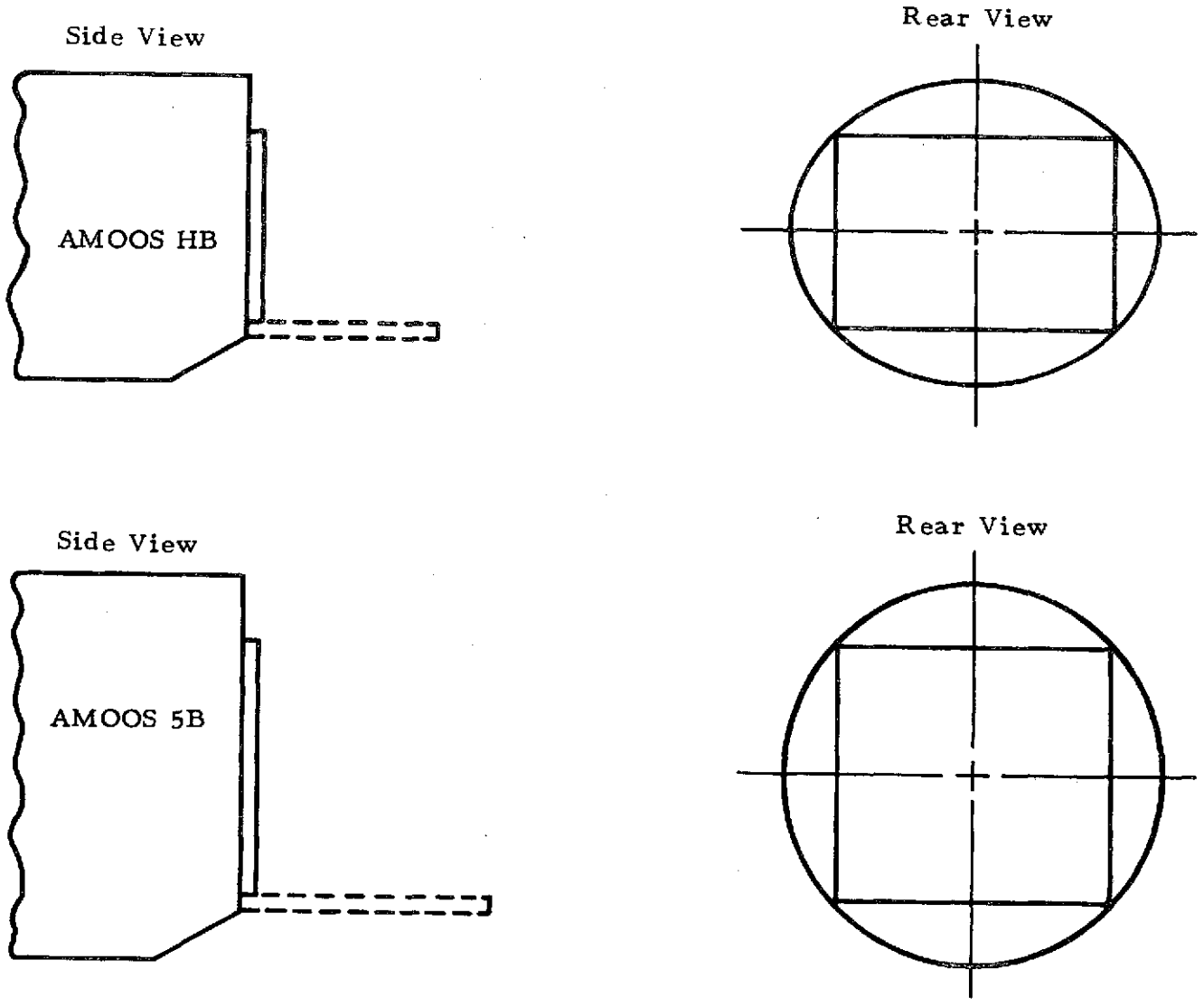

Fig. 47 - Flat Plate Flap with Ramp Fore-Surface Without Slot (Ramp Flap)

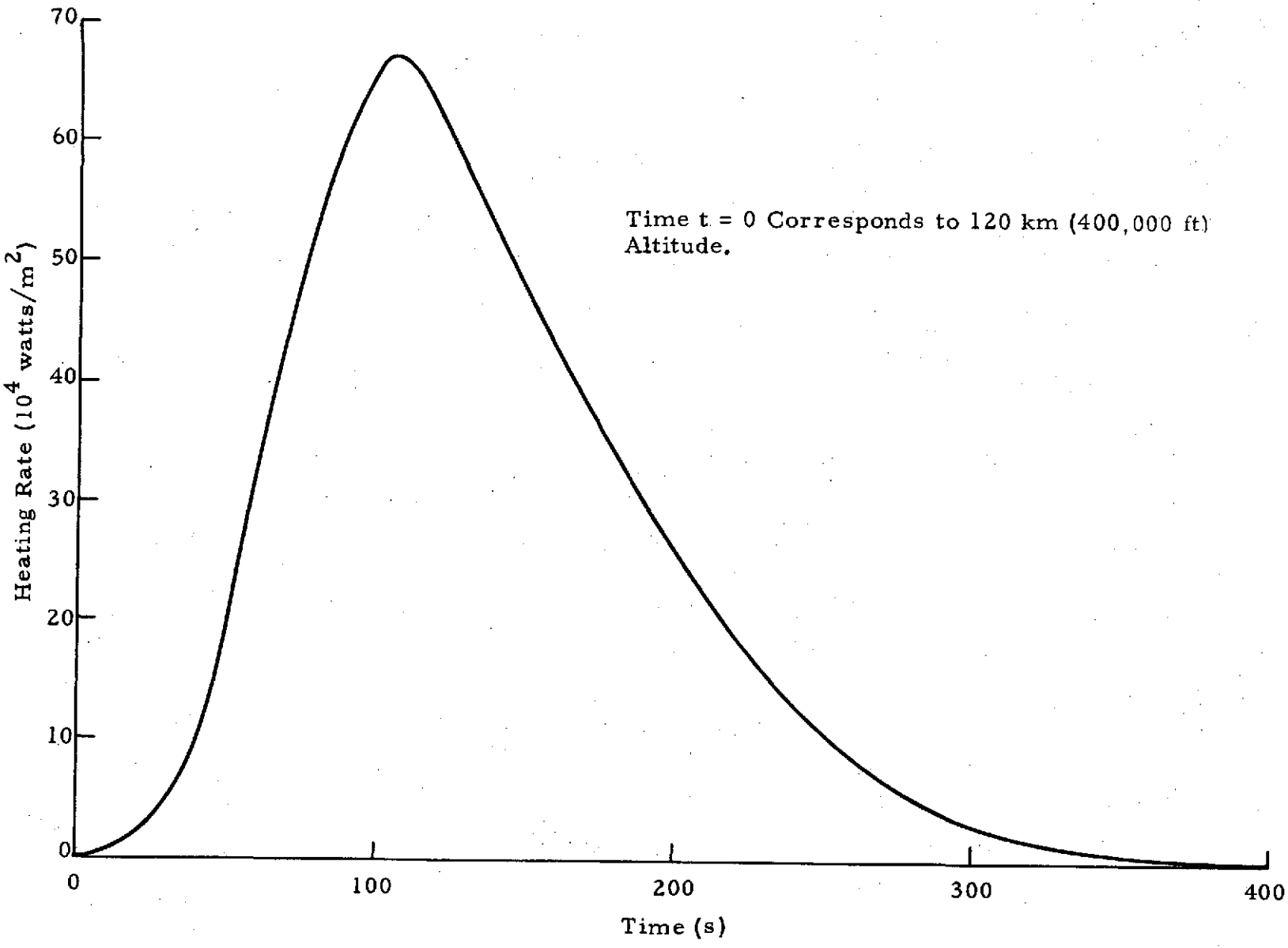

Fig. 48 - Typical Heating Rate-Time History to the Stagnation Line of AMOOS Configuration 5B at an Angle of Attack of 45° (One-Pass Trajectory)

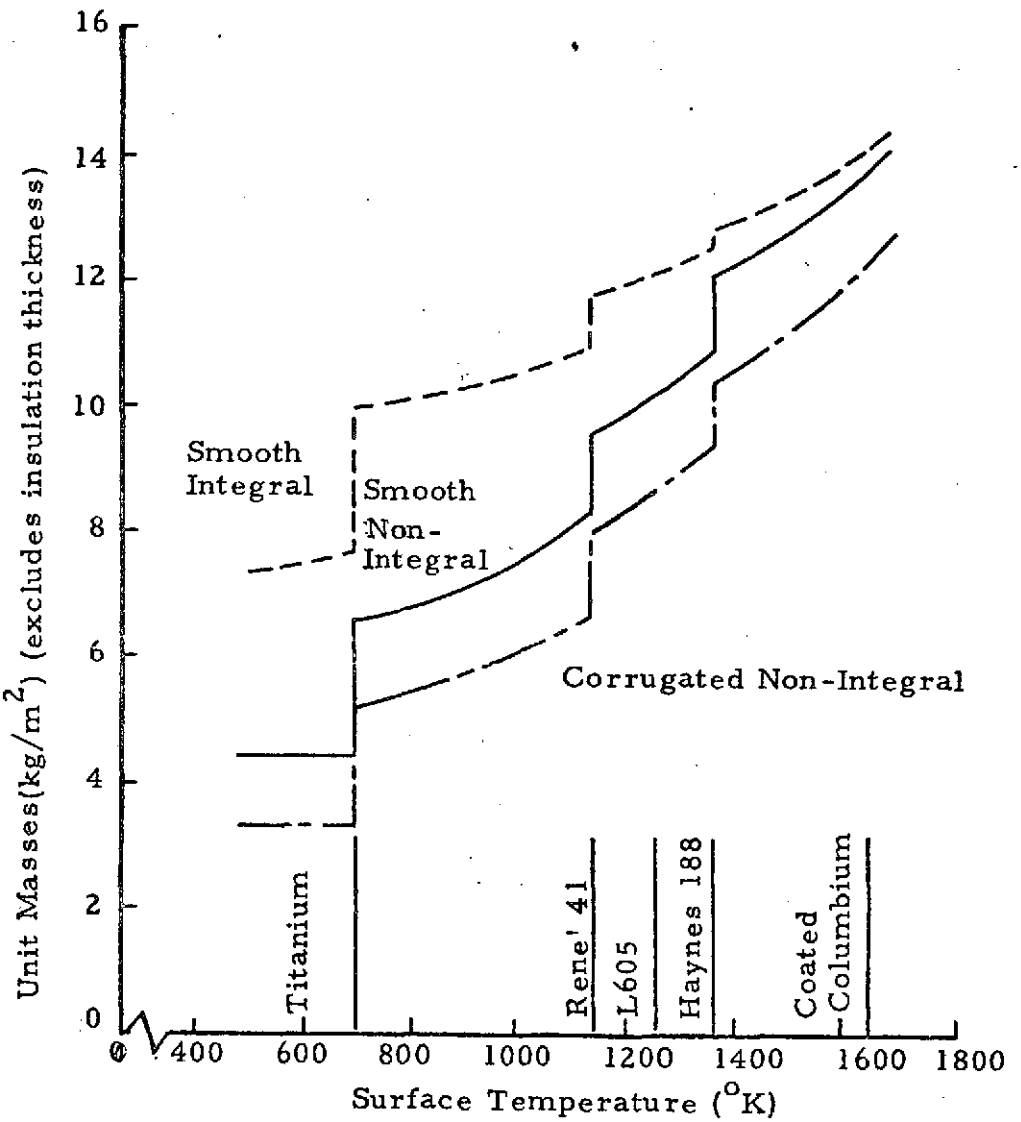

Fig. 49 - Masses per Unit Area vs Surface Temperature for Various Radiative Type TPS Materials

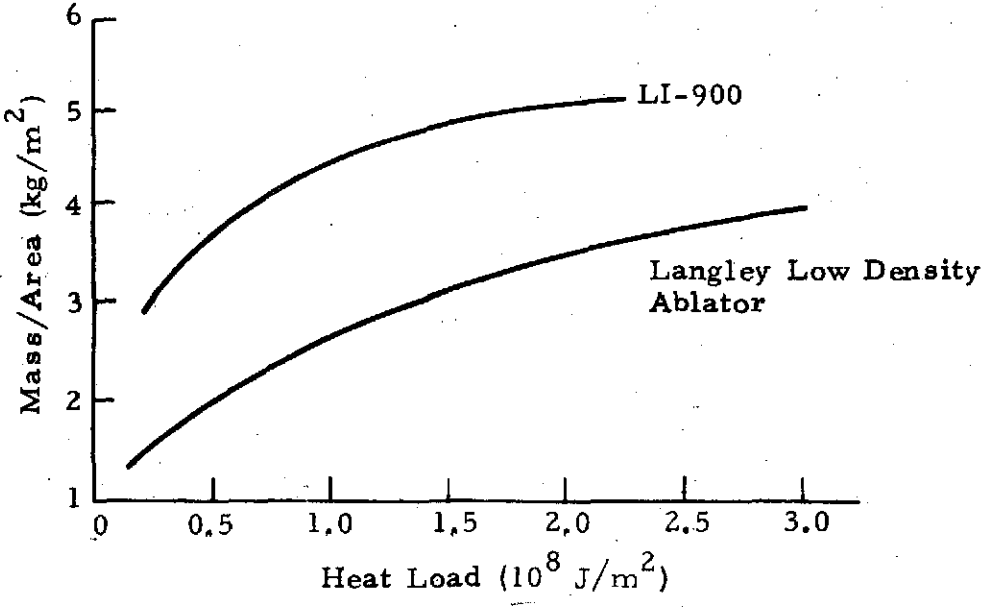

Fig. 50 - Comparison of Weight per Unit Area of LI-900 and Langley Low Density Ablator

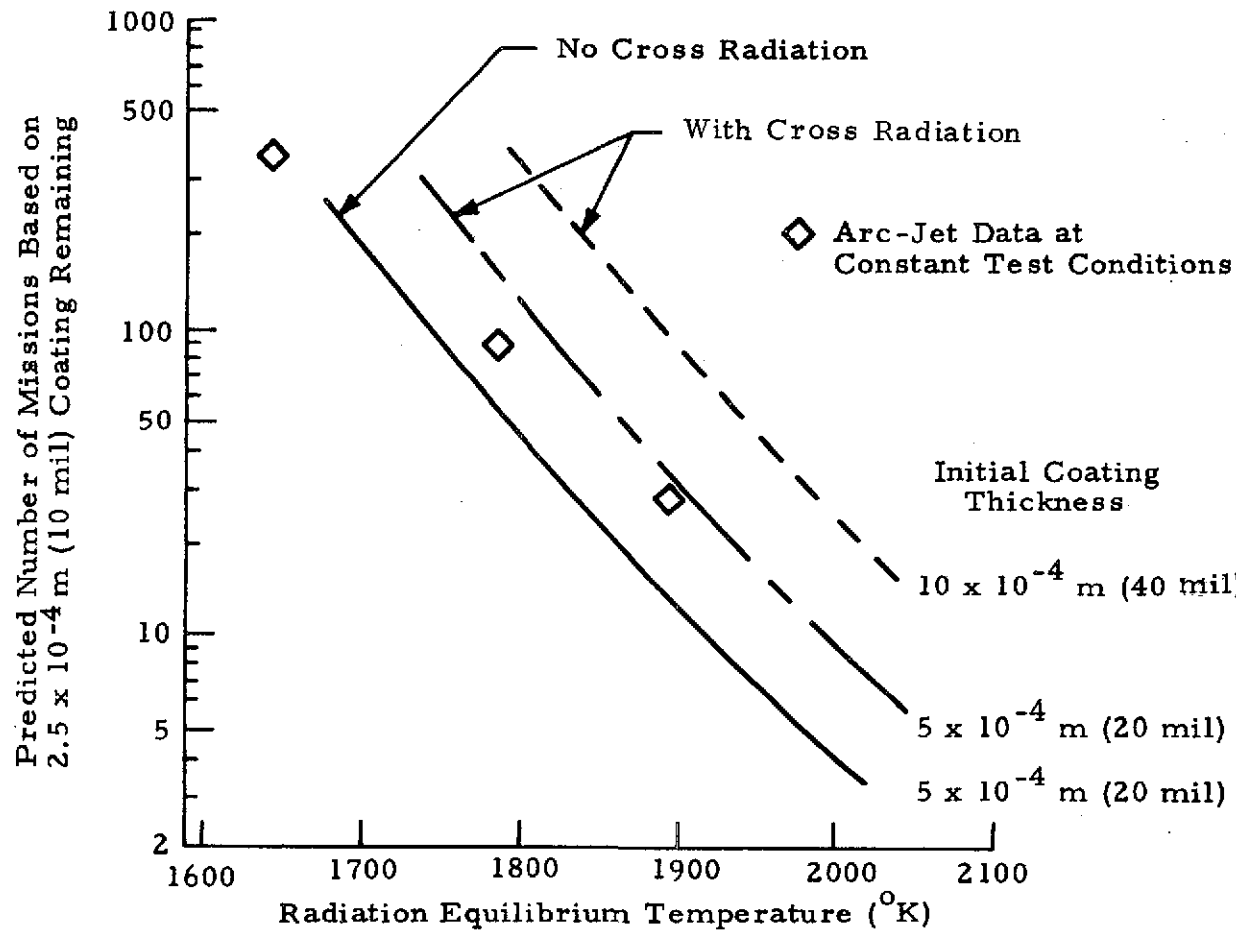

Fig. 51 - Number of Missions vs Maximum Radiation Equilibrium Temperature for Carbon/Carbon, from Ref. 17, p. 347

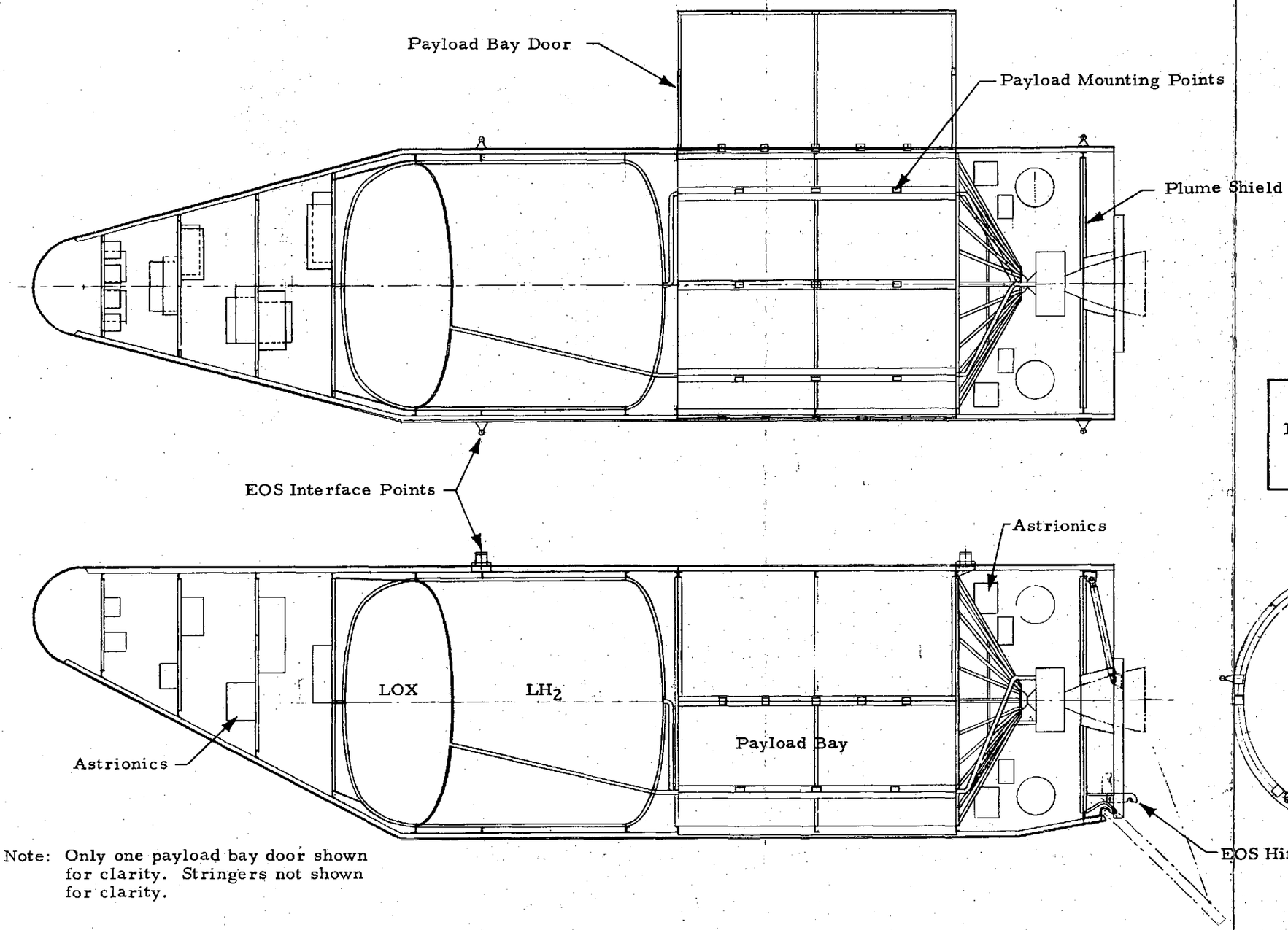

Note: Only one payload bay door shown for clarity. Stringers not shown for clarity.

Fig. 52 - AMOOS 5B Configuration

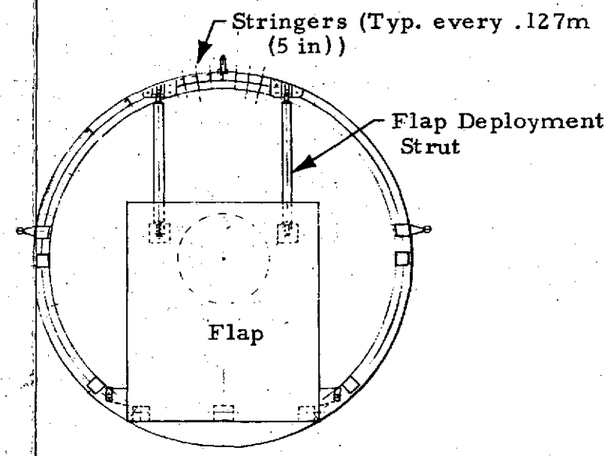

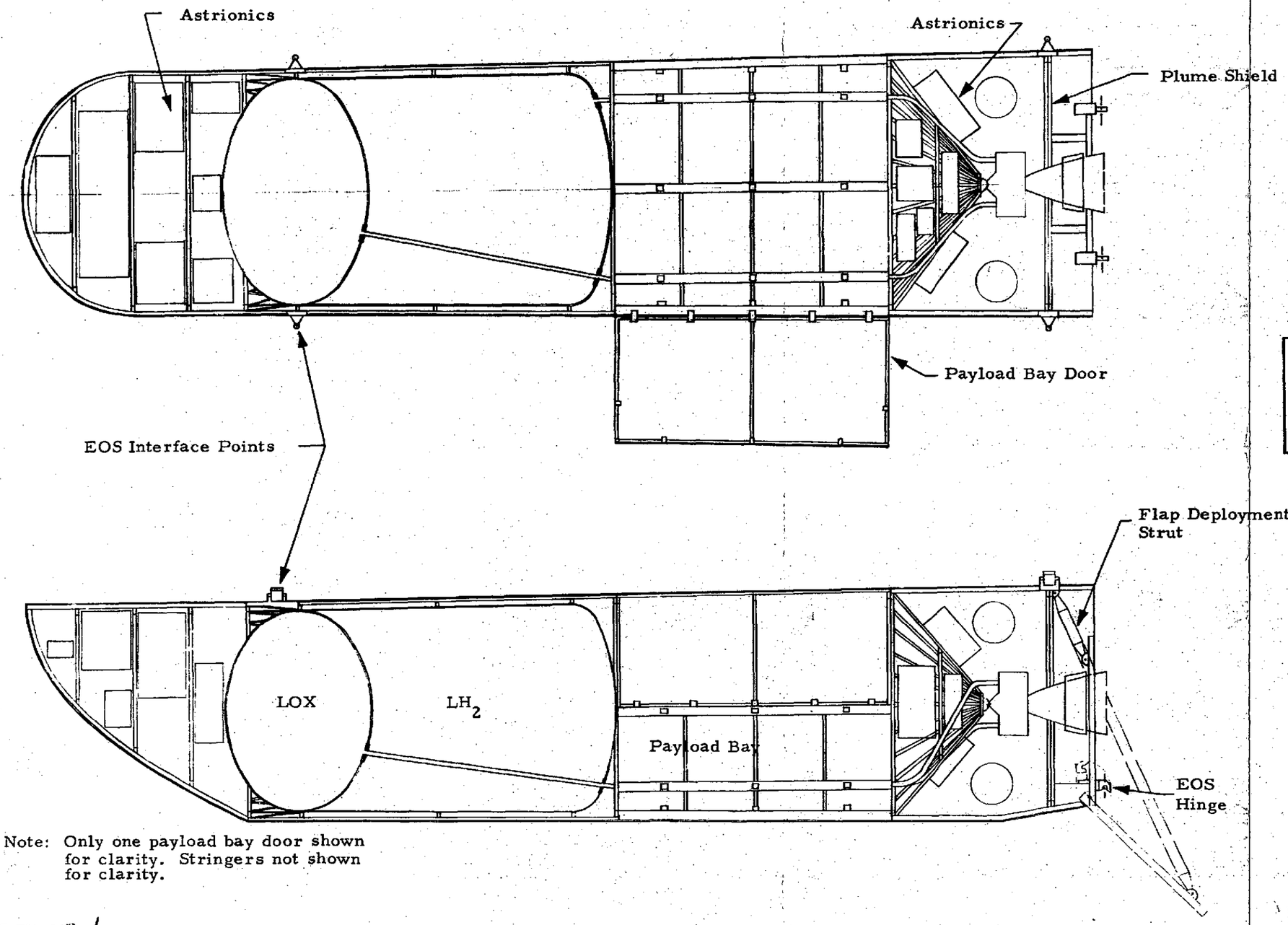

Note: Only one payload bay door shown for clarity. Stringers not shown for clarity.

Fig. 53 - AMOOS HB Configuration

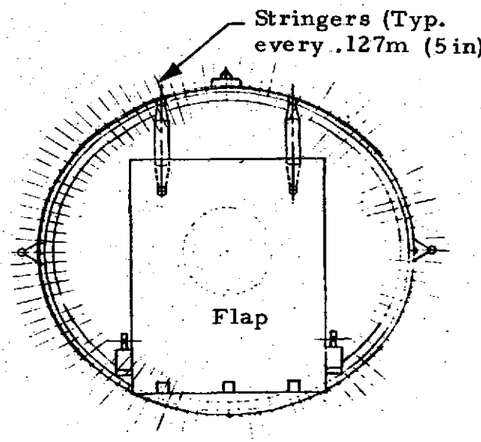

FOLDOUT FRAME 1

FOLDOUT FRAME 2

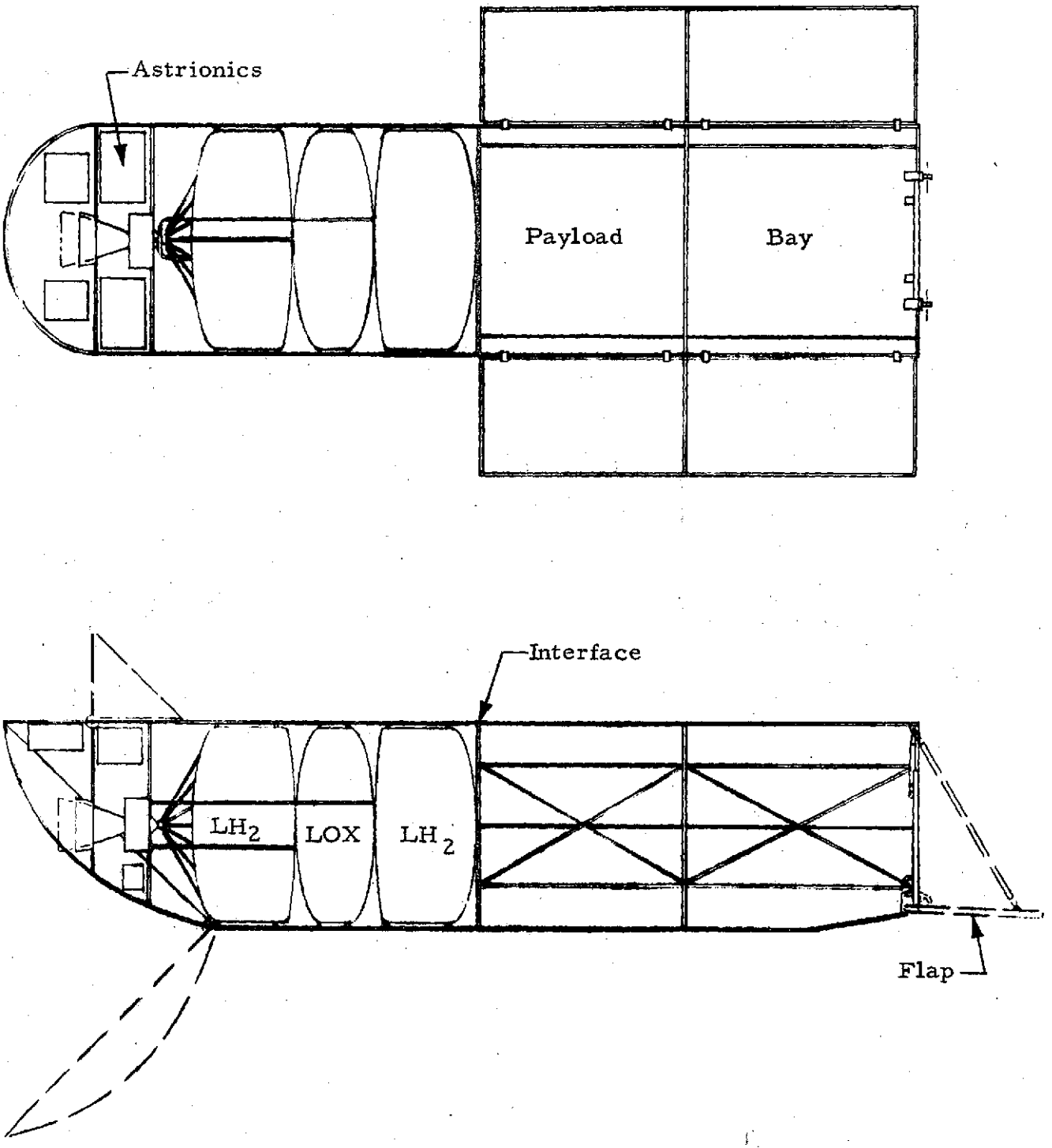

Fig. 54 - AMOOS HB Aft Cargo Bay Configuration

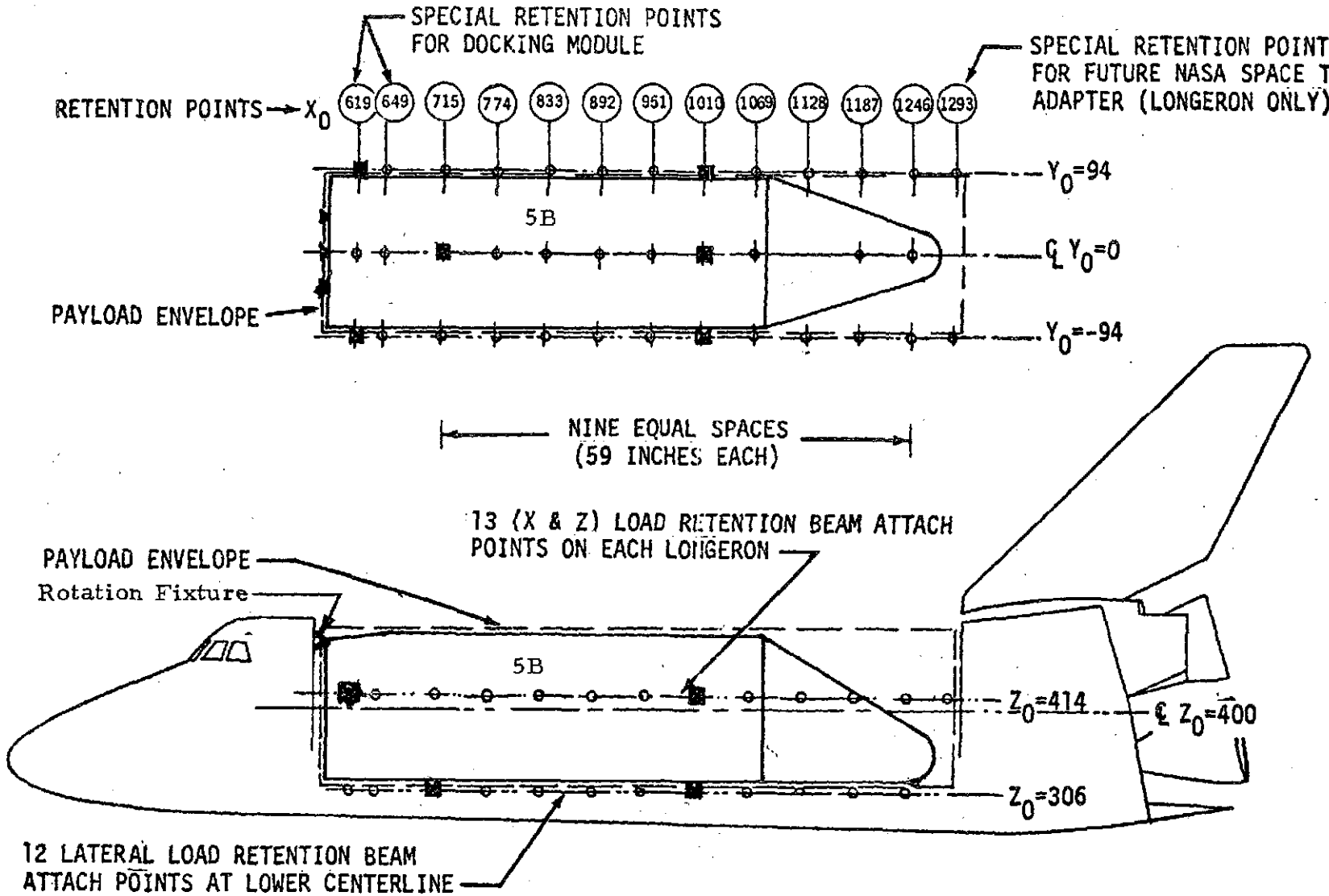

Fig. 55 - Shuttle Payload Attachment Locations

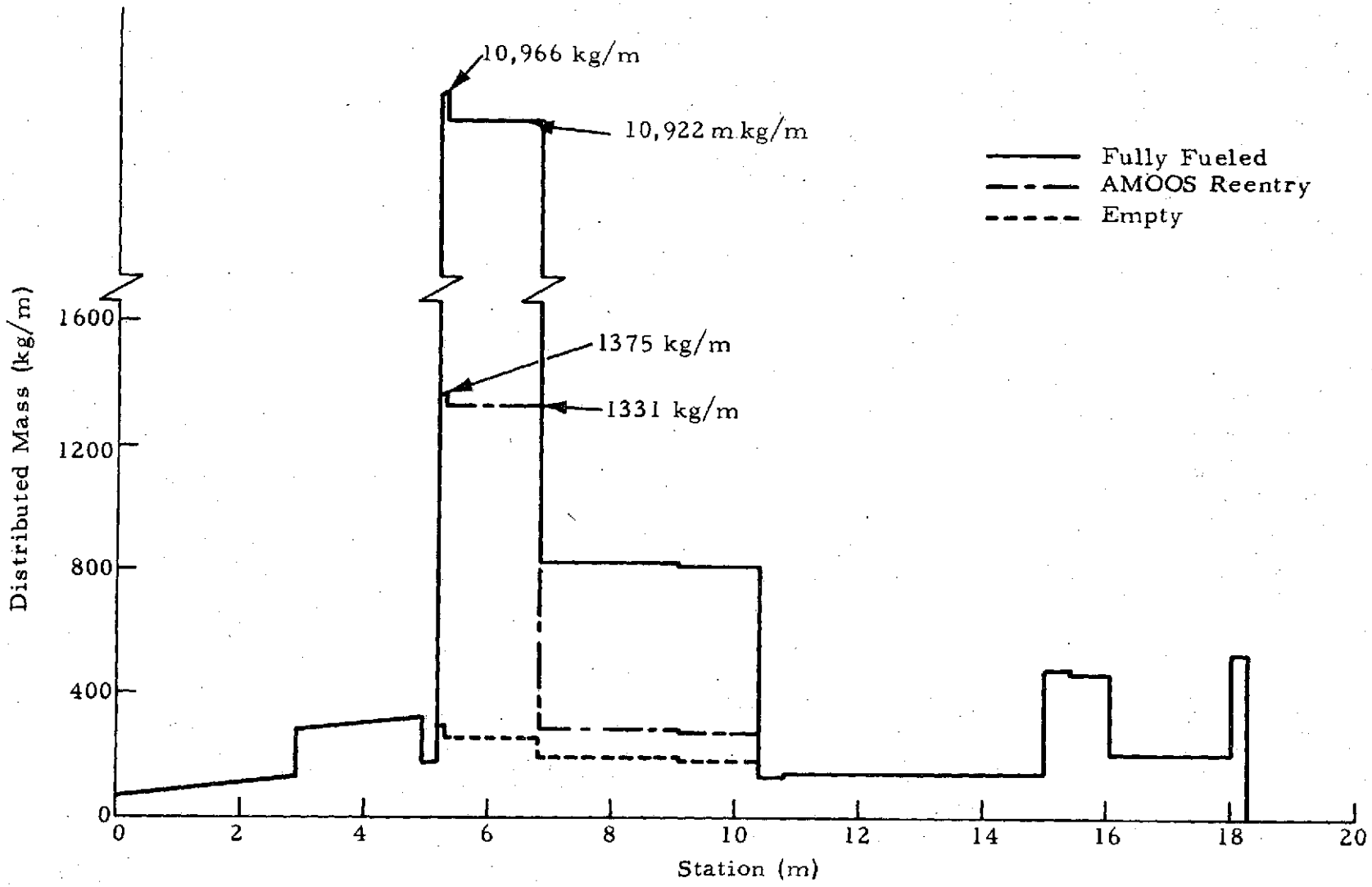

Fig. 56 - AMOOS 5B Distributed Mass

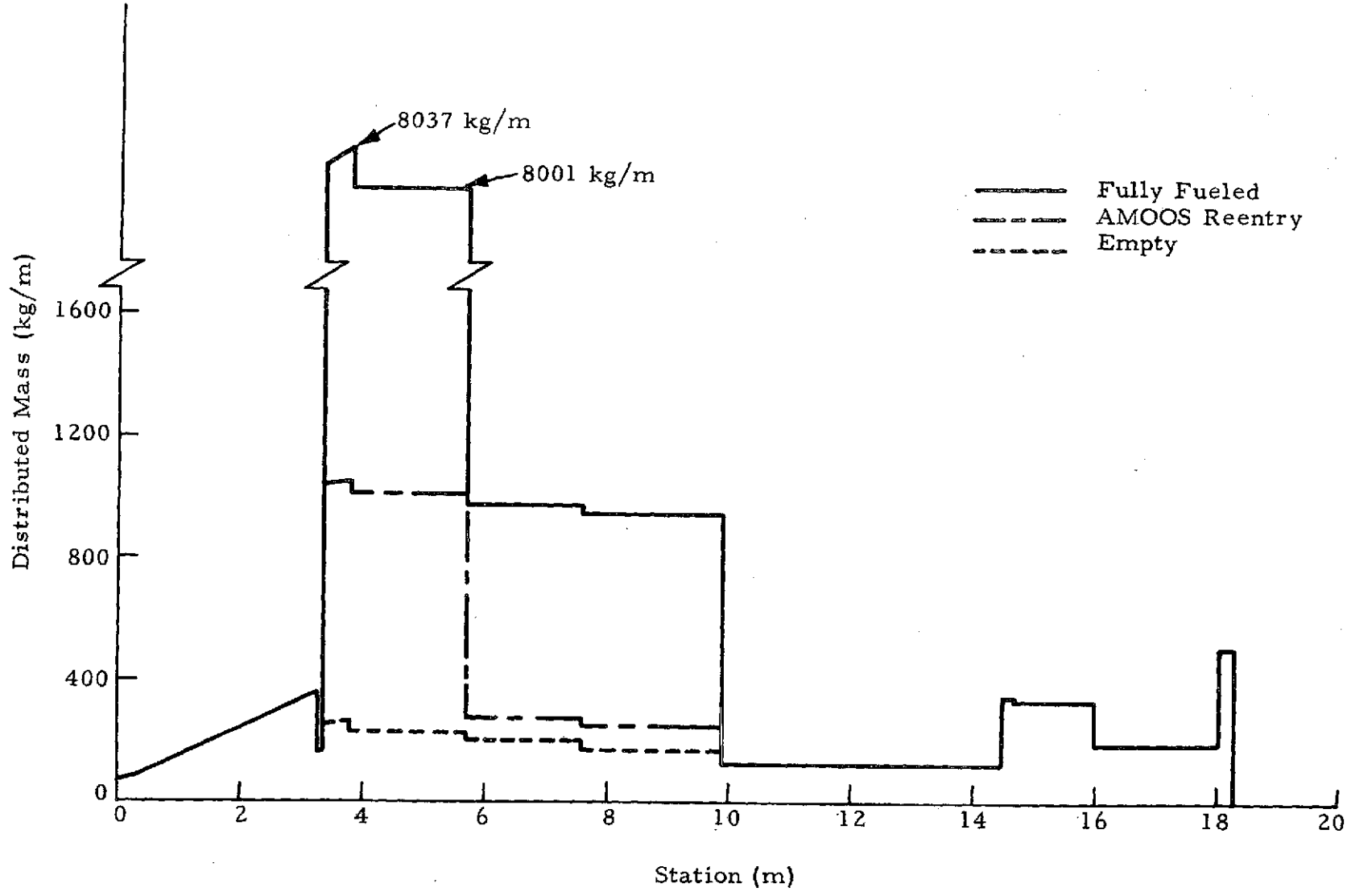

Fig. 57 - AMOOS HB Distributed Mass

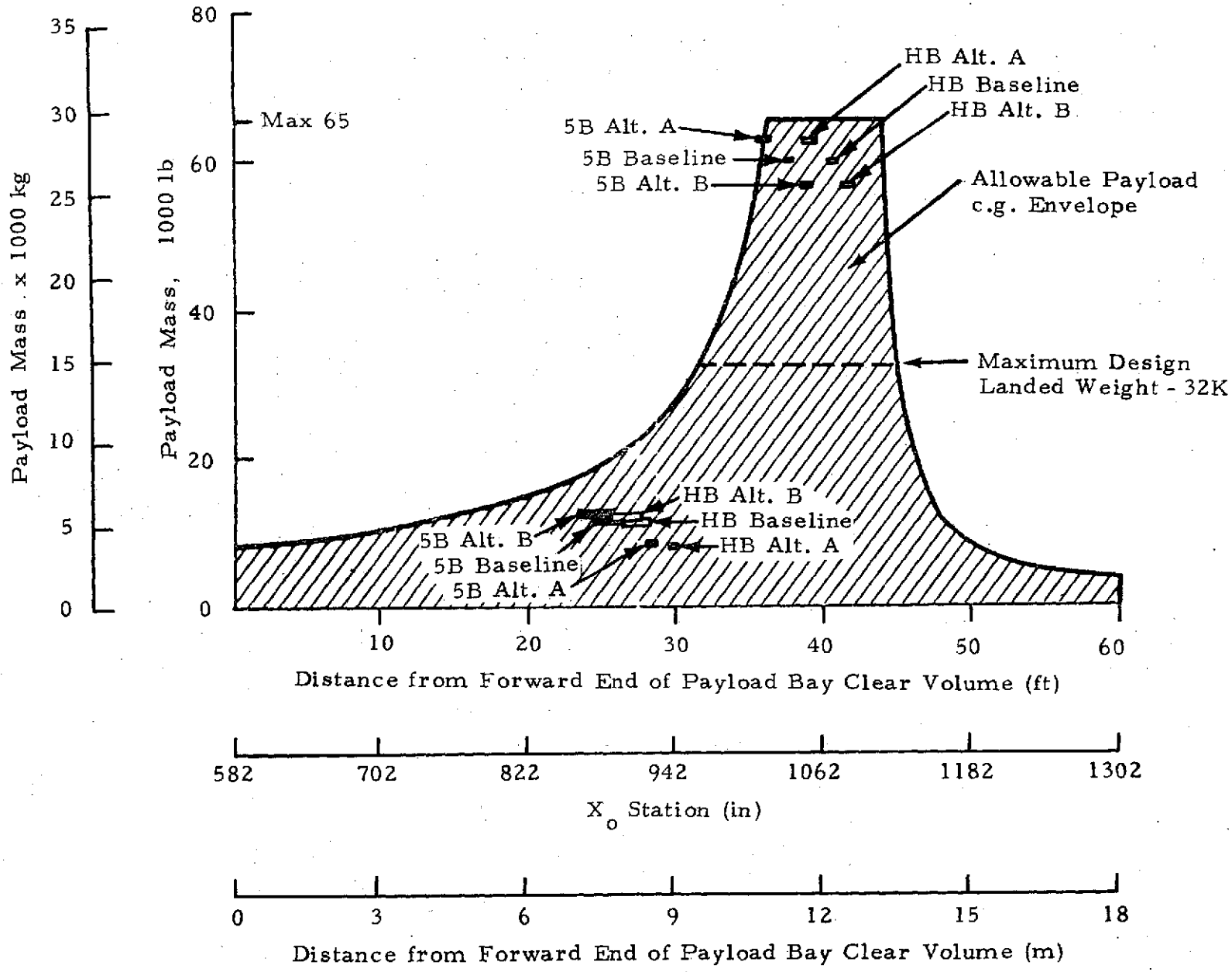

Fig. 58 - Shuttle Payload Longitudinal Center-of-Gravity Envelope

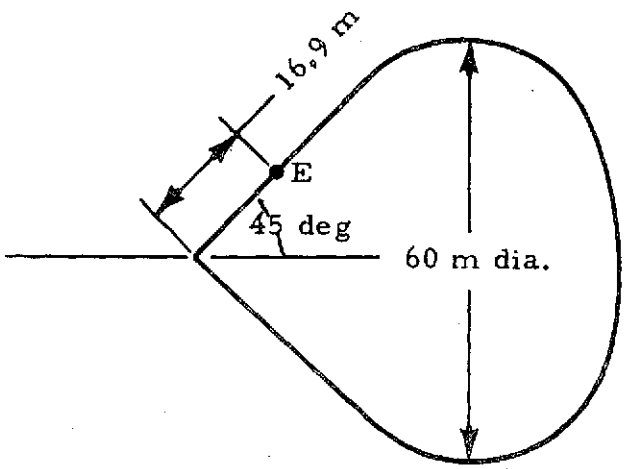

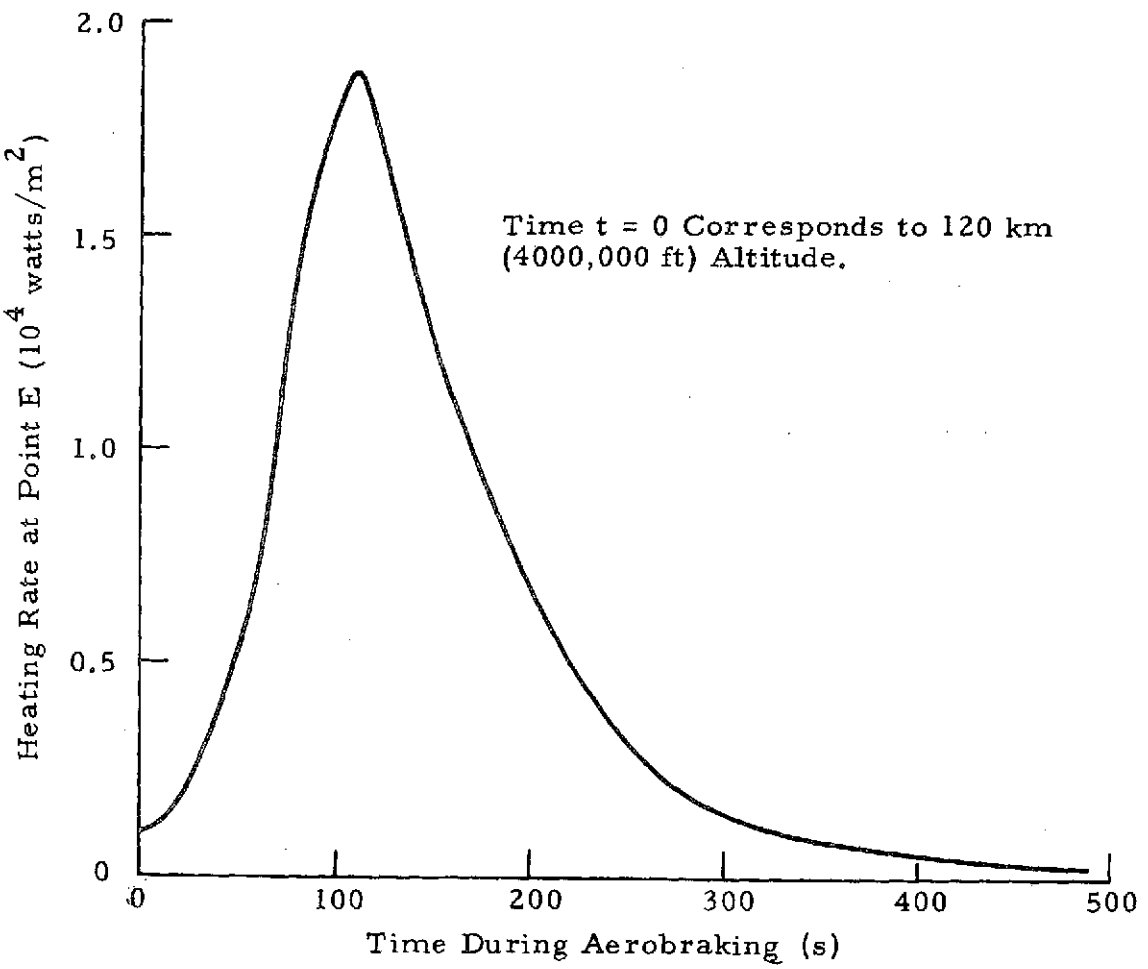

Fig. 59 - Heating Rate vs Time at a Typical Point on the 60 m Diameter Ballute

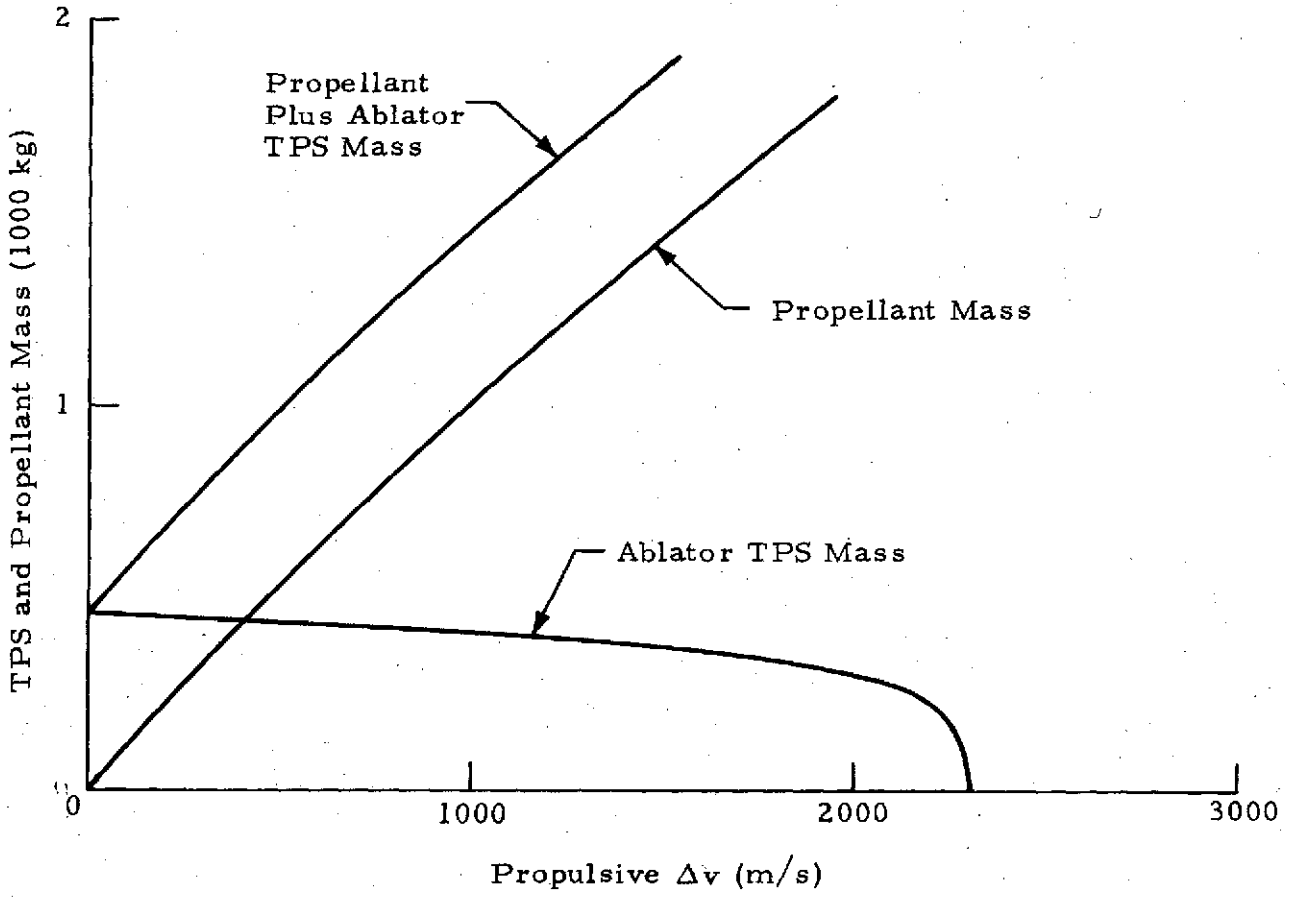

Fig. 60 - Trade of TPS vs Propellant Mass. (Propellant mass based on 5000 kg vehicle. A return from geosynchronous orbit was assumed. Vehicle HB.)

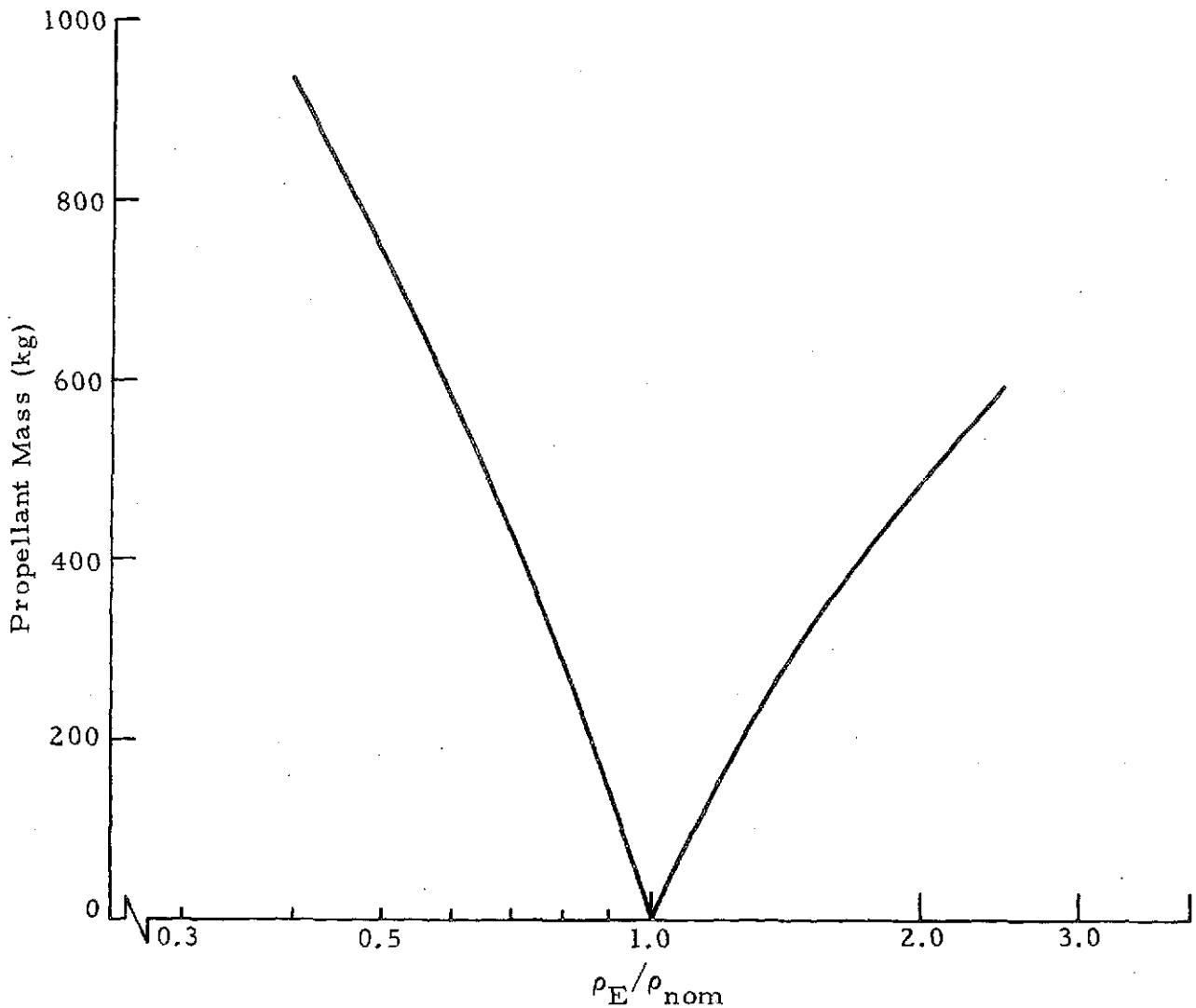

Fig. 61 - Propellant Mass Required if Thrust is Used to Compensate for Off-Nominal Conditions During Aeromaneuvering. (Off-nominal conditions are represented by the ratio of effective density to nominal density. A return from geosynchronous orbit was assumed. Vehicle mass = 10,000 kg.)

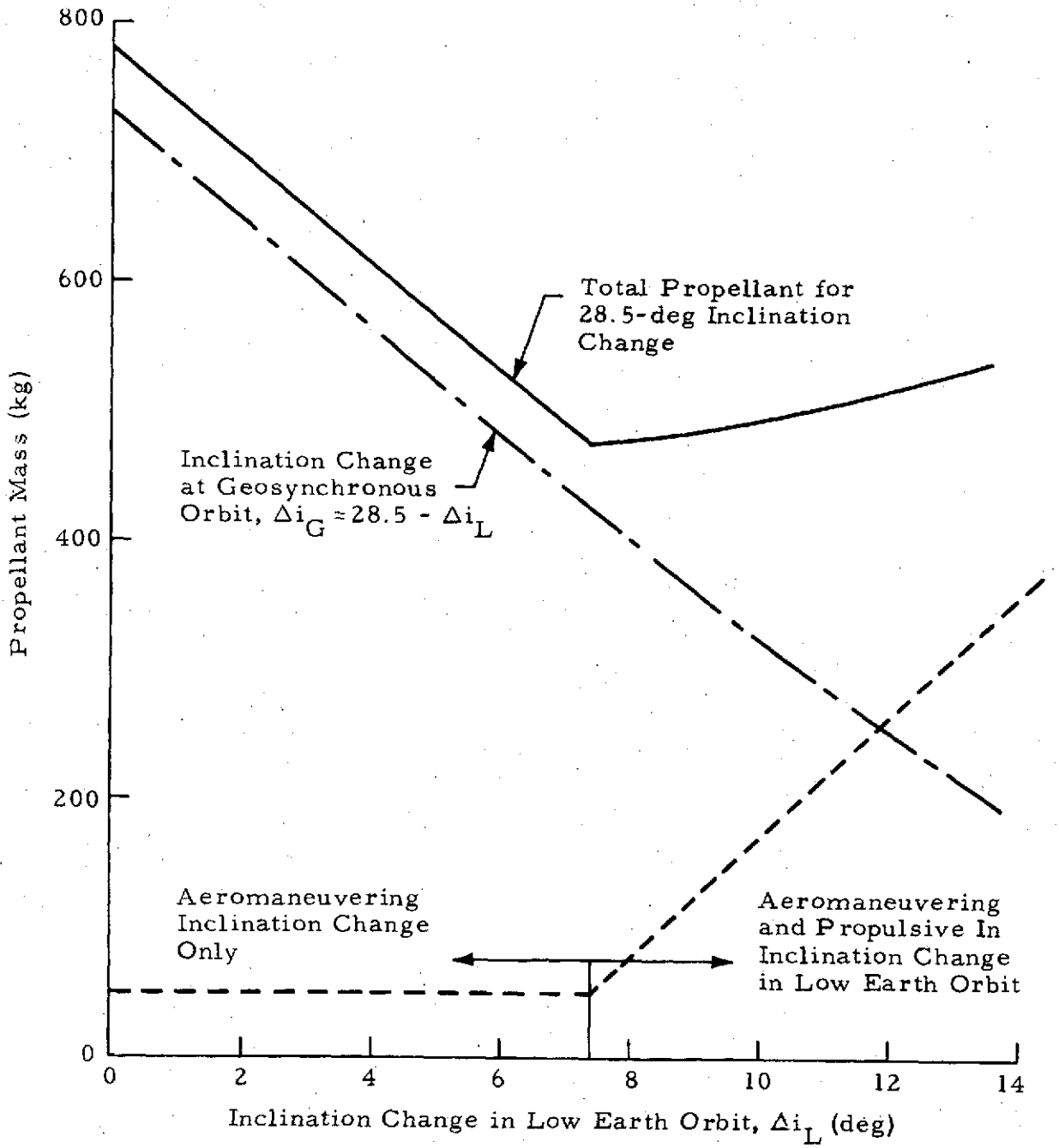

Fig. 62 - Propellant Required for a 28.5-deg Inclination Change as a Function of the Fraction of the Inclination Change Performed in Low Earth Orbit (Return from geosynchronous orbit with an aeromaneuvering inclination change capability of 7.4 deg., Vehicle mass 10,000 kg)

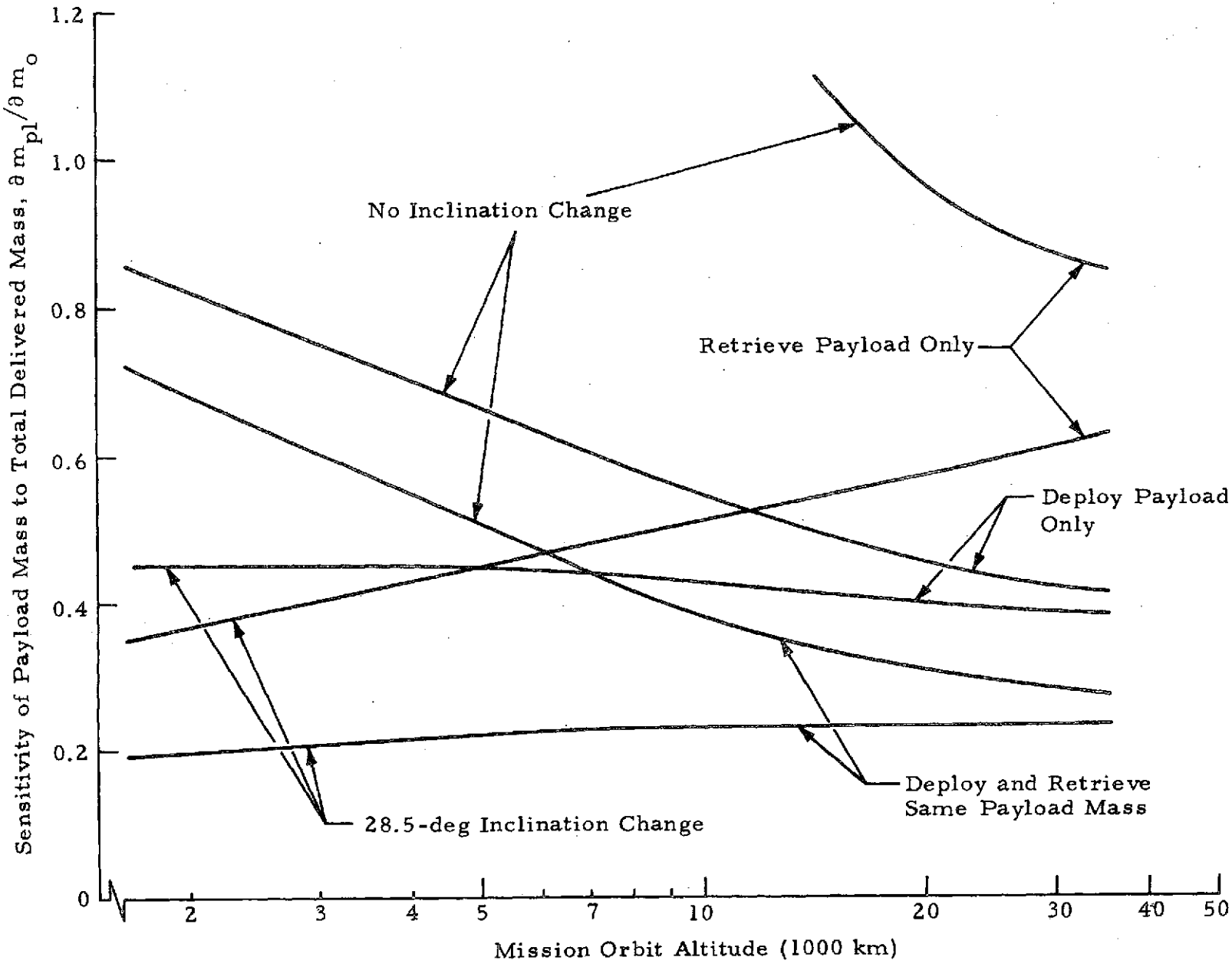

Fig. 63 - Sensitivity of Payload Mass to Total Delivered Mass as a Function of Mission Orbit Altitude. The Sensitivities are for a Total EOS Delivered Mass of 28,848 kg, a Dry Mass of 4247 kg and a Specific Impulse of 470 s.

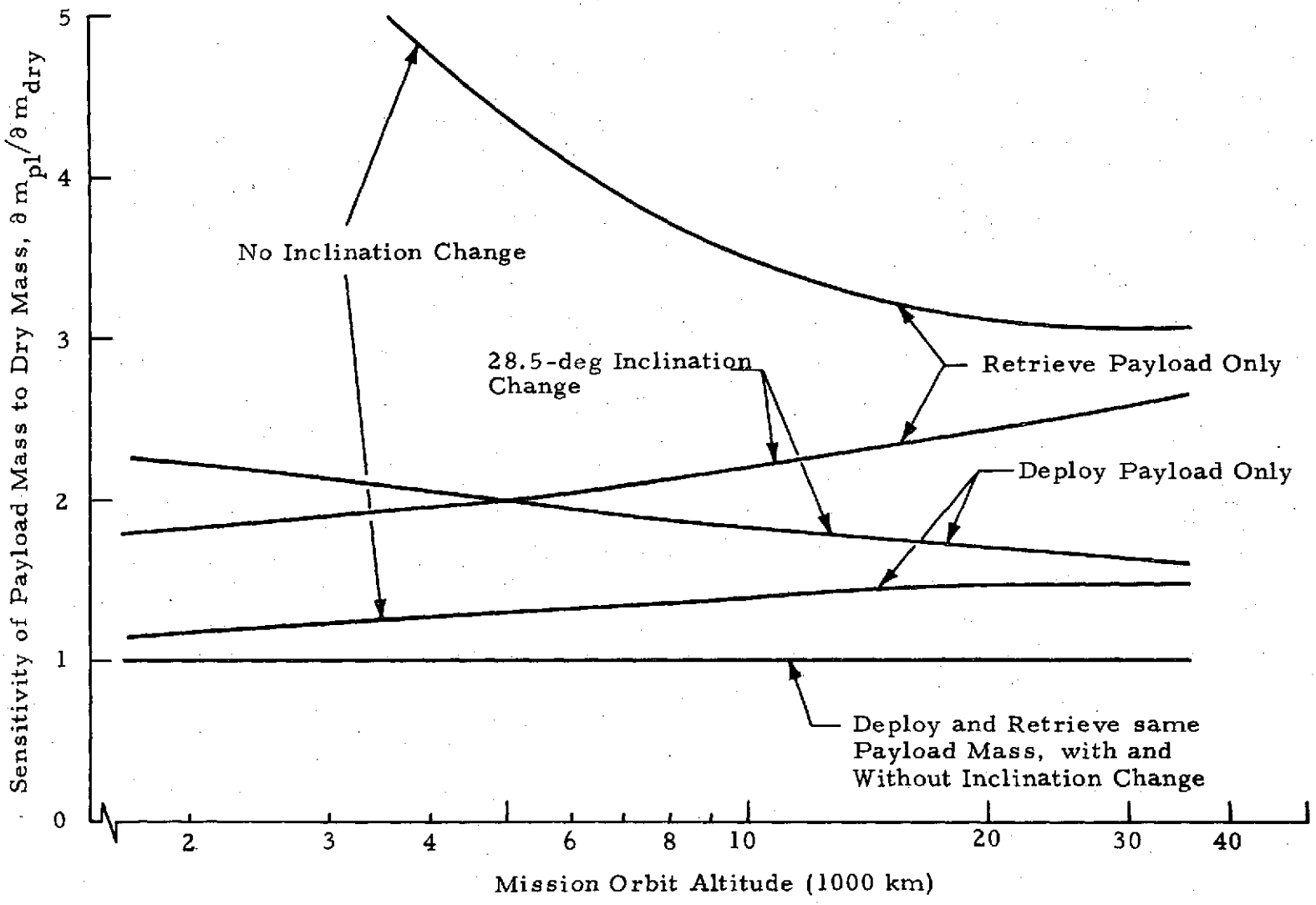

Fig. 64 - Sensitivity of Payload Mass to Dry Mass as a Function of Mission Orbit Altitude. The Sensitivities are for a Constant Total EOS Delivered Mass of 28.848 kg, a Dry Mass of 4247 kg and a Specific Impulse of 470 s

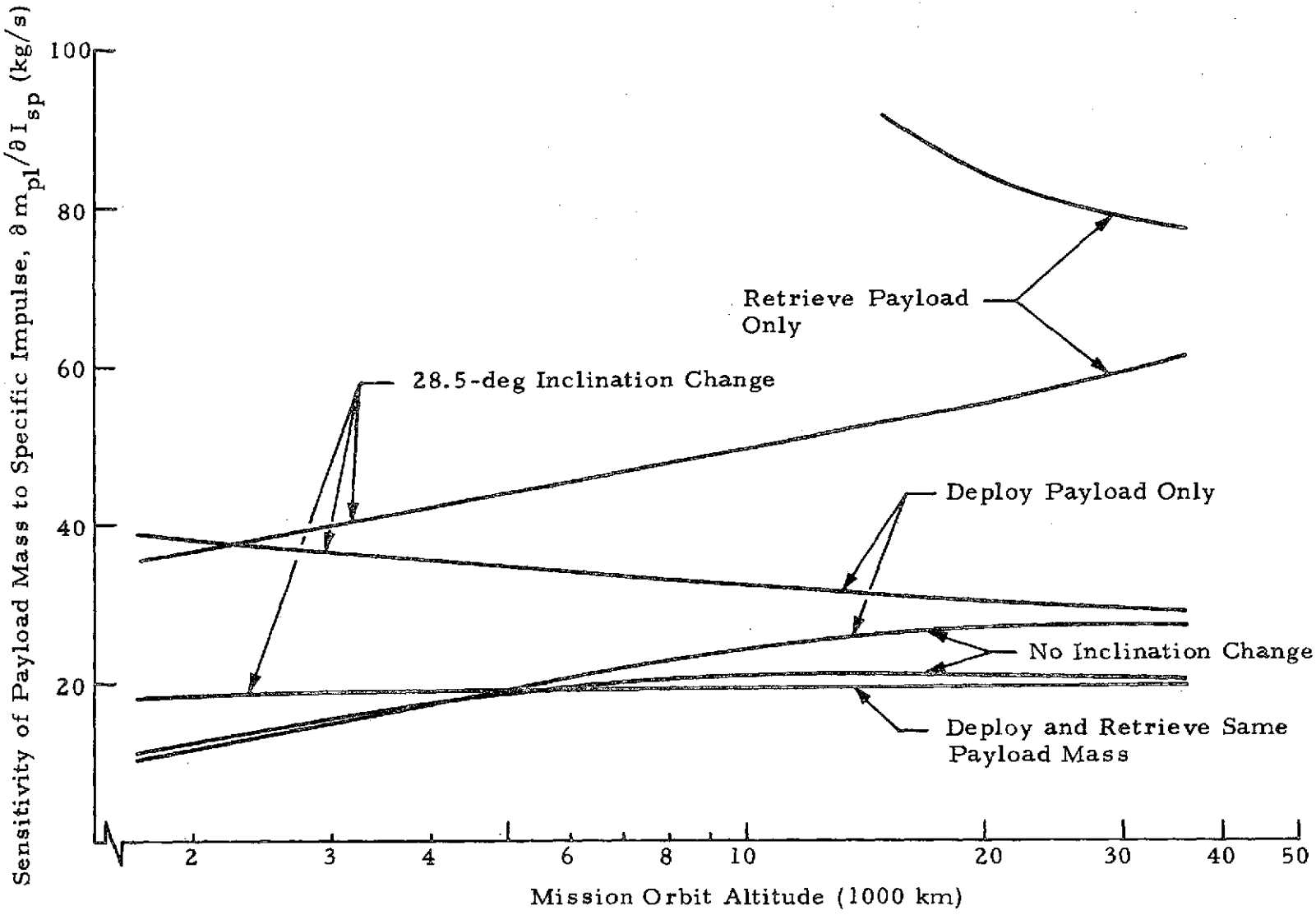

Fig. 65 - Sensitivity of Payload Mass to Specific Impulse as a Function of Mission Orbit Altitude. The Sensitivities are for a Constant Total EOS Delivered Mass of 28,848 kg; a Dry Mass of 4247 kg; and a Specific Impulse of 470 s.

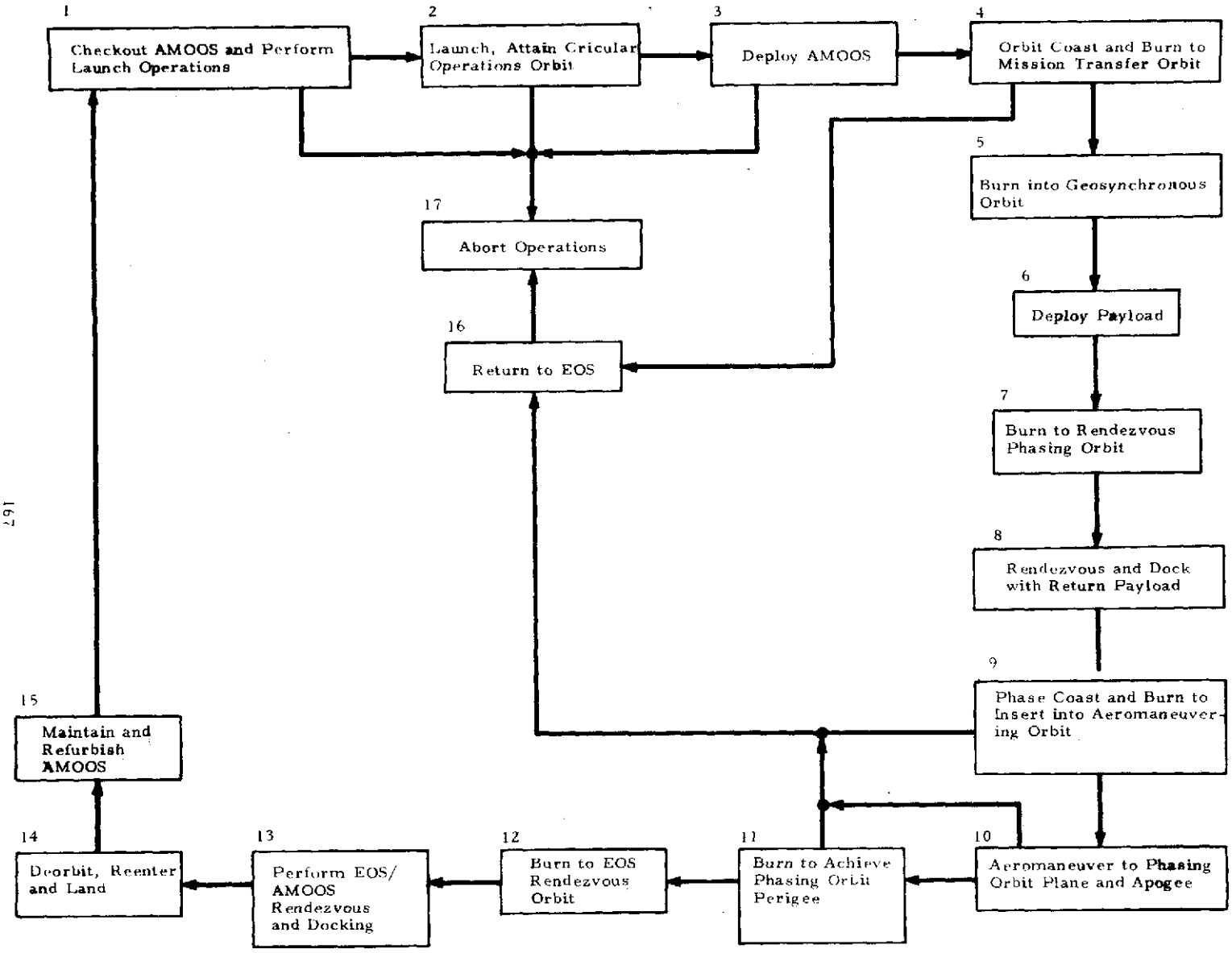

Fig. 66 - Operations Analysis for Baseline Mission Functional Flow Block Diagram

Appendix A

PERFORMANCE AND FLIGHT MECHANICS

Appendix A
NOMENCLATURE

Symbol	Description
A	aerodynamic reference area of vehicle (m^2)
C_D	aerodynamic drag coefficient
C_L	aerodynamic lift coefficient
$\hat{D}$	unit aerodynamic drag vector
g_o	reference gravitational acceleration (m/s^2)
I_{sp}	specific impulse of propulsive system (s)
$\hat{L}$	unit aerodynamic lift vector
m_o	vehicle mass before propulsive velocity change (kg)
m_p	propellant mass required for velocity change (kg)
m_f	vehicle mass after propulsive velocity change (kg)
m	vehicle mass (kg)
p	perigee altitude (km)
R	altitude
$\ddot{\bar{r}}$	vehicle acceleration vector in inertial earth-centered coordinate system (m/s^2)
$\bar{r}$	vehicle inertial radius vector in earth-centered coordinate system (m)
$\bar{v}$	inertial velocity vector in earth-centered coordinate system (m/s)
$\bar{v}_r$	velocity vector of vehicle with respect to surrounding air mass (m/s)
γ	flight path angle (deg)

NOMENCLATURE (Continued)

Symbol	Description
Δv	velocity change performed (m/s)
μ	earth's gravitational constant (m^3/s^2)
ρ	atmospheric density (kg/m^3)
ρ/ρ_{nom}	density ratio used for perturbed trajectories

A.1 TRAJECTORY SIMULATION PROGRAM

A digital computer program was chosen as the trajectory simulation tool. In this program the three degree-of-freedom equations of motion are integrated using a Runge-Kutta technique with double precision arithmetic to obtain the required accuracy. The equations of motion are based on an inertial earth-centered coordinate system. The equations of motion are:

$$\ddot{\bar{r}} = -\frac{\mu}{|\bar{r}|^3}\,\bar{r} + \tfrac{1}{2}\rho\,\frac{v_r^2\,AC_L}{m}\,\hat{L} + \tfrac{1}{2}\rho\,\frac{v_r^2\,AC_D}{m}\,\hat{D}$$

The definitions of the symbols is given in the Nomenclature. The unit lift vector ($\hat{L}$) and the unit drag vector ($\hat{D}$) are defined as:

$$\hat{L} = \frac{\bar{v}_r \times (\bar{r} \times \bar{v}_r)}{|v_r|^2\,|\bar{r}|}\cos(\text{Bank angle}) + \frac{\bar{r} \times \bar{v}_r}{|\bar{r}|\,|\bar{v}_r|}\sin(\text{Bank angle})$$

$$\hat{D} = -\frac{\bar{v}_r}{|\bar{v}_r|}$$

The vehicle bank angle is a rotation about the relative velocity vector ($\bar{v}_r$), measured positive clockwise, looking forward, from the local vertical plane.

Spherical rotating earth gravitation and atmosphere models are used. The aerodynamic lift and drag coefficients can be input as functions of angle of attack, Mach number or Knudsen number. The vehicle attitude is input as a function of lapsed flight time or Mach number. The integration and output step size can be varied during the trajectory phases to hold program run time and output to a minimum without affecting the accuracy.

Atmospheric density variations can be simulated by specifying a factor by which the nominal density is to be multiplied.

The atmospheric model used for the trajectory simulation is based on the 1962 U. S. Standard Atmosphere. The maximum deviation of the atmospheric density from nominal which may be encountered during the atmospheric flight of the AMOOS vehicle are based on a study by the Aerospace Environment Division, MSFC. The results of this study are shown in Figs. A-1 and A-2. They show the mean and range of the density in percent of the 1962 U.S. Standard Density for summer and winter, respectively.

The maximum density variations a particular AMOOS vehicle may encounter were then determined from the nominal target perigee and Figs. A-1 and A-2.

A.2 MISSION INCREMENTAL VELOCITY REQUIREMENTS

The incremental velocity requirements for a large spectrum of missions were computed for the AMOOS vehicle as well as for the propulsive Space Tug. The mission profiles for the AMOOS and the Space Tug are shown in Figs. A-3 and A-4, respectively. The mission begins with Tug-EOS separation in a 296 km circular orbit and ends with Tug-EOS docking for return flight to earth. A Hohman transfer was assumed between EOS orbit and mission orbit and for return from mission orbit to EOS orbit. The mission orbit was assumed to be circular. The orbit inclination change was optimally split between perigee and apogee of the transfer ellipse except for the return flight of the AMOOS vehicle where the total inclination change was performed at apogee (no aeromaneuvering plane change). The return flights from the mission orbit differ for AMOOS and Space Tug. The Space Tug returns to a 315 km x 720 km phasing orbit, while AMOOS returns via an aeromaneuver with a perigee of typically 70 km followed by insertion into a 315 km x 720 km phasing orbit.

The incremental velocities required for orbital maneuvers, midcourse correction, docking and attitude control as well as the gravity losses were obtained from the Baseline Tug Definition Document. A 2% contingency was added to all main engine burns.

Typical Δv budgets for AMOOS and propulsive OOS are shown in Tables A-1 and A-2, respectively. They are for a geosynchroneous mission orbit with a 28.5-deg inclination change.

Incremental velocity requirements versus mission altitude are shown in Fig. A-5. Curves are shown for missions involving a 28.5-deg inclination change as well as no inclination change. For the AMOOS vehicle the propulsive and the aeromaneuvering Δv requirements are shown separately. The sum of the two, of course, is identical to the Δv requirement of the purely propulsive OOS. Gravity losses, contingency and the Δv values for small orbital maneuvers are not included.

A.3 MISSION EXPENDABLES SCHEDULE

Tables A-3, A-4 and A-5 present schedules of the consumables expended in executing the baseline mission (deploy and retrieve payload), the alternate mission A (deploy payload only) and the alternate mission B (retrieve payload only), respectively. The data presented are for a mission to geosynchronous orbit involving a 28.5-deg orbit inclination change.

The main engine propellant listed includes 2% Δv contingency and gravity losses. The column headed "RCS Propellant" contains the propellant used for small translational maneuvers and for aeromaneuvering involving the Reaction Control System (RCS). The fourth column contains additional fuel used for the fuel cells, propellant feed line conditioning and other RCS maneuvers (attitude hold, attitude maneuvers, propellant settling, etc.). The fifth column shows propellant used for the Main Propulsion System (MPS) chill-down and start and stop losses. The heat input to the AMOOS propellant from lift-off to the time of main engine burn for descent ellipse injection (DEI), is dissipated by a venting of propellant gases after propellant settling just prior to the main engine DEI burn. A total of 37.7 kg of propellant gases are vented, which is included in column five under Descend Ellipse Insertion Burn. The propellant mass expended for each burn was determined by the standard propellant mass equation

$$m_p = m_o \left(1 - \exp\left(\frac{-\Delta v}{I_{sp} g_o}\right)\right)$$

The specific impulse used was 470s and 460s for the main propulsion system full thrust mode and pumped idle mode, respectively, and a value of 380s was used for the Reaction Control System.

Sources of information used in constructing the expendables schedules are the Baseline Tug Definition Document (Ref. A.1) and the Space Tug Point Design Study performed by North American Rockwell (Ref. A.2).

A.4 NAVIGATION AND GUIDANCE ERRORS

All the earlier studies concerned with the concept of aerobraking have pointed out the need of some method to compensate for off-nominal atmospheric and trajectory conditions. Some of the methods suggested are the use of aerodynamic lift, propulsive thrusting, varying the number of atmospheric passes, release of the drag device at the appropriate time during the atmospheric flight, drag modulation, etc.

The present study points out the advantages of a single atmospheric pass with a vehicle flying at a high angle of attack. The need to compensate for off-nominal conditions with this concept is evident when considering the atmospheric density variations encountered. It was found that the density can vary between + 40% and -35% from its nominal value. In addition to these variations come the effects of off-nominal trajectories due to navigation errors. A trajectory for a return flight from geosynchronous orbit, which results in a phasing orbit apogee altitude of 720 km after passing through a nominal atmosphere will cause the vehicle to reenter if the density is 15% above nominal and results in an apogee altitude of about 5500 km if the density is 35% below nominal. This clearly establishes the need to compensate for off-nominal conditions.

The guidance problems connected with the aerobraking concept have received little attention in the literature. These problems are considerably different from the ones encountered with an Apollo or Space Shuttle-type reentry vehicle or with the synergetic inclination change problem. With the former almost all of the vehicle's energy is to be dissipated during reentry

while with the latter the energy lost is to be minimized. In contrast, the aerobraking concept requires that a specific amount of energy be dissipated, with the vehicle's energy at the end of the maneuver being above low earth orbit values. Guidance strategies developed for reentry vehicles of the Apollo or Space Shuttle type or the synergetic inclination change concept do therefore not directly apply to the aerobraking problem. During the present phase of this study the guidance problem was not specifically addressed except that a literature search was performed, but it was determined that a significant amount of development work will be needed to find a satisfactory solution.

A preliminary investigation was performed of the navigation requirements. The return flight from a geosynchronous orbit received primary interest since the navigation uncertainties at atmospheric entry are of prime interest.

To determine the impact of navigation errors on the perigee altitude, P, the partial derivatives of the velocity, V, altitude, R, and flight path angle, γ, with respect to the radial perigee position were computed for a nominal transfer ellipse which brings the vehicle from geosynchronous orbit to a perigee altitude of 70 km. These partial derivatives are shown in Fig. A-6 as a function of time after deorbit insertion burn. The partial derivatives can be used to approximately compute the radial perigee position uncertainty resulting from navigation uncertainties at any given point along the nominal trajectory. Conversely, they can also be used to determine approximately the change in velocity required at any given point along the nominal trajectory to effect a certain change in perigee altitude.

The Space Tug Baseline Document specifies 3σ values for the position and velocity uncertainty at geosynchronous orbit of 50 km and 5 m/s, respectively. These uncertainties result in a 3σ perigee altitude uncertainty of 50 km, where the effects of the position and velocity uncertainties at geosynchronous orbit were combined by the root sum square, RSS, method.

C-3

The Δv and the RCS fuel consumption required for a midcourse correction was computed based on the requirement to correct the perigee altitude by 50 km. The Δv and the fuel consumption are shown in Fig. A-7 as a function of time after deorbit ellipse insertion burn. The propellant mass shown is based on a vehicle mass of 10,000 kg. As expected, the midcourse correction is most economical at high altitudes and becomes prohibitively expensive close to perigee in terms of fuel consumption.

The primary purpose of the midcourse correction during the transfer from a high altitude orbit to the phasing orbit is to reduce the uncertainty in the perigee altitude of the transfer ellipse. The maximum allowable uncertainty in perigee altitude is determined by the vehicle's capability to compensate for deeper or shallower penetration of the atmosphere and by the vehicle's thermal protection system. This study has indicated that the HB and 5B vehicles have the capability to compensate for $\pm$ 6 km variation from nominal target perigee. This 6 km variation is taken as the allowable 3σ uncertainty in perigee altitude after the last midcourse correction.

An analysis of the navigation techniques and accuracies achievable with an autonomous navigation system during an AMOOS type mission was performed in (Ref. A-3). This analysis assumed an autonomous navigation system with the sensor package consisting of the following items:

- IMU – Typified by Kearfoot KT-70

  The IMU consists of two two-degree-of-freedom gyros for attitude reference and three orthogonal accelerometers for velocity increment measurement.

- Star Tracker – Typified by ITT AEROBEE 150A

  The Star Tracker is a strapped down optical sensor using electronic gimballing to determine star positions within an eight-degree field-of-view (FOV).

- Landmark Tracker – Typified by the Westinghouse Design

  This optical sensor measures tracking angles to earth features such as islands and lakes.

- Horizon Scanner — Typified by the Lockheed Edge Tracker (under development)

  This horizon sensor is an infrared radiometer that scans the earth's horizon to determine the vehicle's local vertical.

The landmark tracker was found to be the best available sensor for obtaining navigation updates. However, the operational range of the landmark tracker is limited to the order of 7500 km. The landmark tracker observations began approximately 1800 seconds prior to perigee to assure that the tracker's maximum range is not exceeded.

The analysis of the transfer trajectory in Ref. A-3 was based on initial 3σ uncertainties in radial position and tangential velocity at geosynchronous orbit of 18 km and 0.6 m/s, respectively. These two uncertainties are the main contributors to the radial perigee position uncertainty. These uncertainties are considerably less than the 50 km and 5 m/s, respectively, specified in the Space Tug Baseline Document (Ref. A-1) and which was assumed for the present study, but the results obtained in Ref. A-3 are still approximately applicable to the present study.

The impact of the midcourse correction on the perigee uncertainty was investigated in Ref. A-3 if the midcourse correction were made: (1) at the conclusion of the horizon sensor updates; (2) 500 seconds after initiation of the landmark tracker updates; or (3) 1300 seconds after initiation of the landmark tracker updates. The resulting uncertainties in radial perigee position are shown in Fig. A-7. To achieve a radial perigee position uncertainty of 6 km (3σ) the midcourse correction would have to be performed approximately 1400 sec prior to perigee. This may require up to 140 kg of RCS propellant. This is a considerable amount of propellant and means to reduce it should be investigated.

To perform the midcourse correction at a higher altitude with the required accuracy would either require a ground-based navigation update system or an advancement in technology like, for example, the extension of the range of the landmark tracker.

From this preliminary investigation, it is concluded that the autonomous navigation system, which is based on Shuttle era technology, is marginally adequate.

A.5 REFERENCES

A.1 National Aeronautics and Space Administration, "Baseline Tug Definition Document, Revision A," PD-DO-SI(72-56), Marshall Space Flight Center, Ala., 26 June 1972.

A.2 Greeg, C., "Space Tug Point Design Study, Final Report," SO72-SA-0032, North American Rockwell Corp., Downey, Calif., 11 February 1972.

A.3 Corso, C. J. et al., "Space Tug Aerobraking Study," Boeing Document No. D5-17142, The Boeing Co., Huntsville, Ala., 12 April 1972.

Table A-1

AMOOS Δv BUDGET FOR GEOSYNCHRONOUS ORBIT MISSION WITH 28.5-DEG INCLINATION CHANGE

Event	Main Engine	Orbital Maneuver	RCS
Separate from EOS			3
Perigee Burn for Transfer Orbit Injection	2448		
Gravity Loss	94		
Midcourse Correction			15
Apogee Burn to Circularize	1786		
Gravity Loss	3		
Station Keeping			9
Deploy Payload			3
Phasing Orbit Insertion		30	
Retrieve Payload		30	5
Deorbit to Transfer Orbit Injection	1841		
Gravity Loss	3		
Midcourse Correction			15
Aeromaneuvering		30	
Adjust to 315 x 720 km		61	
Circularization Burn into 315 km	112		
Terminal Rendezvous		30	5
Dock with EOS			3
2% Contingency	126		
Total	6413	181	58

Table A-2

SPACE TUG Δv BUDGET FOR GEOSYNCHRONOUS ORBIT MISSION WITH 28.5-DEG INCLINATION CHANGE

Event	Main Engine	Orbital Maneuver	RCS
Separate from EOS			3
Perigee Burn for Transfer Orbit Injection	2448		
Gravity Loss	94		
Midcourse Correction			15
Apogee Burn to Circularize	1786		
Gravity Loss	3		
Station Keeping			9
Deploy Payload			3
Phasing Orbit Insertion		30	
Retrieve Payload		30	5
Deorbit to Transfer Orbit Injection	1784		
Gravity Loss	3		
Midcourse Correction			15
Perigee Burn to Inject into 315 x 720 km	2331		
Gravity Loss	8		
Circularization Burn into 315 km	112		
Terminal Rendezvous		30	5
Dock with EOS			3
2% Contingency	171		
Total	8740	90	58

Table A-3

MASS BREAKDOWN AND EXPENDABLES BUDGET FOR BASELINE MISSION, DEPLOY AND RETRIEVE SAME PAYLOAD, GEOSYNCHRONOUS ORBIT WITH 28.5-DEG INCLINATION CHANGE (A DRY MASS OF 4247 kg WAS ASSUMED)

Maneuver	Main Engine Propellant	RCS Propellant	Fuel Cell, Feed Line Conditioning and Other RCS	Start and Stop Losses and MPS Chilldown	Mass after Maneuver
AMOOS Deployed Mass					28848.0
Separate from EOS to AEI Burn		23.2	19.3		28805.5
Ascend Ellipse Insertion (AEI) Burn	12371.8			13.5	16420.2
After AEI Burn to MCC			3.2		16417.0
Midcourse Correction (MCC)		65.8			16351.2
After MCC to MOI Burn			9.1		16342.1
Mission Orbit Insertion (MOI) Burn	5331.0			13.5	10997.6
After MOI to Payload Deployment		35.3	1.5		10960.8
2140 kg Payload Deployment					8820.8
After Payload Deployment Through Payload Rendezvous		152.0	68.3		8600.5
2140 kg Payload Docking		14.4	1.4		10724.7
After Docking to DEI			15.3		10709.4
Descend Ellipse Insertion (DEI) Burn	3566.3			51.6*	7091.5
After DEI to MCC			3.0		7088.5
Midcourse Correction (MCC)		28.4			7060.1
Aeromaneuvering		73.0	7.3		6979.8
Adjust to 720 x 315 km Phasing Orbit	96.4				6883.4
After Phasing Orbit Insertion to Circularization			24.5		6858.9
Circularize to 315 km	170.6			8.9	6679.4
Terminal Rendezvous and Docking		67.6	2.8		6609.0
Burn-out Mass					6609.0
Trapped Propellant and Gases 222kg					6387.0
Payload 2140kg					4247.0
Dry Mass					4247.0

*Includes 37.7 kg of vented propellant

Table A-4

MASS BREAKDOWN AND EXPENDABLES BUDGET FOR ALTERNATE MISSION A, DEPLOY PAYLOAD ONLY, GEOSYNCHRONOUS ORBIT WITH 28.5-DEG INCLINATION CHANGE (A DRY MASS OF 4247 kg WAS ASSUMED)

Maneuver	Main Engine Propellant	RCS Propellant	Fuel Cell, Feed Line Conditioning and Other RCS	Start and Stop Losses and MPS Chilldown	Mass after Maneuver
AMOOS Deployed Mass					28848.0
Separate from EOS to AEI Burn		23.2	19.3		28805.5
Ascend Ellipse Insertion (AEI) Burn	12371.8			13.5	16420.2
After AEI Burn to MCC			3.2		16417.0
Midcourse Correction (MCC)		65.8			16351.2
After MCC to MOI Burn			9.1		16342.1
Mission Orbit Insertion (MOI) Burn	5331.0			13.5	10997.6
After MOI to Payload Deployment		35.3	1.5		10960.8
3663 kg Payload Deployment					7297.8
After Payload Deployment to DEI			15.3		7282.5
Descend Ellipse Insertion (DEI) Burn	2419.3			51.6*	4811.6
After DEI to MCC			3.0		4808.6
Midcourse Correction (MCC)		19.3			4789.3
Aeromaneuvering		48.1	7.3		4733.9
Adjust to 720 x 315 km phasing orbit	67.6				4666.3
After Phasing Orbit Insertion to Circularization			24.5		4641.8
Circularize to 315 km	115.4			8.9	4517.5
Terminal Rendezvous and Docking		45.7	2.8		4469.0
Burnout Mass					4469.0
Trapped Propellant and Gases 222kg					4247.0
Dry Mass					4247.0

*Includes 37.7 kg of vented propellant

Table A-5

MASS BREAKDOWN AND EXPENDABLES BUDGET FOR ALTERNATE MISSION B, RETRIEVE PAYLOAD ONLY, GEOSYNCHRONOUS ORBIT WITH 28.5-DEG INCLINATION CHANGE (A DRY MASS OF 4247 kg WAS ASSUMED)

Maneuver	Main Engine Propellant	RCS Propellant	Fuel Cell, Feed Line Conditioning and Other RCS	Start and Stop Losses and MPS Chilldown	Mass After Maneuver
AMOOS Deployed Mass					27488.0
Separate from EOS to AEI Burn		22.1	19.3		27446.6
Ascend Ellipse Insertion (AEI) Burn	11787.9			13.5	15645.2
After AEI Burn to MCC			3.2		15642.0
Midcourse Correction (MCC)		62.7			15579.3
After MCC to MOI Burn			9.1		15570.2
Mission Orbit Insertion (MOI) Burn	5079.0			13.5	10477.7
After MOI to Payload Docking		33.6	1.5		10442.6
5187 kg Payload Docking		20.9	1.4		15607.3
After Docking to DEI			15.3		15592.0
Descend Ellipse Insertion (DEI) Burn	5200.2			51.6*	10340.2
After DEI to MCC			3.0		10337.2
Midcourse Correction (MCC)		41.5			10295.7
Aeromaneuvering		108.1	7.3		10180.3
Adjust to 720 x 315 km Phasing Orbit	140.0				10040.3
After Phasing Orbit Insertion to Circularization			24.5		10015.8
Circularize to 315 km	249.3			8.9	9757.6
Terminal Rendezvous and Docking		98.8	2.8		9656.0
Burn-out Mass					9656.0
Trapped Propellant and Gases 222kg					9434.0
Payload 5187 kg					4247.0
Dry Mass					4247.0

*Includes 37.7 kg of vented propellant

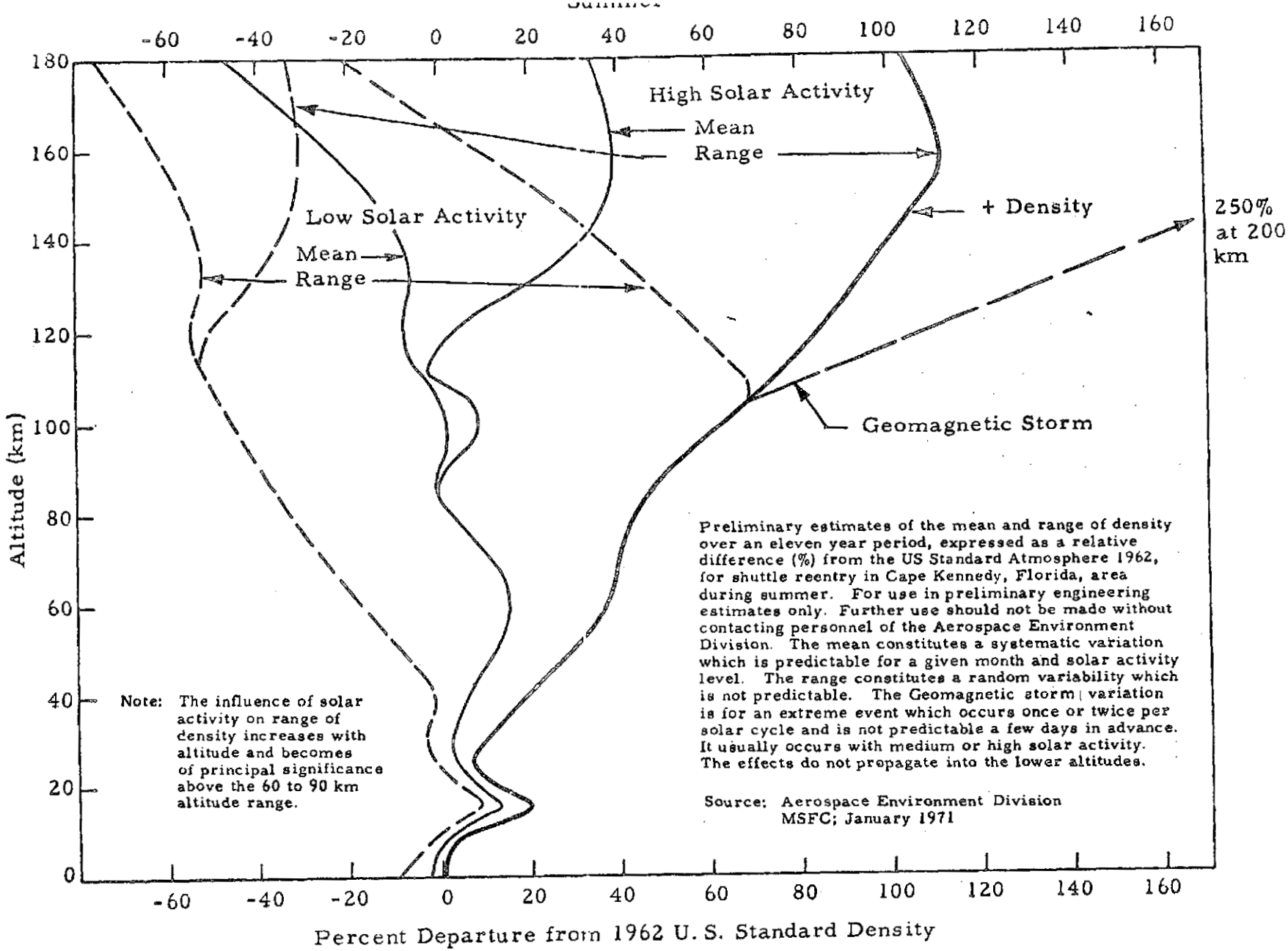

Fig. A-1 - Atmospheric Density Dispersions Based on 1962 U.S. Standard Atmosphere - Summer

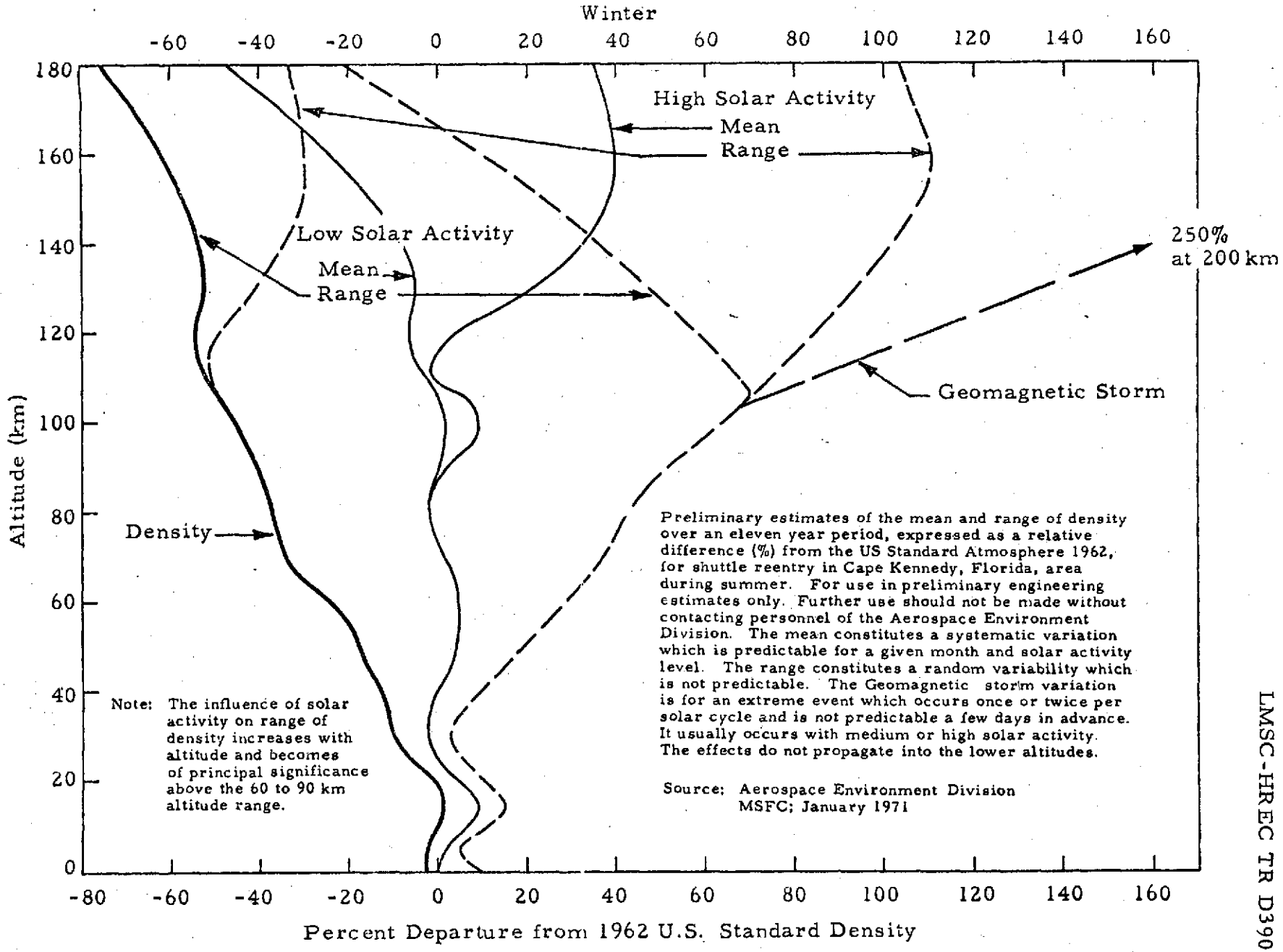

Fig. A-2 - Atmospheric Density Dispersions Based on 1962 U.S. Standard Atmosphere - Winter

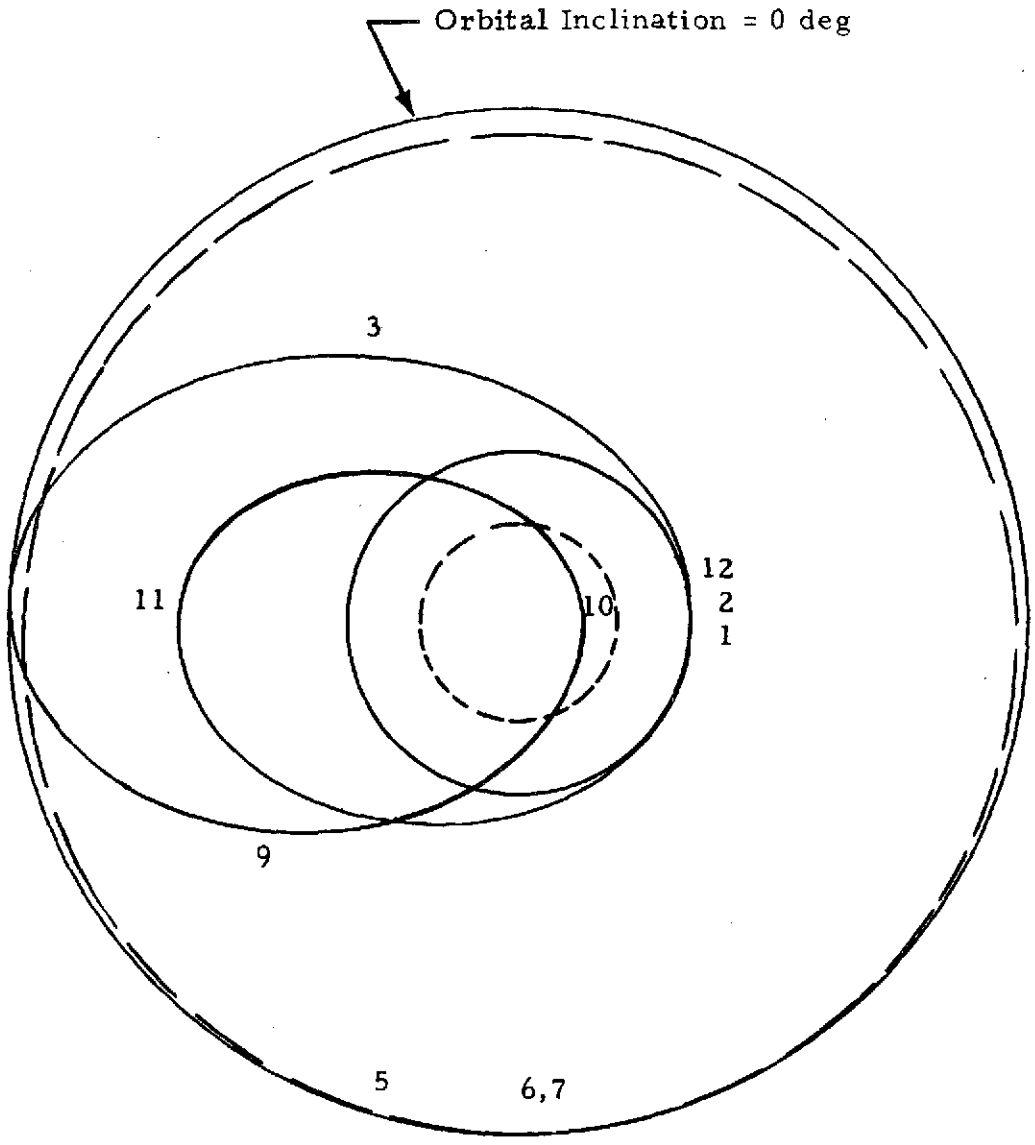

1. Delivered to 296 km Circular Orbit by the EOS
2. Burn to Mission Transfer Orbit
3. Midcourse Correction
4. Burn-to-Mission Orbit
5. Deliver Payload
6. Burn-to-Phasing Orbit for Rendezvous with Return Payload
7. Rendezvous and Dock with Return Payload
8. Burn-to-Transfer to Aeromaneuvering Orbit*
9. Midcourse Correction*
10. Aeromaneuver to Phasing Orbit Plane and Apogee*
11. Burn-to-Achieve Phasing Orbit Perigee
12. Burn-to-EOS Rendezvous Orbit

*Denotes AMOOS Maneuvers Distinct from Space Tug Maneuvers.

Fig. A-3 - AMOOS Mission Profile

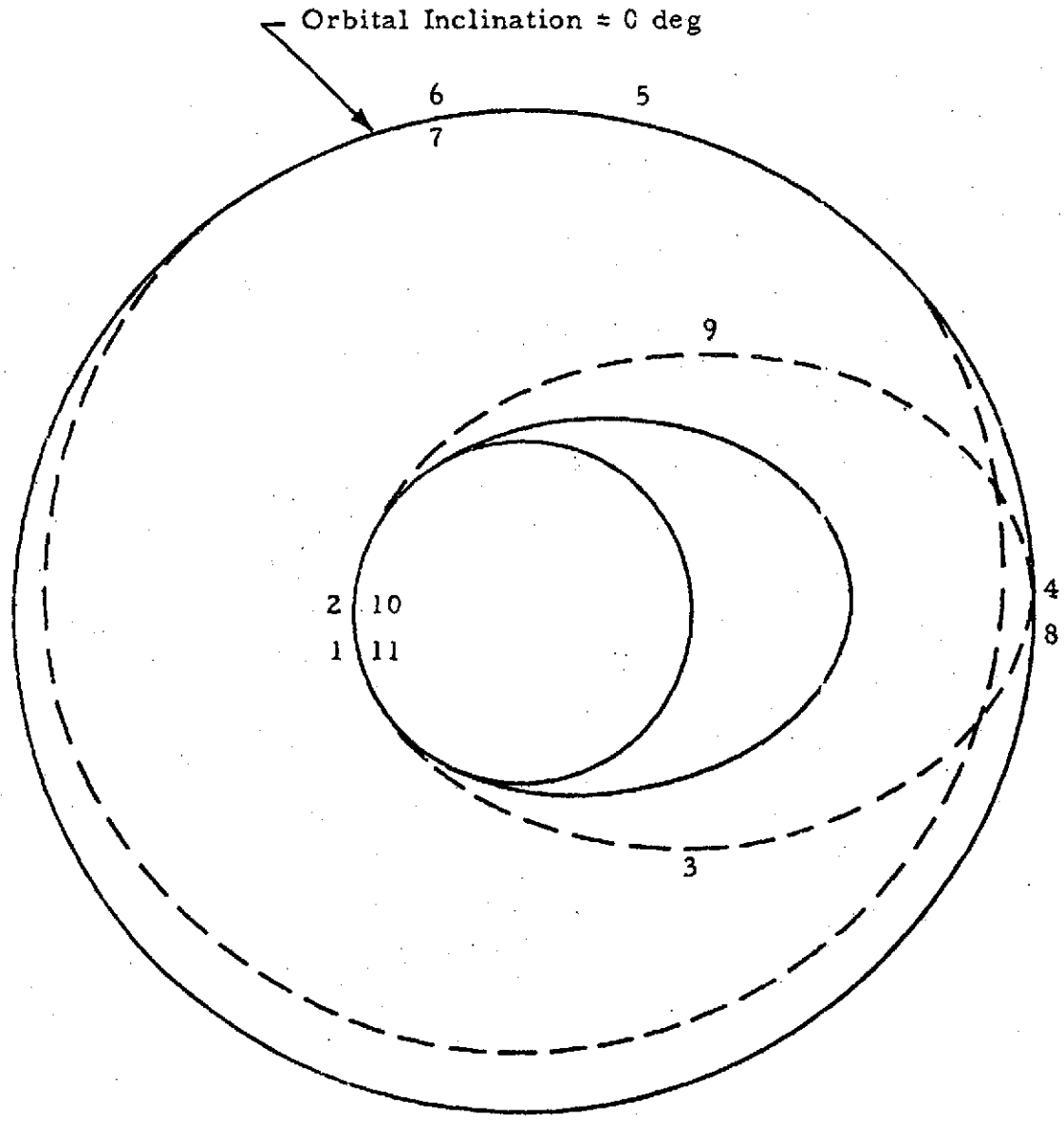

1. Delivered to 296 km Circular Orbit by the EOS
2. Burn to Mission Transfer Orbit
3. Midcourse Correction
4. Burn-to-Mission Orbit
5. Deliver Payload
6. Burn-to-Phasing Orbit for Rendezvous with Return Payload
7. Rendezvous and Dock with Return Payload
8. Burn-to-Transfer Orbit
9. Midcourse Correction
10. Burn to Achieve Phasing Orbit Apogee
11. Burn-to-EOS Rendezvous Orbit

Fig. A-4 - Space Tug Mission Profile

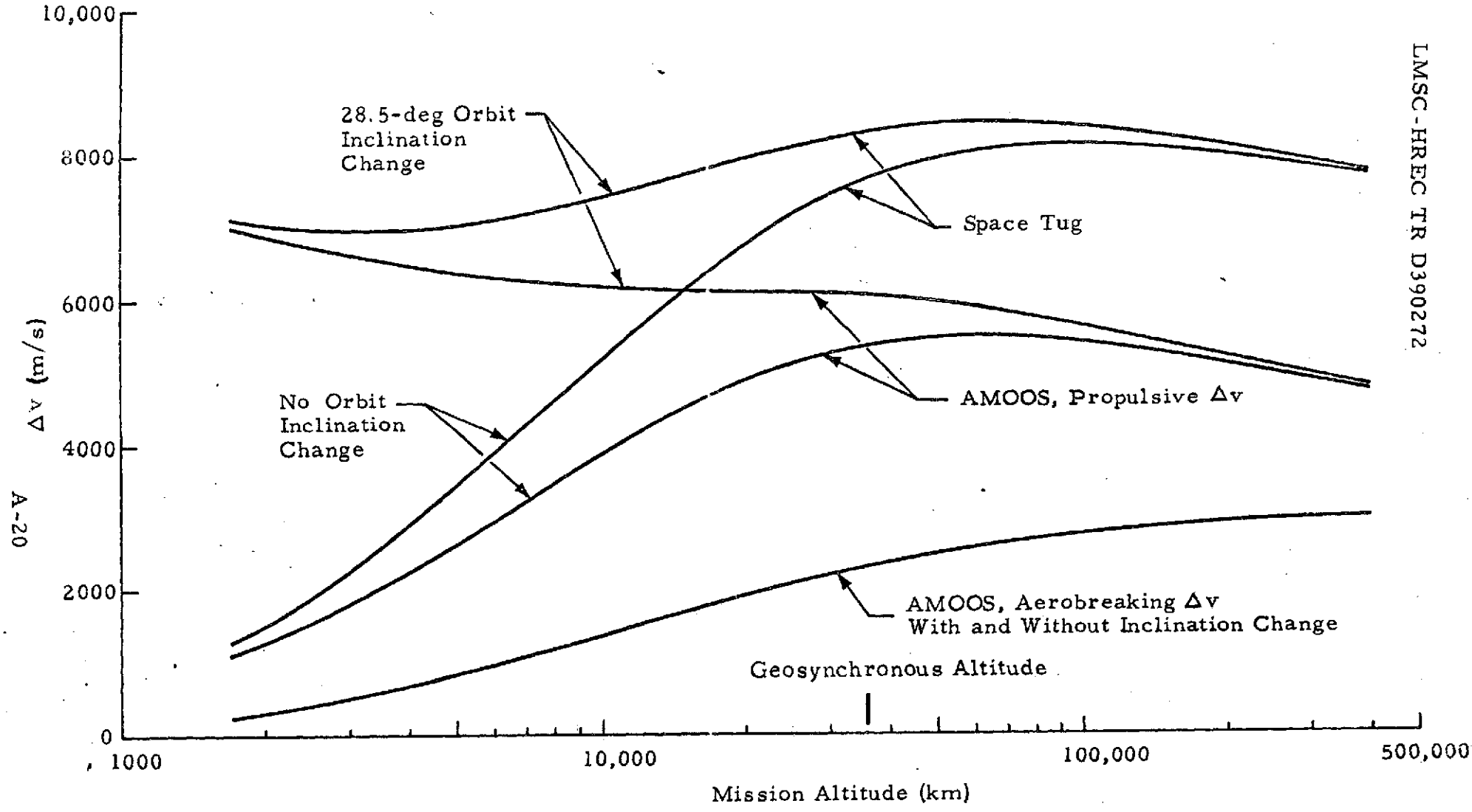

Fig. A-5- Incremental Velocity Requirements vs Mission Altitude With and Without Orbit Inclination Change (Gravity losses, contingency and Δv for orbital maneuvers not included)

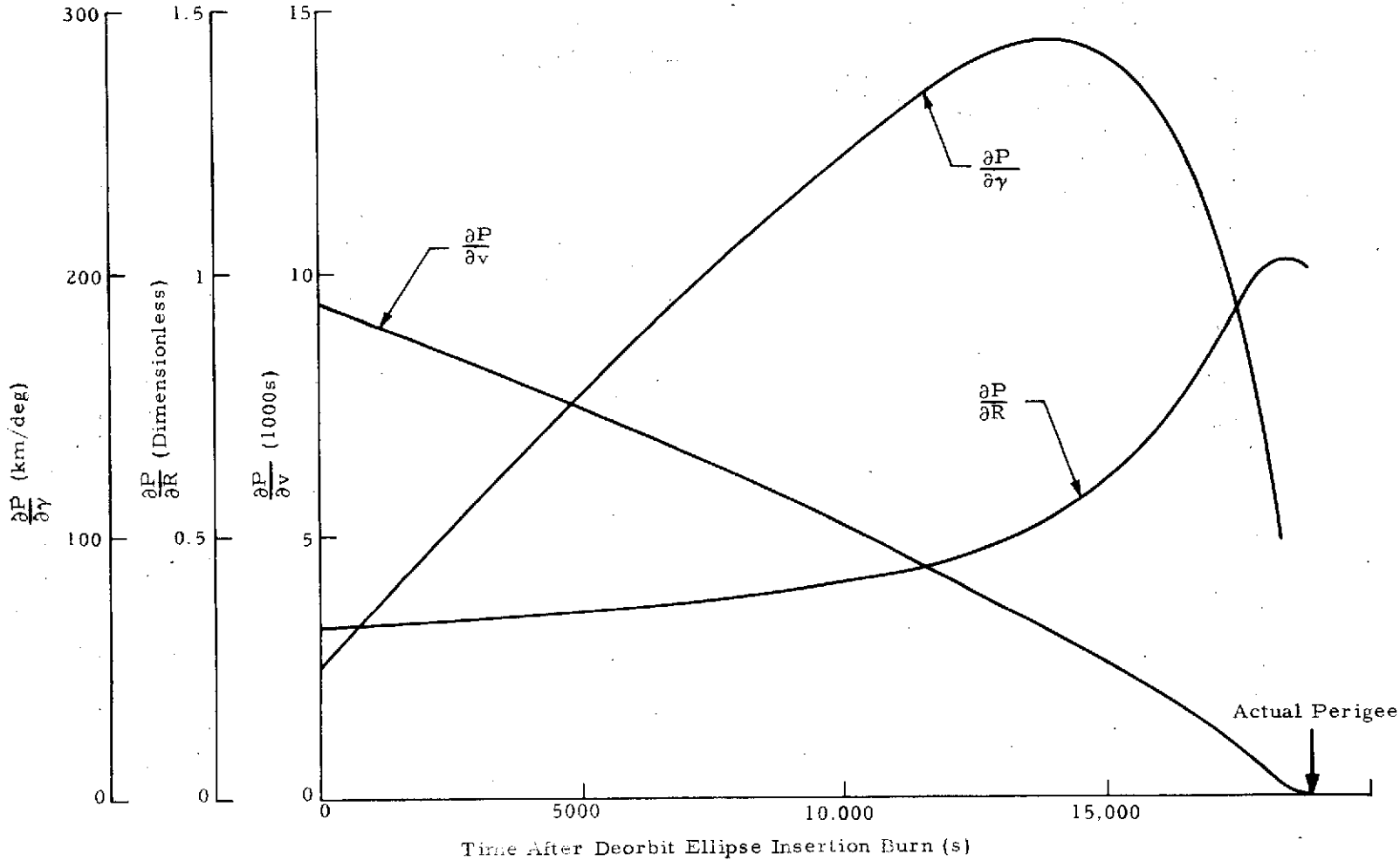

Fig. A-6 Partial Derivative of the Transfer Ellipse Perigee with Respect to Velocity, Radial Distance to Earth Center and Flight Path Angle (Transfer Ellipse from Geosynchronous Orbit to a Target Perigee of 70 km Altitude)

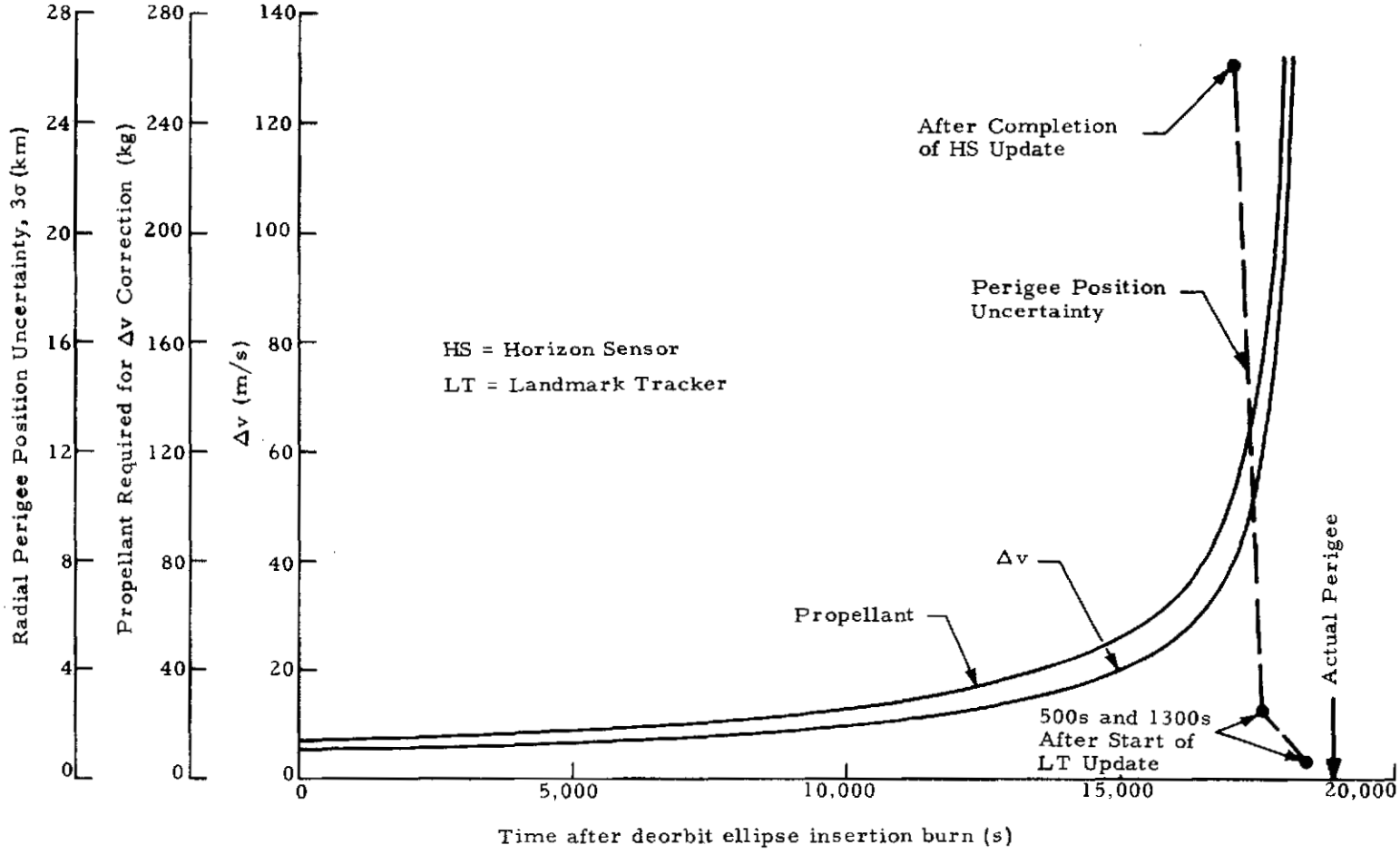

Fig. A-7 - Δv, Fuel Consumption for Midcourse Correction and Radial Perigee Position Uncertainty for Return from Geosynchronous Orbit

Appendix B
AERODYNAMIC ANALYSIS

Appendix B
NOMENCLATURE

Symbol	Description
C_D	drag force coefficient in the wind axis system, $F_D/q_\infty S_{ref}$ positive in the negative direction of X_w (dimensionless)
c.g.	abbreviation for center of gravity
C_L	lift force coefficient (stability or wind axis system) $F_L/q_\infty S_{ref}$, positive in the negative direction of Z_s or Z_w (dimensionless)
C_ℓ	rolling moment coefficient in the body axis system, $M_X/q_\infty S_{ref}\ell$ (dimensionless)
C_m	pitching moment coefficient in the body axis system, $M_Y/q_\infty S_{ref}\ell$ (dimensionless)
C_n	yawing moment coefficient in the body axis system, $M_Z/q_\infty S_{ref}\ell$ (dimensionless)
C_Y	side force coefficient (body or stability axis system), $F_Y/q_\infty S_{ref}$, positive in the positive direction of Y (dimensionless)
ΔC_m	incremental pitching moment coefficient defined as the pitching moment coefficient determined with flap deflection at a particular angle of attack minus the pitching moment coefficient with no flap deflection at the same angle of attack (dimensionless)
F_D	drag force in the wind axis system, positive in the negative direction of X_w (N, lb)
F_L	lift force (stability or wind axis system), positive in the negative direction of Z_s or Z_w (N, lb)
F_Y	side force, positive in the positive direction of Y (N, lb)
L/D	lift-to-drag ratio, C_L/C_D (dimensionless)

NOMENCLATURE (Continued)

Symbol	Description
l_{ref}	reference length (body length) (m, ft), constant, equal to 17.88 m (58.66 ft)
M	Mach number (dimensionless)
M_X	rolling moment in the body axis system; i.e., moment about the X-axis (a positive rolling moment tends to rotate the positive Y-axis toward the positive Z-axis), (N-m, ft-lb)
M_Y	pitching moment in the body (or stability) axis system; i.e., moment about the Y-axis (a positive pitching moment tends to rotate the positive Z-axis toward the positive X-axis), (N-m, ft-lb)
M_Z	yawing moment in the body axis system; i.e., moment about the Z-axis (a positive yawing moment tends to rotate the positive X-axis toward the positive Y-axis), (N-m, ft-lb)
q_∞	dynamic pressure, $\rho_\infty V_\infty^2/2$ (N/m^2, psi)
Re_∞/L	freestream Reynolds number per unit length (1/m, 1/ft)
S_{ref}	reference area (m^2, ft^2), constant, equal to 15.69 m^2 (168.9 ft^2)
T_o	tunnel supply temperature (^oK, ^oR)
T_∞	freestream static temperature (^oK, ^oR)
V_∞	freestream airspeed or speed of the vehicle relative to the surrounding atmosphere (m/sec, ft/sec)
X, Y, Z	body axis system coordinates (the X, Z-plane is the plane of symmetry and the origin of the axis system is the center of gravity, center of mass, or any other convenient point) (m, ft)
Greek	
α	angle of attack, angle between the projection of the wind X_w-axis on the body X, Z-plane and the body X-axis (deg)
β	sideslip angle, angle between the wind X_w-axis and the projection of this axis on the body X, Z-plane (deg)
δ	flap deflection angle, positive when the trailing edge is deflected down (deg)
ρ_∞	freestream air density (kg/m^3, $slug/ft^3$)

Appendix B

Presented herein are pertinent analytical data plots for the AMOOS 5B and HB configurations with the ramp flap. The ramp flap dimensions are identical for both configurations, namely, the ramp angle is 10 deg and the flap area is 6.13 m^2 (Fig. B-1). The reference data pertinent to the aerodynamic data presented are:

- Reference area = 15.69 m^2
- Reference length = 17.88 m
- Pitching moment reference point (X_{cg}) is measured from vehicle nose.
- Rolling and yawing moment reference points lie on the centerline of the vehicles.

The analytical variation of maximum lift coefficient with trim center-of-gravity location is shown in Figs. B-2 and B-3 for the 5B and HB ramp flap configurations. The experimental variation of maximum lift coefficient with trim center of gravity is shown in Figs. B-4 and B-5 for the 5B and HB configurations, respectively, for various settings of the expansion flap. The trim characteristics for forward and aft center-of-gravity locations are shown in Figs. B-6 through B-9 for various settings of the ramp flap. Data are presented for both the 5B and HB configurations. It may be concluded from these data that the ramp flap is capable of trimming either vehicle throughout its expected center-of-gravity range. The lift-to-drag ratio is exhibited in Figs. B-10 and B-11.

Static stability about all three axes is shown in Figs. B-12 through B-19.

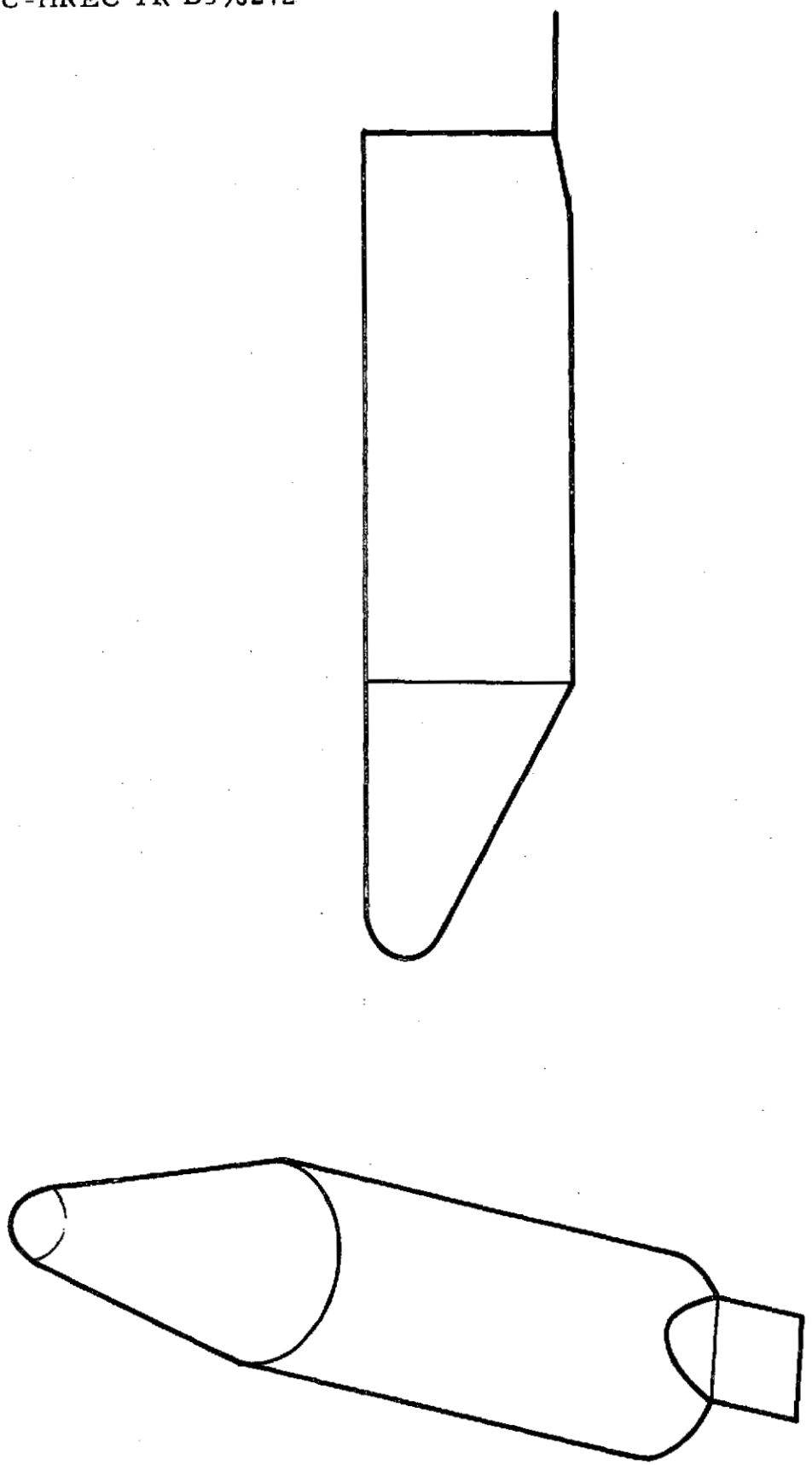

Fig. B-1 - A 10-Degree Ramp Flap on AMOOS 5B with Flap Area = 6.13 m^2

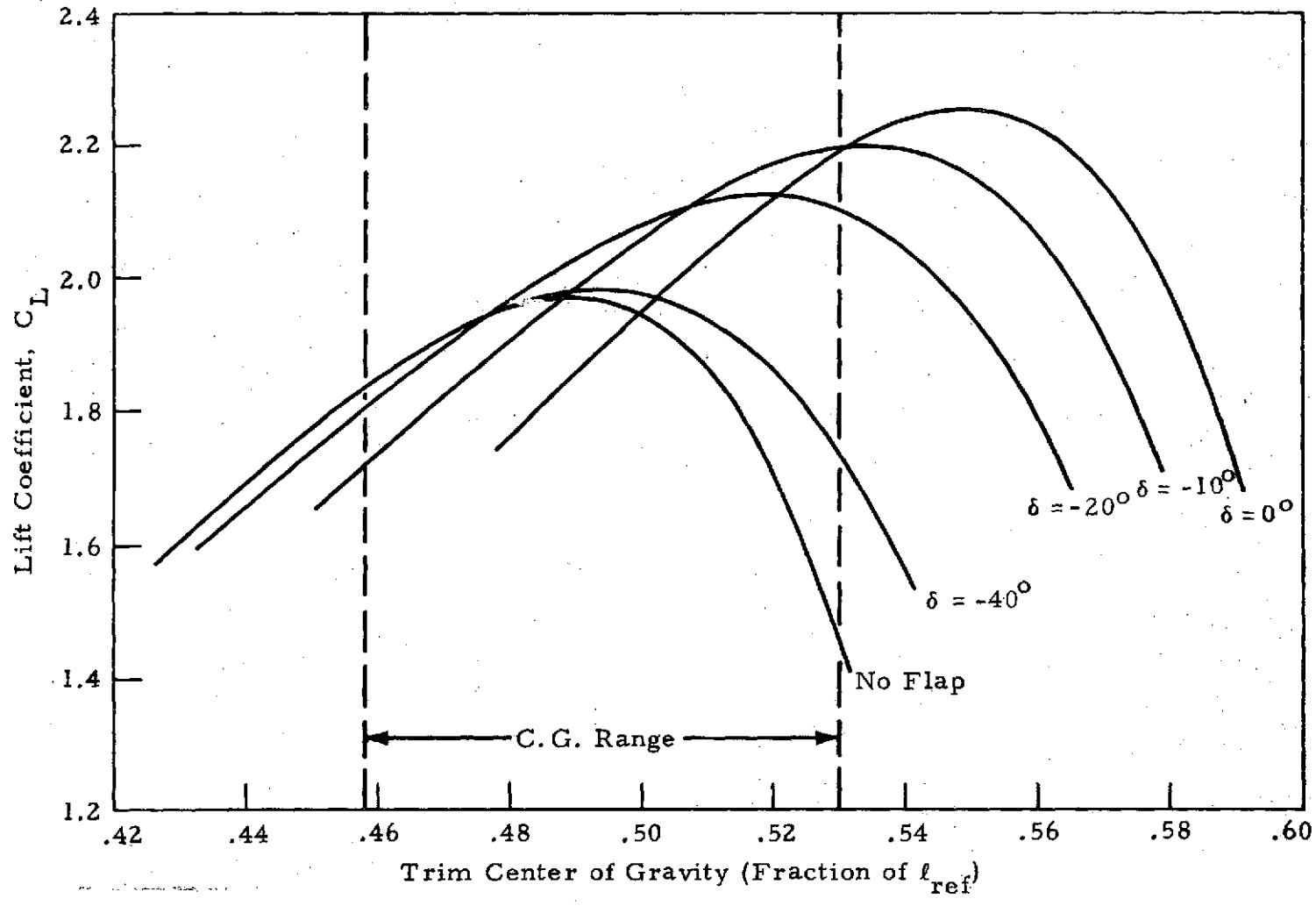

Fig. B-2 - Analytical Variation of $C_{L_{max}}$ with Trim C.G. for Particular Flap Deflections for AMOOS 5B with Ramp Flap

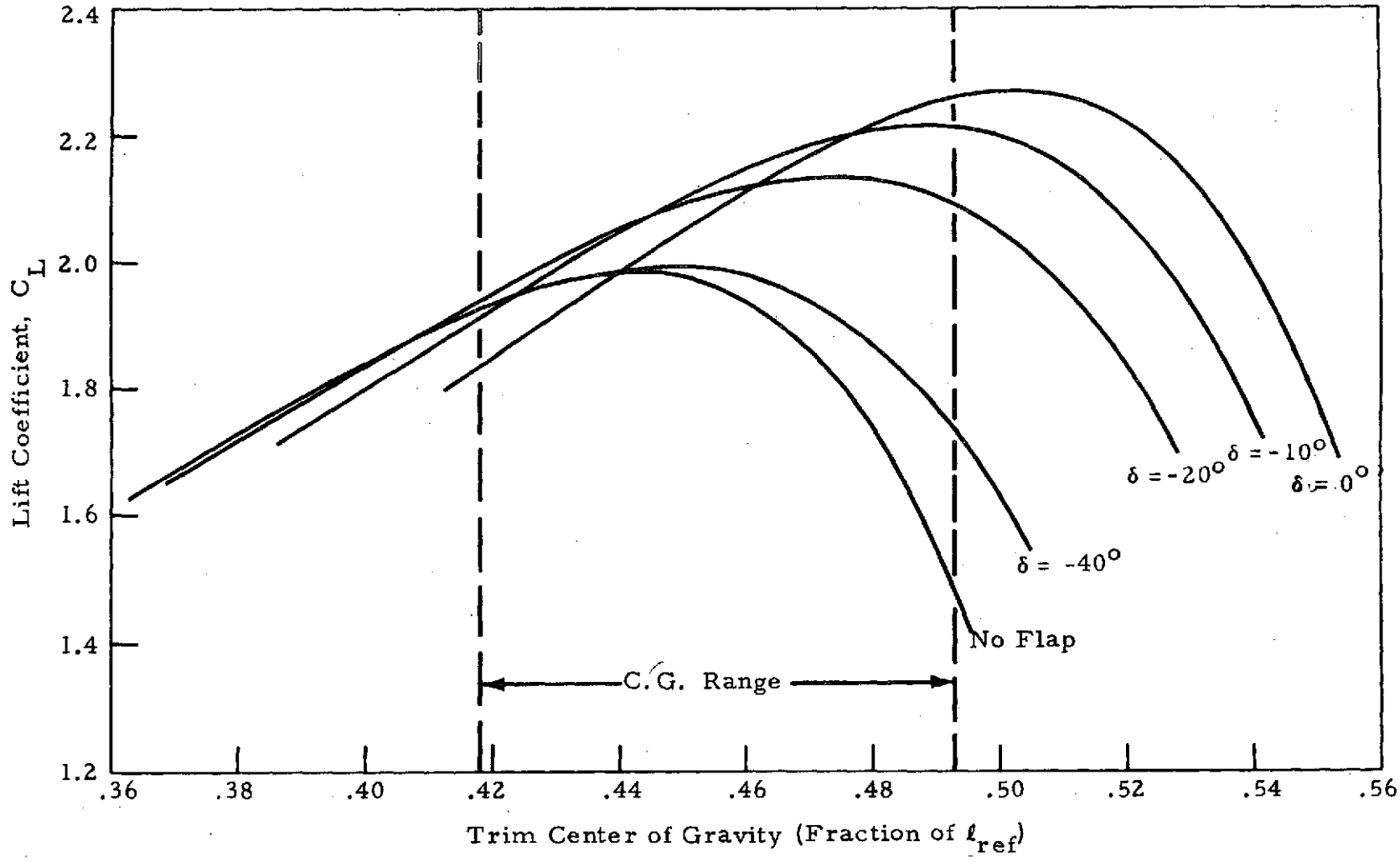

Fig. B-3 - Analytical Variation of $C_{L_{max}}$ with Trim C.G. for Particular Flap Deflections for AMOOS HB with Ramp Flap

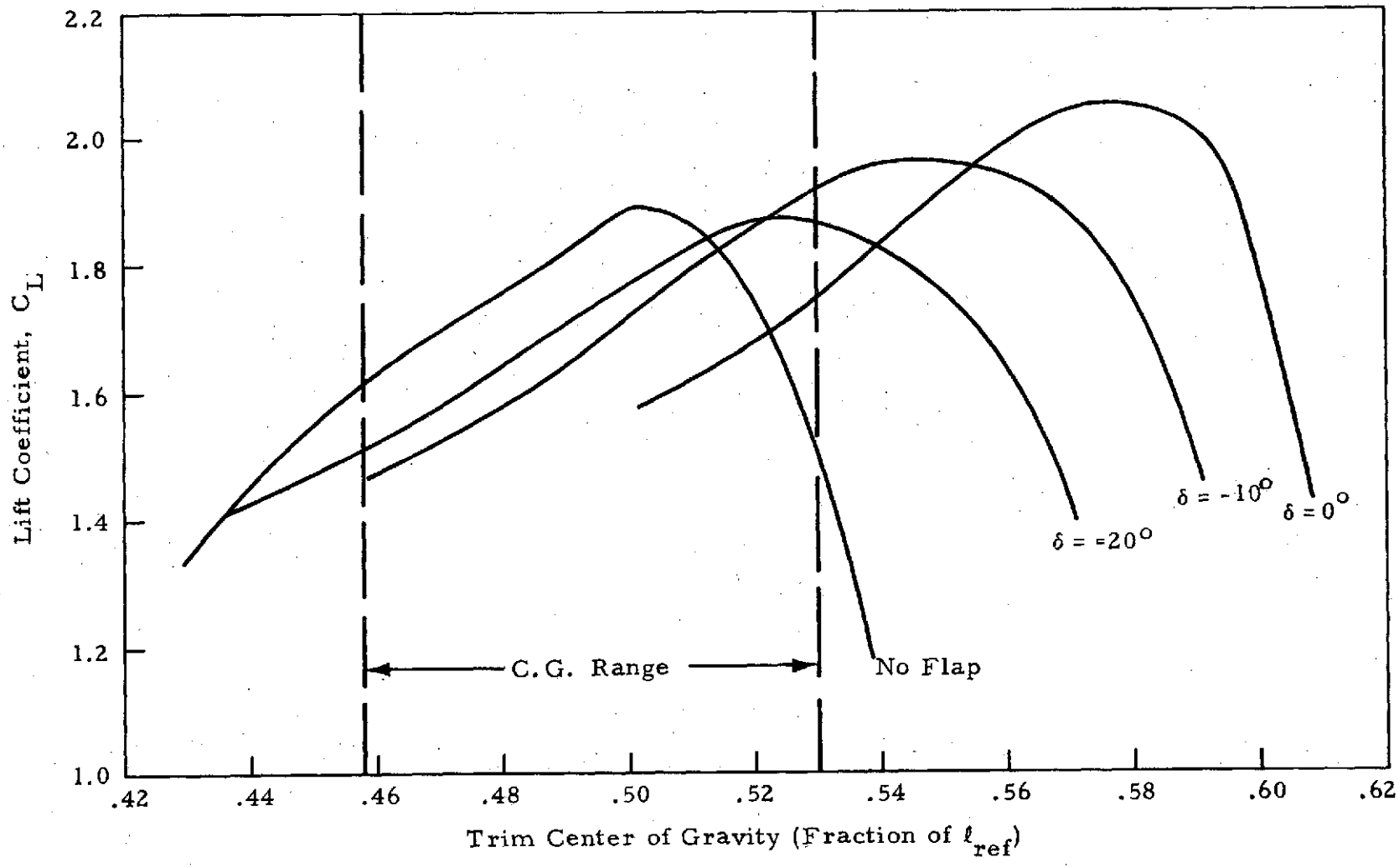

Fig. B-4 - Variation of $C_{L_{max}}$ with Trim C.G. for Particular Expansion Flap Deflections for AMOOS 5B

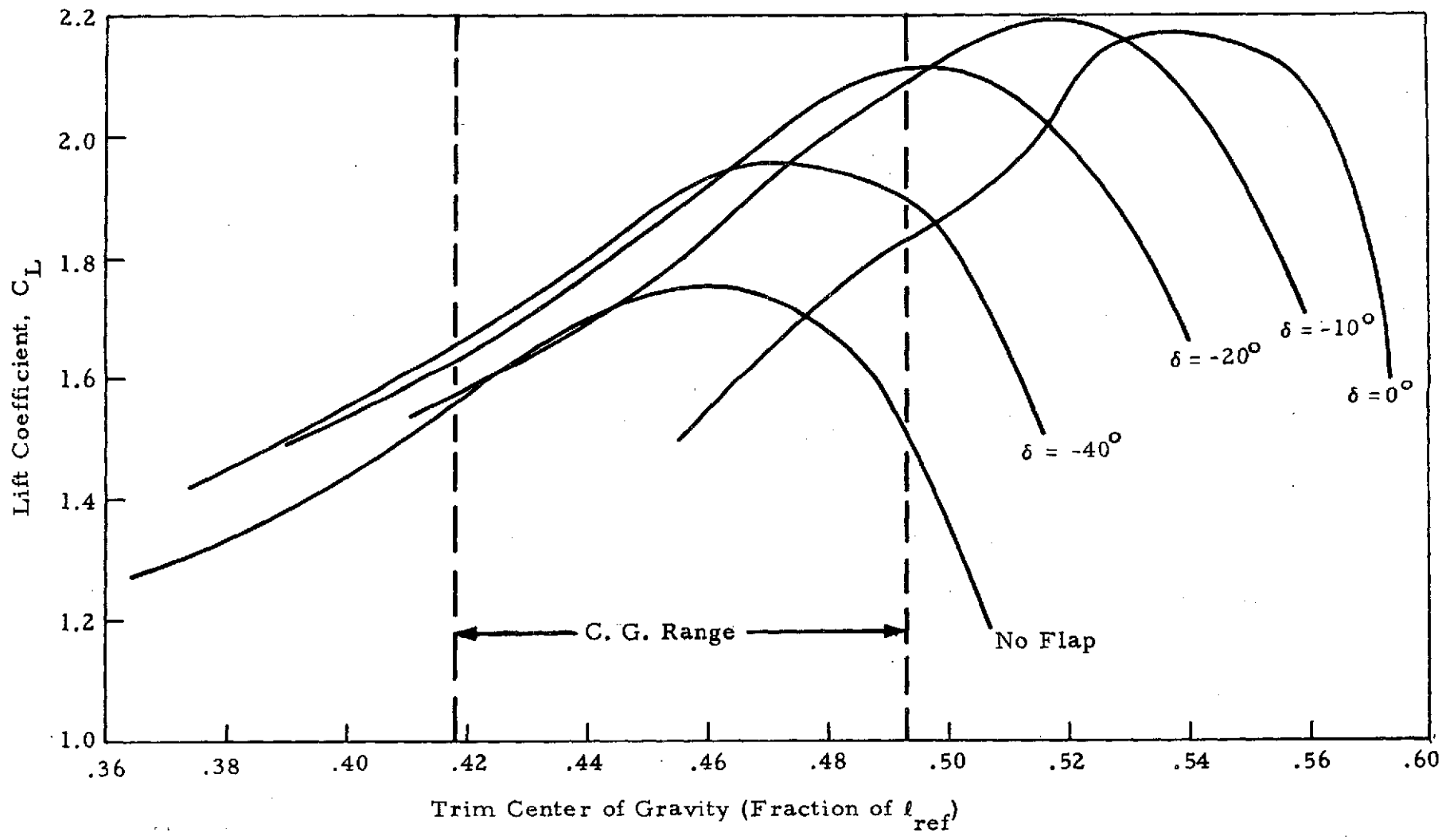

Fig. B-5 - Variation of $C_{L_{max}}$ with Trim C.G. for Particular Expansion Flap Deflections for AMOOS HB

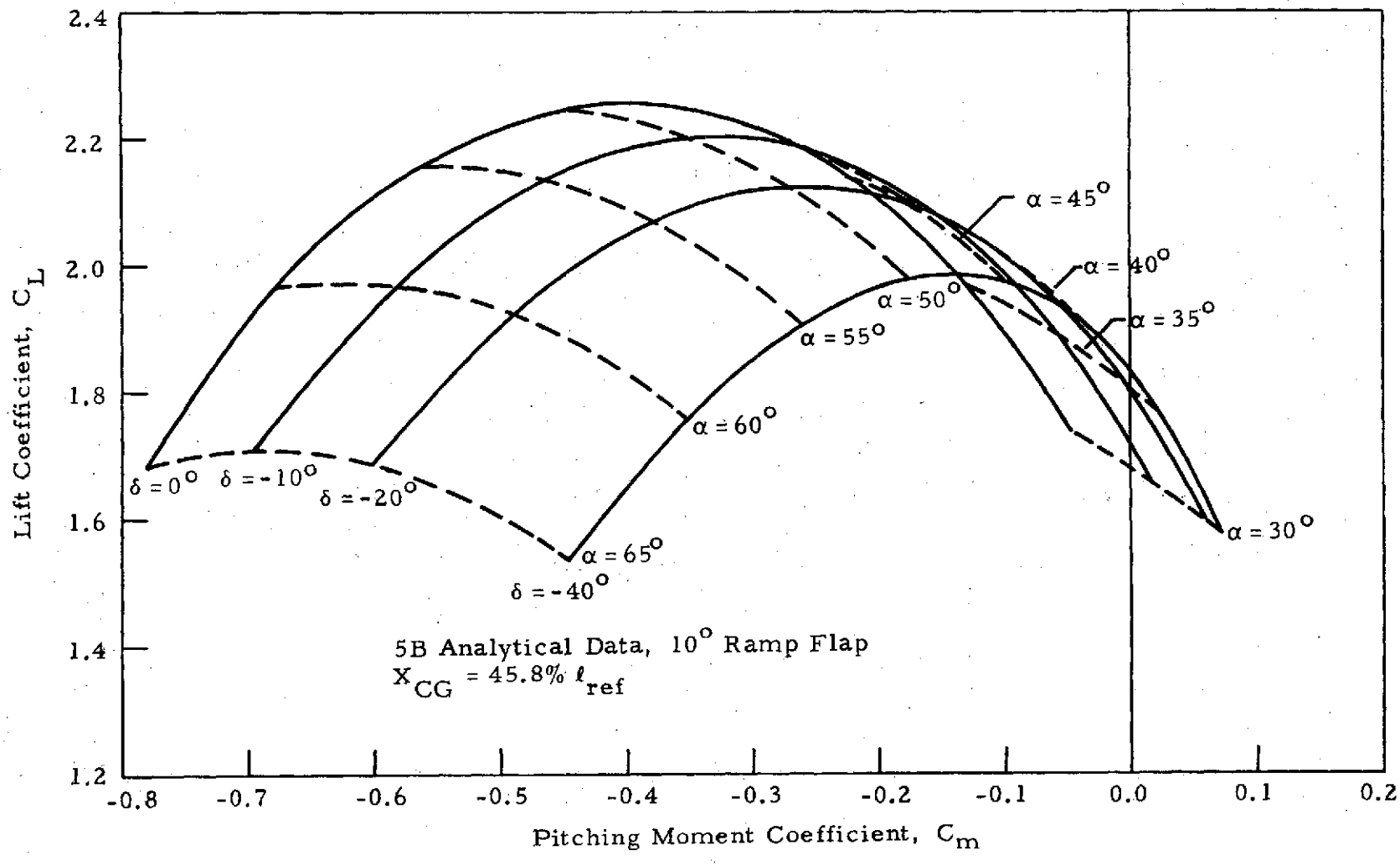

Fig. B-6 - Trim Characteristics of AMOOS 5B at Forward C.G.

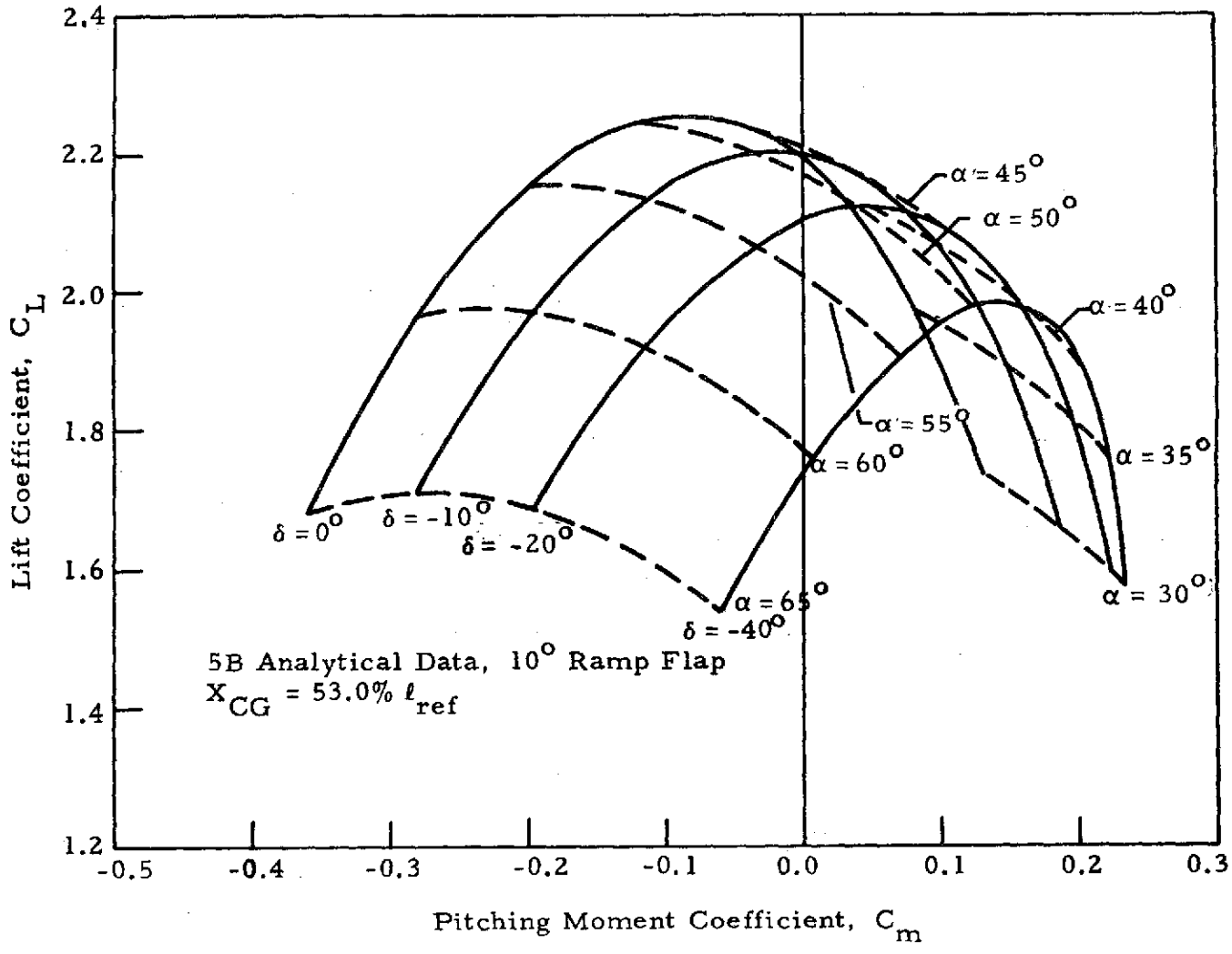

Fig. B-7 - Trim Characteristics of AMOOS 5B at Aft C.G.

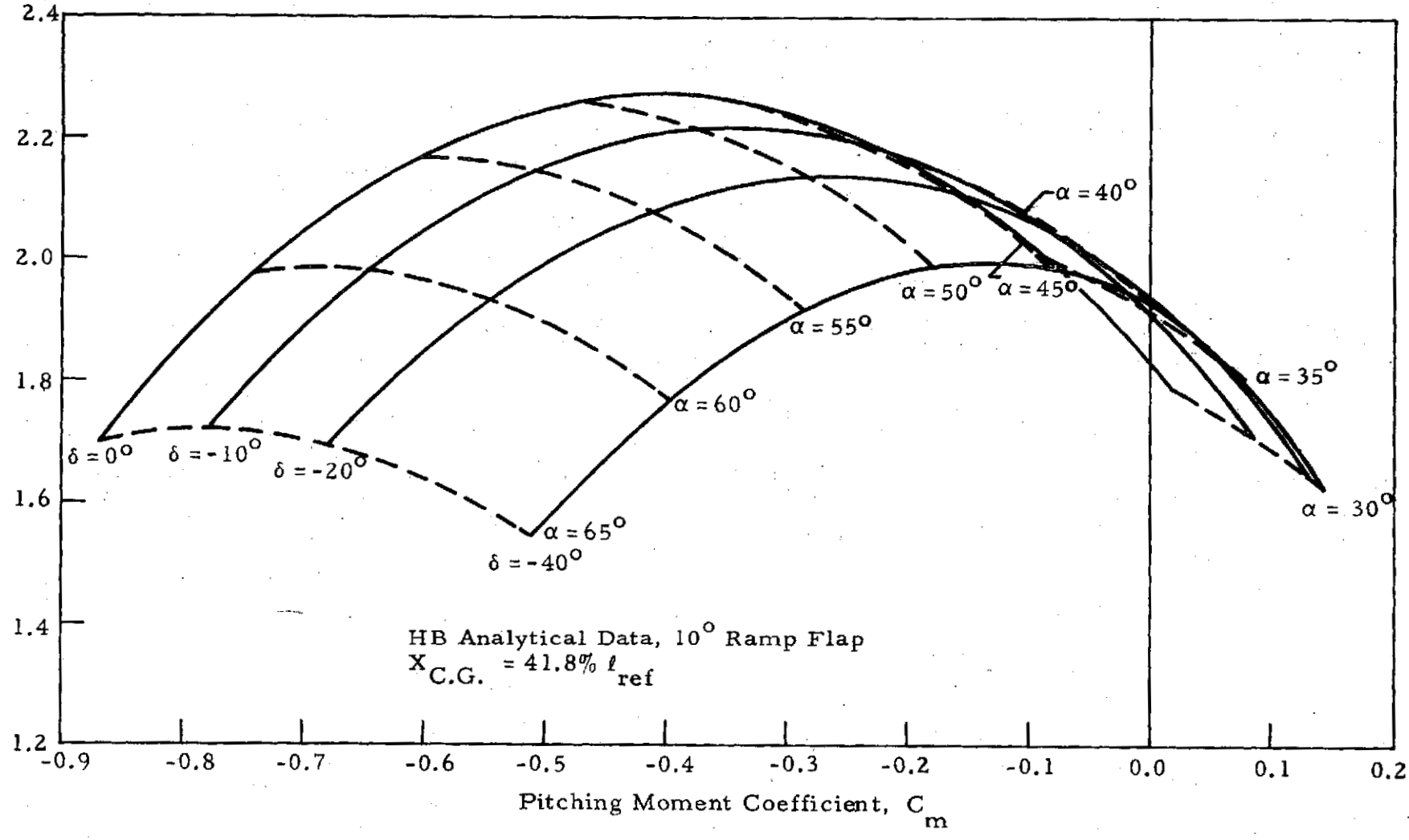

Fig. B-8 - Trim Characteristics of AMOOS HB at Forward C.G.

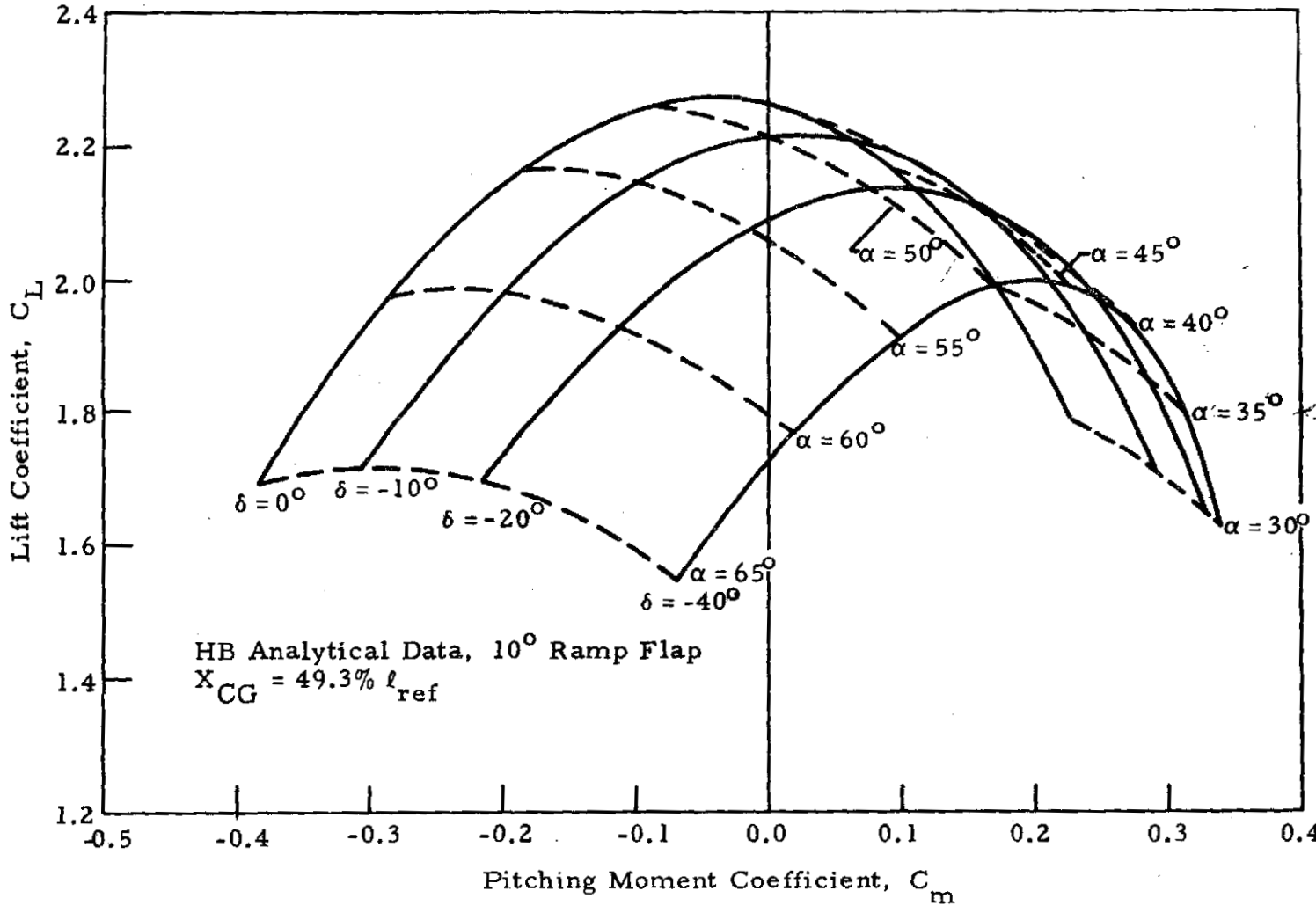

Fig. B-9 - Trim Characteristics of AMOOS HB at Aft C. G.

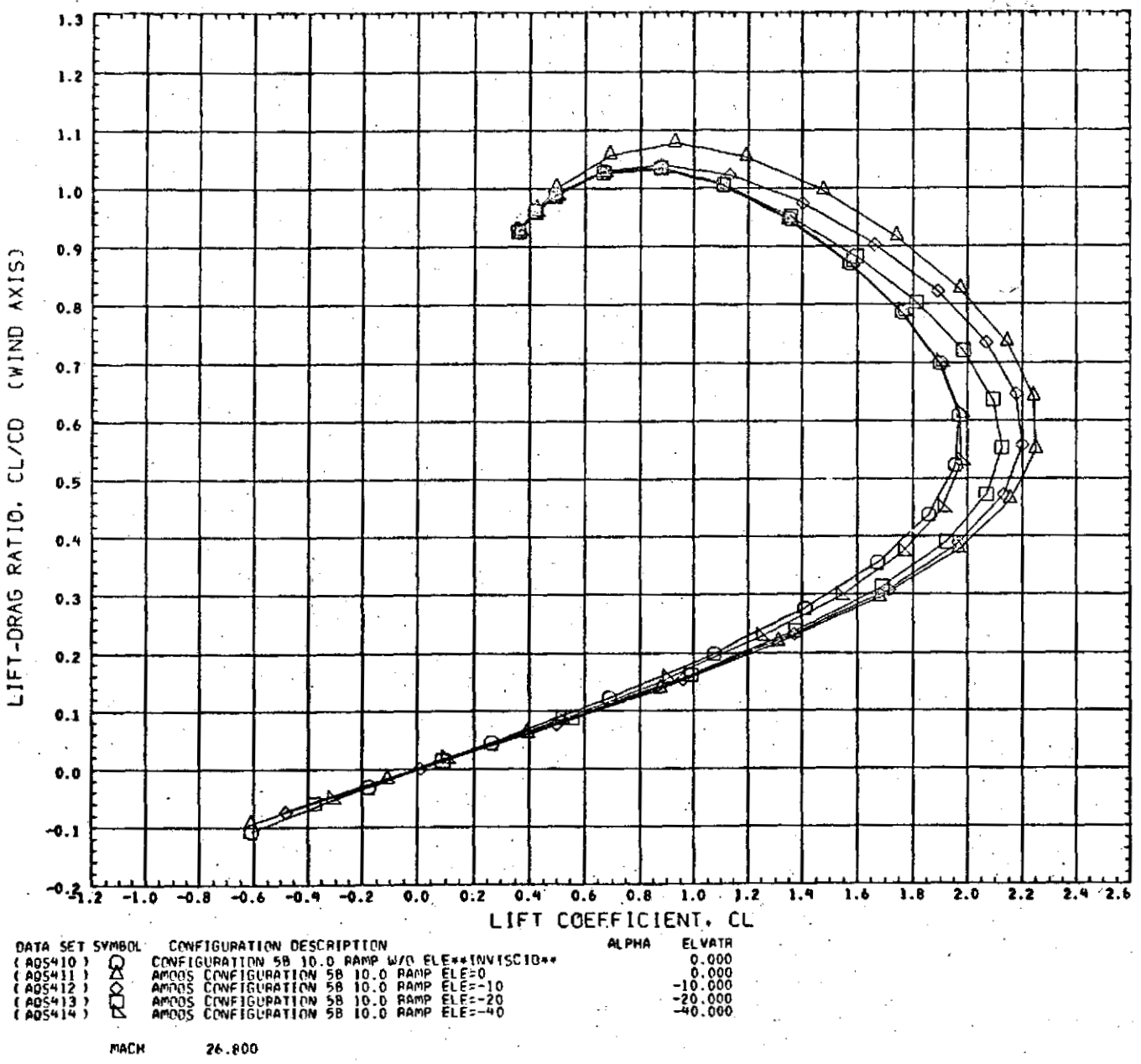

Fig. B-10 - Analytical Lift-to-Drag Ratio vs Lift Coefficient for 5B with 10 deg Ramp Flap for 0, -10, -20, -40 and -90 deg (no flap) Flap Deflections

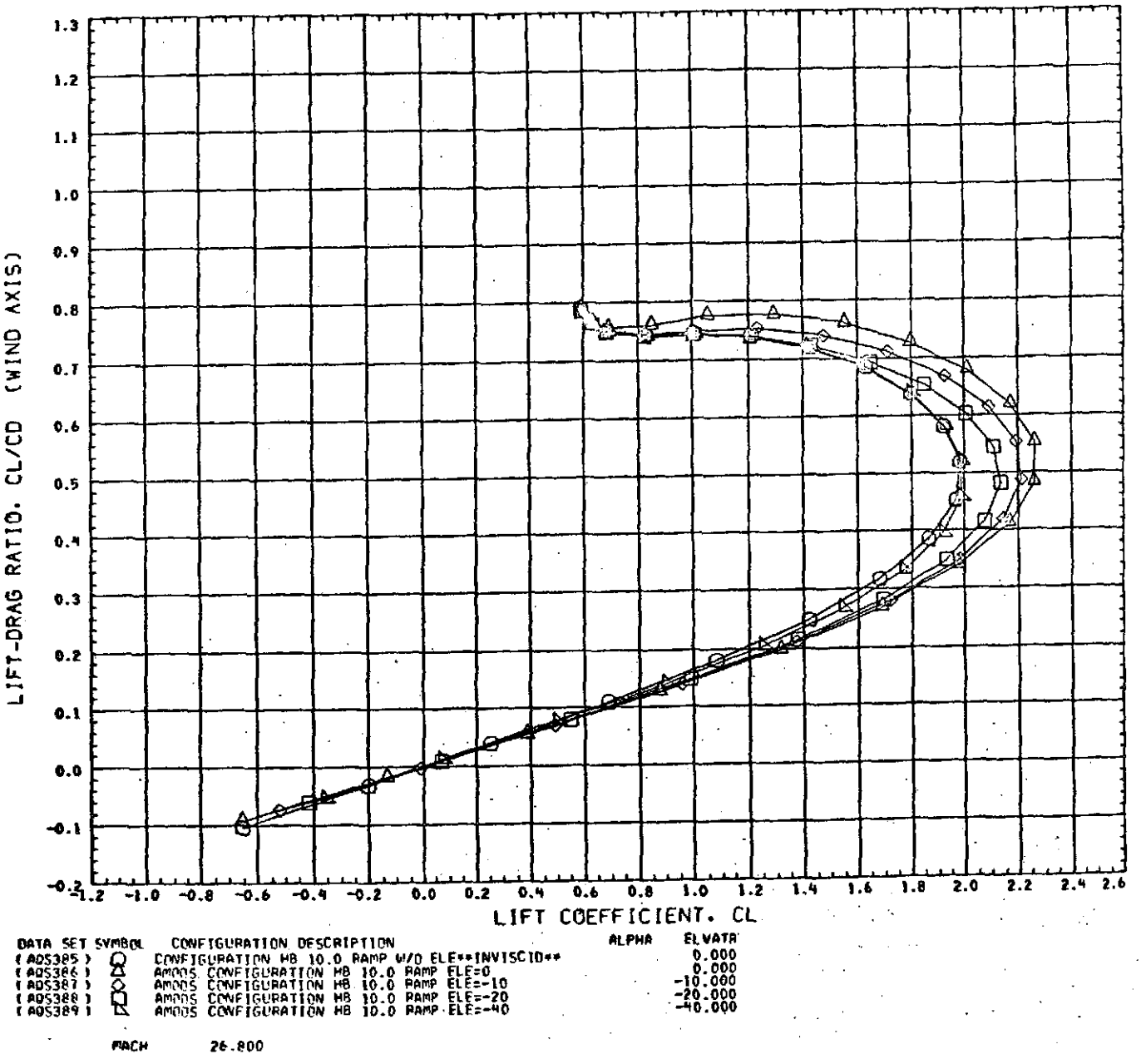

Fig. B-11 - Analytical Lift-to-Drag Ratio vs Lift Coefficient for HB with 10 deg Ramp Flap for 0, -10, -20, -40 and -90 deg (no flap) Flap Deflections

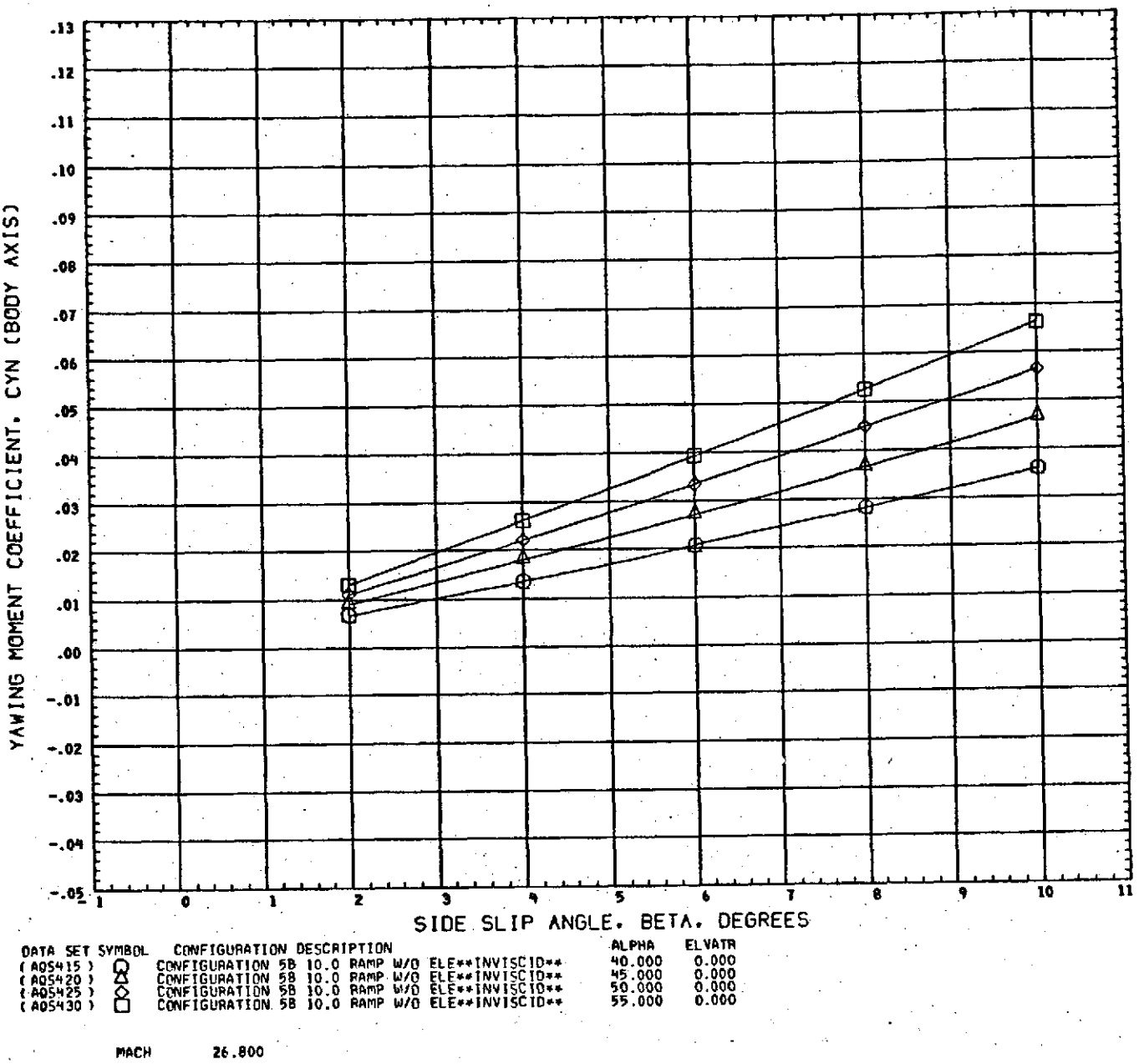

Fig. B-12 - Analytical Yawing Moment Coefficient vs Side Slip Angle with Angle of Attack as a Parameter for the 5B Configuration with a 10-Degree Ramp Flap Deflected -90 Degrees (no flap) and a Trim $X_{c.g.}$ of 45.8% ℓ_{ref}

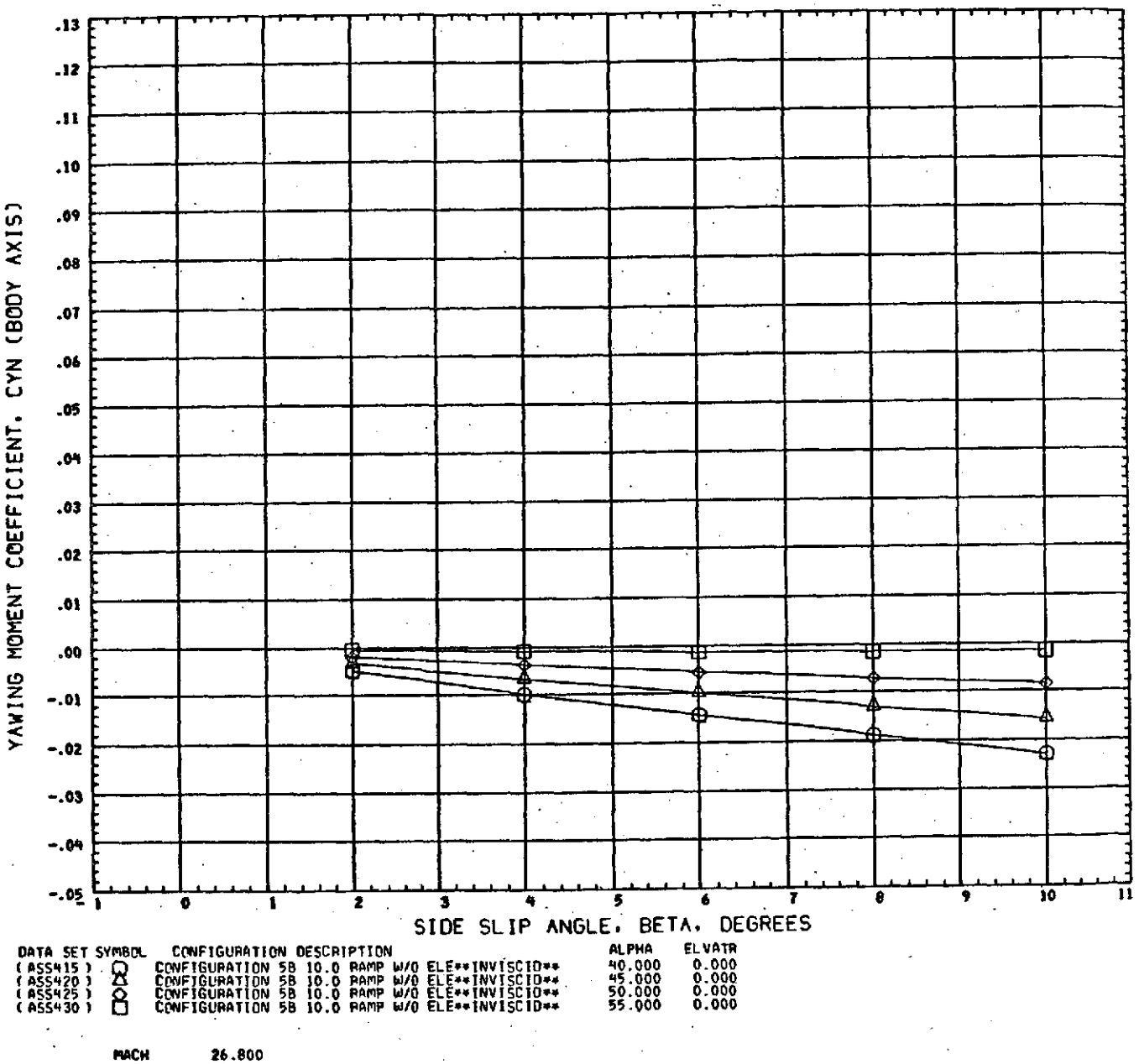

Fig. B-13 - Analytical Yawing Moment Coefficient vs Side Slip Angle with Angle of Attack as a Parameter for the 5B Configuration with a 10-Degree Ramp Flap Deflected -90 Degrees (no flap) and a Trim $X_{c.g.}$ of 53.0% ℓ_{ref}

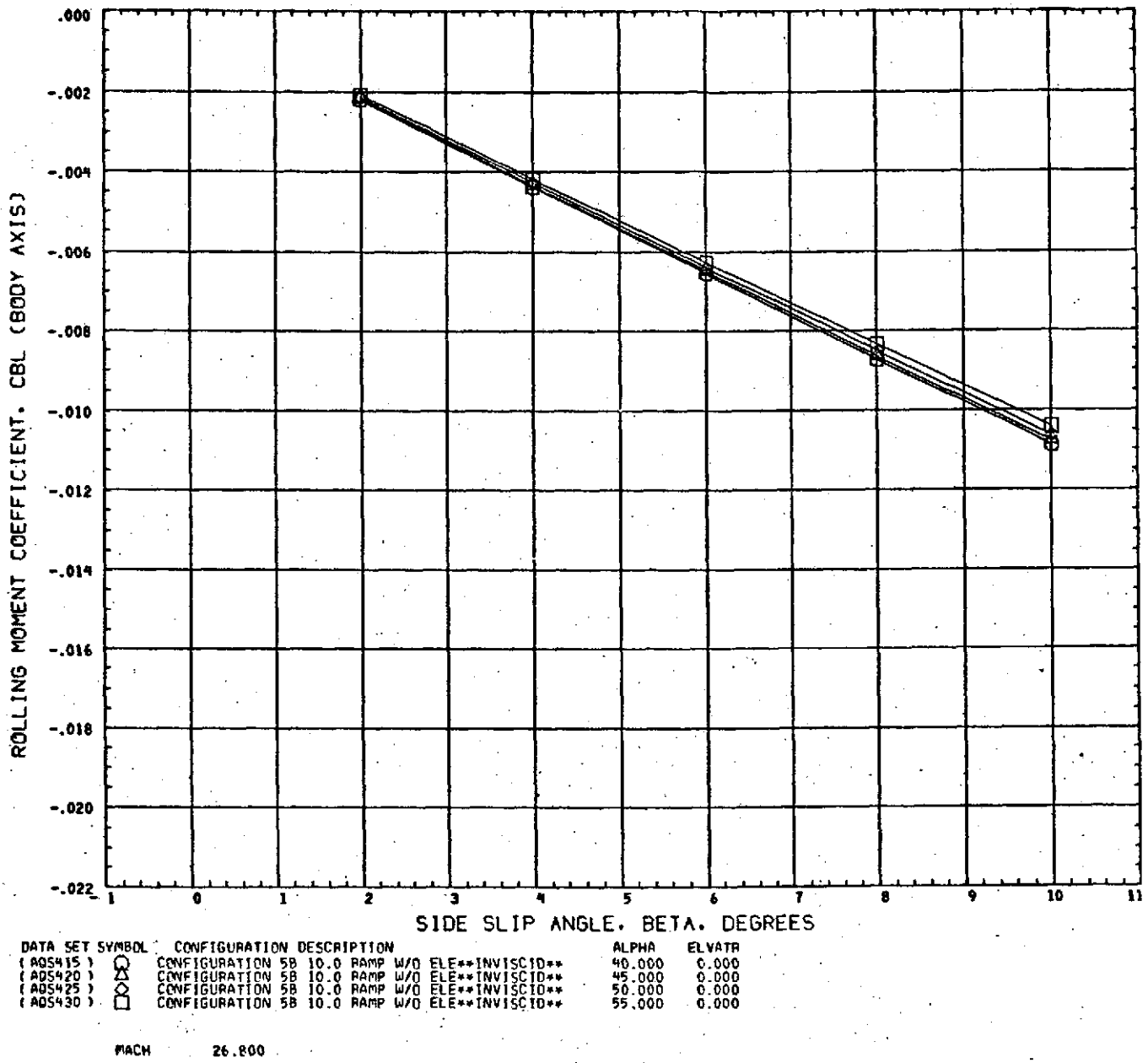

Fig. B-14 - Analytical Rolling Moment Coefficient vs Side Slip Angle with Angle of Attack as a Parameter for the 5B Configuration with a 10-Degree Ramp Flap Deflected -90 Degrees (no flap)

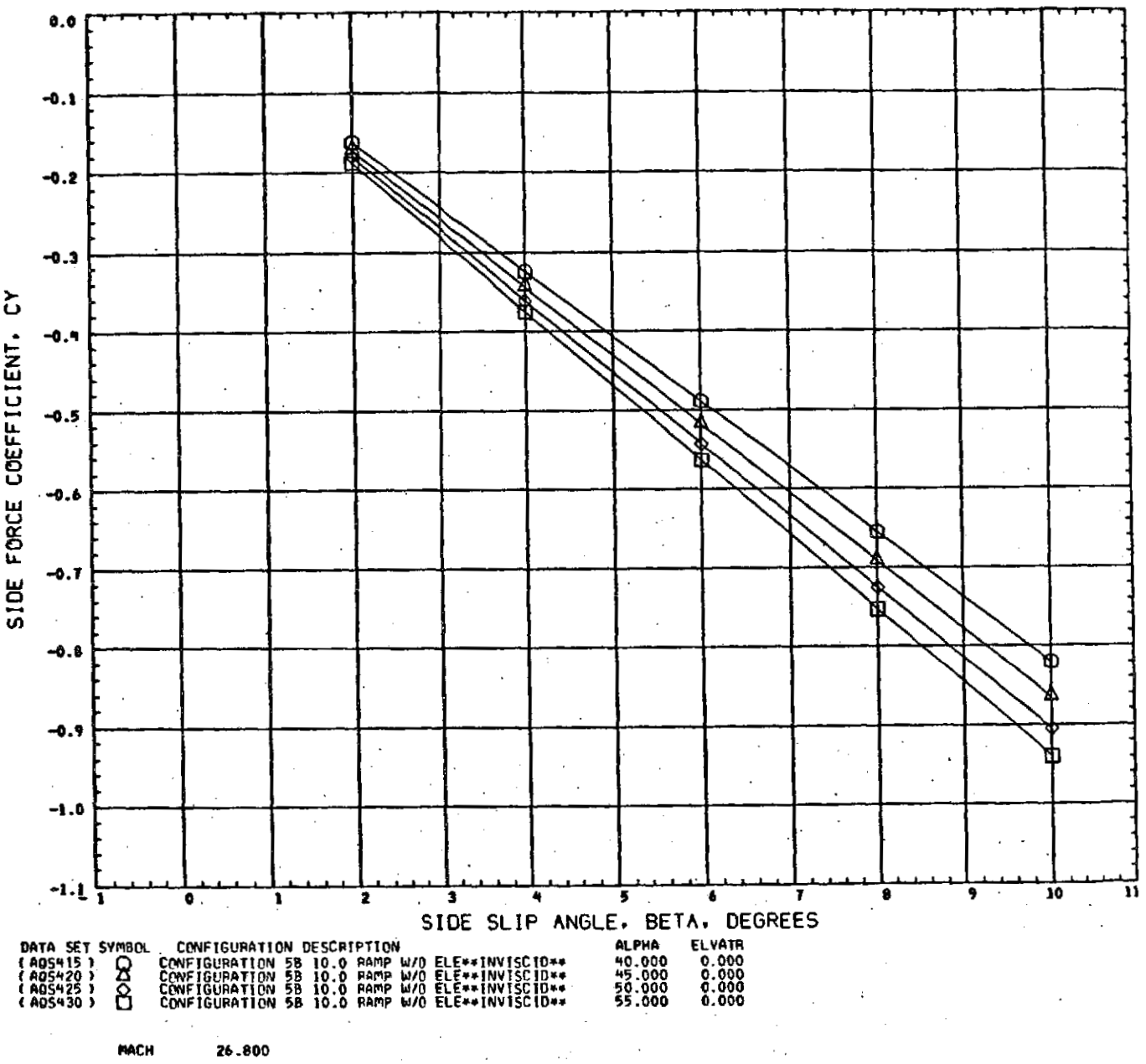

Fig. B-15 - Analytical Side Force Coefficient vs Side Slip Angle with Angle of Attack as a Parameter for the 5B Configuration with a 10-Degree Ramp Flap Deflected -90 Degrees (no flap)

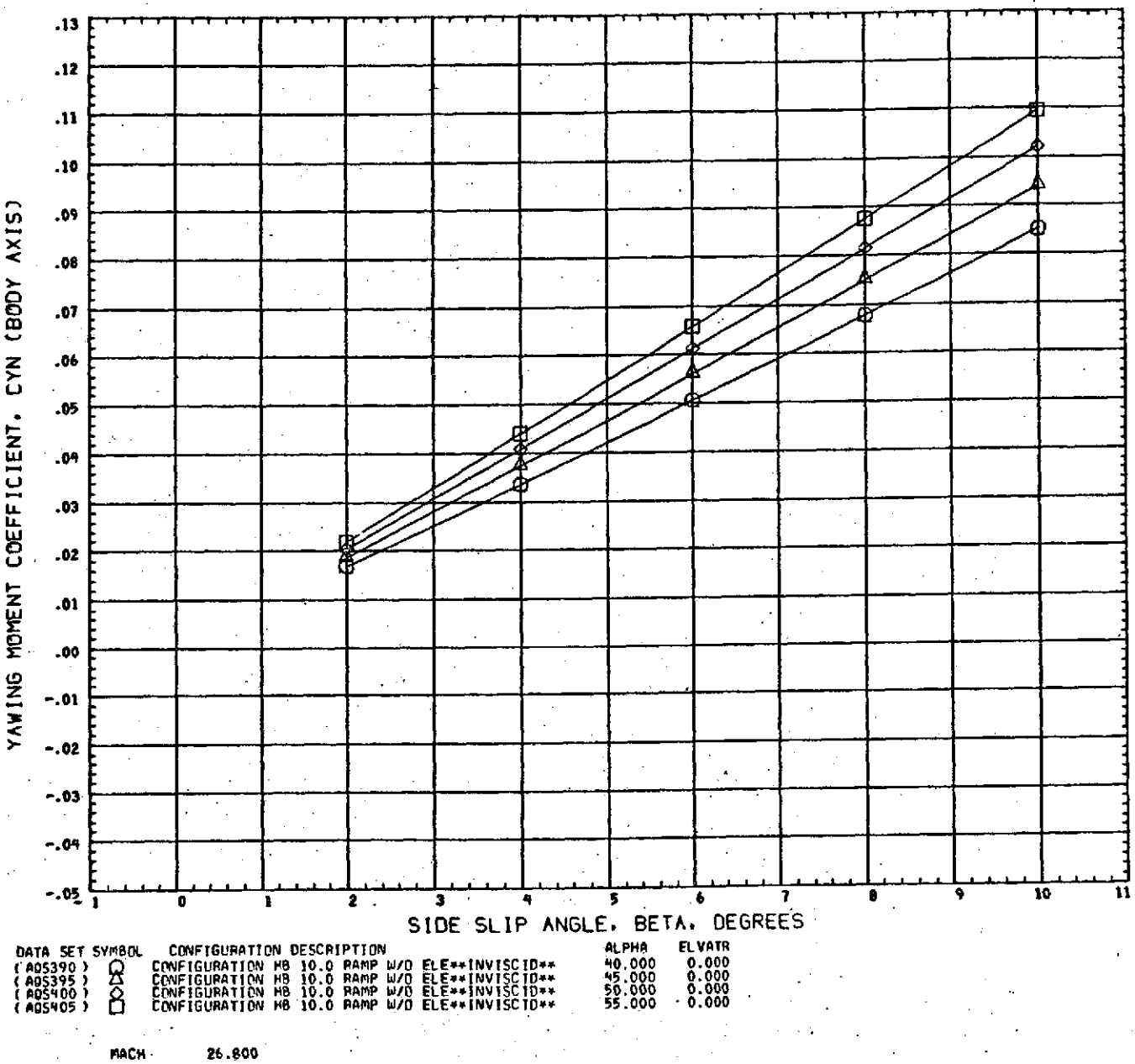

Fig. B-16 - Analytical Yawing Moment Coefficient vs Side Slip Angle with Angle of Attack as a Parameter for the HB Configuration with a 10-Degree Ramp Flap Deflected -90 Degrees (no flap) and a Trim $X_{c.g.}$ of 38.3% ℓ_{ref}

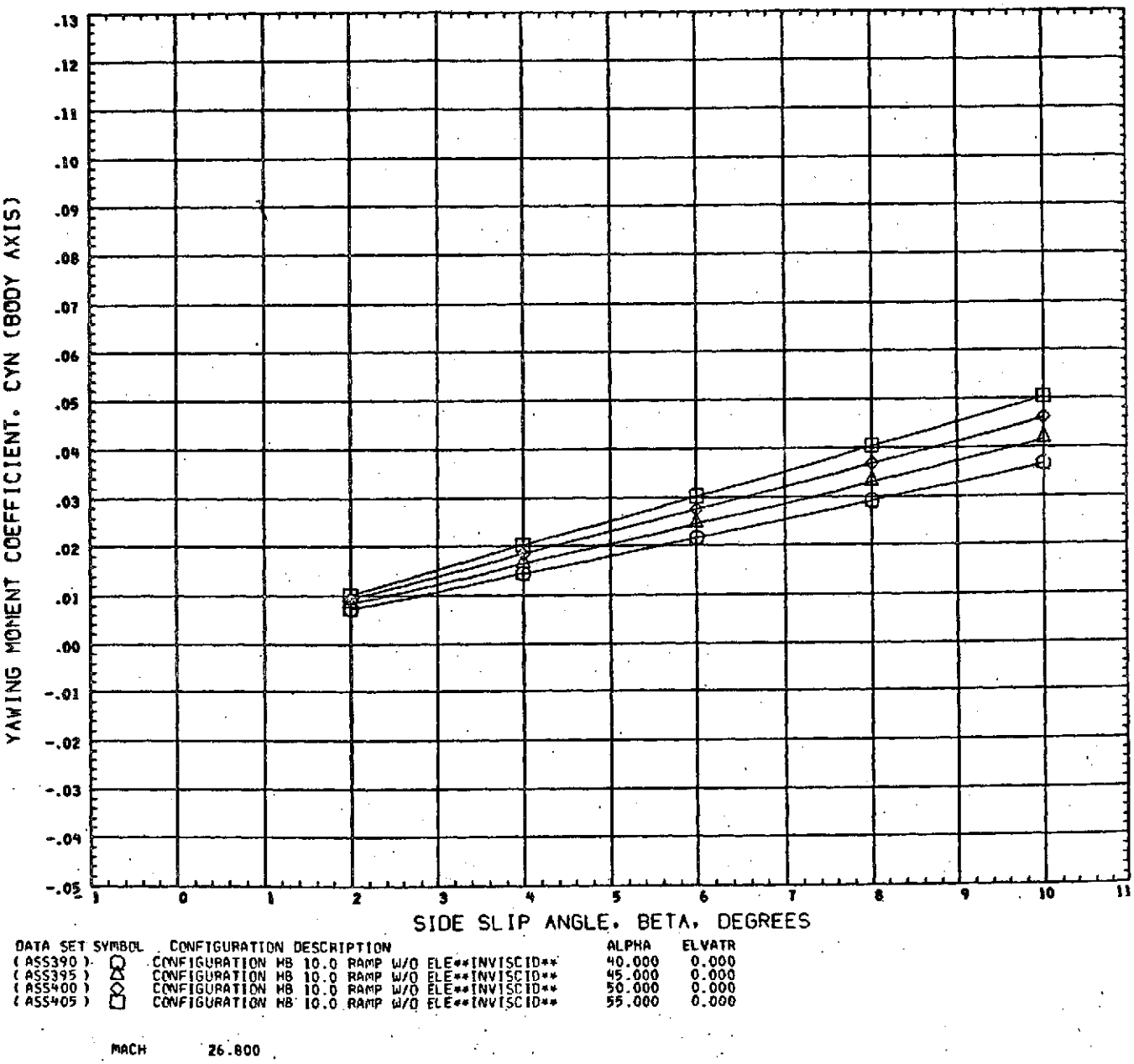

Fig. B-17 - Analytical Yawing Moment Coefficient vs Side Slip Angle with Angle of Attack as a Parameter for the HB Configuration with a 10-Degree Ramp Flap Deflected -90 Degrees (no flap) and a Trim $X_{c.g.}$ of 49.3% ℓ_{ref}

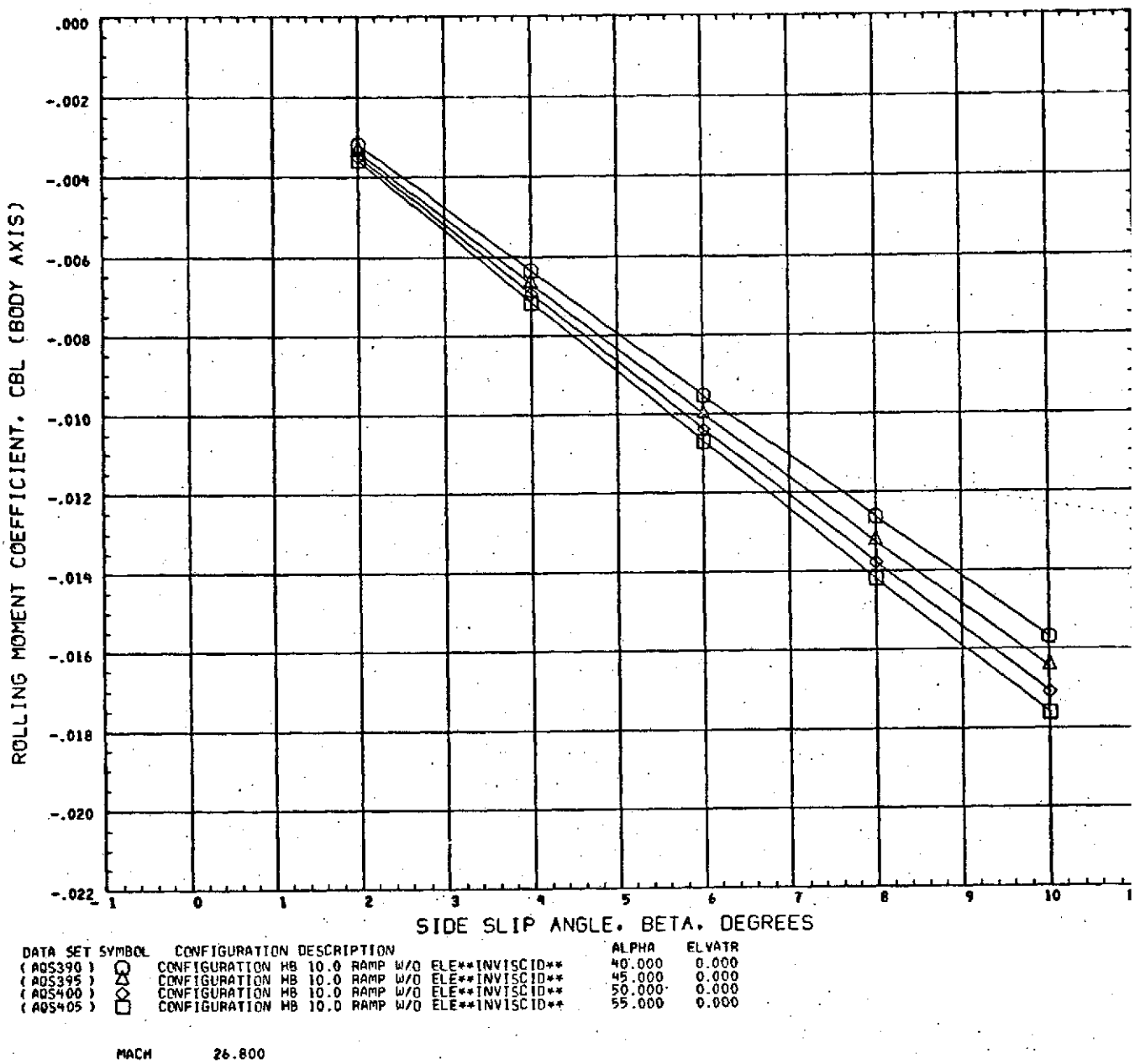

Fig. B-18 - Analytical Rolling Moment Coefficient vs Side Slip Angle with Angle of Attack as a Parameter for the HB Configuration with a 10-Degree Ramp Flap Deflected -90 Degrees (no flap)

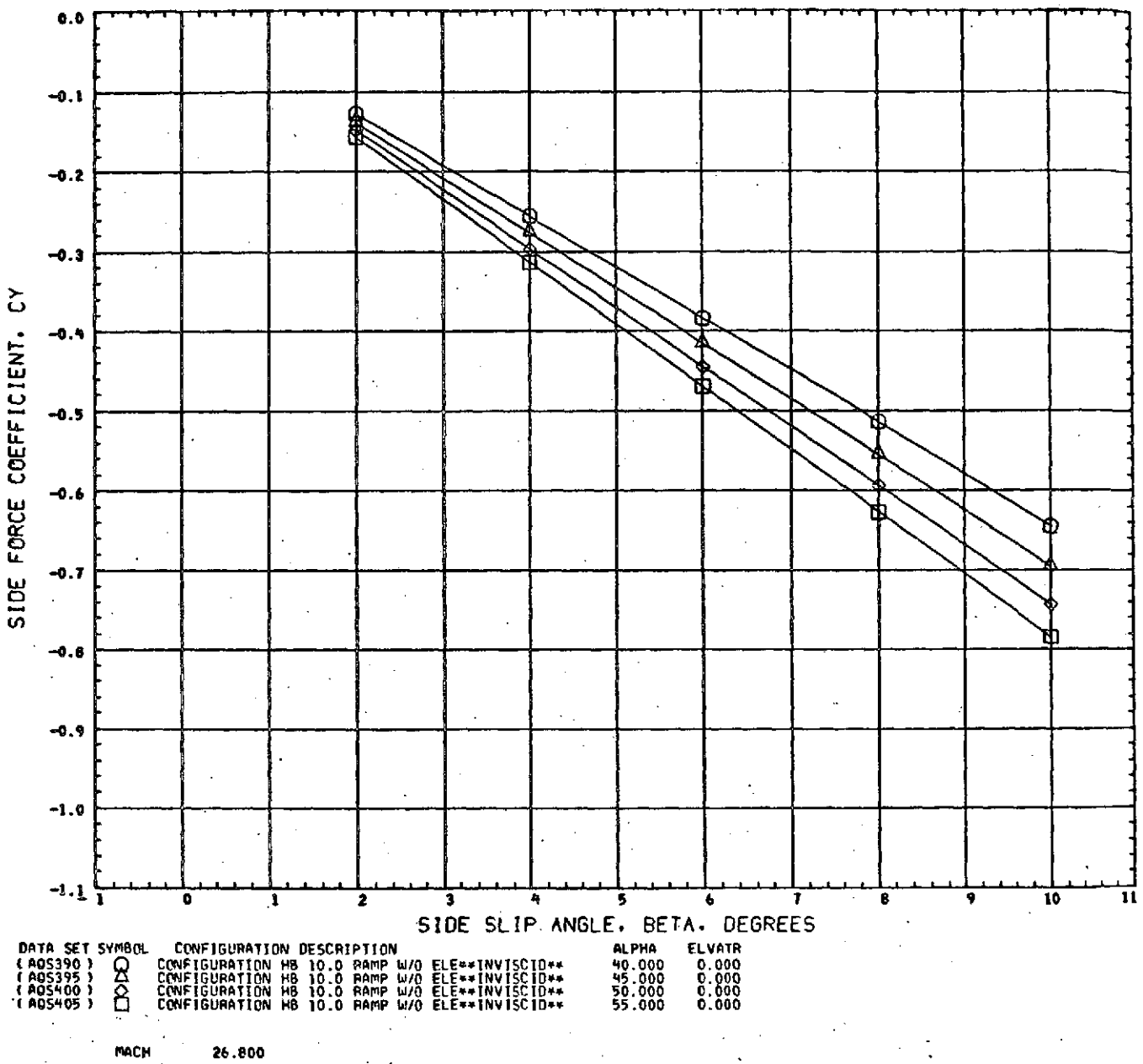

Fig. B-19 - Analytical Side Force Coefficient vs Side Slip Angle with Angle of Attack as a Parameter for the HB Configuration with a 10-Degree Ramp Flap Deflected -90 Degrees (no flap)

Appendix C

LOADS ANALYSIS, MATERIAL PROPERTIES AND STRUCTURAL DESIGN

Appendix C
NOMENCLATURE

Symbol	Description
A_{skin}	skin area (m^2, in^2)
A_{str}	stringer area (m^2, in^2)
b_s	stringer flange width (m, in)
d	stringer spacing (m, in)
E	material elastic modulus (N/m^2, lb/in^2)
F_{cr}	critical stress (N/m^2, lb/in^2
f	stress (N/m^2, lb/in^2)
g	acceleration factor
h_s	stringer web height (m, in)
ℓ	ring spacing (m, in)
ℓ_{cr}	stringer critical column length (m, in)
M	bending moment (N-m, in-lb)
N	axial line load (N/m, lb/in)
N_D	design line load (N/m, lb/in)
P	axial load (N, lb)
P_D	axial load per typical stringer spacing d (N, lb)
R	radius (m, in)
t	thickness (m, in)
t_s	stringer thickness (m, in)

NOMENCLATURE (Continued)

Greek	Description
μ	Poisson ratio
ρ	density (kg/m^3, lb/in^3)
σ	stress (kg/m^2, lb/in^2)

Appendix C

LOADS ANALYSIS

Loads analyses were performed to determine the critical bending moments and axial loads during AMOOS flight and transportation by the Space Shuttle. Aerodynamic normal and axial force distribution for a one-pass mission were obtained for the critical dynamic pressure and angle of attack. These aerodynamic force distributions for a dynamic pressure of 5920 N/m^2 for the 5B configuration and 5038 N/m^2 for the HB configuration are shown in Figs. C-1 and C-2, respectively. Using the mass distribution (Figs. C-3 and C-4) corresponding to the AMOOS reentry configuration the bending moment and axial force distributions were determined (Figs. C-5 and C-6). From these the maximum compressive limit load, N, in the shell body structure from aero forces was determined,

$$N = \frac{P}{2\pi R} + \frac{M}{\pi R^2}$$

The design load, N_D, equals $f \times N$ where the factor of safety $f = 1.25$.

The AMOOS mass distribution corresponding to the EOS flight configuration and the interface points in the Shuttle cargo bay were analyzed to obtain the AMOOS vehicle loads. The EOS payload g factors for the different flight phases are given in Table C-1. These factors were applied to the force distributions to obtain the maximum loads. The EOS orbiter end burn was the maximum condition. The factor of safety of 1.25 was applied to obtain the design load.

The EOS flight environment during orbiter end burn was the maximum load condition and was used to determine the required body shell cross-sectional properties. The design loads for the aero reentry and EOS orbiter end burn conditions are given in Table C-2.

MATERIAL PROPERTIES

Four candidate materials were selected for study for the AMOOS vehicles: (1) titanium, Ti-6Al-4V; (2) beryllium-38% aluminum, Be-38Al; (3) magnesium, HM21A-T8; and (4) graphite/polyimide, Gr/Pi. The first three are metallic materials and state-of-the-art while the fourth, Gr/Pi, is a non-metallic composite. Further development work needs to be performed for Gr/Pi, especially in the areas of fabrication and additional test data. Large size stiffened panels as would be required for AMOOS-type vehicles have not yet been fabricated using Gr/Pi. All four materials meet the 589°K (600°F) temperature requirement set for the body shell during AMOOS reentry.

Magnesium is not a high strength nor high modulus material when compared with the others. Since the AMOOS vehicle is a lightly loaded shell structure and cross sections were determined by local instability rather than material strength properties magnesium is competitive.

The material properties for the metallic materials for room temperature and 589°K (600°F) are given in Table C-3.

Data from structural tests on Gr/Pi specimens for a symmetrical $(0, \pm 45, 90)$ orientation are given in Table C-4 for HT-S/710 composites.

STRUCTURAL DESIGN

Typical structural cross-sections were determined from the maximum design load considering the following constraints: (1) standard skin gages were considered; (2) no skin gage less than .081 cm (0.032 inches) was used due to scraping the TPS for refurbishment; (3) uniform stringer spacing or constant number of stringers were maintained for each vehicle; and (4) skin buckling was not allowed.

A skin gage was assumed and the allowable stringer spacing for a minimum mass designed stiffened cylindrical shell was determined based on the design load N_D (Ref. C-1)

$$d \leq \sqrt{\frac{\pi^2 E t^3}{3(1-\mu^2) N_D}}$$

The critical skin buckling stress was then determined for this stringer spacing.

$$F_{cr} = \frac{4\pi^2 E}{12(1-\mu^2)} (t/d)^2$$

The total axial load P_D for the typical stringer spacing was determined by

$$P_D = N_D(d)$$

From this load the required stringer area, A_{str}, to prevent the panel skin from buckling is determined using

$$A_{str} = P/F_{cr} - A_{skin}$$

Skin buckling is not allowed since this would cause failure in the TPS bond. A channel section stringer is determined based on the required area. The flanges and web buckling stresses are computed to be sure positive margins of safety exist.

$$F_{cr_{flange}} = \frac{1.27\pi^2 E}{12(1-\mu^2)} (t_s/b_s)^2$$

$$F_{cr_{web}} = \frac{5.42\pi^2 E}{12(1-\mu^2)} (t_s/h_s)^2$$

The critical ring spacing was determined by Euler's column buckling equation

$$\ell_{cr} = \rho \sqrt{\pi^2 E/F_{cr}}$$

where F_{cr} is the skin buckling stress. Ring size was determined by the method presented in Ref. C-1.

Each AMOOS vehicle configuration consisted of a forward body section and an aft body section. The forward section contained the LOX and LH_2 tanks and experienced heavier loads than did the aft section. The aft section consisted of the payload bay and engine. Different skin gages were determined for each section based on their respective loadings. A common stringer spacing or constant number of stringers was determined based on the minimum spacing of the two sections and the skin gages optimized for this spacing.

The primary structural weights for the candidate materials were determined in this method. These masses are presented in Table C-5. Since the mass for the 5B and HB configurations are approximately the same, only the 5B values were determined for all materials. The mass values do not represent the optimum weight structures but does prove that the AMOOS vehicle is practical and is well within the dry mass constraints for this vehicle. A 5% mass increase was added to the calculated value to include mass due to fasteners, local increases at tank supports, etc.

REFERENCE

C-1. Block, D.L., "Minimum Weight Design of Axially Compressed Ring and Stringer Stiffened Cylindrical Shells," AIAA 9th Aerospace Sciences Meeting, Paper No. 71-147.

Table C-1

SHUTTLE PAYLOAD BAY LIMIT LOAD FACTORS

Condition*	(Long. (+ Rear) X	Lat. (+ Rt) Y	Vert. (+ Up) Z
Liftoff***	-1.7 ± 0.6	±0.3	-0.8
			-0.2
High Q Boost	-1.9	±0.2	+0.2
			-0.5
Booster End Burn	-3.0 ± 0.3	±0.2	-0.4
Orbiter End Burn	-3.0 ± 0.3	±0.2	-0.5
Space Operations	-0.2	±0.1	±0.1
	+0.1		
Entry	±0.25	±0.5	+3.0
			-1.0
Subsonic Maneuvering	±0.25	±0.5	+2.5
			-1.0
Landing and Braking	±1.5	±1.5	+2.5
Crash**	+9.0	±1.5	+4.5
	-1.5		-2.0

*Positive X, Y, Z directions equal aft, right and up. Load factor carries the sign of the externally applied load.

**Crash load factors are ultimate and only used to design payload support fittings and payload attachment fasteners. Crash load factors for the nominal payload of 29,485 kg (65,000 lb). Longitudinal load factors are directed in the forward azimuth within 20 deg of the orbiter longitudinal axis. The specified load factors shall operate separately.

***These factors include dynamic transient load factors at liftoff.

Table C-2

AMOOS DESIGN AXIAL LINE LOADS

	5B		HB	
	Aero	EOS	Aero	EOS
Fwd Body	1786 (100)	6679 (374)	2286 (128)	4589 (257)
Aft Body	1786 (100)	3947 (221)	1500 (84)	1696 (95)

Note: Load in N/m (lb/in).

Table C-3
MATERIAL PROPERTIES

Mechanical Properties Basis	Titanium T_i - 6 Al - 4V (Sheet, Annealed) A	Beryllium-Aluminum Be-38 Al (Sheet, Annealed) A	Magnesium HM 21A-T8 (Sheet) A
F_{tu}, MN/m^2 (ksi):			
294°K (70°F)	924 (134)	303 (44)	228 (33)
589°K (600°F)	724 (105)	179 (26)	76 (11)
F_{ty}, MN/m^2 (ksi):			
294°K (70°F)	869 (126)	214 (31)	124 (18)
589°K (600°F)	586 (85)	152 (22)	55 (8)
F_{cy}, MN/m^2 (ksi):			
294°K (70°F)	910 (132)	193 (28)	103 (15)
589°K (600°F)	921 (90)	124 (18)	69 (10)
F_{su}, MN/m^2 (ksi):			
294°K (70°F)	545 (79)	159 (23)	145 (21)
589°K (600°F)	400 (58)	97 (14)	48 (7)
E, GN/m^2 (10^3 ksi:)			
294°K (70°F)	110 (16)	193 (28)	45 (6.5)
589°K (600°F)	90 (13)	172 (25)	36 (5.2)
μ	.31	.14	.35
Physical Properties			
ρ, kg/m^3 (lb/in^3)	4430(.16)	2080(.075)	1770(.064)

Ref: Ti-6Al-4V, MIL-HDBK-5, Sept. 1971
Be-38Al, LMSC Report 679606, Oct. 17, 1967
HM 21A, MIL-HDBK-5, Sept. 1971

Table C-4

DESIGN PROPERTIES OF HT-S/710 COMPOSITES (0, ± 45 DEGREES, 90)
(GRAPHITE/POLYIMIDE)

Test Temperature °K (°F)	Post-cure Cycle	Laminate Orientation (deg)	Test Orientation (deg)	Tensile Strength MN/m² (ksi)	Tensile Modulus GN/m² (psi×10⁶)	Strain to Failure (in./in.×10⁻⁶)	Compression Strength MN/m² (ksi)	Compression Modulus GN/m² (psi×10⁶)	Strain to Failure (in./in.×10⁻⁶)	Flexural Strength MN/m² (ksi)	Flexural Modulus GN/m² (psi×10⁶)	Short Beam Shear Strength MN/m² (ksi)
77 (-320)	1	$(0, \pm 45, 90)_{2s}$	0	346 (50.4)	33 (4.8)	(4200)	444 (63.9)	56.7 (8.22)	(8900)	353 (50.6)	29.4 (4.26)	25.5 (3.70)
				290 (42.0)	59 (8.5)	-	423 (61.4)	55.3 (8.02)	(9600)	367 (53.2)	27.9 (4.04)	30.5 (4.42)
				311 (45.0)	68 (9.9)	-	367 (53.2)	46.4 (6.73)		388 (56.3)	30.1 (4.36)	33.5 (4.5)
				304 (43.8)	66 (9.6)	-	325 (47.0)	34.9 (5.07)	(10500)	304 (44.1)	- -	20.8 (3.02)
				262 (38.4)	47 (6.8)	-	339 (49.2)	61.2 (8.88)	(9800)	339 (48.9)	- -	24.4 (3.54)
				290 (41.7)	43 (6.3)	-	360 (52.2)	56.6 (8.20)	(10400)	367 (52.6)	28.8 (4.18)	23.2 (3.36)
			Average	301 (43.6)	53 (7.7)	(4200)	376 (54.5)	51.8 (7.52)	(9800)	353 (51.0)	29.1 (4.22)	25.3 (3.62)
297 (75)	1	$(0 \pm 45, 90)_{2s}$	0	276 (39.6)	53 (7.7)	-	374 (53.7)	60.0 (8.70)	(6700)	458 (65.5)	25.2 (3.66)	23.2 (3.37)
				283 (40.9)	59 (8.5)	(3140)	353 (51.4)	60.2 (8.73)	(7600)	388 (55.7)	24.1 (3.50)	24.5 (3.55)
				297 (43.2)	59 (8.6)	(5200)	360 (51.8)	53.5 (7.76)	(7700)	367 (52.9)	24.8 (3.59)	26.7 (3.88)
				339 (48.9)	66 (9.6)	(5320)	304 (43.7)	59.2 (8.58)	(7900)	353 (50.9)	24.5 (3.55)	19.7 (2.86)
				311 (44.7)	50 (7.2)	(7660)	311 (45.1)	46.5 (6.74)	(8200)	353 (51.3)	24.0 (3.48)	19.7 (2.85)
				283 (41.4)	57 (8.2)	(4200)	283 (41.0)	48.8 (7.07)	(7800)	402 (58.4)	26.2 (3.80)	19.3 (2.80)
			Average	298 (43.1)	57 (8.3)	(5100)	331 (47.8)	54.7 (7.93)	(7700)	387 (55.8)	24.8 (3.60)	21.9 (3.17)
589 (600)	1	$(0, \pm 45, 90)_{2s}$	0	374 (53.5)	48 (7.0)	(6620)	283 (41.1)	24.6 (3.57)	(11600)	283 (41.0)	17.7 (2.56)	20.7 (3.00)
				325 (46.9)	46 (6.6)	(6600)	255 (37.2)	24.3 (3.53)	(9300)	227 (33.1)	16.1 (2.34)	21.7 (3.14)
				318 (46.3)	46 (6.6)	(5950)	234 (34.4)	24.8 (3.60)	(9700)	255 (37.0)	15.5 (2.25)	21.1 (3.06)
				325 (47.2)	42 (6.1)	(7320)	241 (35.0)	25.4 (3.68)	(10200)	255 (36.6)	17.6 (2.55)	23.9 (3.46)
				290 (42.3)	66 (9.5)	(5040)	262 (37.5)	22.9 (3.33)	(12100)	311 (44.5)	- -	22.3 (3.24)
				304 (43.9)	48 (6.9)	(5660)	255 (37.2)	21.2 (3.04)	(11600)	290 (42.4)	- -	21.2 (3.13)
			Average	323 (46.7)	49 (7.1)	(6200)	255 (37.1)	23.9 (3.46)	(10800)	270 (39.1)	16.8 (2.43)	21.9 (3.17)
297 (75)	2	$(0, \pm 45, 90)_{2s}$	0	332 (48.4)	70 (10.2)	(4400)	360 (51.9)	66 (9.6)	(7890)	318 (46.3)	32.4 (4.70)	22.3 (3.24)
				290 (42.1)	50 (7.2)	(4800)	395 (57.0)	55 (8.0)	(10000)	297 (43.1)	28.3 (4.10)	26.1 (3.78)
				339 (49.3)	74 (10.8)	(4800)	332 (48.0)	58 (8.4)	(8220)	290 (41.5)	26.9 (3.90)	24.6 (3.56)
				269 (39.2)	51 (7.4)	(5900)	332 (47.5)	54 (7.9)	(10000)	276 (39.8)	22.3 (3.23)	31.5 (4.57)
				283 (41.4)	66 (9.6)	(6100)	332 (47.9)	41.1 (6.0)	(11550)	234 (34.1)	23.4 (3.40)	37.7 (5.47)
				339 (49.3)	48 (6.9)	(4000)	381 (54.6)	43.3 (6.3)	(11100)	283 (41.0)	21.0 (3.05)	35.6 (5.16)
			Average	309 (45.0)	60 (8.7)	(5000)	355 (51.2)	53 (7.7)	(11300)	283 (41.0)	25.7 (3.73)	29.6 (4.30)

Table C-5

PRIMARY STRUCTURE DRY MASS

Material	5B	HB
Titanium	2165 kg (4774 lb)	
Beryllium-Aluminum	1158 kg (2548 lb)	1052 kg (2320 lb)
Magnesium	1168 kg (2574 lb)	
Graphite/Polyimide	1888 kg (4162 lb)	

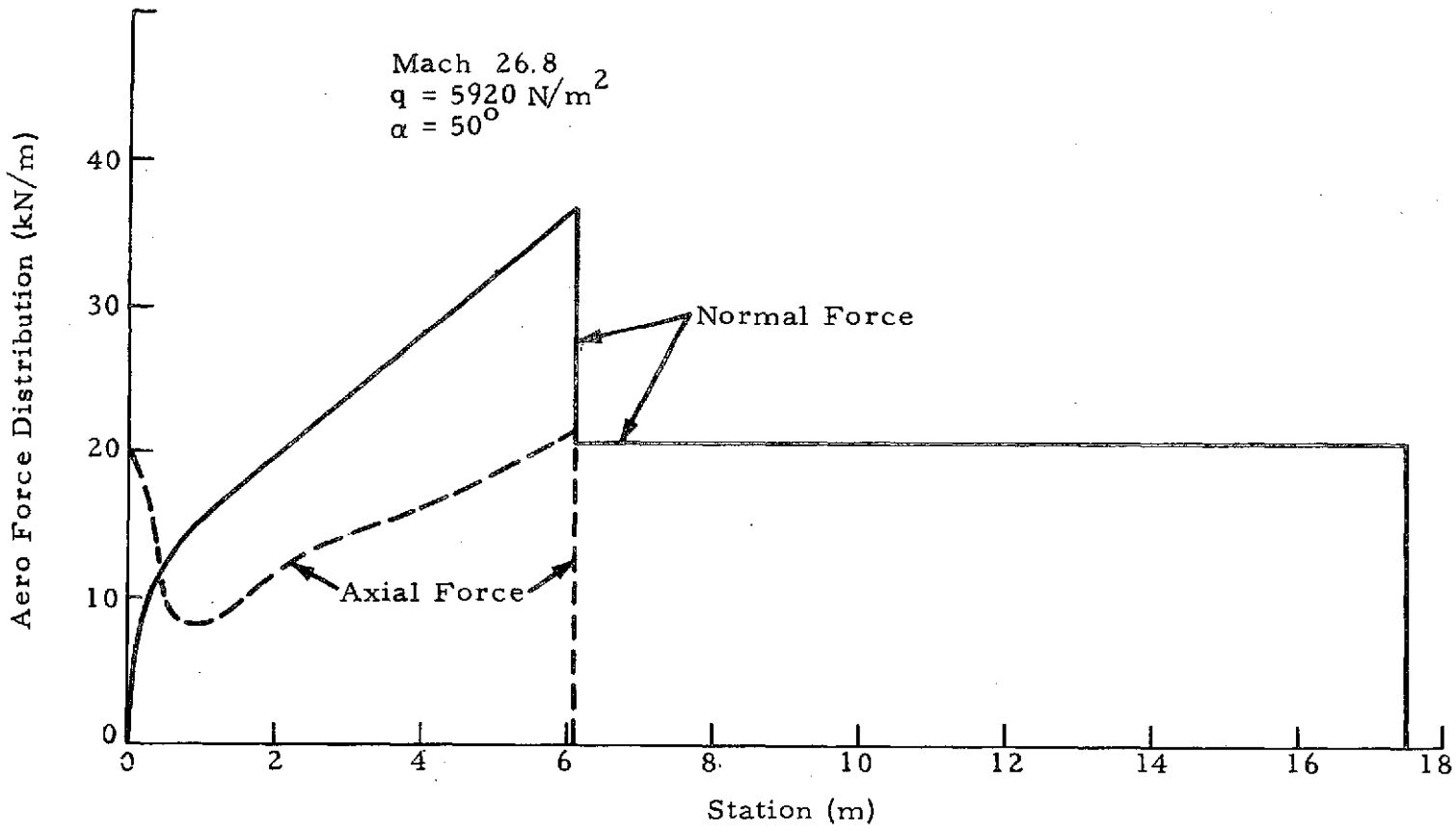

Fig. C-1 - Aerodynamic Force Distribution for the AMOOS 5B Configuration

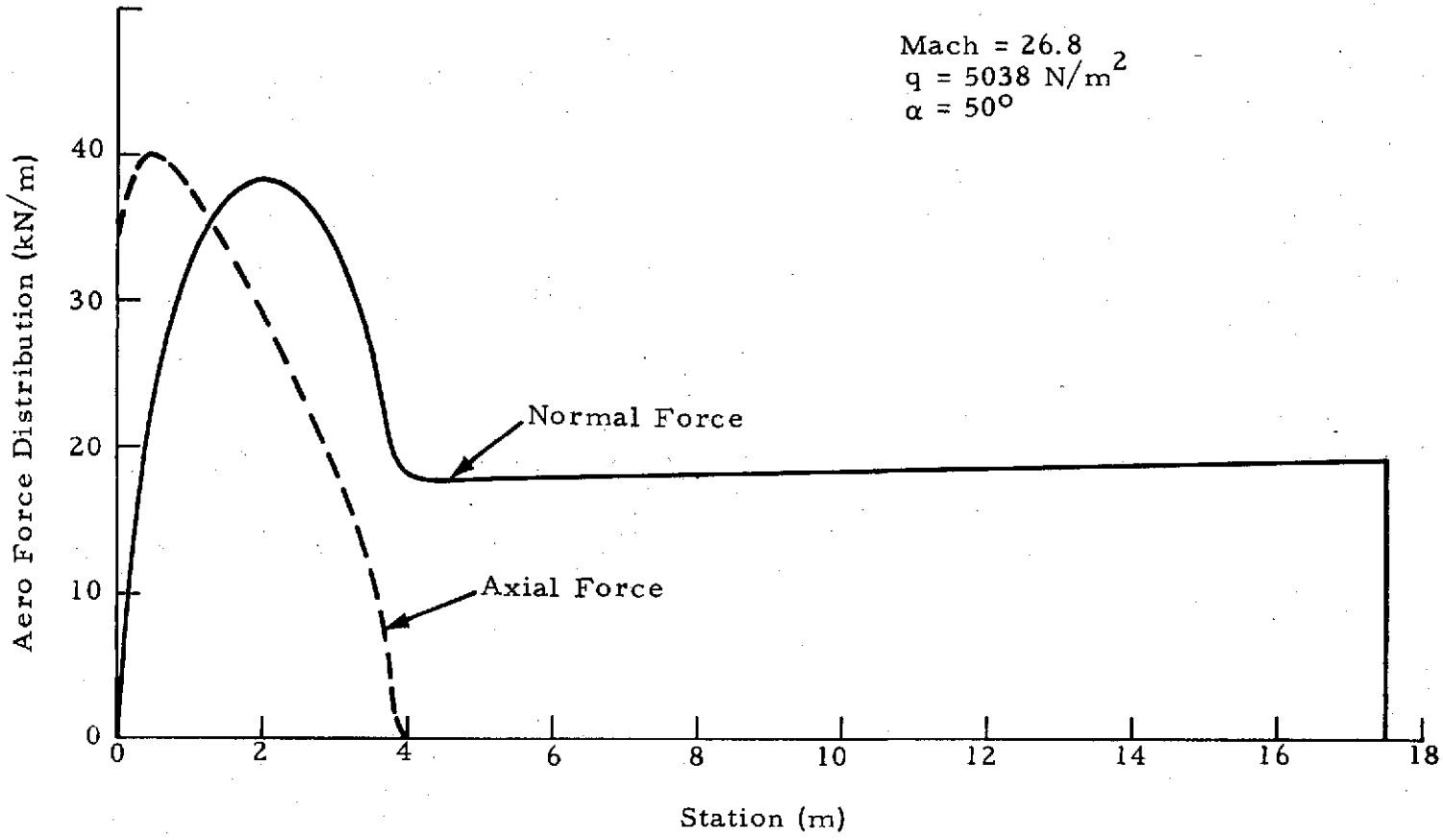

Fig. C-2 - Aerodynamic Force Distribution for the AMOOS HB Configuration

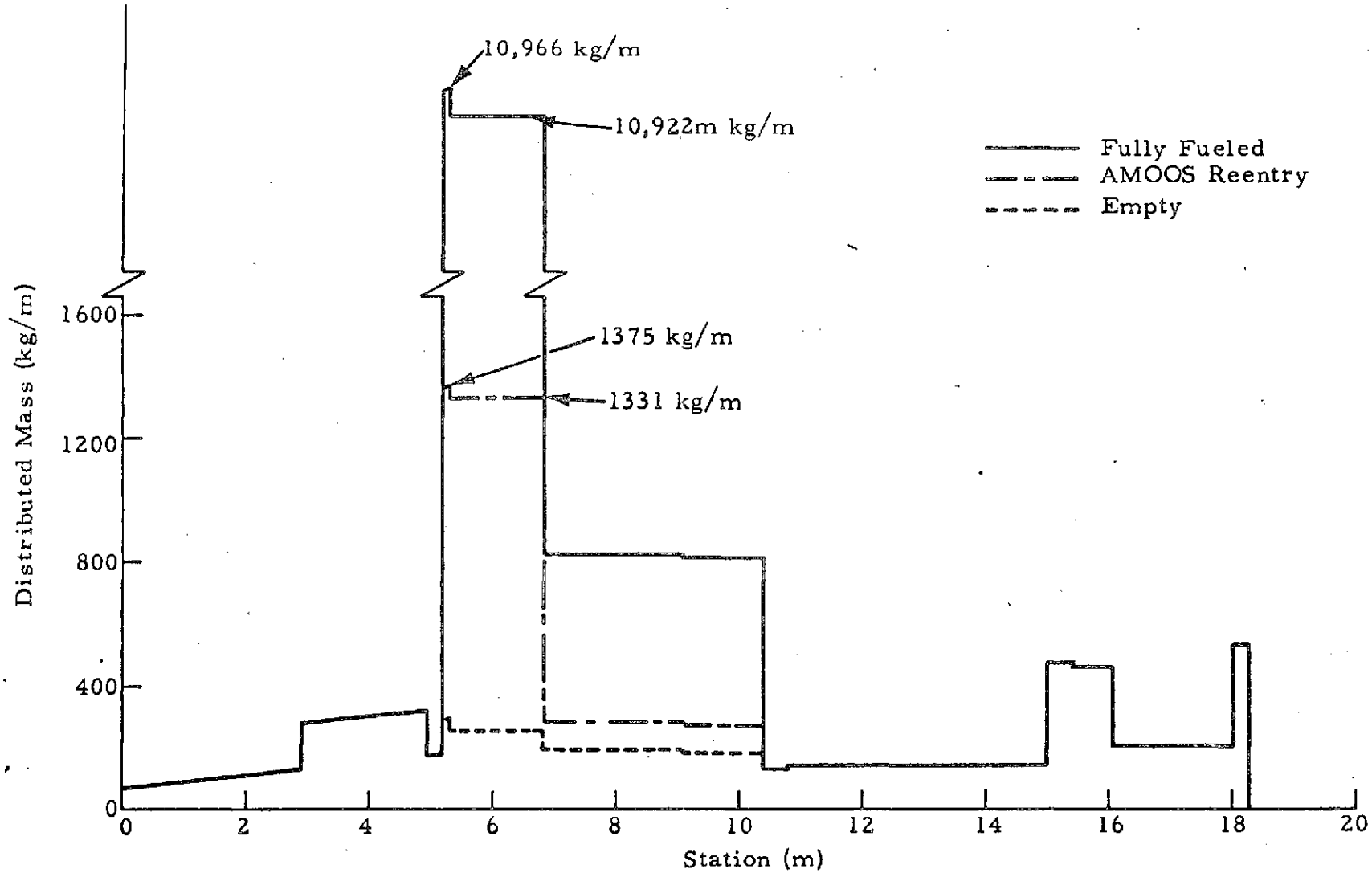

Fig. C-3 - AMOOS 5B Distributed Mass

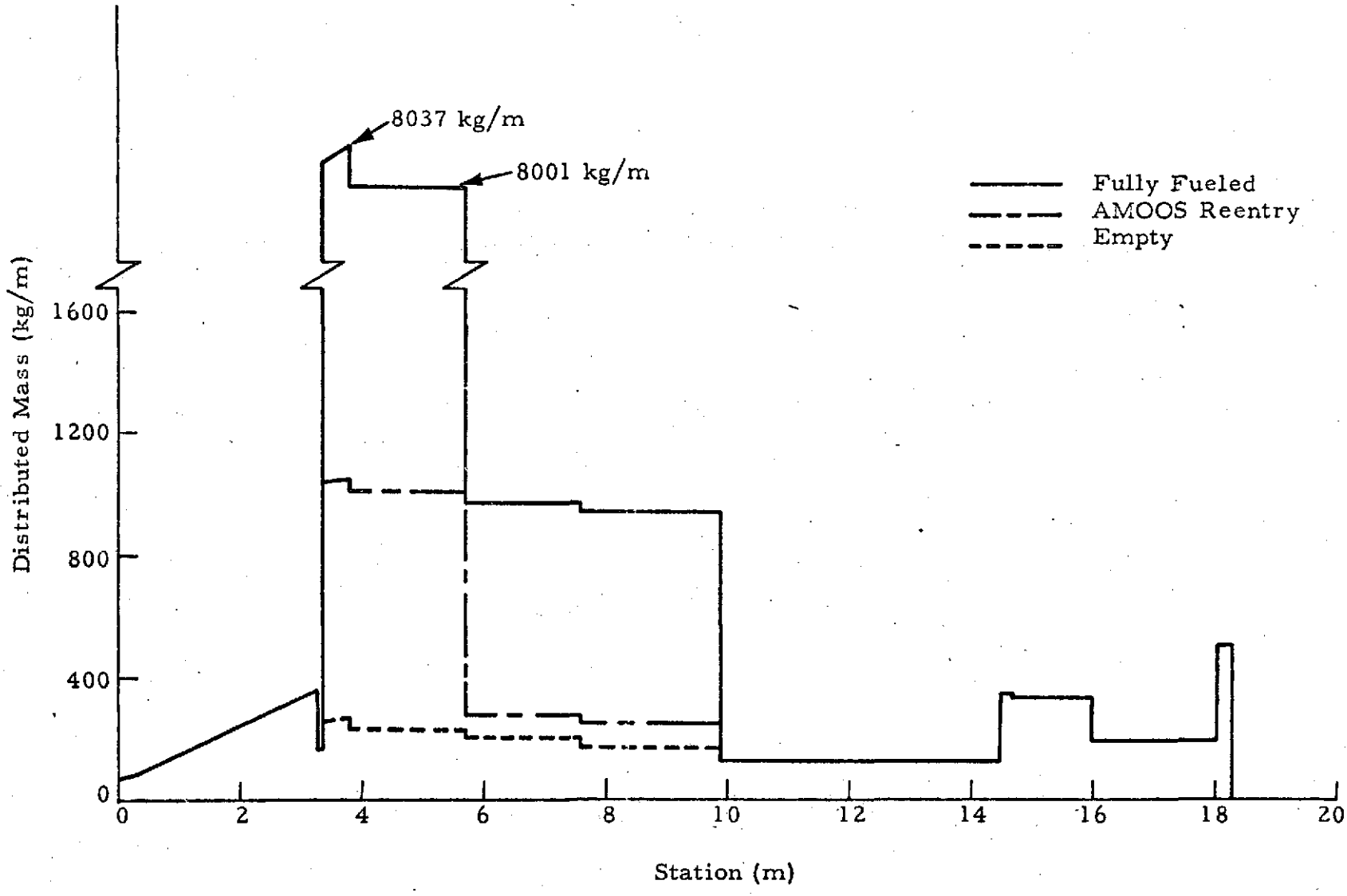

Fig. C-4 - AMOOS HB Distributed Mass

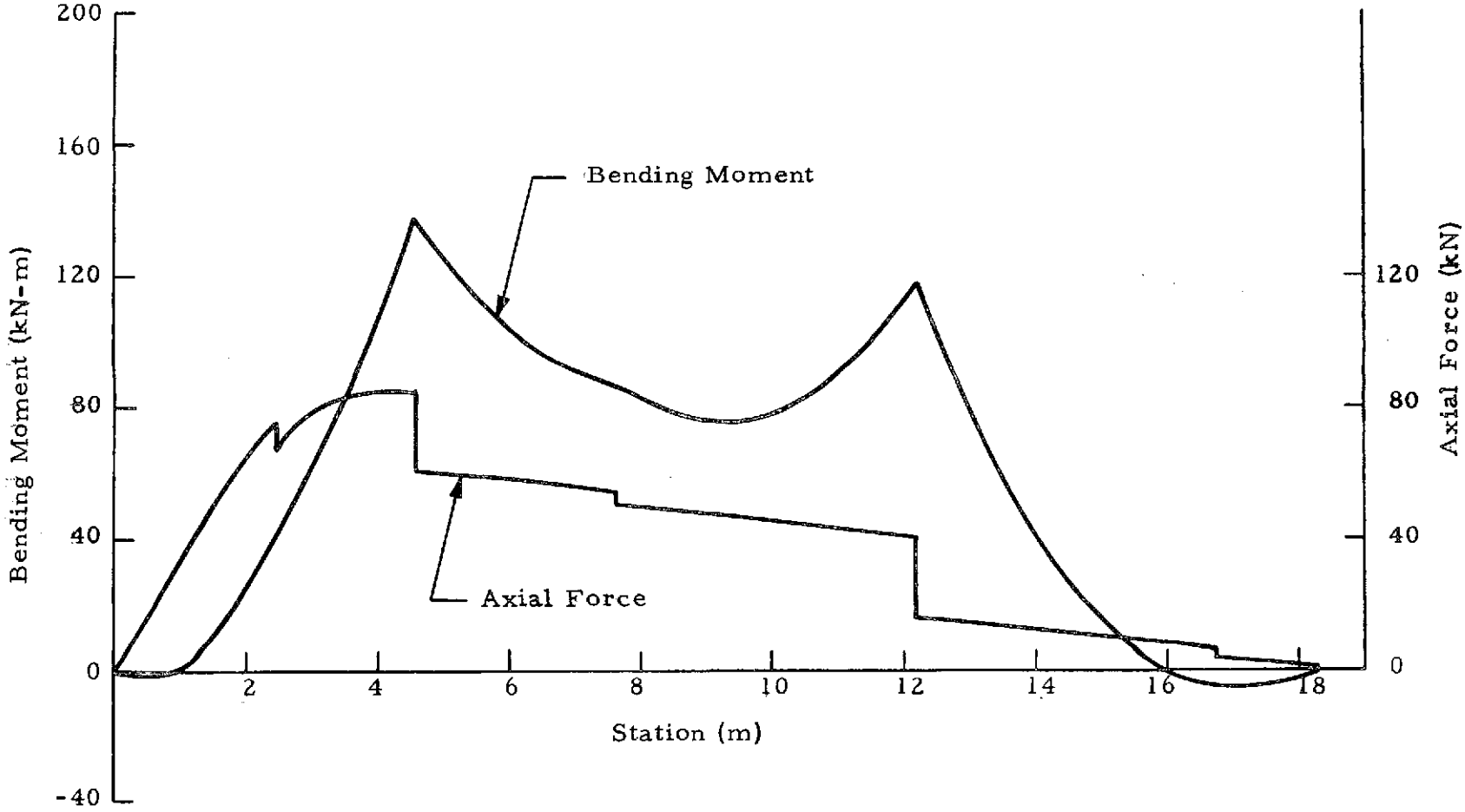

Fig. C-5 - AMOOS HB Reentry Force Distribution

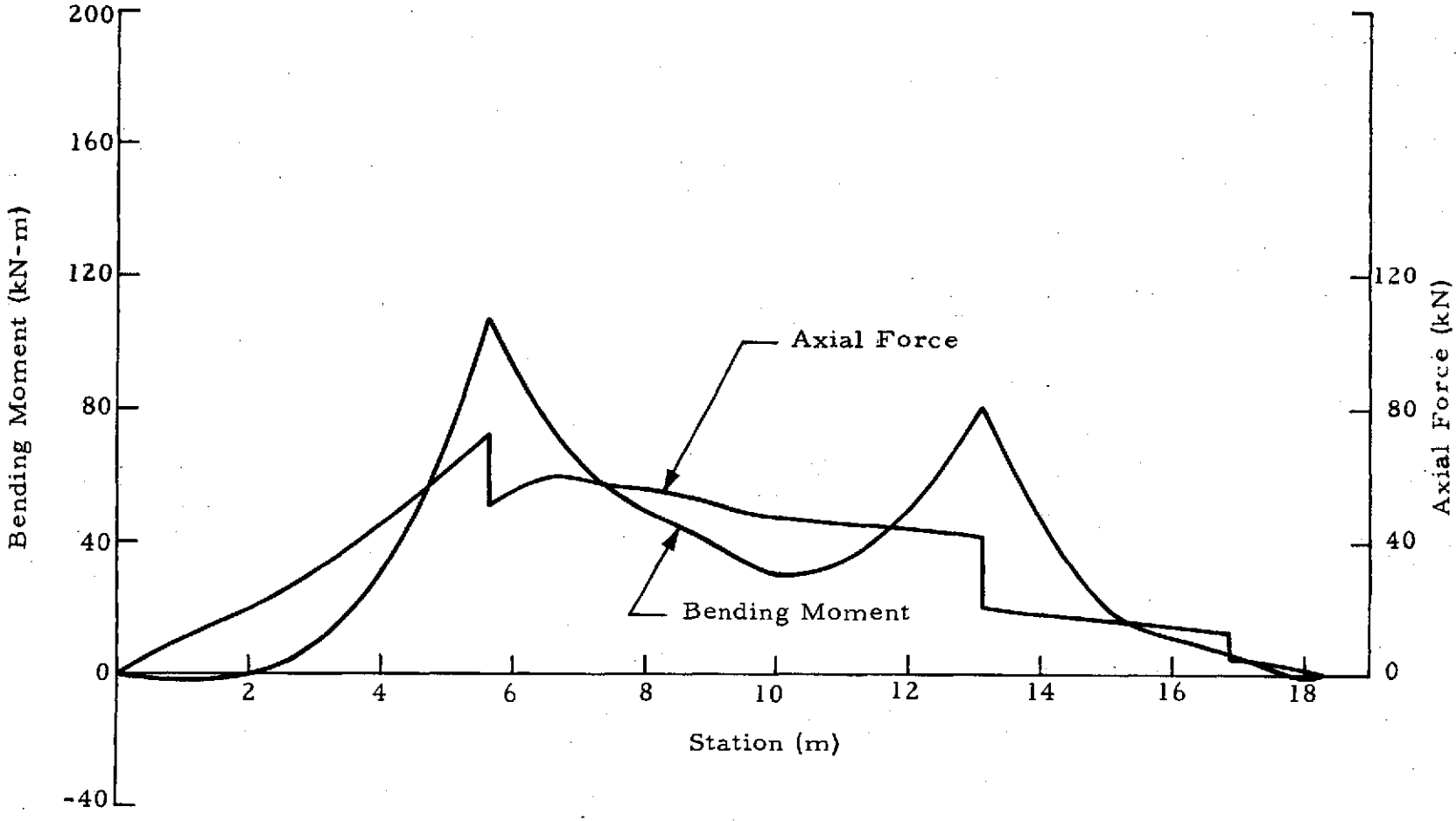

Fig. C-6 - AMOOS 5B Reentry Force Distribution

Appendix D

THERMODYNAMICS

Appendix D
NOMENCLATURE

Symbol	Description
C_*	$\mu_r T/\mu T_r$ defined for specific geometries in Tables D-1 and D-3 dimensionless
C_H	Stanton Number, $q/(\rho_\infty U_\infty (H_\infty - H_W))$ dimensionless
H	Total enthalpy, (J/kg, Btu/lbm)
K	Thermal conductivity (W/m-$^\circ$K, Btu/ft-sec-$^\circ$R)
M	Mach number, dimensionless
q	Convective heat transfer rate, (W/m^2, Btu/ft^2-sec)
R	Local body radius, (ft, m)
Re_∞	Free stream Reynolds number, $\rho_\infty U_\infty R/\mu_\infty$, dimensionless
$\tilde{Re}$	Post shock Reynolds number, $\rho_\infty U_\infty R/\mu_\delta = \rho_\delta U_\delta R/\mu_\delta$, dimensionless
T	Temperature, ($^\circ$K, $^\circ$R)
U_∞	Free stream velocity, (m/s, ft/s)
x	Surface distance, (m, ft)
Greek	
γ	Ratio of specific heats, dimensionless
θ	Local body angle with respect to free stream velocity vector, deg
θ_c	Cone semi vertex angle, deg
Λ	Sweep angle, deg

NOMENCLATURE (Concluded)

Symbol	Description
μ	Viscosity, (kg/m-sec, lbm/ft-sec)
ρ	Density, (kg/m^3, lbm/ft^3)
Subscripts	
c	Cone
o	Total
r	Reference
W	Wall
∞	Free stream
δ	Post shock conditions
si	Strong interaction

Appendix D

D.1 NON-CONTINUUM HEATING RATE CALCULATION METHODS

Given in Tables D-1 through D-4 are the equations from Ref. D-1 which were used to develop the computer program for calculation of non-continuum heating rates

D.2 MATERIAL CHARACTERISTICS

The following properties were used for the Langley low density ablative material:

$$\rho = 224 \text{ kg/m}^3$$
$$K = 6.74 \times 10^{-2} \text{ W/m-}^\circ\text{K}$$
$$C_p = 1.5 \times 10^3 \text{ J/kg-}^\circ\text{K}$$
$$\epsilon = 0.8$$

For the LI-900 material the following properties were used:

(Room Temperature, 10^{-4} Atm)

$$\rho = 144 \text{ kg/m}^3$$
$$K = 1.56 \times 10^{-2} \text{ W/m-}^\circ\text{K}$$
$$C_p = 0.71 \times 10^3 \text{ J/kg-}^\circ\text{K}$$
$$\epsilon = 0.8$$

D.3 LEE-SIDE HEATING

Figure D-1 shows the heating rate distribution curve used in predicting lee-side heating rates for the AMOOS vehicles. Figure D-1 is from Ref. D-2.

D.4 RADIATIVE-TYPE TPS MASSES

Figure D-2 shows the curve used in determining masses per unit area and temperature limits for various radiative type TPS materials.

REFERENCES

D-1. Engel, C. D., "Aeroheating Correlations for Non-Continuum Hypersonic Flight," RTR-008-2, REMTECH, Inc., Huntsville, Ala., December 1972.

D-2. Stevens, R. A. et al., "Reentry Heat Transfer to a Delta Wing Space Shuttle Booster at High Angles of Attack," FZA-452, General Dynamics, Convair Division, Fort Worth, Texas, March 1971.

Table D-1

TRANSITIONAL FLOW SHARP CONE HEAT TRANSFER EQUATIONS

(1) $T_r = T_W + (T_\delta - T_W)/2 - T_\delta \cos^2 \theta_c/3$

(2) $R_{e_\infty} = \dfrac{\rho_\infty U_\infty X}{\mu_\infty}$

(3) $C^* = \dfrac{\mu_r T_\infty}{\mu_\infty T_r}$

(4) $\xi = \dfrac{C_H}{\sin\theta_c} \left(1 - \dfrac{T_W}{T_\delta}\right)$

(5) $X_c = \dfrac{Re_\infty}{M_\infty^2 \gamma_\infty C_* \cos\theta_c}$

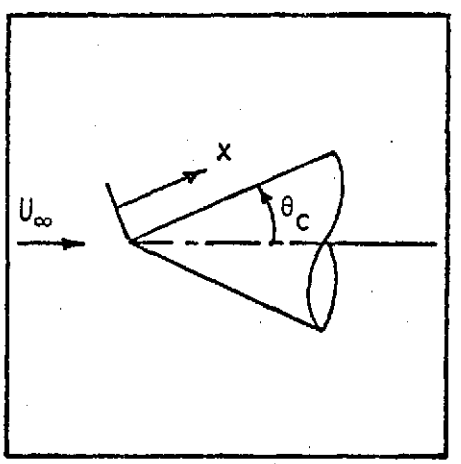

(6) Correlation Equation

$$\log_{10}(\xi) = \sum_{i=0}^{2} a_i (\log_{10} X_c)^i$$

$a_0 = -0.392510$

$a_1 = -0.266308$

$a_2 = -0.0598724$

(7) Heat Transfer

$q = \rho_\infty U_\infty C_H (H_\infty - H_W)$

Table D-2

TRANSITIONAL FLOW SHARP FLAT PLATE
HEAT TRANSFER EQUATIONS

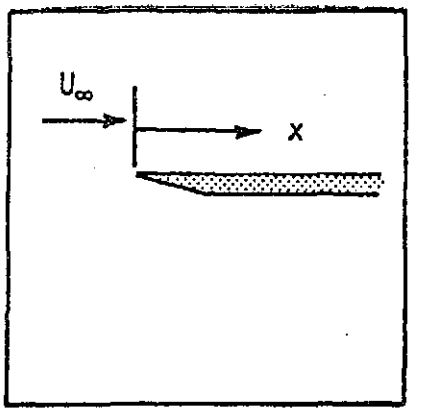

(1) $T_o = T_\infty \left(1 + \frac{\gamma - 1}{2} M_\infty^2\right)$

(2) $Re_\infty = \frac{\rho_\infty U_\infty X}{\mu_\infty}$

(3) $C_* = \frac{\mu_W T_\infty}{\mu_\infty T_W}$

(4) $\beta = (T_W/T_o)^{1/2} M_\infty^2 C_*/Re_\infty$

(5) $C_{H_{si}} = (0.368 T_W/T_o + 0.0684) \left[M_\infty (C_*/Re_\infty)^{1/2}\right]^{3/2}$

(6) $\frac{C_H}{C_{H_{si}}} = \frac{1}{2}\left[1 - \tanh (0.91 \log_{10} \beta + 1.10)\right]$

for $\beta < 0.1$

(7) Heat Transfer

$q = \rho_\infty U_\infty C_H (H_\infty - H_W)$

Table D-3

TRANSITIONAL FLOW YAWED CYLINDER
STAGNATION LINE HEAT TRANSFER EQUATIONS

(1) $T_r = \frac{1}{2} (T_w + T_\delta \cos^2 \Lambda)$

(2) $Re_\infty = \frac{\rho_\infty U_\infty R}{\mu_\infty}$

(3) $C_* = \frac{\mu_r T_\infty}{\mu_\infty T_r}$

(4) $\tilde{k}^2_\Lambda = \frac{Re_\infty}{\gamma_\infty M_\infty^2 C_* \cos\Lambda}$

(5) $\xi = C_H / \cos\Lambda$

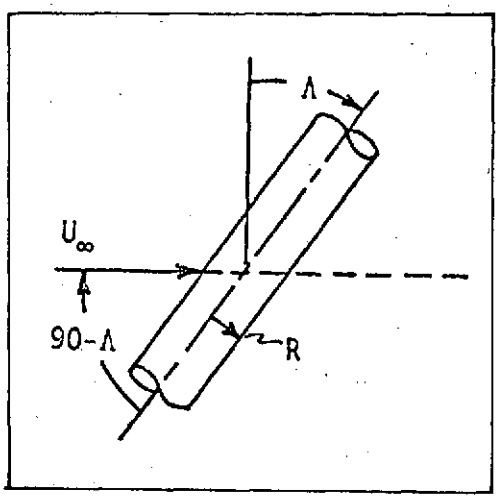

(6) Heat Transfer Correlation

$$\log_{10} \xi = \sum_{i=0}^{2} a_i (\log_{10} \tilde{k}^2_\Lambda)^i$$

$a_o = -0.377656$

$a_1 = -0.368580$

$a_2 = -0.0461064$

(7) Heat Transfer

$q = \rho_\infty U_\infty C_H (H_\infty - H_W)$

Table D-4

TRANSITIONAL FLOW STAGNATION POINT HEAT TRANSFER EQUATIONS

(1) $T_r = (T_\delta + T_w) / 2$ (Reference temperature)

(2) $T_o = T_\infty \left(1 + \frac{\gamma - 1}{2} M_\infty^2\right)$ (Free stream stagnation temperature)

(3) $k^2 = \varepsilon \left(\frac{\rho_\infty U_\infty R}{\mu_r}\right) \left(\frac{T_r}{T_o}\right)$

where $\varepsilon = \frac{\gamma - 1}{2\gamma}$

(4) Heat transfer coefficient

$$\log_{10} (C_H) = \sum_{i=0}^{2} a_i (\log_{10} k^2)^i$$

$a_o = -0.235256$

$a_1 = -0.303095$

$a_2 = -0.0779538$

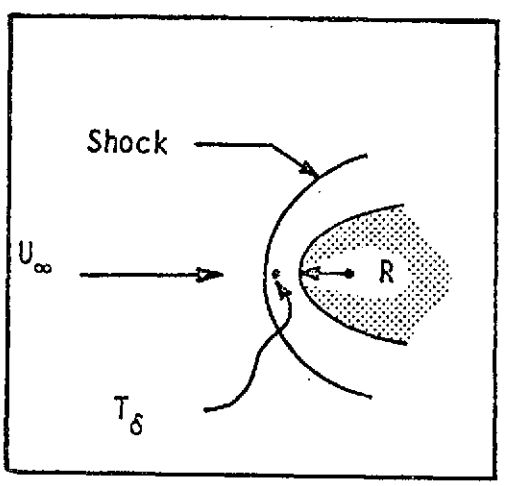

(5) Heat transfer

$q = \rho_\infty U_\infty C_H (H_\infty - H_w)$

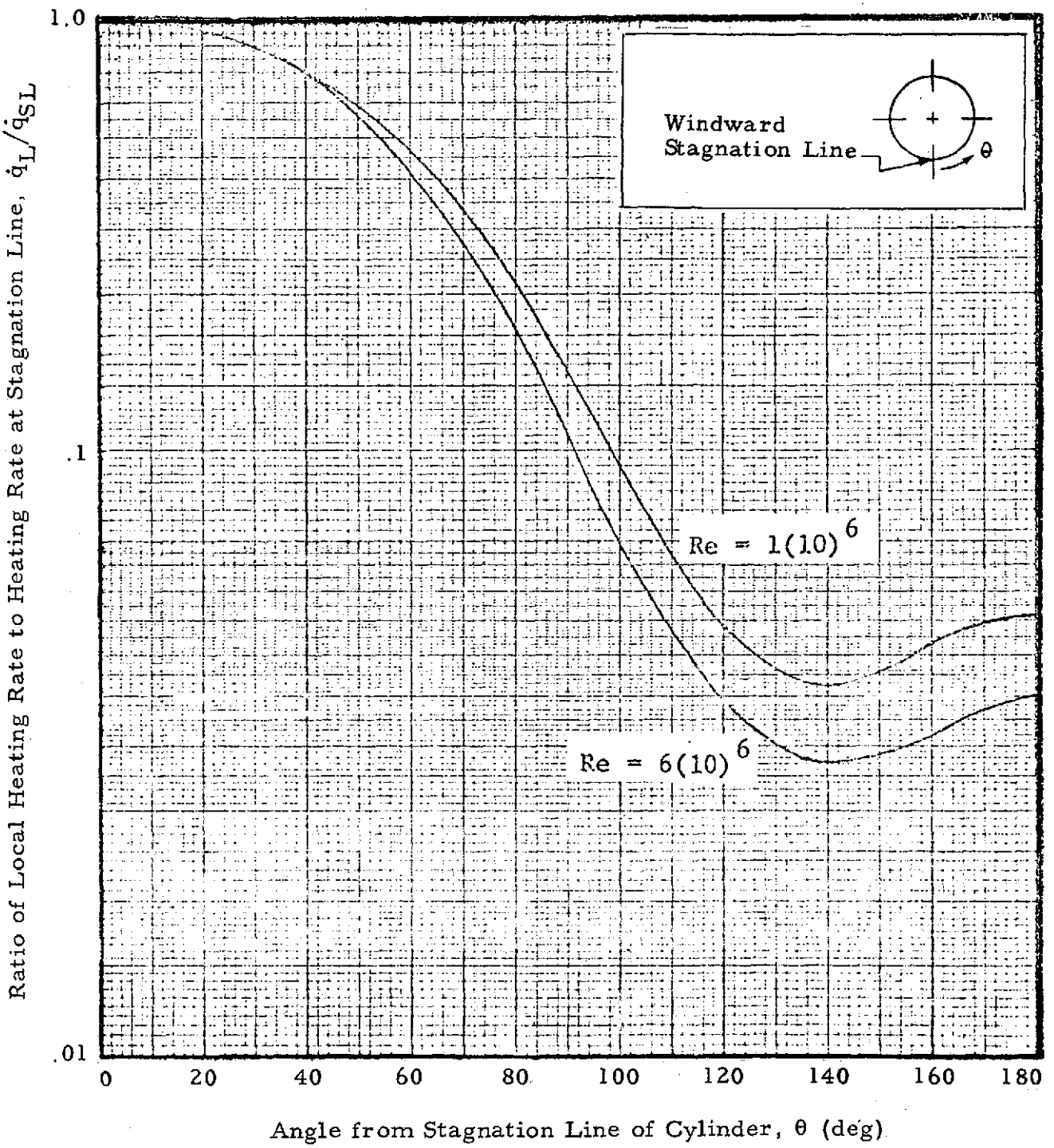

Fig. D-1 - Heating Rate Distribution Around AMOOS Vehicle at 45° Angle of Attack

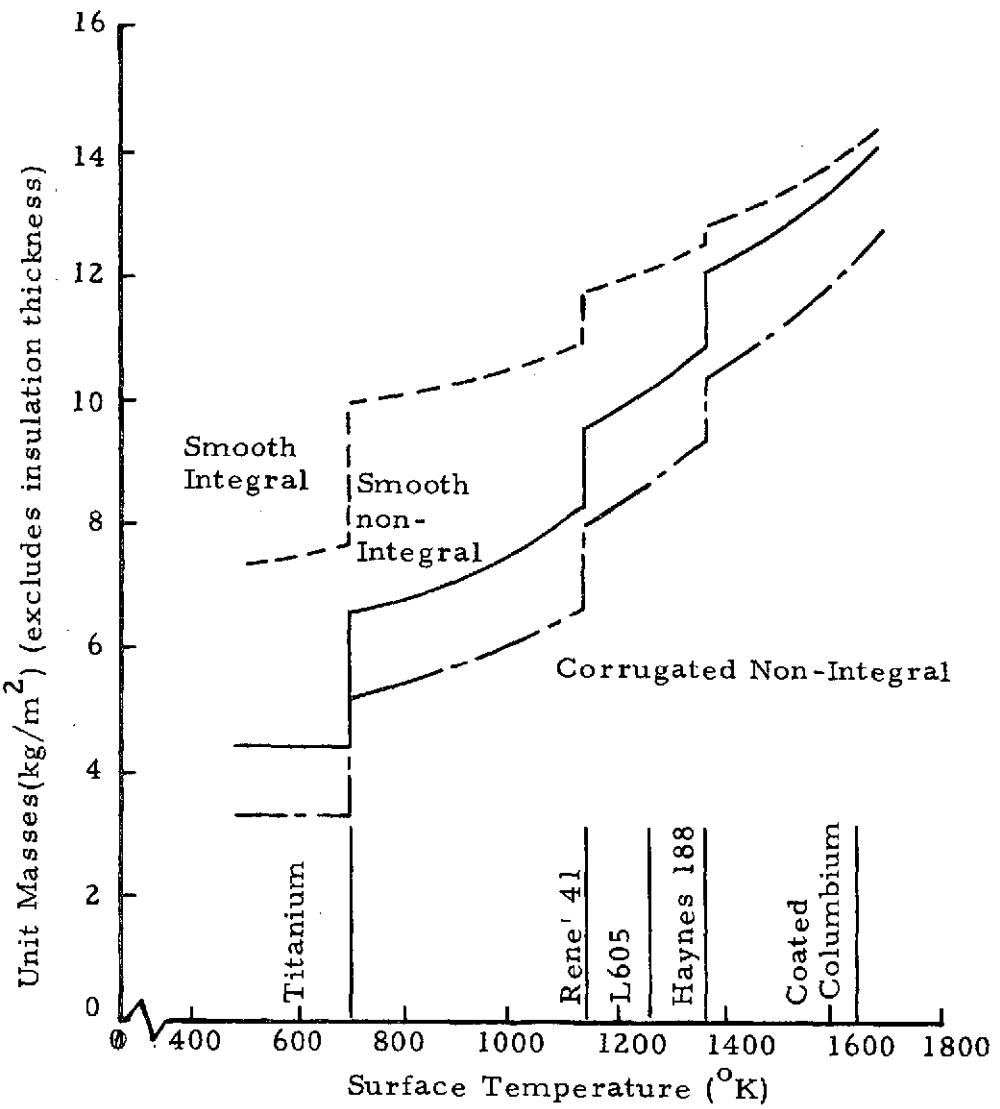

Fig. D-2 - Mass per Unit Area for Various Radiative-Type TPS Materials

Appendix E
AMOOS BASELINE MISSION OPERATIONS ANALYSIS

Appendix E

E.1 GROUND OPERATIONS FOR LAUNCH

- Ground support equipment (GSE) is connected and systems are checked.
  a. Electrical checkout
  b. Leak checks
  c. Visual checks
  d. Simulated flight checkout.

- Payload is installed in AMOOS and AMOOS/payload interface is checked.

- AMOOS is installed in orbiter and AMOOS/orbiter interface is checked.
  a. AMOOS is covered with an ablative thermal protection system (TPS) that is relatively fragile compared to the metallic structure. Careful unloading and loading is critical.
  b. All EOS/AMOOS hard attachment points are located on the sides and top of AMOOS. No hatches or hard points are on the bottom side of the vehicle due to the extreme heating experienced during aeromaneuvering.
  c. Due to (b) all umbilical attachments are on the leeward side of the vehicle and the vehicle is installed upside down in the orbiter cargo bay.
  d. With (a), (b) and (c) in mind, special loading and unloading devices must be designed so that AMOOS can be loaded and unloaded from the EOS cargo bay with the EOS in a vertical or horizontal position.

- AMOOS is fueled while in the orbiter; vents are working. (Vented gases pass through umbilicals to the orbiter for venting to the outer environment.)

E.2 LAUNCH AND ABORT

- During launch AMOOS propellant gases are vented through the Shuttle system.
- The orbiter inserts into initial orbit.
- The orbiter inserts into operations orbit.
- Abort procedures for AMOOS
  a. If separated from the orbiter, AMOOS returns to the orbiter if the emergency allows.
  b. If AMOOS malfunctions in the cargo bay or is nearby the orbiter, e.g., from (a) then abort can be carried out according to preplanned procedures.
  c. If the emergency is with the Shuttle system instead of AMOOS the basic abort procedure for AMOOS is to dump its propellants.
     - If abort occurs in suborbital flight after liftoff, then only partial dumping can be accomplished due to time limitation.
     - If abort occurs in orbital flight then there is time to dump all propellants.
  d. If an AMOOS emergency occurs when the Shuttle system is on the launch pad, AMOOS is removed with the orbiter still in its vertical launch position.

E.3 DEPLOYMENT AND RETRIEVAL OF AMOOS

- Due to the relatively fragile ablative TPS, considerable care in deployment must be observed.
- Upon retrieval the temperature of AMOOS must be measured to determine the necessity of using special procedures to deal with a hot vehicle.

- AMOOS deployment

  a. Propellant and electrical umbilicals are disconnected.

  b. The secure hard points are released.

  c. The orbiter pole arm locks onto AMOOS and rotates the vehicle about an orbiter residing structure that is attached to the base of the vehicle.

  d. The base structure releases the vehicle and the pole arm extends AMOOS and releases it.

- AMOOS retrieval is just the opposite of deployment.

E.4 ORBITAL MANEUVERS (see Fig. E-1)

- Prior to EOS separation, AMOOS subsystems are activated and checked out, and EOS inputs AMOOS and target state vectors to AMOOS computer.

- EOS deploys AMOOS and burns APS until a safe distance away.

  a. AMOOS flap is deflected, main engine nozzle is extended and main engine and APS systems are checked.

  b. EOS checks rest of AMOOS system for mission readiness.

  c. If readiness is not indicated abort procedures are inacted.

- AMOOS will fly on its side with respect to the earth due to navigation requirements (except for aerobraking and if broiling method of thermal control is used). See Fig. E-2.

  a. Earth sensors — horizon tracker, landmark tracker, etc. — are on the side of the fuselage that faces the earth.

  b. Star sensor is on the opposite side that faces away from the earth.

- Orbit coast operations

  a. APS are fired to orient AMOOS for star sensor and earth sensor data acquisition.

b. Using sensor data, the IMU is aligned and the state vector is updated.

c. EOS sends AMOOS a set of orbital data to verify the updated state vector on (b).

d. AMOOS computes the burn parameters for geosynchronous transfer orbit insertion.

e. AMOOS maneuvers to burn attitude.

f. AMOOS downlinks its subsystems status to ground.

- Transfer orbit

a. Main engine perigee burn into transfer orbit is performed.

b. After required Δv is obtained sensor data is acquired, IMU is aligned and the state vector is determined.

c. AMOOS checks subsystems and downlinks subsystem status.

d. The above procedure for transfer orbit insertion is essentially the same for any orbit insertion.

e. If a midcourse correction is required IMU is aligned, state vector is updated, burn parameters are computed, AMOOS is maneuvered to burn attitude and APS engines are fired.

f. After burn the IMU is aligned, the state vector is updated and subsystems status is downlinked.

- Geosynchronous orbit insertion

a. Main engine burn inserts AMOOS into synchronous orbit.

b. Preburn and post-burn procedures are similar to those of the transfer orbit burn.

c. A ground based navigation update system is likely to be required to achieve a payload positioning at geosynchronous orbit such that the drift rate is within generally accepted limits.

d. Variance from planned orbit is determined and an APS correction burn is performed.

- Deploy payload

a. AMOOS is maneuvered to attitude for payload deployment.

b. TV camera makes sure payload clears AMOOS safely and then inspects payload.

c. AMOOS maneuvers a safe distance away and performs stationkeeping until payload operational status is verified.

- Rendezvous phasing orbit

  a. APS or main engine is burned for rendezvous phasing orbit insertion.

  b. Midcourse correction is performed if necessary.

- Rendezvous burn is performed with APS or main engine

- Payload retrieval

  a. AMOOS points to target line of sight based on onboard data.

  b. Search mode is actuated until laser radar locks onto payload.

  c. AMOOS updates its own state vector with data it acquires.

  d. AMOOS maneuvers to intercept payload using APS.

  e. TV is activated when range is sufficiently close (optional).

  f. Guidance and control data are transmitted to ground control. The onboard computer will accept override signals for attitude control and translational maneuvers.

  g. Ground commands are executed as needed.

  h. Docking maneuvers are computed and executed

  i. APS nozzles must be properly located such that no plume impinges upon payload while docking maneuvers are being performed.

  j. The payload is attached and secured in AMOOS.

- Aeromaneuvering orbit

  a. AMOOS phase coast to burn time.

  b. Main engine burn inserts vehicle into aeromaneuvering orbit.

  c. A ground based update to AMOOS enables an accurate midcourse correction to be made at an economical attitude.

d. After the update, the midcourse correction is made to hit the aeromaneuvering reentry corridor.

- Aeromaneuvering

  a. Immediately before reentry, an onboard sensor or a ground link will update state vector. The IMU alone will be used during reentry. The flap is deflected so the vehicle will trim at angle of attack of maximum lift.

  b. APS is used for bank angle modulation which varies the lift vector. Consequently some of the motors have much larger thrust than the ones on the Tug.

  c. The varying lift vector in (b) is used to adjust trajectory for density errors and to give AMOOS an aerodynamic plane change capability.

  d. TPS smoke contamination must be taken into account.

  e. The effects of center-of-gravity travel due to burned-off TPS must be determined.

  f. Heat sensors will be used to help predict abort conditions due to overheating.

  g. Thermal space radiators and/or louvers and G, N&C sensors must be protected from both heat and particle contamination.

  h. The aerodynamic drag causes a Δv drop to achieve phasing orbit apogee.

- A main engine burn to achieve phasing orbit perigee is performed.

- The main engine inserts AMOOS into EOS rendezvous orbit.

- EOS/AMOOS docking

  a. EOS senses position of AMOOS relative to itself.

  b. AMOOS maintains attitude and provides passive docking support for EOS sensors so the EOS can determine its position and attitude.

  c. If necessary AMOOS can become the active docking vehicle.

  d. The two vehicles perform terminal maneuvers and AMOOS then holds its attitude.

  e. EOS sensors detect and lock onto AMOOS.

f. Communications are established.

g. EOS approaches docking range to AMOOS.

h. AMOOS propellant is vented and dumped.

i. EOS performs docking maneuvers and docks and secures AMOOS.

j. Propellant tanks are vented again and made inert with helium.

k. All subsystems are deactivated for reentry.

- EOS deorbits, reenters and lands with AMOOS in an essentially dormant state.

E.5 PAYLOAD DEPLOYMENT AND RETRIEVAL

- Laser radar and TV camera must be protected with hatches which are opened for payload deployment and retrieval. (Subsystems for docking are optional.)

- TV camera must be capable of viewing payload while docking and deploying and both inside and outside of AMOOS.

- AMOOS cargo bay doors are configured like those of the orbiter.

- The docking and retrieving modes are to be developed.

- Hard points and/or a special docking truss must be designed into the AMOOS cargo bay.

E.6 POST-LAUNCH OPERATIONS

- Upon return from a mission, AMOOS propellant tanks are inerted, insulation is purged and payload is unloaded.

- AMOOS is transferred to maintenance facility where GSE checks subsystems and maintenance is performed as scheduled or required.

a. NDE tests
b. Visual tests
c. Electrical tests

} Valves, actuators, computer, G, N&C equipment, structure, seals, etc.

d. Check operation of external moving parts such as hatches and flap.

e. In addition to seeing forces like those on the Tug, AMOOS incurs high temperature and aerodynamic forces and therefore maintenance and checkout analysis must take this into consideration.

f. Refurbishment

- Ablative TPS must be completely stripped down to structural skin and replaced.
- High temperature bearings and seals (e.g., those on flap) have limited life.

g. Again, during storage of vehicle, precautionary measures must be taken to avoid damaging ablative TPS.

- Flight performance data are analyzed.

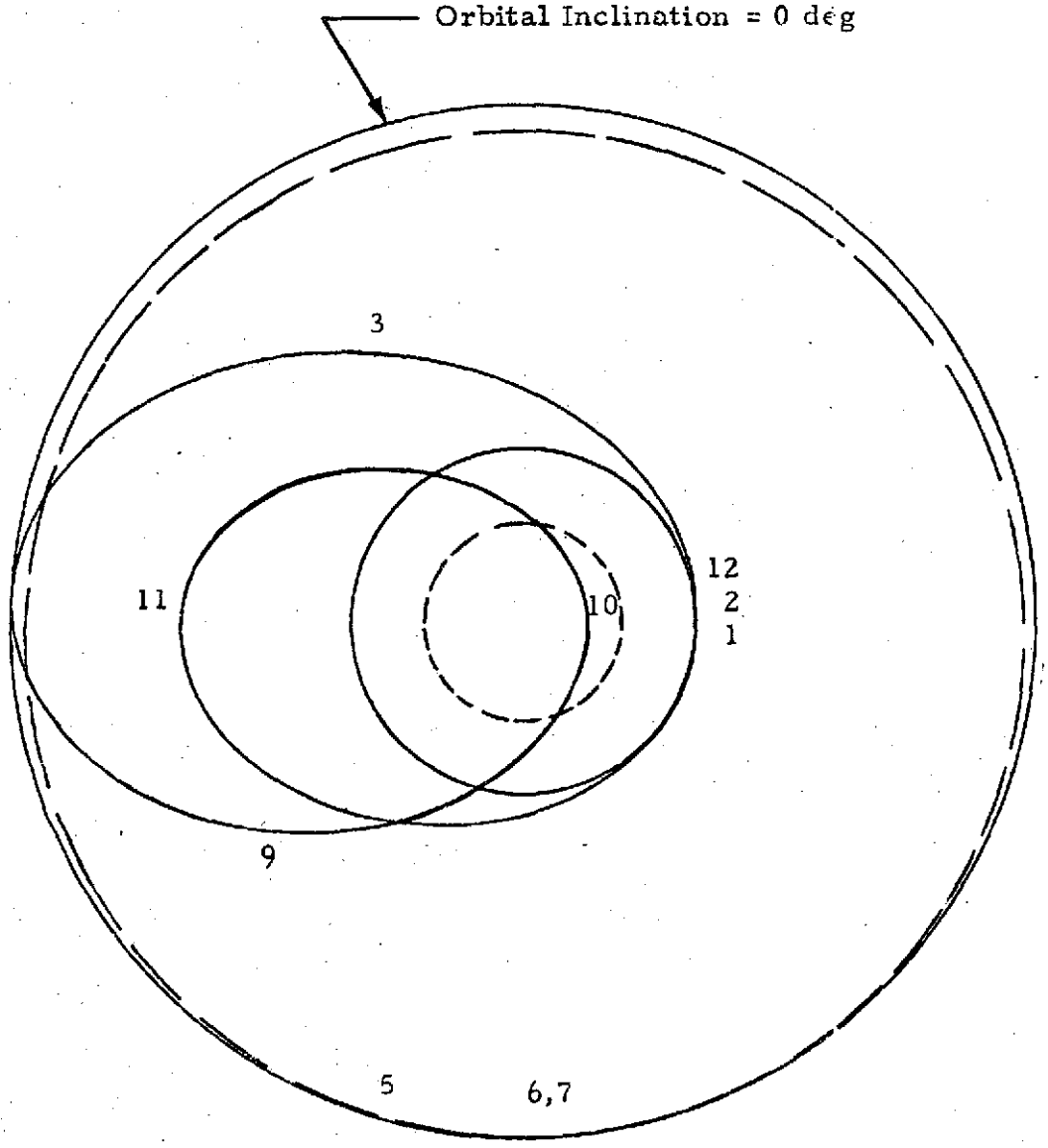

1. Delivered to 296 km Circular Orbit by the EOS
2. Burn to Mission Transfer Orbit
3. Midcourse Correction
4. Burn-to-Mission Orbit
5. Deliver Payload
6. Burn-to-Phasing Orbit for Rendezvous with Return Payload
7. Rendezvous and Dock with Return Payload
8. Burn-to-Transfer to Aeromaneuvering Orbit*
9. Midcourse Correction*
10. Aeromaneuver to Phasing Orbit Plane and Apogee*
11. Burn-to-Achieve Phasing Orbit* Perigee
12. Burn-to-EOS Rendezvous Orbit

*Denotes AMOOS Maneuvers Distinct from Space Tug Maneuvers.

Fig. E-1 - AMOOS Mission Profile

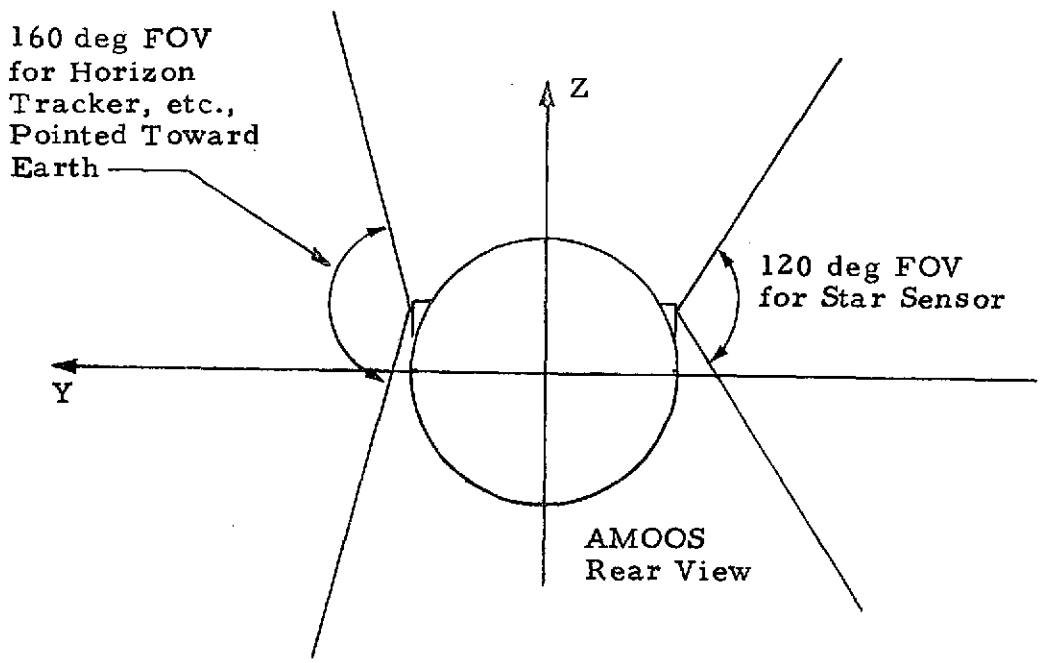

Fig. E-2 - AMOOS Sensor Locations

Appendix F
COSTING ASSUMPTIONS

Appendix F
COSTING GROUND RULES

A. All costs are based on Government fiscal year 1970 dollars.

B. No prime contractor fee is included.

C. Facility costs are not included.

D. Operations costs are not included.

E. NASA program management and integrating contractor's costs are not included.

F. Only the first production unit is costed.

G. AMOOS flight test costs include $5.0M per Space Shuttle launch.

H. Two flight test vehicles and four Space Shuttle launches are the basis for flight test costing.

I. NASA provided the main engine costs: DDT&E is $130.0M and first production unit is $0.7M.

AMOOS COST WORK BREAKDOWN STRUCTURE

I. TOTAL STRUCTURE

A. Body Structures: tank supports; thrust structure; primary structure; mounting hardware, meteoroid shield, and umbilicals; and flap.

B. Main Tanks: LOX and LH_2 tanks.

C. Docking: refers to AMOOS/payload and EOS/AMOOS interface equipment that remains with AMOOS upon separation from EOS.

II. PROPULSION

A. 44,480 N (10,000 lb) thrust main engine.

B. Pressure, Feed and Vent: feed, fill, drain and vent systems; main tank's pressurization system; and main engine propellant utilization system.

C. APS (Auxiliary Propulsion System): includes rocket motors, mechanism to produce gaseous oxygen and hydrogen, and associated plumbing.

III. AVIONICS

A. Data Management: computer system and data input/output interface units.

B. G,N&C (Guidance, Navigation and Control): IMU, star tracker, horizon sensor and landmark tracker.

C. Communications and Tracking: laser radar; TV camera and control; and S-Band communications equipment including antennas.

D. Instrumentation: sensors and associated circuitry.

E. Electrical Power Distribution: circuitry buses, switches and wiring.

IV. THERMAL PROTECTION

A. High Performance Insulation: multilayer insulation and mounting hardware and accommodations for LOX and LH_2 tanks.

B. Insulation Purge System.

C. Thermal Control: passive avionics thermal control and APS plume impingement protection.

D. External TPS: ablative TPS and microquartz insulation.

V. POWER

A. Fuel Cell.

B. Hydraulics: engine gimbal and actuation system.

VI. EOS/AMOOS Interface (all equipment to stay with EOS): docking structure, fluid and electric umbilicals and AMOOS subsystem checkout equipment.

VII. TESTING

A. Ground Test Operations: the planning, conducting, and data analyzing of structural, hot firing, and thermal vacuum tests.

B. Flight Test Operations: the planning, conducting and data analyzing of tests of on-orbit ascent, descent and aero-maneuvering characteristics.

C. Test Hardware: a battleship, four static test articles, a dynamic test article and two flight test vehicles.

D. Wind Tunnel Testing: the planning, conducting and data analyzing of wind tunnel tests and model construction.

VIII. GSE: Ground Support Equipment such as subsystem checkout, ground handling and maintenance and refurbishment equipment.

IX. Initial Tooling and Special Test Equipment: design, fabrication, modification and maintenance of all tools and test equipment needed in the production of the AMOOS vehicle.

X. Logistics and Spares: spares and repair parts required for operations.

XI. Training: ground crew instruction and associated simulators and equipment.

XII. Systems Engineering and Integration: integration of development activities such as establishing design characteristics and criteria; defining procedures for vehicle tests; creating maintenance procedures; and assuring safety and reliability.

XIII. Program Management: program planning, control and other administration functions.

Table F-1

MASSES USED AS A BASIS FOR COSTING

Cost Item	Mass (kg)
Body Structures	1425.8 (5B Be-38Aℓ) 1320.8 (HB Be-38Aℓ) 1339 (5B Magnesium) 2341 (5B Titanium)
Tank Supports	67.0
Thrust Structure	30.8
Primary Structure	1255 (5B Be-38Aℓ) 1150 (HB Be-28Aℓ) 1168 (5B Magnesium) 2170 (5B Titanium)
Mounting Hardware, Meteroid Shield, Umbilicals	73.0
Main Tanks	301.3
Docking Mechanisms, Payload/AMOOS and AMOOS/EOS	48.0
Main Engine	Mass Not Used
APS	Mass Not Used
Pressurization, Feed & Vent	Mass Not Used
Data Management	204.8
Guidance, Navigation and Control	68.8
Communications and Tracking	85.1
Instrumentation	22.7
Electrical Power Distribution	107.2
High Performance Insulation	Mass Not Used
Insulation Purge	Mass Not Used
Thermal Control	Mass Not Used
External TPS	646.6 (5B LRC Ablator) 669.2 (HB LRC Ablator) 708.1 (5B Martin Ablator)
Fuel Cell	35.7
Hydraulics	Mass Not Used